

3D BIOPRINTING FOR POTENTIAL
USE IN NASAL CARTILAGE
RECONSTRUCTION

Laura Alejandra Ruiz Cantu, DS. MSc.

Thesis submitted to the University of Nottingham for the degree
of Doctor of Philosophy

September 2017

Abstract

3D printing is an additive manufacturing technique that is rapidly gaining traction in health and medical applications. This technique could potentially benefit plastic and reconstructive surgeries by fabricating patient-specific tissue replacements with tissue-like functions and mechanical properties. One specific example in the field of plastic and reconstructive surgery is nose reconstruction. Current gold standard for nasal reconstruction after rhinectomy or severe trauma involves a three stage surgery that requires a minimum of three and maximum of seven operations to achieve an acceptable result. The surgical procedure require transposition of autologous cartilage grafts in conjunction with coverage using an autologous skin flap. Harvest of autologous rib cartilage requires a major additional procedure which creates donor site morbidity. Additionally, major nasal reconstruction also requires sculpting autologous cartilages to form a cartilage framework, which is complex, highly-skill demanding and time-consuming.

These drawbacks of the current approach for nasal reconstruction are some of the reasons why facial plastic and reconstructive surgeons are interested in the application of tissue engineering and 3D printing for reconstructive surgeries. To address these clinical challenges, the aim of the work presented in this thesis was to fabricate a personalised 3D bioprinted composite scaffold for nasal reconstruction mimicking the mechanical properties and architecture of nasal cartilage. The composite consists of

biodegradable thermoplastic polycaprolactone (PCL) to provide structural support, and cell-laden thermoresponsive and UV crosslinkable gelatin methacrylate (GelMA) to act as a cell carrier.

We first investigated the appropriate cell source to use for cartilage tissue engineering and 3D bioprinting. Primary sheep articular chondrocytes (ShCh) and sheep bone marrow derived Mesenchymal Stem Cells (ShMSCs) were isolated, expanded and differentiated; followed by an assessment of the effects of the 3D printing process on cell viability and functionality. From these studies it was observed that ShCh were easier to isolate and expand than ShMSCs because less steps are required and the doubling time is 50% shorter. Additionally, 80% of the ShCh survived the printing process compared to a 50% of the ShMSCs, suggesting that chondrocytes were able to tolerate higher stress caused by the 3D printing process.

PCL and poly (lactic-co-glycolic acid) (PLGA) scaffolds were printed and seeded with chondrocytes post-printing. The printing process and the 3D printed structures of these polymers were characterised before and after printing by measuring their molecular weight, thermal and mechanical properties. It was found that the printing process reduced the molecular weight of PLGA by 50% percent due to thermal degradation. Consequently, its glass transition temperature and young's modulus decreased post printing. On the contrary, PCL's molecular weight remain unchanged after printing. Characterisation of the chondrocytes showed that whilst both scaffold materials supported cell attachment the ECM secreted deformed the PLGA whilst the PCL

scaffolds were unaffected. Due to superior mechanical properties PCL was selected to 3D print the personalised nose scaffolds. Additional studies on the 3D printed scaffolds showed that controlling the surface pores of scaffolds was important for cell infiltration and proliferation. Scaffolds with larger surface pores were 3D printed and these resulted in increased cell seeding and proliferation demonstrated by DNA quantification.

Moreover, the printing process of the cell carrier GelMA was optimised by utilising its thermoresponsive properties. A rheological study of three different concentrations of GelMA was performed in order to identify the most suitable for bioprinting. GelMA 15% and 20% at 15 °C and 18 °C respectively were found the appropriate ones. Finally, multi-material 3D bioprinting of PCL and chondrocyte-laden GelMA was utilised for making cartilage constructs. The 3D bioprinted constructs showed neocartilage formation and similar mechanical properties to nasal alar cartilage after a 50-day culture period. Neocartilage formation was evidenced by the presence of glycosaminoglycans and collagen type II after cultivation. The findings in this thesis therefore support the feasibility of using 3D bioprinted composite constructs for nasal reconstruction.

Acknowledgements

I would like to take this opportunity to thank my supervisors Dr Jing Yang, Professor Kevin Shakesheff and Dr Joel Segal for their patient guidance, enthusiastic encouragement and useful critiques throughout the four years of my PhD studies

My grateful thanks to my collaborators Dr Andrew Gleadall for the 3D printing software he designed for me, his help on constructing the hood for the 3D printer and for our publication on characterization of the surface geometry of the 3D printed scaffolds, to Mr. Callum Faris for allowing me to come into his surgical theater to observe the different stages of a nose reconstruction.

I would like also to acknowledge the following people who provided me valuable training during my PhD Research: Dr James Rose for GelMA synthesis, Dr Helen Cox for rheology, Dr Glen Kirkham for microscopy, histology and immunohistochemistry, Dr Hasan Rishadi for cryo sectioning, Dr Lisa White and Dr Jane McLaren for microCT, Mr. Raphael VVenger from Regengu for 3D printing and Mrs. Teresa Marshal for various lab equipment. Many thanks to Dr Jane McLaren for allowing me to come and harvest cartilage from the sheep she was using on her *in vivo* studies. Also many thanks to my colleague Pritesh Mistry for bringing endless fun to each day of lab work.

Finally, I want to express my gratitude to my mum for her support and encouragement during my study and my husband for guiding me during my first year of PhD, always been there for discussing my research and being patient with me on my stressful times.

Declaration of Figures & Data Authorship

All graphics, diagrams and videos were authored solely by Laura Ruiz for the purposes of this thesis or presentations during the course of doctoral study.

All figures, tables and other associated data were produced solely by Laura Ruiz with exceptions listed below.

1. Figure 3.8 was produced by Andrew Gleadall for our collaborative paper
2. The images on Figure 3.27 and 3.28 were taken by my master student Bin Hairuddin Haikhal under my supervision
3. The GPC data on figure 3.29 was obtained by Vincenzo Taresco from the GPC facilities.
4. The mock surgery on Figure 3.31 was performed by Mr Callum Faris
5. The microscopy images on Figure 3.32 were taken by Andrew Gleadall for our collaborative paper
6. Diagram on Figure 4.2 was produced by Andrew Gleadall for our collaborative paper.

Current Published Papers

Ruiz, L., Gleadall, A., Faris, C., Segal, J., Yang, Y., Shakesheff, K. Characterisation of the surface geometry of 3D printed scaffolds for cell infiltration and surgical suturing. *Biofabrication*. 8(1), 015016

Liao,Z., Sinjab, F., Nommeots-Nomm, A., Jones, J., Ruiz, L., Yang, J., Rose, F., Notingher, I. Feasibility of spatially-offset Raman spectroscopy for in-vitro and in-vivo monitoring mineralisation of bone tissue-engineering scaffolds

Conferences Presented at

- FIRM Symposium (2014) (Oral presentation)
- Termis America 2014, Washington DC, USA (2014) (Oral presentation)
- Advances in 3D Printing Technology for Medical and Biological Applications Conference (2014) (Oral presentation)
- Tissue and cell engineering society conference (2015) (Oral presentation)
- TERMIS World Congress (2015) (poster)
- Biofabrication conference (2015) (poster)
- EPSRC centre closing conference (2015) (Oral presentation)
- Tissue and cell engineering society conference (2016) (Oral presentation)
- FIRM symposium (2016) (Oral presentation and invited speaker)

Contents

Abstract	3
Acknowledgements	6
Declaration of Figures & Data Authorship	8
Current Published Papers	9
Conferences Presented at	9
List of figures	19
List of Tables	24
List of Abbreviations	25
Chapter 1. Introduction to current nose reconstruction techniques and the field of 3D bioprinting for Renegerative Medicine	25
1.1. Introduction	25
1.1.1. Nose anatomy	26
1.1.1.1. External nose anatomy	26
1.1.1.2. Internal nose anatomy	32
1.1.2. Nasal disorders requiring surgery	33
1.1.3. Current surgical reconstruction method	34
1.1.3.1. Nasal lining	36
1.1.3.2. Nasal framework	37
1.1.3.3. External skin covering	39

1.1.3.4. Limitations of current surgical approach	41
1.1.4. Tissue engineering approaches for cartilage reconstruction	42
1.1.4.1. Cartilage biology and types	42
1.1.4.2. Materials used in cartilage tissue engineering	44
1.1.4.3. Cell sources for tissue engineering cartilage	48
1.1.5. 3D printing in tissue engineering and Regenerative medicine	51
1.1.5.1. 3D printing techniques	53
1.1.6. Materials for 3D bioprinting	56
1.1.6.1. Hydrogels	57
1.1.6.2. Thermoplastics	58
1.2. Summary of introduction and future aims	61
Chapter 2. Identification of a suitable cell type and characterisation of cell viability during 3D Bioprinting process	65
2.1. Introduction	65
2.2. Materials and methods	70
2.2.1. Isolation of cellular material	70
2.2.1.1. Chondrocytes isolation	70
2.2.1.2. Bone Marrow derived Mesenchymal stromal cells isolation	72
2.2.2. Monolayer cell culture and cryopreservation	72
2.2.2.1. Culture of Sheep Chondrocytes	72
2.2.2.2. Culture of Bone Marrow derived Mesenchymal Stromal Cells	73
2.2.2.3. Sheep Chondrocytes and Sheep Bone Marrow derived Mesenchymal Stromal Cells cryopreservation	73

2.2.3. Sheep Chondrocytes characterisation	74
2.2.3.1. Monolayer culture of Sheep Chondrocytes in TGF- β supplemented medium	74
2.2.3.2. ShCh population doubling time	74
2.2.3.3. Pellet culture of Sheep Chondrocytes in TGF- β supplemented medium	75
2.2.4. Sheep bone marrow derived Mesenchymal Stromal Cells characterisation	75
2.2.4.1. Osteogenic differentiation	75
2.2.4.2. Adipogenic differentiation	76
2.2.4.3. Chondrogenic differentiation	76
2.2.5. Histological staining	76
2.2.6. Viability studies	77
2.2.5.1. GelMA concentration effect on cells viability	77
2.2.5.2. Temperature effect on cells viability	78
2.2.5.3. UV effect on cells viability	78
2.2.5.4. Genotoxicity effect of UV on cells	78
2.2.5.6. Needle gauge effect on cells viability.	79
2.2.5.7. 3D Bioprinting process effect on cell viability	79
2.3. Results and discussion	81
2.3.1. Sheep chondrocytes isolation from different sources	81
2.3.2. Sheep chondrocytes characterisation	84
2.3.2.1. Sheep chondrocytes expansion	84
2.3.2.2. Sheep chondrocytes differentiation	88
2.3.3. Sheep bone marrow derived stromal cells isolation and characterisation	89
2.3.4. Viability studies of Sheep chondrocytes	91
2.3.4.1. GelMA effect on sheep chondrocytes viability	91

2.3.4.2. Temperature effect on sheep chondrocytes viability	92
2.3.4.3. UV exposure effect on sheep chondrocytes viability	93
2.3.4.4. Genotoxicity effect of UV exposure on sheep chondrocytes	95
2.3.4.5. Effect of needle size on ShCh viability	96
2.3.4.6. Effect of the complete 3D bioprinting process on ShCh viability	98
2.3.5. Viability studies of Sheep bone derived mesenchymal stromal cells	99
2.3.5.1. Effect of GelMA on the ShMSCs	99
2.3.5.2. Effect of UV exposure on bone marrow derived mesenchymal stromal cells	100
2.3.5.3. Effect of the complete Bioprinting process on bone marrow derived mesenchymal stromal cells	102
2.4. Conclusions	104
Chapter 3. Personalised 3D models design and development of techniques for 3D printing polycaprolactone and poly (lactic-co-glycolic acid)	105
3.1. Introduction	105
3.2. Materials and methods	110
3.2.1. Design of 3D models, g-code generation and 3D printing	110
3.2.3.1. Design of the personalised nose models	110
3.2.3.2. 3D model CAD design and g-code generation using SLT converter	114
3.2.3.3. Design of models with BioCAD	115
3.2.3.3. Design of the models with newly-developed software	115
3.2.3.4. 3D printing thermoplastics	116
3.2.2. Material and 3D printed scaffolds characterisation	117

3.2.2.1. Rheological measurements	117
3.2.2.2. Differential Scanning calorimetry and gel permeation chromatography	117
3.2.2.3. MicroCT	118
3.2.2.4. Tensile and compression mechanical test	119
3.2.2.5. Microscopy	119
3.2.3. Cell seeding in 3D printed scaffolds	120
3.2.3.1. Scaffolds treatment before seeding	120
3.2.3.2. Static cell seeding	120
3.2.3.3. Dynamic cell seeding	121
3.2.3.4. Cell number quantification and proliferation	121
3.2.3.5. Osmium tetroxide and histological staining	122
3.3. Results and Discussion	123
3.3.1. Design of the models	123
3.3.2. Characterisation of 3D printing polycaprolactone	124
3.3.2.1. Rheological properties	125
3.3.2.2. Thermal analysis	128
3.3.2.3. Characterisation of the 3D printing method for polycaprolactone	128
3.3.2.4. Effect of porosity on mechanical properties	134
3.3.2.5. Effects of the heat on polycaprolactone during the 3d printing process	135
3.3.2.6. 3D printed PCL nose	137
3.3.2.7. Culture of chondrocytes on the 3d printed scaffolds PCL scaffolds	139
3.3.3. Characterisation of 3D printing poly (latic-co-glycolic acid)	140
3.3.3.1. Rheological properties of PLGA	141
3.3.3.2. Thermal analysis of PLGA	142

3.3.3.3. Optimisation of the 3D printing method for PLGA	143
3.3.3.4. Effects of the 3D printing process on poly (lactic-co-glycolic acid)	149
3.3.3.5. Culture of cells on the PLGA 3D printed scaffolds	151
3.3.4. Surgical test of the 3D printed nose scaffolds	153
3.3.5. Surface porosity characterisation	155
3.3.5.1. Surface porosity and pores size and mechanical properties	155
3.3.5.2. Cells seeding with static and dynamic method	159
3.3.5.3. Cells distribution and proliferation	165
3.4. Conclusions	169
Chapter 4. 3D bioprinting: characterisation of GelMA and 3D printing of multi-material cellular composites for cartilage regeneration	171
4.1. Introduction	171
4.2. Materials and methods	176
4.2.1. Gelatin methacrylation	176
4.2.2. GelMA hydrogels preparation	177
4.2.3. Rheological testing	177
4.2.4. 3D printing of GelMA hydrogels	178
4.2.5. 3D bioprinting and cell culture of GelMA/chondrocytes constructs	179
4.2.6. Microscopy	180
4.2.7. Turbidity assay	180
4.2.8. Biochemical assays	180
4.2.7.1. DMMB assay	181
4.2.7.2. DNA content assay	182

4.2.9. Histological analysis	182
4.2.10. Cryo sectioning	182
4.2.11. Histological staining	182
4.2.12. Immunohistochemistry	183
4.2.13. Mechanical testing	183
4.2.14. 3D multi-material bioprinting	184
4.3. Results and Discussion	185
4.3.1. GelMA characterisation	185
4.3.1.1. GelMA degree of methacrylation	185
4.3.1.2. GelMA rheological properties	186
4.3.1.3. Effect of UV crosslinking time on GelMA complex modulus	189
4.3.2. Optimisation of GelMA printing process	190
4.3.3. Bioprinting of cells encapsulated in GelMA and characterisation of the tissue engineered cartilage-like structures	193
4.3.3.1. Non-porous GelMA/chondrocytes constructs.	193
4.3.3.2. Porous GelMA/chondrocytes constructs	196
4.3.4. Co-printing thermoplastics and GelMA	204
4.4. Conclusions	209
Chapter 5. Summary and future directions	210
References	220
Appendices	243

Appendix 1: videos	243
Appendix 1.1. PCL 3D printed nose	243
Appendix 1.2. PCL-GelMA co-printing	243
Appendix 2: solutions	243
2.1. Isolation of cells	243
2.1.1. PBS solution	243
2.1.2. PBS A/A	244
2.1.3. Collagenase digestion medium (0.2%)	244
2.1.4. Heparinised medium	244
2.2. Cell culture	244
2.2.1. Standard ShCh culture medium	244
2.2.2. ShMSCs culture medium	245
2.2.3. Cryopreservation medium	246
2.2.4. Osteogenic medium	246
2.2.5. Adipogenic medium	246
2.2.6. Chondrogenic differentiation medium	247
2.3. Biochemical analysis	247
2.3.1. LIVE/DEAD solution	247
2.3.2. Papain solution	248
2.3.3. DMMB solution	248
2.4. Histological analysis	249
2.4.1. Histology working solutions	249
2.5. Immunohistochemistry analysis	249

List of figures

Figure 1.1 External nose anatomy.	27
Figure 1.2. Bony pyramid.....	28
Figure 1.3. Septolateral cartilage and lobule parts.	30
Figure 1.4. Blood and nerve supply.....	32
Figure 1.5. The aesthetic topographical subunits of the nose.....	35
Figure 1.6. Radial forearm free flap	37
Figure 1.7. Nasal framework reconstruction using rib cartilage	39
Figure 1.8. External skin covering with forehead flap to ensure ideal blood supply ...	40
Figure 1.9. The main 3D printing methods used for bioprinting are inkjet printing, laser assisted printing and extrusion printing.....	53
Figure 1.10. Main objectives of the thesis.....	62
Figure 2.1 Hyaline cartilage and fibrocartilage isolation.	71
Figure 2.2 Auricular cartilage isolation.....	71
Figure 2.3 Representative images of Sheep Chondrocytes monolayer culture after isolation from the condyle.	85
Figure 2.4 Representative images of monolayer cell culture of ShCh in standard medium and TGF- β supplemented medium.	87
Figure 2.5 Alcian blue staining of ShCh cultured in monolayer and pellet	89
Figure 2.6. Sheep Bone Marrow derived Stem Cells monolayer culture.....	90
Figure 2.7. Trilineage differentiation of ShMSCs.....	90
Figure 2.8. Viability of ShCh in different concentrations of GelMA	92
Figure 2.9. Viability of chondrocytes at different temperatures for different timing...	93
Figure 2.10 ShCh viability after UV exposure.....	94

Figure 2.11 Genotoxicity assessment of ShCh after UV exposure for different timings.	96
Figure 2.12. ShCh viability after been printed with different nozzle gauges.....	98
Figure 2.13 ShCh viability after being 3D Bioprinted in different GelMA concentrations.....	99
Figure 2.14 ShMSCs viability when cultured in different GelMA concentrations....	100
Figure 2.15. ShMSCs viability after UV exposure.....	101
Figure 2.16 ShMSCs viability after being 3D bioprinted.....	103
Figure 3.1 Import DICOM files.....	111
Figure 3.2 Thresholding.	111
Figure 3.3. Segmentation.....	112
Figure 3.4. Cropping.....	112
Figure 3.5. Cropping.....	113
Figure 3.6. Create 3D model	113
Figure 3.7 . Edition of 3D model and create STL file.....	114
Figure 3.8 Schematic of the six scaffold types investigated in this study.....	116
Figure 3.9 3D nose model created using the CT scan of the patient	124
Figure 3.10 Viscosity of polycaprolactone against temperature	126
Figure 3.11 Viscosity of polycaprolactone with increasing shear rates going from 10^{-3} (1/s) to 10^2 (1/s).	127
Figure 3.12 Polycaprolactone melting point measured with DSC was 58 °C.....	128
Figure 3.13. Images of samples 3D printed at feeding rates of 10, 15 and 20 rpm....	129
Figure 3.14. Samples 3D printed at building speeds of 10, 16 and 20 mm/s.....	130
Figure 3.15 Scaffolds of layer thickness of 100 μ m.....	131

Figure 3.16 Scaffolds with layer thickness of 150 μ m.....	132
Figure 3.17 Control of environmental printing temperature	133
Figure 3.18 porosity of scaffolds related with spacing within the strands.	134
Figure 3.19 Mechanical properties of samples with (A) 24% porosity, (B) 57% porosity (C) and 72% porosity.....	135
Figure 3.20 Effects of the heat during the 3D printing process on PCL stability.	137
Figure 3.21 3D printed nose-shaped PCL scaffolds.....	139
Figure 3.22 Chondrocytes seeded on PCL scaffolds after 14 days in culture.....	140
Figure 3.23 Viscosity of PLGA.....	142
Figure 3.24 Glass transition temperature of PLGA.....	143
Figure 3.25 PLGA 3D printed scaffolds.....	144
Figure 3.26 3D printed PLGA scaffolds.....	146
Figure 3.27 PLGA scaffolds printed at different environmental temperatures.....	147
Figure 3.28 PLGA scaffolds after culture for 14 days in PBS at 37 °C.....	148
Figure 3.29 Effect of 3D printing on PLGA 50 material properties.	150
Figure 3.30 Chondrocytes seeded in PLGA scaffolds.....	152
Figure 3.31. Mock surgery using the PCL 3D printed nose model.....	154
Figure 3.32 . Microscope and microCT images of the different scaffold designs.	156
Figure 3.33. A) Surface porosity measured from microCT images,	159
Figure 3.34. Cell infiltration into 3D printed scaffolds using both static and dynamic seeding methods.	162
Figure 3.35. 3D plots representing the relation between pore size, porosity and cell number with static and dynamic seeding.....	164

Figure 3.36. Cell distribution inside the scaffolds on day 1 for static and dynamic seeding.....	165
Figure 3.37. Cell proliferation on the different end angles and repeated layers	167
Figure 3.38 PCL nose 3D created with different software.....	168
Figure 4.1. Formula to calculate GelMA degree of methacrylation.....	177
Figure 4.2. Model for the multi-material bioprinting of PCL and GelMA/chondrocytes.	184
Figure 4.3 ¹ H NMR spectra of gelatin and GelMA samples.	186
Figure 4.4. Rheological properties of GelMA.....	188
Figure 4.5. Complex modulus of 10%, 15% and 20% GelMA after UV exposure ...	190
Figure 4.6. Images of GelMA printing optimisation.....	192
Figure 4.7. Overall change in appearance of the 3D bioprinted GelMA/chondrocytes constructs from day 0 to 46	194
Figure 4.8. Cells proliferation and GAGs secretion during 50 days in culture.....	196
Figure 4.9. Images of the gross morphology of 3D bioprinted porous GelMA cell laden constructs from day 0 to 50 in culture.	198
Figure 4.10. Chondrocytes stained with calcein AM (green) to study cell distribution.	199
Figure 4.11. Cryo sections of day 50 GelMA/chondrocytes constructs stained with DAPI (blue) representing cells distribution.	200
Figure 4.12. Proliferation, GAGs secretion and mechanical properties of 3D bioprinted GelMA/chondrocytes constructs during culture.....	203
Figure 4.13. Multi-material constructs	205

Figure 4.14. Control showing the PCL scaffold submerged in GelMA and crosslinked	205
Figure 4.15.....	207
Figure 4.16. Co-printed GelMA/PCL samples in culture.....	208

List of Tables

Table 1.1. Materials used in cartilage tissue engineering.....	45
Table 2.1. Chondrocytes isolation from condyle, meniscus and ear.....	82
Table 2.2 Cell counts from different cartilage sources.....	83
Table 2.3 ShCh cultured in TGF- β supplemented medium population doublings and doubling time.....	88
Table 4.1 chondroitin sulphate standards	181

List of Abbreviations

ACI	autologous chondrocytes implantation
CAD	computer aided design
CIJ	continuous inkjet printing
CT	computer tomography
dH ₂ O	distilled water
DICOM	digital imaging and communications medicine
DM	degree of methacrylation
DMEM	Dulbecco's Modified Eagle's medium
DMSO	Dimethyl sulfoxide
DNA	deoxyribonucleic acid
DOD	drop on demand
DT	doubling time
EBM	electronic beam melting
ECM	extra cellular matrix
EDTA	ethylenediaminetetraacetic acid
FCS	fetal calf serum
FDA	food and drug administration
FDM	fused deposition modelling
FDM	fused deposition modelling
FGF-2	fibroblastic growth factor 2
GA	glycolic acid
GAGs	glycosaminoglycan

GelMA	gelatin methacrylate
HEPA	High efficiency particulate air
HIF	hypoxia inducible factor
ID	internal diameter
LA	lactic acid
LAB	laser assisted bioprinting
MACI	matrix assisted autologous chondrocytes implantation
microCT	micro computer tomography
Mn	average molecular weight
Mpa	mega pascals
MSCs	mesenchymal stromal cells
MW	molecular weight
NEEA	non-essential aminoacids
OCT	optimal cutting temperature
Pa-s	pascals per second
PBS	phosphate buffer saline
PCL	polycaprolactone
PD	population doublings
PDLA	poly (D-lactic co-glycolic acid)
PED	precision extrusion deposition
PEG	poly ethylene glycol
PFA	paraformaldehyde
PLGA	poly (lactic co-glycolic acid)

PLLA	poly (L-lactic co-glycolic acid)
RS	residual stress
ShCh	sheep chondrocytes
ShMSCs	sheep mesenchymal stromal cells
SLA	stereolithography
SLS	selective laser sintering
STL	stereolithography
TFG-B1	Transforming growth factor B1
Tg	glass transition temperature
UV	ultra violet
α -MEM	minimum essential medium

Chapter 1. Introduction to current nose reconstruction techniques and the field of 3D bioprinting for Regenerative Medicine

1.1. Introduction

The nose is the most identifiable feature that defines human face. Deformities caused by trauma, cancer surgery and malformations can have physical and psychological effects on the patients (Borges et al. 2000). The nose is comprised of hyaline cartilage, fibro-fatty tissues, internal nasal lining and skin (Watelet & Van Cauwenberge 1999). The current surgical approach for nose reconstruction is a three stage surgery that involves harvesting rib cartilage, and manually fashioning it into a nose-shaped framework. The technical requirements to fashion the rib into a nose-shaped framework are high because of requirements for a complex three-dimensional architecture and multilayer construct. Once completed the framework is then covering by autologous skin and inner nasal lining (Menick 2009). Due to the complexity of the technique, the duration of the operation can exceed 8 hours, during which time the patient is under general anaesthesia (Cannady, T. A. Cook, et al. 2009). In addition, the harvest large amounts of rib cartilage is associated with postoperative chest wall deformities, high levels of postoperative pain and risks iatrogenic pneumothorax. These drawbacks of the current approach for nasal reconstruction are the reasons why facial plastic and reconstructive surgeons are interested in the application of tissue engineered tissues and 3D printing for reconstructive surgeries. In this chapter we are going to review the anatomy of the nose, the different nasal disorders that can lead to nose deformity and the current surgical methods for reconstruction. Additionally, we will review the tissue engineering approaches for cartilage regeneration and the 3D printing and bioprinting

techniques and materials that could be used for cartilage tissue engineering and nose reconstruction.

1.1.1. Nose anatomy

For study and surgical purposes, human nose anatomy has been divided into two discreet areas, the external and internal nose (Watelet & Van Cauwenberge 1999). The external nose comprises the bony pyramid, the cartilaginous pyramid and the soft tissue pyramid while the internal nose is composed from the mucosa, turbinates and septum (Jones 2001). Detailed description of the external and internal nasal anatomy is described below as well as the how nasal anatomy relates to nasal reconstruction.

1.1.1.1.External nose anatomy

The external nose is comprised of four main parts. The upper third is made up by the bony pyramid, the middle third by the cartilaginous pyramid and the lower third by the lobule (Figure 1.1A). The fourth part comprises the soft tissue areas (Jones 2001) (Figure 1.1B). These four parts construct the nasal framework formed by the underlying rigid fixation of the cartilaginous pyramid with the bony pyramid, and the overlapping junction between the cartilaginous pyramid and the lobule (Natvig et al. 1971). According to some authors, there are four soft tissue areas and they allow the outward and inward movement of the triangular cartilages during respiration (Huizing and Groot 2003).

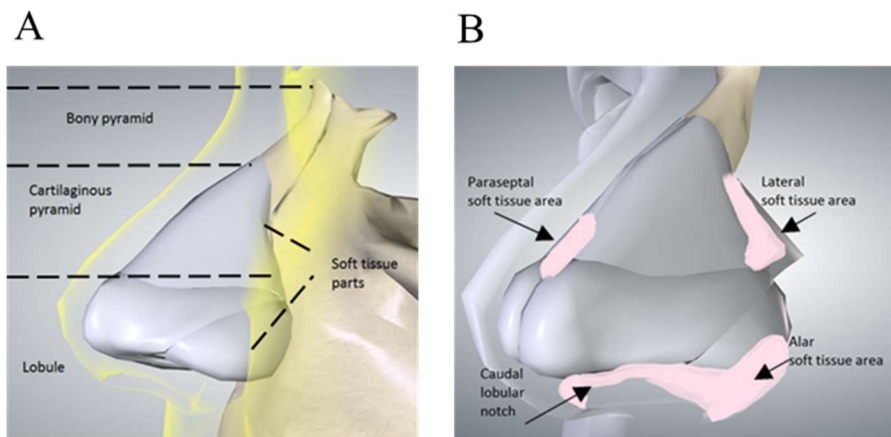


Figure 1.1 External nose anatomy. (A) Four main parts of the external nose: bony pyramid, cartilaginous pyramid, lobule and soft tissue parts. (B) Soft tissue areas of the nose: paraseptal lateral, alar and caudal lobular notch.

The bony pyramid comprise of the nasal bones, the nasal spine of the frontal bone and the two frontal processes of the maxilla (Huizing and Groot 2003) (Figure 1.2). The nasal bones are attached to each other in the midline by serrated borders that form the internal nasal suture. (Driscoll, Baker, and Drisco 2001). The frontal processes of the maxillary bones are strong plates that construct the dorsal part of the bony pyramid.

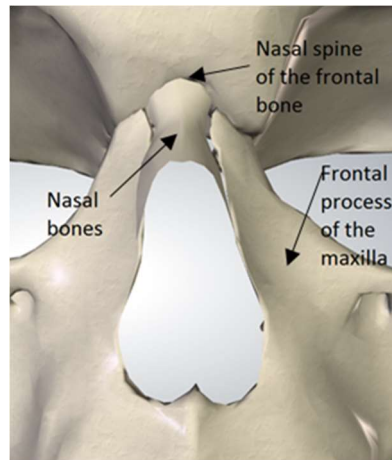


Figure 1.2. Bony pyramid comprised by the nasal spine, nasal bones and frontal process of the maxilla

The cartilaginous pyramid consists of the septolateral cartilage and two lateral membranous areas with one to three accessory cartilages. The septolateral cartilage is made up by the two upper lateral cartilages or triangular cartilages and the cartilaginous septum (Figure 1.3A). The cartilaginous septum at its caudal portion has a free end that is connected to the collumela. Ventrally, it is continuous with the two upper lateral cartilages. Forming together a single cartilaginous unit named dorsum. The cartilaginous septum serves as a principal structural support of the dorsum and is shock absorber (Holden, Liaw, and Wong 2008). The upper later cartilage cranial margin is firmly attached to the nasal bones. The dorsal margin is connected to the lateral soft tissue with a very loose fixation that allows the inward and outward movements from the upper lateral cartilage during respiration. The caudal margin is related with the lobular cartilage (Figure 1.3B). This relationship can vary, but the most common is an

overlapping from the caudal margin of the lateral cartilage to the cranial margin of the lateral crus of the lobular cartilage (Huizing and Groot 2003).

The lobule is the caudal third of the external nose (Figure 1.3C). It is structurally supported by two lobular cartilages, muscle fibres, subcutaneous connective tissue and fatty tissue. The lobular cartilage determines the configuration of the nasal tip, and gives cosmetic definition to the nose (Holden, Liaw, and Wong 2008). Many important anatomic landmarks exist with respect of this structure (Michelotti and Mackay 2012). According to some authors, the lobular cartilage is divided into medial, intermediate and lateral crus, and the dome.

Anatomically the lobule is divided into five parts that are the tip, the alae, the columella, the nostrils and the vestibule (Figure 1.3C). The tip is made from the union of the two domes of the lobular cartilages. Its size, shape and orientation depend from them. The alae are the mobile lateral walls of the lobule that are constructed by the lateral crura of the lobular cartilage, and the overlaying muscles and skin. The collumela is the midline structure running from the upper part of the lobule and the upper lip. It is composed of the medial and intermediate crus of the lobular cartilage, and the cartilaginous septum. Its configuration is influenced by the lobular cartilage as well as that of the caudal septum. The nostrils or nares are the orifices of the lobule. They are surrounded by the collumela, the alae and the nostril sill. The vestibule is the cavity between the nostril and the valve area. It is cover squamous epithelium with vibrissae that offer protection to the entrance of the respiratory tract (Jones 2001).

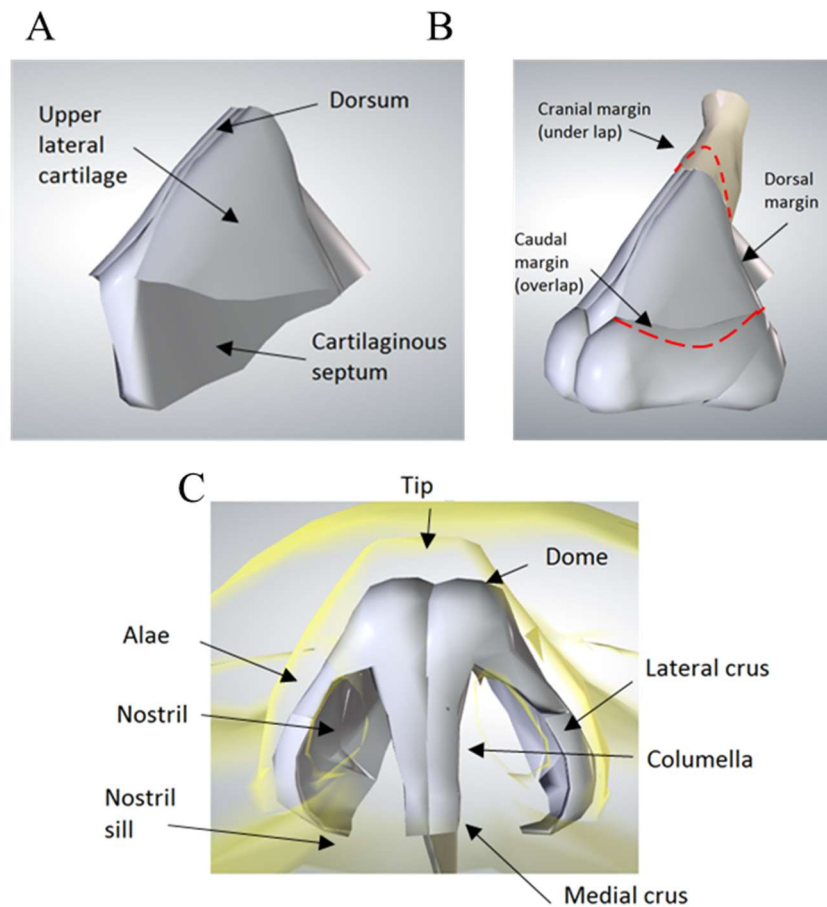


Figure 1.3. Septolateral cartilage and lobule parts. (A) The septolateral cartilage parts are the cartilaginous septum, upper lateral cartilage and dorsum. (B) Margins of the septolateral cartilage and over and under laps with cartilage and bone parts. (C) the lobule parts that determine the shape of the nasal tip.

The external nose is covered from outside to inside by the skin, the superficial fatty panniculus, the fibromuscular layer, the deep fatty layer and the periosteum or perichondrium. The thickness of the skin varies according the gender, age, climatological influences (Huizing and Groot 2003) and the region of the nose. The skin is thinner and more mobile in the upper half of the nose and along the nostril rims and inferior columella; while, it is thicker and more adherent at the nasal tip and alae (Oneal and Beil 2010). The superficial fatty panniculus is made up by adipose tissue and

vertical fibrous septa running from the dermis to the fibromuscular layer. The fibromuscular layer is composed by the nasal musculature and the nasal subcutaneous muscular aponeurotic system. The deep fatty layer does not contain fibrous septa, and here are located most of the superficial blood vessels and nerves. The periosteum and perichondrium are dense connective tissue layers that cover and provide nutrient blood flow to the nasal bones and the perichondrium, respectively (Bleys et al. 2007).

The blood supply of the external nose (Figure 1.4A) is mostly provided from branches of the facial artery and the ophthalmic artery. The alae and nostril are supplied by the lateral nasal artery a branch from the facial artery. The collumelar and nostril sill are supplied by the collumelar artery a branch from the superior labial artery which is a branch from the facial artery. The nasal tip is supplied by the external nasal artery, a branch from the ethmoidal artery which is a branch from the ophthalmic artery. The dorsum is supplied by the dorsal nasal artery a branch from the ophthalmic artery (Baker 2011).

The nerve supply of the external nose (Figure 1.4B) is derived from five different nerves originated from the ophthalmic nerve and maxillary nerve. The nasal root is innervated by the supraorbital nerve. The bony pyramid is innervated by the supratrochlear and infratrochlear nerves. The cartilaginous pyramid is innervated by the infratrochlear, external branch of the anterior ethmoidal and infraorbital nerves. The last two nerves also innervate the lobule (Huizing and Groot 2003).

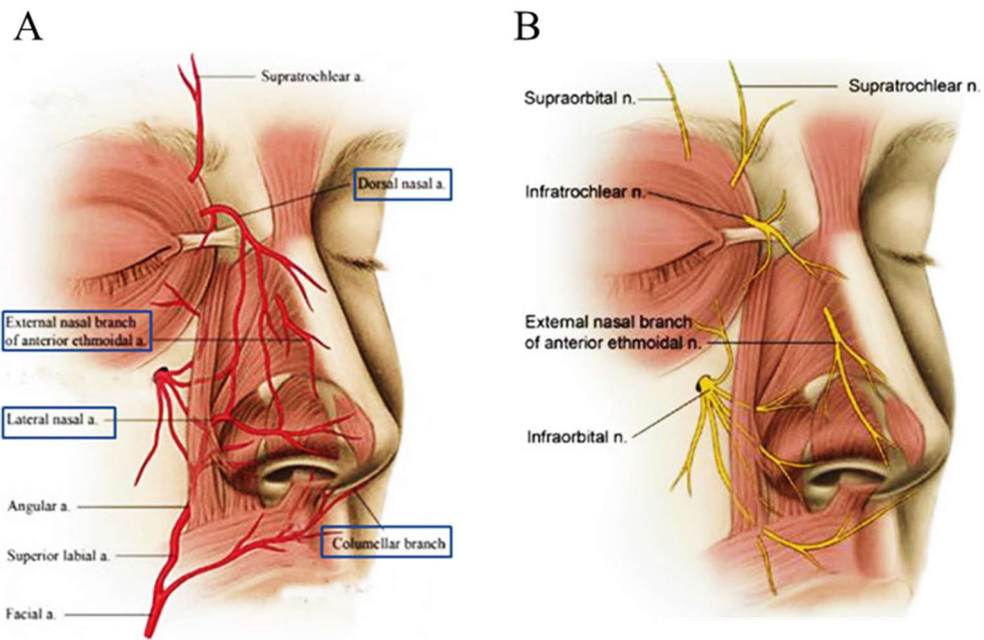


Figure 1.4. Blood and nerve supply (A) Blood supply of the nose is mainly provided by the dorsal nasal artery, lateral nasal artery, the external nasal branch of the anterior ethmoidal artery and the columellar branch. (B) nerve supply of the external nose is derived from branches of the ophthalmic nerve and the maxillary nerve.

1.1.1.2. Internal nose anatomy

The internal nose or nasal cavities are composed from the nasal valve, the turbinates, the septum and the mucosa. The nasal cavities are two independent passages that begin at the limen nasi which is a bridge between the vestibule and the nasal cavity. The end of these passages is the nasopharynx. The floor of the nasal cavities is formed by the upper side of the hard palate, while the roof is formed by the underside of the nasal pyramid (Baker 2011). The nasal valve is a teardrop shape area which gives access to the internal nose and also is the narrowest part of the same (Huizing and Groot 2003)

The lateral wall of the nasal cavities supports the three turbinates: superior, middle and inferior (Watelet and Van Cauwenberge 1999). The turbinates are scrolls of bone covered by mucosa. The superior turbinate and middle turbinates are part of the ethmoid bone, whilst the inferior turbinate is derived from the maxillary bone. The nasal cavities are separated by the septum. The septum is composed from two different structures: the cartilage and bone. The anterior part is formed by the cartilaginous septum and the posterior part by the perpendicular plate of the ethmoidal bone (Huizing and Groot 2003).

1.1.2. Nasal disorders requiring surgery

The destruction of the external nose can be caused by several conditions including traumatism, infections, abuse of toxic substances, inflammatory processes and cancer. Among them, cancer is the principal cause of a subtotal or total nasal destruction. The most common type of nasal cancer is squamous cell carcinoma which principally affects the nasal vestibule. Over half of nasal cancer are these types. This cancer is derived from the transformation of the squamous epithelial cells, a type of cell that line the vestibule, into squamous cell carcinomas. Other types of nasal cancer are adenocarcinomas, adenoid cystic carcinomas, and mucoepidermoid carcinomas, but these are less frequent (Dulguerov et al. 2001)

According to Surveillance, Epidemiology, and End Results Program (SEER) Cancer Statistics Review 1975-2014 from the National Cancer Institute, 2,000 people in the United States develop these cancers each year (Howlander et al. 2017). Based on Cancer Research UK statistic in the UK around 400 nasal cavity and paranasal sinus cancer are

diagnosed each year. The average age of people when they are diagnosed with these cancers is 64 and Men are slightly more likely than woman to get these cancers (Young et al. 2010).

The treatment for nasal cavity cancer depends on the stage, location, size and depth of penetration of the tumour. Depending on the stage of the cancer diverse treatment options can be used including resection surgery, radiotherapy, chemotherapy and targeted therapy. During the surgery of these cancers the entire tumour and a small amount of normal tissue around have to be removed. In some cases, after these surgeries the patients end with a hemi-nasal defect, but in others where the tumour is widely spread the patient ends with a total nasal defect. After resection surgery, the patient can undergo to surgical reconstruction techniques, prosthetic rehabilitation or a combination of both the methods to restore these facial disfigurements. The site, size, and aetiology of the defect, age, general medical condition and desire are used to determine the methods of reconstruction.

1.1.3. Current surgical reconstruction method

The nose has a three dimensional architecture divided in nine aesthetic subunits that are identified topographically because each one has different convex or concave surface. These units comprise the lobule, dorsum, paired sidewalls, paired alae, paired soft tissue triangles, and the columella (Baker 2011) (Figure 1.5). Because of the three dimensional shape, the reconstruction of the structures of the nose is one of the most difficult compare with other structures in the face. Moreover, reconstruction of the nose requires

restoring aesthetic and normal nasal function. The nasal defects can be classified as partial, which just affect parts of the aesthetic subunits or complete subunits, subtotal when affects several subunits, and total nasal defects. The total nasal defect is defined as “bilateral through –and- through loss of nasal skin, cartilage/bone, and lining mucosa”(Cannady et al. 2009).

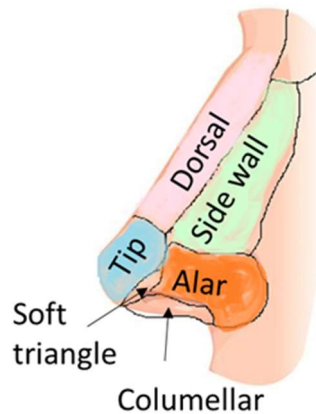


Figure 1.5. The aesthetic topographical subunits of the nose are paired sidewalls, paired alae, paired soft tissue, collumella and tip.

Reconstruction of total or near total nasal defects is complicated because involves the re-creation of a 3 layer construction: internal nasal lining, cartilaginous and bone nasal framework, and external skin covering (Pabla, Gilhooly, and Visavadia 2013). Reconstruction should ideally use tissue similar to native tissue. The gold standard for total nasal reconstruction is the use of microvascular free flaps for nasal lining, cartilage and rib grafts for the framework and paramedian forehead flap for skin coverage (Burget and Walton 2007). Suitable techniques will be reviewed below.

1.1.3.1.Nasal lining

The primary functions of the nasal lining are moistening and humidify the inhaled air (Cannady et al. 2009). Each nasal subunit is lined by different types of tissue that can vary between skin, hairy skin and mucosa. Different options exist for reconstruct the nasal lining some of them are skin grafts, mucosal flaps, local flaps, and microvascular free flaps.

The most used free flap for reconstruction is the radial forearm free flap (Figure 1.6) . Other kinds of free flaps have been described, such as the dorsal metacarpal artery flap and the free anterolateral thigh fascia lata flap. The main advantages of free flaps are that they offer good vascularization to the bone and cartilage grafts and can be used to replace large sections (Cannady et al. 2009). The radial forearm free flap is elevated as a skin subcutaneous flap based on the multiple fine perforators of the radial artery. In some cases these free flaps are prelaminated before being transferred (Walton, Burget, and Beahm 2005) and in others the inner lining are constructed by using the flap three islands in order to avoid contraction (Burget and Walton 2007). After being transferred the vascular pedicle is tunnelled subcutaneously and anastomosed to the facial artery (Seth et al. 2013).

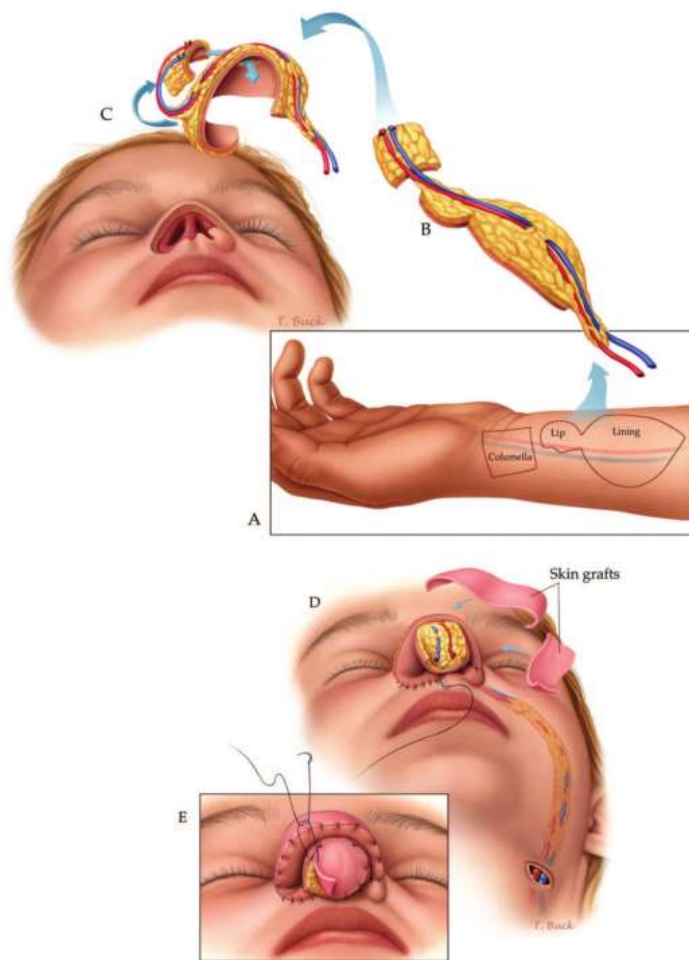


Figure 1.6. Radial forearm free flap (Burget and Walton 2007).

1.1.3.2. Nasal framework

The nasal framework is composed from the nasal bones, septolateral cartilage and the lobular cartilage. This framework gives structural support and aesthetics to the nose. It can be restored with autogenous or allogenic grafts. The most common procedure involves the use of autogenous grafts which normally are bone and cartilage. The source of grafts can be the nasal septum, cranium and rib. The source of cartilage grafts can be alar cartilage, nasal septum, auricle, rib cartilage and composite chondrocutaneous

auricular graft (Figure 1.7). Among the alloplastic materials that have been used are titanium meshes (Rodriguez-Prieto, Alonso-Alonso, and Sánchez-Sambucety 2009) and porous polyethylene implants (Thornton and Mendelsohn 2006). The grafts can be classified according to the function they have. They can be restorative, supportive or contour grafts. Restorative grafts replace the missing nasal framework restoring volume and shape. Support grafts reinforce nasal structures that are not well attached to the nasal skeleton. These grafts can also be used when it is predicted that the native nasal cartilage is going to be altered by the contracting forces of the scarring tissue. Contour grafts are used to improve shape and projection of the nasal tip (Baker 2011).

When autogenous material is used the restoration of a total nasal defect needs the employment of multiple grafts of bone and cartilage. One method that has been used involves harvesting of cartilage from the seventh and eighth ribs, after this, they are shaped into specific grafts to support the dorsum, nasal tip, columella, alae and sidewalls. These grafts are sutured together or attached with miniplates to form the framework (Burget and Walton 2007). In other methods the bone is harvested from the calvarial and carved into an L-strut, and then the construction is attached with miniplates. For the reconstruction of the lateral side walls and ala auricular cartilage is used (Cannady et al. 2009).

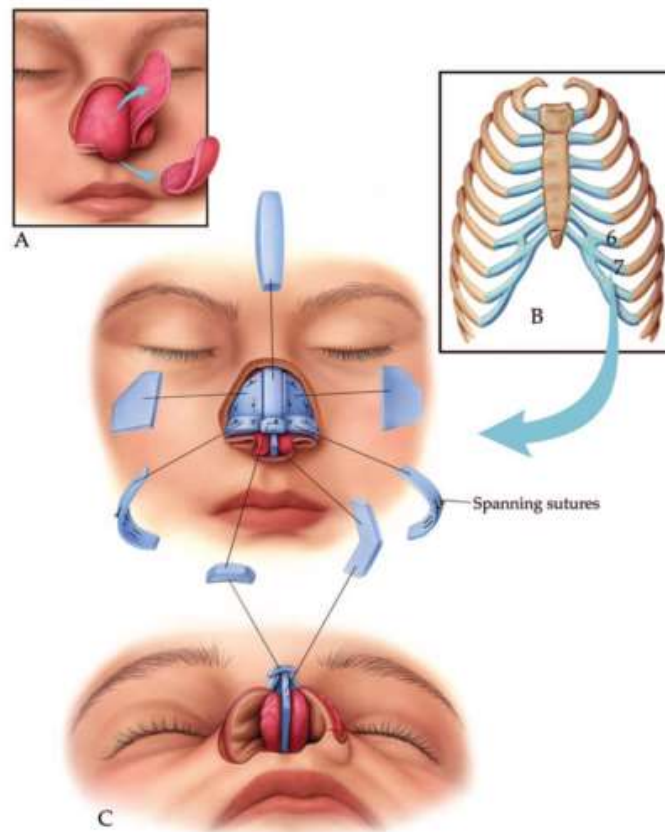


Figure 1.7. Nasal framework reconstruction using rib cartilage (Burget and Walton 2007)

1.1.3.3. External skin covering

The third layer of the reconstruction is the external skin covering. Similar to the other two layers, different options exist for the restoration such as skin grafts and flaps. The use of skin grafts has several disadvantages, one of the most important is the lack of good colour match (Cannady et al. 2009). For a total nasal defect the best flap that can be used is the forehead flap, it has a natural colour and after thinning an acceptable contour can be created (Menick 2009) (Figure 1.8). The forehead is richly perfused for five different vessels; this fact allows the safe transfer of vascular pedicles. The flap is harvested based on the supratrochlear vessels and designed using a template. The donor

site can be closed primary and healed by secondary intention, any remaining gap can be closed with a skin graft but this is not recommended as the patch will look mismatched.

The flap can be transferred in two or three stages, for total defects the preferable technique is in three stages. In this procedure a full-thickness flap is elevated by making an incision through the skin, subcutaneous tissue and muscle until the periosteum is reached. Usually the width of the pedicle is form 1-1.5 cm. The flap is transferred to the nasal defect and sutured. Three weeks later the flat is elevated, thinned and repositioned. The pedicle is divided in the third stage. This method ensures ideal blood supply and contouring of the tissues (Menick 2009) (Cannady, Cook, and Wax 2009).

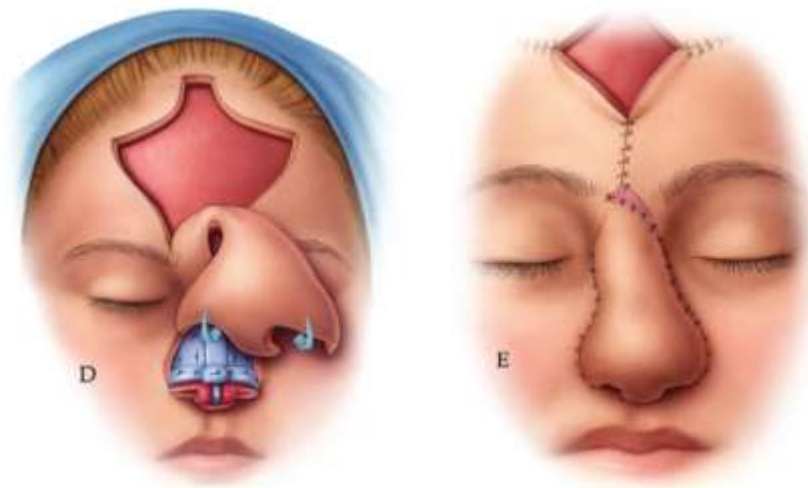


Figure 1.8. External skin covering with forehead flap to ensure ideal blood supply (Burget and Walton 2007)

1.1.3.4.Limitations of current surgical approach

The current surgical approach involves harvesting large amounts of rib cartilage which could be associated with postoperative chest wall deformities, high levels of postoperative pain and risks iatrogenic pneumothorax (Sajjadian, Rubinstein, and Naghshineh 2010). To avoid the use of autologous grafts several allogenic materials have been used, such as the titanium mesh and the porous polyethylene implant. The titanium mesh is cut it and manually moulded to recreate the absent structure (Rodriguez-Prieto et al. 2009). The porous polyethylene is a stable material, strong but at the same time flexible. Its porous structure allows the integration of the surrounding tissue into the implant. In one reported case this material was used in combination with the prelaminated radial forearm flap having satisfactory results (Tsiliboti et al. 2008). However, clinical data showed that there is a propensity for alloplastic grafts to migrate or extrude (Sajjadian, Rubinstein, and Naghshineh 2010). They also increase the risk of infection. For these reasons autologous grafts are still the gold standard even with their drawbacks. Another limitation of the current approach is the duration of the surgery. Due to the complexity of the cartilage harvesting and contouring into a nose shape, the duration of the operation can exceed 8 hours during which time the patient is under general anaesthesia. These drawbacks of the current approach for nasal reconstruction are the reasons why facial plastic and reconstructive surgeons are interested in the application of cartilage tissue engineered and personalised 3D printing for reconstructive surgeries.

1.1.4. Tissue engineering approaches for cartilage reconstruction

Tissue engineering (TE) involves the use of living cells, manipulated through their extracellular environment or even genetically, to develop biological substitutes for implantation into the body and/or to foster the remodeling of tissue in some other active manner. The purpose is to either repair, replace, maintain, or enhance the function of a particular tissue or organ (Nerem & Sambanis 1995). The basic strategy of tissue engineering comprises several factors. The first factor is a biocompatible and biodegradable scaffold that mimics the architecture of the native ECM by providing space for vascularisation, new tissue formation and nutrient transport. The scaffold should be able to interact with the cellular component to facilitate their activities such as proliferation and differentiation. In addition, the scaffold has to provide a 3D structural support whilst matching the mechanical properties of native tissues/organs (Yang et al. 2001). This structure acts as a supportive matrix for the biological payload which becomes part of the host tissue following transplant or acts to support the repair process of native cells (Chan & Leong 2008). Finally, culture conditions such as additive growth factors and mechanical stimulation play an important role to the pseudo-tissue in defining characteristics or growth potential (Hansmann et al. 2013)

1.1.4.1. Cartilage biology and types

In order to tissue engineer cartilage, it is important to first understand the basic biology of cartilage and its different types. Cartilage is a specialized connective tissue conformed by a single cell type called chondrocytes and an extracellular matrix enriched with proteoglycans macromolecules that interact with collagen and elastic fibres (Lin et

al. 2006). Mature chondrocytes are round cells with a mean size of 13 μ m (Bush & Hall 2003) located in a matrix cavity called lacunae. Chondrocytes anabolize and catabolize ECM macromolecules being crucial in maintenance of a stable ECM. Cartilage is avascular and is nourished by the diffusion of nutrients from capillaries in adjacent tissue (Mescher, A. L., & Junqueira 2013).

There are three different types of cartilage within the body. The primary differences between them is the matrix composition. The most common type of cartilage is hyaline cartilage which is located in articular surfaces of movable joints, the walls of large respiratory passages (nose, larynx, trachea, bronchi) and in the vertebral ends of ribs. Hyaline cartilage is formed by collagen type II, IX, and VI, with type II being the main one and responsible of cartilage tensile strength. The proteoglycans component of hyaline cartilage is formed by the glycosaminoglycans chondroitin 4-sulfate, chondroitin 6-sulfate and keratan sulfate linked to a core of proteins. Because of the negative charge of GAGs they draw water into the cartilage making it able to resist compression (Bhosale & Richardson 2008). Other type of cartilage is elastic cartilage which is very similar to hyaline except that it contains a network of fine elastic fibres in addition to the collagen II fibres. This type of cartilage is found in the auricle of the ear, the walls of the external auditory canals, the auditory tubes, the epiglottis and the cuneiform cartilage in the larynx. The third type of cartilage is fibrocartilage. This type of cartilage contains fewer proteoglycans than the other types and the majority of collagen is type I. Fibrocartilage can be found in the intervertebral disks (Mescher 2013).

1.1.4.2. Materials used in cartilage tissue engineering

The function of the scaffold is to recapitulate both the physical and biological characteristics of cartilage to allow the cells to regenerate the tissue. There are a large number of potential materials to consider for tissue engineering approaches and in establishing the best candidate materials, the relative strengths and weaknesses must be established for each one. Different natural and synthetic polymeric materials have been used for cartilage tissue engineering. Sometimes combinations of them have also been used to improve the mechanical properties of the materials (Dai et al. 2010). Some examples can be found in Table 1.1.

The advantage of some like collagen, gelatin and hyaluronan natural materials is that they can interact with the cells due to their interactions with cell surface receptors; allowing cell migration, proliferation and ECM production (Bian et al. 2013). In some cases, these interactions can be a disadvantage because these polymers may also stimulate an immune response and be subject to very fast biological degradation processes. Additionally, these materials also suffer from batch to batch variability (Tibbitt & Anseth 2009). Common natural materials used in cartilage tissue engineering include alginate (Yen et al. 2009), fibrin (Almeida et al. 2016), collagen (Sanz-Ramos et al. 2014), hyaluronan (Mahapatra et al. 2016), chitosan (Fan et al. 2017) and gelatin (Thiem et al. 2016). These materials are either proteins sources or polysaccharides.

Table 1.1. Materials used in cartilage tissue engineering.

Type	materials	cell source	Type of study	References
natural	collagen	sheep auricular chondrocytes	in vivo	(Zhao et al. 2015)
	alginate	porcine articular chondrocytes	in vivo	(C.-C. Wang et al. 2012)
	fibrin	rabbit auricular chondrocytes	in vivo	(Fussenegger et al. 2003)
	hyaluronan	rabbit chondrocytes and MSCs	in vitro	(Aulin et al. 2011)
	chitosan	human MSCs	in vitro	(Naderi-Meshkin et al. 2014)
	gelatin	bovine articular chondrocytes	in vitro	(S. Chen et al. 2016)
synthetic	PLGA	porcine auricular chondrocytes	in vitro	(Y. Zhang et al. 2012)
	PCL	bovine auricular chondrocytes and MSCs	in vivo	(Dahlin et al. 2014)
	PEG	porcine articular chondrocytes	in vitro	(Sridhar et al. 2015)

Alginate is a polysaccharide extracted from brown algae, and is widely used for cartilage tissue engineering, chondrocytes cell expansion and redifferentiation (Lin et al. 2009) (D. A. Lee, Reisler, and Bader 2003) (Homicz et al. 2003). Mainly used because of its biocompatibility, ambient gelling conditions and ability to maintain chondrocytes phenotype when expanded in vitro (Wan et al. 2011). Chitosan is also a polysaccharide; it is derived from the natural polymer chitin via partial deacetylation. The major advantage of chitosan is that its physicochemical and biological characteristics can be highly tailored by utilizing the reactivity of glucosamine residues. Like other naturally derived polysaccharides, chitosan is typically combined with other materials such as polycaprolactone to enhance its properties in cartilage repair (Neves et al. 2011).

Fibrin is a fibrous protein mainly responsible for the formation of blood clots. Fibrin hydrogels are easily fabricated by cross-linking fibrinogen. *In vivo* animal studies have shown that the combination of autologous chondrocytes and allogenic devitalized cartilage matrices suspended in fibrin glue allows the formation of cartilage-like tissue (Peretti et al. 2006). Collagen is the most abundant protein present in the cartilage ECM. This protein is able to polymerize into a stable gel at neutral pH and physiological temperatures. In addition, collagen hydrogels have good cell adhesion properties. It has shown to be able to support growth of chondrocytes preserving their chondrogenic potential (Urgery, Incorporated, and Chondrocytes 2014). Gelatin exists as a mixture of water soluble protein fragments, comprised of the same amino acid sequences as collagen, from which it is derived. Importantly, the bioactive sequences of collagen for cell attachment and matrix metalloproteinase (MMP)-sensitive degradation sites are retained in the gelatin backbone (Van den Steen et al. 2013). As such, essential cellular functions, such as migration, proliferation, and differentiation, can be facilitated via integrin-mediated cell adhesion and cell-mediated enzymatic degradation (Rose et al. 2014). A more detailed review on gelatin based hydrogels will be provided in chapter 4.

Synthetic polymers are more controllable and predictable in terms of degradation. The chemical composition of a synthetic polymer can be modified to alter mechanical and degradation characteristics. However, unless specifically incorporated, synthetic polymers do not possess surface motifs that support cell adhesion and signalling. In addition, the acidic degradation by-products of some synthetic polymers such as poly (lactic acid) and glycolic acid can be toxic in large quantities (Taylor et al. 1994) or

elicit an inflammatory response (Gibbons 1992) . Synthetic materials including poly (lactic-co-glycolic) acid (Hong et al. 2014), polycaprolactone (PCL) (Garcia-Giralt et al. 2008) and poly-(ethylene glycol) (PEG) (Nguyen et al. 2012) and poly (vinyl alcohol) have been used for cartilage engineering.

PLGA is a synthetic linear copolymer that consists of different ratios of its constituent monomers, lactic acid (LA) and glycolic acid (GA). PLGA degrades through hydrolysis of the ester bonds. PLGA scaffolds containing porcine chondrocytes have shown be able to form cartilage-like tissue when implanted 12 weeks in a nude mice (Y. Zhang et al. 2012). Another synthetic polymer frequently used in tissue engineering is PCL. Its low glass transition temperature (approximately -60°C) and melting point (approximately 60°C) enables easy formability at relative low temperatures. *In vivo* studies of PCL scaffolds seeded with chondrocytes have demonstrated cartilage-like matrix formation and the engineered constructs showed histologically good integration to the subchondral bone and surrounding cartilage with accumulation of extracellular matrix (Jeong, Zhang, and Hollister 2012). PCL properties will be discussed in more detail in chapter 3.

PEG has been extensively studied in the form of hydrogels and the polymer is already FDA-approved for its use in different implant and drug delivery applications. It has been shown that PEG hydrogels are capable of promoting chondrogenic differentiation of embryonic stem cells when cultured in the presence of transforming growth factor- β 1 (TGF- β 1) (Hwang et al. 2006).

1.1.4.3. Cell sources for tissue engineering cartilage

One of the most important challenges in cartilage tissue engineering is to find the ideal cell source that can be isolated, expanded and cultured to express and synthesize cartilage-specific extracellular matrix. Autologous chondrocytes were the first cells to be introduced in the clinical setting after *in vitro* culture expansion in what was called later autologous chondrocytes implantation (ACI) (Zopf et al. 2014). They are the most obvious choice of source because chondrocytes are the only cell type in mature cartilage. Other cell types have also been investigated including stem cells isolated from different tissues of the body such as bone marrow, adipose tissue, periosteum and umbilical cord (Bhardwaj, Devi, and Mandal 2015). Here, the two types that will be described are chondrocytes and bone marrow derived mesenchymal stem cells because they are the ones that have been most investigated for clinical use.

1.1.4.3.1. Chondrocytes

Adult chondrocytes are the only cell type present in mature cartilage, thus the most straightforward cell source to use for implantation. However, while these cells are able to produce ECM components specific of hyaline cartilage in large amounts, the use of autologous chondrocytes has also several drawbacks. Chondrocytes in hyaline cartilage represent only 1–5% of the total tissue volume. Only a very small number of chondrocytes can be isolated from biopsies, which consequently cause the requirement of further expansion *in vitro*. In addition, the expansion of chondrocytes in monolayer results in de-differentiation of the cells. When chondrocytes de-differentiate they become fibroblast-like, losing their round phenotype in favour of an expansive flat

morphology with extended processes. Consequently, their collagen production switches from types II, IX and XI to I and V leading to formation of fibrocartilage tissue (Brodkin et al. 2004).

Different methods have been studied in order to avoid this de-differentiation occurring and improve the chondrocytes expansion in vitro. Some of these include cell expansion in dynamic bioreactors, cell culture in serum-free conditions, hypoxic cell culture and culturing in 3D matrices. Under physiological conditions, cartilage is subjected to various mechanical stimuli, such as hydrostatic pressure, as well as compressive and shear stresses. To address the problem of de-differentiation during expansion, those parameters have been integrated into bioreactors, in which specific physicochemical parameters, mechanical stimuli and fluid flow can be controlled and applied to the cells (Gharravi et al. 2014). Articular chondrocytes naturally experience low oxygen tension, with the oxygen concentration in the articular cartilage varying from 1 to 7%. The adaptation of chondrocytes to low oxygen tension is mediated by transcription factors, such as hypoxia inducible factor (HIF) (Fedele et al. 2002). HIF-1a has been shown to be essential for growth arrest and survival of chondrocytes. Hypoxia has also been shown to increase the synthesis of ECM proteins in cultured chondrocytes in vitro (Coyle et al. 2009). The dedifferentiation process has however been shown to be reversible in nature with chondrocytes expanded in monolayer and subsequently re-differentiated to chondrocytes through long-term culture in high-density three dimensional systems (Zhang et al. 2004) or in alginate beads (De Ceuninck et al. 2004).

1.1.4.3.2. Mesenchymal stromal cells

Among the different types of stromal cells in the body, mesenchymal stromal cells (MSCs) derived from the bone marrow have been the ones most studied for clinical use. They are reasonably easy to isolate and proliferate readily, allowing for the potential to acquire them from the donors and store them in cell banks. Bone marrow-derived mesenchymal stromal cells MSCs are plastic adherent, colony forming cells that demonstrate the ability to differentiate into osteoblasts, adipocytes and chondrocytes (Pittenger et al. 1999). Since this, numerous attempts to define what makes a functional population of MSCs has been argued with the position paper by Dominici *et al.* also demonstrating the minimal criteria for MSC should also include positive marker expression of CD105, CD73 and CD90 whilst lacking expression of CD45, CD34, CD14 or CD11b, CD79a or CD19 and HLA-DR. This is however the minimal criteria and it is likely that new criteria to define clinically functional MSCs is overdue (Dominici et al. 2006)(Bianco et al. 2013).

For cartilage repair the particular interest is on the chondrogenic differentiation capacity of MSCs which has been demonstrated by forming cell aggregates (Solorio et al. 2010) or pellets cultured with a defined medium containing dexamethasone, ascorbate-2-phosphate, insulin and transforming growth factor beta (TGF- β)(L. Zhang et al. 2010). Tissue engineering of cartilage from bone marrow-derived MSCs has produced constructs with lower mechanical properties compared to their counterparts seeded with chondrocytes (Chung et al. 2008). This has been explained to be due to the continuous MSCs secretion of collagen I and X after the cells have already differentiated into chondrocytes, suggesting hypertrophy and that the differentiation of MSCs will continue

towards osteogenic phenotypes (Barry et al. 2001). While the use of stem cells promises significant opportunities, their use in the context of cartilage engineering is still immature because of the hypertrophy problems that still need to be solved.

1.1.5. 3D printing in tissue engineering and Regenerative medicine

While previous tissue engineering approaches have shown to be successful in building a number of tissues that have been used in the clinic such as skin and cornea (MacNeil 2007) there are still many challenges to be addressed. Among them are the lack of methods that can simultaneously replicate the tissue micro and macro architecture and methods that can deliver multiple cell types at precise locations. Additive manufacturing or 3D printing has been utilised to try to address these limitations (Mota et al. 2015). As stated in the ISO/ASTM52900:2015 additive manufacturing or more commonly known as 3D printing refers to a group of techniques which apply the additive shaping principle and thereby build physical 3D geometries by successive addition of material (ISO/TEC 261 2015). In 1986 Charles W. Hull was the first person to describe 3D printing in his method named 'stereolithography' (SLA). This method involved the formation of thin layers of material that were cured with ultraviolet light and sequentially printed to form a 3D solid structure (Hull 1986).

Different additive manufacturing technologies have been developed after SLA. They include, among others, fused deposition modelling (FDM) (Comb, Priedeman, and Turley 1994), selective laser sintering (SLS) (Kruth et al. 2003), electron beam melting (EBM) (Murr et al. 2012), inkjet 3D printing (Derby 2010), extrusion 3D printing

(Valkenaers et al. 2013) and laser assisted printing (Guillemot et al. 2010). In the recent years, the use of these technologies for medical applications has increased (Rengier et al. 2010). Some of their main advantages are precise control and personalised customisation (Mandrycky et al. 2016). The term of 3D bioprinting has born as a specialised class of 3D printing. 3D bioprinting is a layer by layer precise positioning of biological materials and living cells (S. V Murphy and Atala 2014). Some applications of 3D bioprinting include stem cell research (Tasoglu and Demirci 2013), cancer model (Albritton and Miller 2017), drug testing (R. Chang, Nam, and Sun 2008), and tissue engineering (Mandrycky et al. 2016). In tissue engineering, for manufacturing scaffolds, these technologies are able to control pore size, shape, distribution and interconnectivity of pores. In addition to this, combined with the ability CAD and 3D medical imaging such as computed tomography (CT), 3D printing permits the fabrication of personalised constructs (patient-specific) (Melchels et al. 2012).

3D bioprinting was first introduced by Thomas Boland in 2003, he patented the use of inkjet 3d printing for cells (Wilson and Boland 2003). According to a recent publication by the founder of one of the biggest 3D bioprinting centres, Antony Atala, 3D bioprinting is based on three central approaches: biomimicry, autonomous-self-assembly and mini-tissue building blocks (S. V Murphy and Atala 2014). Biomimicry consists of the creation of exact reproductions of the cellular and extracellular parts of a tissue and organ (Ingber et al. 2006). Self-assembly, is the scaffold-free method that mimics the cellular behaviour of embryonic stem cells. This technique can help to develop strategies to build living tissues (Jakab et al. 2008). Finally, mini-tissues can be defined as the smallest structural and functional component of a tissue (Shu 2015). The

combination of these approaches are needed in order to print complex 3D biological structures with multiple functional, structural and mechanical properties (S. V Murphy and Atala 2014).

1.1.5.1. 3D printing techniques

The main technologies used for 3D bioprinting living and biological materials are inkjet, laser assisted printing and microextrusion (Figure 1.9). Different specifications and features of them have to be contemplated based on the most important factors that affect bioprinting which are resolution, cell viability and the materials used for printing.

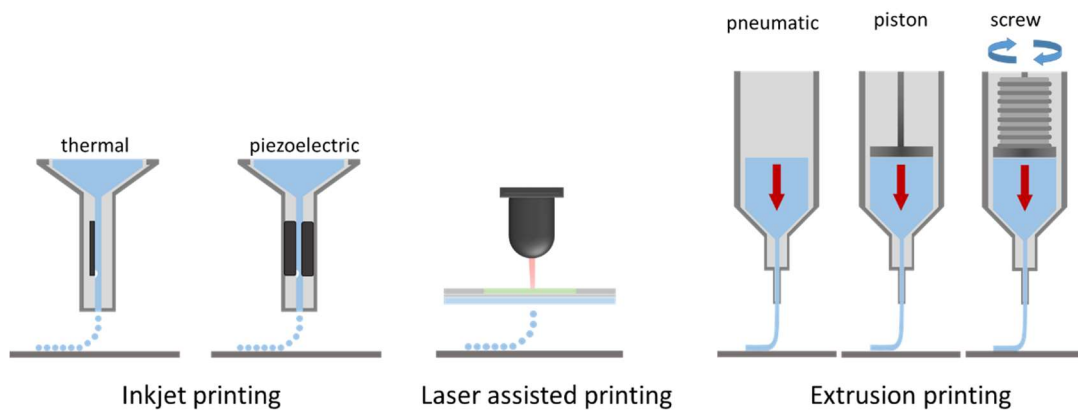


Figure 1.9. The main 3D printing methods used for bioprinting are inkjet printing, laser assisted printing and extrusion printing. Adapted from (Malda et al. 2013).

1.1.5.1.1. Inkjet printing

Inkjet 3D printing is a non-contact (nozzle away from the substrate) printing technology where 2D and 3D structures are generated using picolitre ink droplets jetted onto a substrate following a digital pattern (Seol et al. 2014). There are two types of inkjet

printing: continuous inkjet printing (CIJ) and drop on demand (DOD). DOD is the primary choice for bioprinting. The usual amount of material dispensed is between 1-100 picolitres allowing very high resolution. All drops are spherical in flight and identical to their neighbours (Derby 2008b). Several mechanisms can be used to generate the bioink droplets, the most frequently used for cells are thermal and piezo-electric. In the thermal method a heat generator increases the temperature up to 300°C within the chamber. The heating produces a bubble which expels the droplet (Cui and Boland 2009). With the piezo-electric method a direct mechanical pulse is applied to the bioink which results in the ejection of the droplet (Derby 2008a).

The advantages of inkjet printing are the high resolution that can be achieved which is between 20-100µm (diameter of drops), the digital control, the highly accurate placement of cells and high-throughput possibilities. Some of the challenges of inkjet printing are the requirements of low viscosity bioinks ideally between 1 to 20 mPa-s which can lead to poor mechanical strength in the final printed structure. Another limitation is the need to use low cell concentration usually below 10 million cells/ml in order to avoid nozzle clogging and facilitate drop formation. Finally, the most important limitation for the application of making nasal cartilage is the difficulty of produce clinically relevant size constructs (T. Xu et al. 2005).

1.1.5.1.2. Laser assisted bioprinting

A standard laser assisted bioprinting (LAB) set-up is usually composed of three elements: a pulsed laser source, a target coated with the material to be printed (the

ribbon) and a receiving substrate. Depending on the bioink optical absorption and the laser wavelength, a laser absorbing interlayer may be necessary to induce transfer and is placed between the support and the bioink (Guillemot et al. 2010). LAB functions using focused laser pulses on the absorbing layer of the ribbon to generate a high pressure bubble that propels cell-containing materials toward the collector substrate. This technology allows for the precise deposition of materials and high densities of cells in relatively small 3D structures without affecting cell viability (Ringeisen et al. 2004).

One of the main advantages of this technique is that it is a nozzle free approach, which means it is not affected by nozzle clogging and high cell densities can be used. In addition to these a wider range of materials can be used compared to inkjet due to the wider viscosity tolerance range (1-300 mPa-s)(Yan, Huang, and Chrisey 2012). The main disadvantage is that due to the high resolution making clinically relevant 3D constructs is very time consuming (Malda et al. 2013).

1.1.5.1.3. Extrusion based 3D printing

Extrusion 3D printing is a contact dispensing system (nozzle in contact with the substrate) where continuous strands of material are forced through a micro-nozzle from a movable head onto a platform. The print head can move in three axes (Fedorovich et al. 2007). This printing method can be used for creating scaffolds with defined architectures from biocompatible materials and cell-laden hydrogels. Different extrusion systems have been used for 3D printing such as pneumatic pressure, piston and screw driven. For the pneumatic pressure and piston systems the material is usually

loaded into a syringe and dispensed with the respective methods (Malda et al. 2013). The screw-driven method has a separate reservoir with or without temperature control. This method is usually used for highly viscous materials. The material is transported from the reservoir to the printhead by pressure then the screw assists the deposition process (Domingos et al. 2009).

The main advantages of extrusion printing compared with inkjet printing are the wider range of materials that can be used due to the higher tolerance on viscosity (Hözl et al. 2016). Moreover, it is easier to scale up and generate larger constructs (cm scale) and higher cell densities can be used. On the downside the resolution of extrusion printing is limited to approximately 150 μ m (Nair et al. 2009). Taking into account of all the advantages and disadvantages of the 3D bioprinting techniques described above, the extrusion method is clearly best suited to manufacturing personalised nose implants. Consequently, subsequent introduction on 3D bioprinting inks will focus on biomaterials associated with extrusion printing

1.1.6. Materials for 3D bioprinting

Thermoplastic polymers and hydrogels are two types of commonly used materials in extrusion based 3D bioprinting. Both materials can vary their mechanical and viscoelastic properties through altered composition. Broadly speaking, hydrogels are more suitable for sustaining cells but they lack of sufficient mechanical strength often required for many biomedical applications (Visser et al. 2015). This structural support can be provided by using biodegradable thermoplastics within printed constructs (Visser

et al. 2013a). Thermoplastics can also be used for printing acellular implants that can be seeded afterwards (Shor et al. 2009).

1.1.6.1. Hydrogels

Hydrogels are commonly used in tissue engineering due to their low toxicity and structural similarity to extracellular matrix (ECM) (K. Y. Lee and Mooney 2001). Their highly hydrated network permits exchange of nutrients and gases and makes them an attractive option for the formulation of bioinks. An ideal bioink should satisfy the following properties: printability, biocompatibility, mechanical properties and shape and structure (S. Wang, Lee, and Yeong 2015). Printability means that hydrogels must be suitable for extrusion deposition, with adequate viscosity, shear thinning properties and short response crosslinking time (C. C. Chang et al. 2011). The physicochemical properties of a hydrogel that determine their printability are its rheological properties and crosslinking process (Malda et al. 2013). The hydrogel should be viscous enough to be dispensed as a free-standing filament. However, if the gel is too viscous, large forces are required to extrude the bioink resulting in cell death (Malda et al. 2013). In terms of biocompatibility, the hydrogels should have an appropriate degradation time, be able to support cell attachment and not cause immune response. Other important characteristics that need to be considered is the mechanical strength after crosslinking (Hoffman 2012). The hydrogel should match the mechanical properties of the targeted tissue. The final printed construct should be similar to the natural tissue in terms of shape and structure, meaning that need to have similar nano and microstructure (Song et al. 2010).

A wide range of hydrogels have been used for cell encapsulation in tissue engineering applications, but not all of them are suitable for bioprinting due to the restrictions in printability and mechanical properties. Some of the hydrogels that have been used are alginate (Duan et al. 2013);(D. L. Cohen et al. 2006), collagen (Smith et al. 2004), gelatin (Maher et al. 2009), matrigel (Snyder et al. 2011), gelatin methacrylate (Kolesky et al. 2014), poly (ethylene glycol) diacrylate (Skardal, Zhang, and Prestwich 2010) and combinations of them (M. Xu et al. 2010). Some examples of hydrogel bioinks used for bioprinting chondrocytes include the work by Pescosolido et al. 2011, here hyaluronic acid and hydroxyethyl-metahcrylate-derivatized dextran was used to manufacture bioprinted cell laden chondrocyte constructs. The solutions had sufficient viscosity to be printed and excellent viability was observed for encapsulated chondrocytes. Other combination of materials that has been used for bioprinting chondrocytes is gelatin methacrylate and gellan gum. This combination showed that the addition of gellan gum improved the filament deposition, increased the constructs stiffness and supported chondrogenesis. But it also showed that high concentrations of gellan gum compromised cartilage ECM deposition (Mouser et al. 2016a). Alginate has also been used for chondrocytes bioprinting. You et al. 2016 demonstrated the fabrication of alginate/chondrocyte constructs using a 3D bioprinting system supplemented with a submerged cross-linking process. The constructs showed to support cell viability and deposition of cartilaginous ECM.

1.1.6.2. Thermoplastics

One of the main drawbacks of hydrogels is their poor mechanical strength and this is a critical obstacle for the current 3D bioprinting technology. 3D bioprinted structures comprised only by a hydrogel might not be strong enough to maintain the 3D shape

during the regenerative period, which is why many printed tissues or organs remain thin, two-dimensional structures. Therefore, the use of solid-state synthetic biomaterials such as polycaprolactone (PCL), poly (lactic acid) (PLA) and poly (lactic-co-glycolic acid) (PLGA) together with hydrogel in the printing process to enhance mechanical stability is recommended (J.-H. Shim et al. 2012) . One of the advantages of these polymers is that they are semi-crystalline or amorphous polymers that can be processed in their pure form by melting them and after they will solidify again. The most important characteristics that determine the printability of these polymers are melting point, glass transition temperature and viscosity. Polymers that melt at very high temperatures can be affected by thermal degradation (J.-H. Shim et al. 2010).

Poly (lactic acid) is a highly versatile, biodegradable, aliphatic polyester. PLA is produced by ring opening polymerization of lactic acid. Since lactic acid is a chiral molecule, PLA has stereoisomers poly (L-lactide) (PLLA), poly (D-lactide) (PDLA) and poly (DL-lactide) (PDLLA) (Savioli Lopes, Jardini, and Maciel Filho 2012) . PLLA and PDLA are crystalline polymers while PDLLA is amorphous (Bouapao et al. 2009). The melting point of PLLA and PDLA is approximately 160°C and a glass transition temperature of approximately 60°C. Processing temperatures of them are between 175°- 190°C which can lead to thermal degradation by chain scission. This degradation can lead to decrease of the mechanical properties of the scaffolds (Signori, Coltelli, and Bronco 2009). PLA based scaffold fabrication by hot melt extrusion printing has been successfully performed by monitoring and controlling the time that the polymer is exposed to high temperatures to avoid the degradation (Drummer, Cifuentes-Cuéllar, and Rietzel 2012). Other techniques that haven been used for processing PLA in order

to minimise degradation are blending the material with PEG (Serra et al. 2014) or PCL (Patrício et al. 2013); these blends allowed the PLA to be extruded at 40°C and 130°C respectively.

PCL is a hydrophobic semi-crystalline polymer with a melting point of 60°C, a glass transition temperature of -60°C and excellent blend compatibility. Polycaprolactone was used for the first time in 3D printing by Hutmacher et al. 2001 to fabricate scaffolds for bone regeneration using fused deposition modelling technique. Due to its low melting point, PCL has been the most popular material to use as a supporting material (W Schuurman et al. 2011) (Kang et al. 2016) (Pati et al. 2014). A more detail description of 3D printing of PCL is presented in chapter 3.

1.2. Summary of introduction and future aims

The nose is conspicuously located at the centre of the face and therefore represents a crucial aesthetic focus to the observer and individual. Nose deformities caused by trauma, cancer surgery and malformations can have physical and psychological effects on the patients. The anatomy of the nose, arguably the most complex within the face, is comprised of hyaline cartilage, fibro-fatty tissues, internal nasal lining and skin arranged in a complex three-dimensional architecture. This complexity makes nose reconstruction a very challenging surgery.

The current surgical approach for nose reconstruction is a three-stage surgery that involves harvesting rib cartilage strips, shaping and stitching them into a nose-shaped framework, then covering by autologous skin and inner nasal lining. Due to the high technical skills needed for this surgery and the time required to keep the patient under anaesthesia while the surgeon is grafting and shaping the cartilage grafts, surgeons are looking for different techniques that could simplify the surgery, avoid harvesting large amounts of cartilage and achieving better aesthetic and functional results.

3D bioprinting and cartilage tissue engineering could help overcome the limitations mentioned above. By combining cartilage tissue engineering techniques and the advantages that 3d bioprinting offers for creating patient specific implants, the current method could be improved. This introduction has highlighted the advances in cartilage tissue engineering including the different cell types and the range of materials that have

been previously used for cartilage tissue engineering. We also described the advantages and disadvantages of the different 3D bioprinting techniques that could be used for creating the personalised implants. The thrust of the project described within this thesis, is to investigate the feasibility of using 3D bioprinting to create personalised mechanically stable cartilage implants that could be used for nose reconstruction. In order to achieve this aim the project was divided in two main objectives: the first one was to 3D print a personalised biodegradable nose implant to be used as a surgical guide and the second was to 3D bioprint a multi-material implant that with have enough structural support and cells to form neocartilage (Figure 1.10).

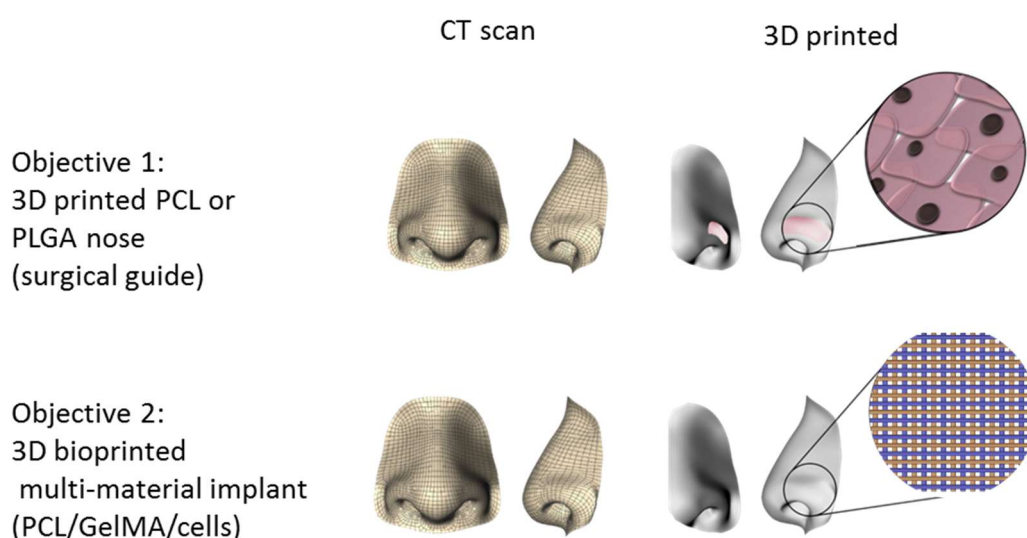


Figure 1.10. Main objectives of the thesis.

PCL and PLGA were chosen as the candidate materials to 3D print the surgical guides and to be used as structural support in the multi-material implants because one of the surgeon requirements for these implants was a degradation time within 1-2 years. Ideally

because the implant should provide support during the entire wound healing process and prevent the collapse of the reconstructed nose that could be caused by the contraction forces of the forehead skin flap. GelMA was chosen as the cell carrier because it has an in vivo degradation time of 15 days (Dong et al. 2017) which is enough to allow the cells to proliferate and secrete their own ECM. More details about the materials properties and their optimisation printing process are described in the following chapters.

The aims of the results chapters are as follows:

Chapter 2

- To create a protocol to isolate and culture primary sheep chondrocytes (ShCh) and primary bone marrow derived mesenchymal stromal cells (ShMSCs)
- To characterise the isolated cells
- To investigate the effects of the printing process on the viability of the cells

Chapter 3

- To create a method to generate the personalised 3D STL models using the medical imaging data
- To optimise the 3D printing process of PCL and PLGA using hot-melt extrusion 3D printing
- To assess the effects of melting the PCL and PLGA during printing
- To evaluate the mechanical properties of the PCL and PLGA 3D printed constructs

- To 3D print PCL and PLGA implants based on the personalised models stl models
- To characterise the surface structure of the PCL 3D printed scaffolds
- To evaluate the effects of different surface porosity on the mechanical properties
- To investigate the effects of different surface porosity on static and dynamic cells seeding

Chapter 4

- To optimise the 3D printing process of GelMA using time pressure extrusion 3D printing
- To investigate cell proliferation, cartilage ECM secretion and mechanical properties of 3D bioprinted porous cell-laden GelMA scaffolds
- To optimise the multi-material 3D printing process
- To evaluate the cells proliferation and cartilage ECM secretion of the multi-material 3D printed cell-laden GelMA-PCL scaffolds.

Chapter 2. Identification of a suitable cell type and characterisation of cell viability during 3D Bioprinting process

2.1. Introduction

Cartilage tissue engineering is an exciting aspect of the tissue engineering field driven by the intense demand for products to treat damage caused by disease or trauma. This technique for the regeneration of cartilage tissue is primarily driven by the poor clinical solutions offered by existing healthcare providers.

Cartilage is an avascular tissue comprising chondrocytes embedded in a dense ECM primarily formed by collagen type II and proteoglycans (Vinatier et al. 2009). The basic approach to cartilage tissue engineering is a combination of responsive cells, biocompatible scaffolds and inductive environment for the optimal differentiation and proliferation of the cells type selected (Chung and Burdick 2008). The ideal cellular source for this application would both be easily isolated and expanded as well as being able to synthesize cartilage specific ECM components. Of the diverse cell sources available for consideration chondrocytes and mesenchymal stromal cells are the most popular cell types that have been already used in therapeutically (Richter et al. 2016).

Of these potential candidates, autologous chondrocytes represent the obvious cell source for regenerating cartilage given that they are the only cell type present in cartilage. Significant progress has been made on isolating and using this cell type *in vivo*. Early human *in vivo* studies (Autologous chondrocytes implantation ACI) demonstrated

enhanced cartilage repair when high density chondrocyte solutions were transplanted to focal defects beneath the periosteal flap (M Brittberg et al. 1994) (Bentley et al. 2012). This became commercially available in the form of the procedure, known as Carticel®, and is the first clinically available tissue engineering strategy to repair cartilage. Following this work, scaffolds have also been incorporated to improve cell retention, this a method called matrix induced autologous chondrocytes implantation (MACI) (Behrens et al. 2006) (Albrecht et al. 2017).

Despite the technical advantages of MACI, such as secure fixation of the grafts or the absence of any cover material like a periosteal flap that may cause transplant delamination and periosteal hypertrophy, clinical studies have revealed that the functional outcomes are the same as ACI (Zeifang et al. 2010). One of the explanations for this outcome was that the chondrocytes seeded onto the scaffolds were implanted within 3 days and the neotissue was still immature (Makris et al. 2015). To counteract this potential bottleneck, novel methodologies are under development to improve the efficacy of engineered tissues. These improvements consist the seeding of chondrocytes on the scaffolds and culturing them in *in vitro* for 4 to 6 weeks prior to implantation. During this period the chondrocytes produce their own ECM in the 3D environment resulting in an implant with more functional and mechanical stability (Mats Brittberg 2014).

In addition to *in vitro* culture, some emerging strategies utilise the addition of growth factors and mechanical loads during the culture period to improve maturation. Some

studies have showed that the use of the transforming growth factor β (TGF- β) family members, specially TGF- β 1 and TGF- β 2, help to maintain the chondrocytes phenotype (Grimaud, Heymann, and R dini 2002) and promotes the development of neotissue with similar properties to native cartilage. The use of mechanical stimuli has proven beneficial for promoting maturation of the engineered cartilage. This stimulation has been applied to seeded chondrocytes in form of hydrostatic pressure or dynamic compression using bioreactors (K. Li et al. 2017). Despite these promising outcomes using primary chondrocytes, there are potential drawbacks. Firstly, the number of cells able to be isolated from mature cartilage is relatively low. Secondly, primary chondrocytes dedifferentiate to a more fibroblastic cell type when expanded in 2D for long periods. Therefore, other cells types have been also explored.

Stromal cells are another cell type that has been investigated to use in cartilage tissue engineering, specially bone marrow derived mesenchymal Stromal Cells (MSCs). MSCs have been implanted into the joint space of osteoarthritic patients. The results were positive, showing some increase in cartilage thickness (Emadedin et al. 2012). Other studies have used a similar approach to MACI but using bone marrow derived MSCs. In these studies, the cells were isolated and encapsulated in collagen hydrogels for treatment of cartilage defects. It was reported that fibrocartilage was formed after 1 year (Wakitani et al. 2004). Overall, these results indicate the potential of using bone marrow MSCs for cartilage regeneration. However, further research is required to improve the quality of engineered cartilage and study the potential benefit of differentiating the cells into chondrogenic lineage before implantation.

In addition to selecting a cell source for engineering cartilage, it is also important to investigate how the 3D bioprinting process affects the viability of the cells. Cells are sensitive to environmental changes (Wong, Leach, and Brown 2004) and therefore when exposed to the 3D printing process, they can be damaged. The parameters that can affect the cells during extrusion bioprinting are: the cells carrier (bioink), the crosslinking method of the bioink, the environmental temperature, the pressure needed to extrude the bioink, the size and diameter of the nozzle and finally the fabrication time (Malda et al. 2013).

The materials in which the cells are encapsulated for bioprinting is referred as bioinks (Melchels et al. 2014). The printability of the bioink is primarily determined by its viscosity. Viscosity is controlled by both polymer concentration and molecular weight (Malda et al. 2013). It is important to consider these viscosity and molecular weight when investigating the viability of the cells because high polymer concentrations can limit cell proliferation, migration and nutrients diffusion, which can lead to cell death (Bryant and Anseth 2002). Another parameter that can affect viscosity are temperature as it can have a detrimental effect on cells viability. In addition to the bioink itself, the crosslinking methodology, which can be chemical, physical or both, can cause cell damage (Panwar and Tan 2016).

During the printing processes the cells are suspended in the bioink and experience shear stress. The parameters that generate the shear stress include the pressure applied, nozzle size, shape and diameter, and the polymer concentration (Panwar and Tan 2016). The shear stress has to be kept at its minimum in order to avoid reduction in cell viability by

optimising the printing process (Billiet et al. 2014). The last factor that has to be consider is the fabrication time because it decides the exposure time of the to all processing conditions and how fast you can create a construct.

In this chapter, firstly the appropriate cell type and source will be identified taking into account feasibility of isolation and expansion. Given that primary chondrocytes and primary bone marrow derived mesenchymal stromal cells are the two cell types that have been more used clinically (M. Wang et al. 2017), it was decided to investigate these two cell types. Their advantages and disadvantages have already been described but it was needed to investigate which one would suit better for this cartilage bioprinting application. Therefore, the impact of bioprinting and processing conditions on cell viability was investigated using both cell types.

2.2. Materials and methods

2.2.1. Isolation of cellular material

2.2.1.1. Chondrocytes isolation

Hyaline cartilage and fibrocartilage were isolated from sheep knee condyle and meniscus respectively. The cells were harvested from sheep cadaver used for the project “The testing of a bone scaffold in sheep” Home Office License number 40/3599. Isolation was performed in four steps. First the knee was located and the skin was sterilised using an antiseptic gel (Figure 2.1A). Second the skin layer open with an L shape cut using a scalpel in order to reveal the fat and muscle layer (Figure 2.1B). Third the fat and muscle layer were removed revealing the knee (Figure 2.1C). Finally, the knee was dislocated and the meniscus (Figure 2.1D red arrow) was detached and placed into cold PBS A/A solution (Appendix 2.1.1 and 2.1.2.). The cartilage from the condyle (Figure 2.1D black arrow) was shaved using a scalpel and placed cold PBS A/A as well. Auricular cartilage was isolated from the ear (Figure 2.2). The skin was sterilised using antiseptic gel (Figure 2.2A), then an incision was done through the skin (Figure 2.2B) and the skin layer was lifted carefully in order to reveal the cartilage (Figure 2.2C). Finally, the cartilage pieces were shaved and placed in cold PBS A/A.

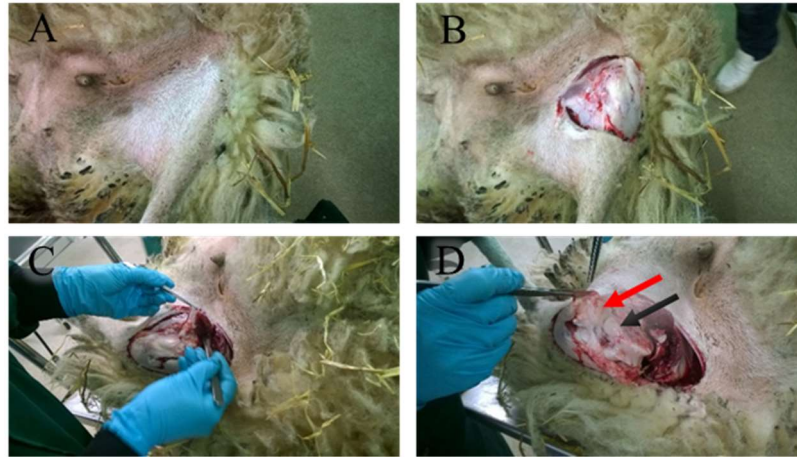


Figure 2.1 Hyaline cartilage and fibrocartilage isolation. (A) skin sterilisation with antiseptic gel, (B) L shape incision to remove the skin layer and reveal muscle and fat tissue, (C) careful removal of the muscle and fat layers to reveal the knee followed by (D) knee dislocation, removal of meniscus and shaving of condyle cartilage.

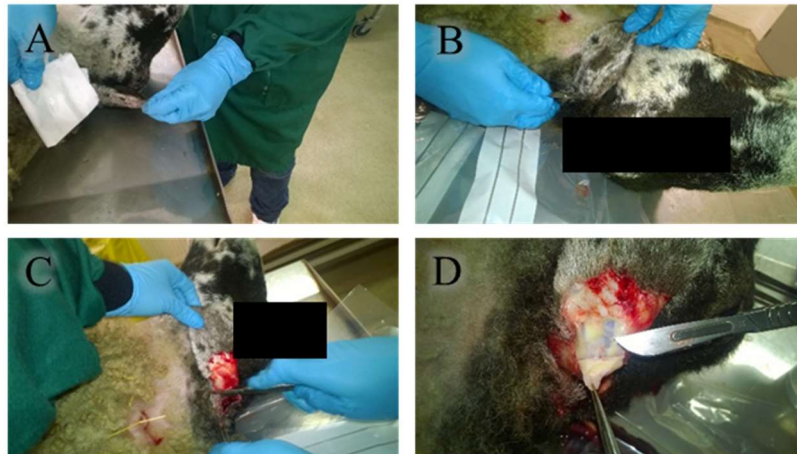


Figure 2.2 Auricular cartilage isolation. (A) skin sterilisation with antiseptic gel, (B) incision to remove skin layer, (C-D) skin removal and shaving of cartilage.

The cartilage pieces were rinsed with PBS A/A solution until all the blood was removed. After washing the perichondrium was removed using a scalpel and then the cartilage was cut into small pieces (2 x 2 mm²). Samples were weighted before being placed in the collagenase digestion medium (Appendix 2.1.3.) (Rogers et al. 2012); 500 mg of

cartilage per 10 ml of collagenase digestion medium. The hyaline cartilage was digested for 4 hours at 37°C in rotation in a humidified incubator. The auricular cartilage and fibrocartilage were digested for 12 hours 37°C in rotation in a humidified incubator. Cell containing cartilage lysate was passed through a 70µm cell strainer (BD Falcon™) and centrifuged at 1000 x g for 5 minutes.

2.2.1.2. Bone Marrow derived Mesenchymal stromal cells isolation

Cells were isolated by bone marrow aspiration of sheep. Bone marrow was aspirated from the sternum of the sheep with a Jamshidi needle 100 mm x 8G (UK Medical Ltd). Aspiration was performed immediately after post euthanasia. Samples were placed in 1% heparinised medium (Appendix 2.1.4.) and transported in ice. Samples were diluted with PBS, passed through a 70µm nylon strainer and centrifuged at 250 x g for 5 minutes. 1 ml of Red Blood cells lysis buffer (Sigma-Aldrich) was added to the samples and the samples were incubated during 1 minute. After incubation samples were diluted by adding 9 ml of PBS and centrifuged at 180 x g for 5 minutes.

2.2.2. Monolayer cell culture and cryopreservation

All monolayer cells culture experiments were performed in a sterile environment in a Class II microbiological safety cabinet (Envair) fitted with HEPA filters.

2.2.2.1. Culture of Sheep Chondrocytes

Sheep chondrocytes (ShCh) were isolated as described in section 2.2.1.1. Isolated cells were counted and seeded 4×10^6 in a T175cm² cell culture flask and left to recover and

attach for 3 days. Cells were cultured under normoxia (37°C, 5% CO₂) in chondrocyte culture medium (Appendix 2.2.1.). Cells took 3 days to recover and attach to the flask. Once the cells attached the medium was replaced and cells were left to expand. When cells were 80% confluent, they were detached with 0.25% (v/v) 0.20% EDTA in PBS. ShCh were centrifuged at 800 x g for 5 minutes, resuspended in medium and counted using a haemocytometer. Cells were seeded for the next experiments or cryopreserved.

2.2.2.2. Culture of Bone Marrow derived Mesenchymal Stromal Cells

Bone marrow derived sheep mesenchymal stromal cells (ShMSCs) were isolated as described in section 2.2.1.2. Isolated cells were seeded 2×10^6 in a T175cm² cell culture flask and left to recover and attach for 5 days. Cells were cultured under normoxia (37°C, 5% CO₂) in ShMSCs culture medium (Appendix 2.2.2.). After day 5 the medium was replaced and cells were left to expand. When cells were 80% confluent, they were detached with 0.25% (v/v) 0.20% EDTA in PBS. ShMSCs were centrifuged at 250 x g for 5 minutes, resuspended in medium and counted using a haemocytometer. Cells were cultured for consecutive passages in T175 flasks and then used for the viability and differentiation studies or cryopreserved.

2.2.2.3. Sheep Chondrocytes and Sheep Bone Marrow derived Mesenchymal Stromal Cells cryopreservation

In order to retain cells for later use they were stored in the vapour phase of liquid nitrogen. To prepare cells for cryopreservation they were trypsinised as for normal passaged, centrifuged as appropriate to the cell type and resuspended in a density of 1.0

X 10^6 cells per/ml in cryopreservation medium (Appendix 2.2.3.). These cell suspensions were transferred into a Nalgene 'Mr. Frosty' (Fisher Scientific, Loughborough, UK) and placed in a -80°C freezer for 48 hours. After this they were transferred to the vapour phase of liquid nitrogen for long-term storage.

2.2.3. Sheep Chondrocytes characterisation

2.2.3.1. Monolayer culture of Sheep Chondrocytes in TGF- β supplemented medium

ShCh passage 0 day 3 were detached with 0.25% (v/v) 0.20% EDTA, centrifuged at 800 x g for 5 minutes, resuspended in medium and counted using a haemocytometer. Cells were seeded in a 6-well tissue culture plate (Corning[®] Costar[®]) at a density of 5×10^3 cell/cm². Nine wells were cultured with ShCh standard medium and other nine wells were cultured with ShCh standard medium supplemented with 10 ng/mL TGF- β -1 (Scientific laboratories supplies Ltd) and 5ng/Ml FGF-2 (Sigma-Aldrich). Cell phenotype was assessed with microscopy histology and immunohistochemistry staining.

2.2.3.2. ShCh population doubling time

ShCh passage 0 day 3 were detached with 0.25% (v/v) 0.20% EDTA, centrifuged at 800 x g for 5 minutes, resuspended in medium and counted using a haemocytometer. Cells were seeded in T75 tissue culture flask at a density of 5×10^3 cell/cm² and cultured under normoxia conditions (37°C , 5% CO_2) with ShCh standard culture medium supplemented with with 10 ng/mL TGF- β -1 and 5ng/Ml FGF-2 (Sigma-Aldrich). Cells were detached, counted and passaged when they reached 80-90% confluence. Cells

were seeded again in a T75 tissue culture flask at a density of 5×10^3 cell/cm² for passage 2. This process was repeated for passage 3. Population doublings was calculated using the formula $PD = \log_{10}(N/N_0) \times 3.33$, where N= number of harvested cells and N₀= number of plated cells. Then, the doubling time was calculated using the formula $DT = PD/\text{number of days in culture}$.

2.2.3.3. Pellet culture of Sheep Chondrocytes in TGF- β supplemented medium

ShCh passage 0 day 3 were detached with 0.25% (v/v) 0.20% EDTA, centrifuged at 800 x g for 5 minutes, resuspended in standard medium and counted using a haemocytometer. ShCh were resuspended in standard medium to obtain 10×10^7 cells/ml and 50 μ L of cell suspension (n=24) were added to V-bottom 96-well non-treated tissue culture plate (Corning[®] Costar[®]). The plate was centrifuged at 900 x g for 5 minutes to pellet the cells. Pellets were incubated under normoxia conditions (37 °C, 5% CO₂) for 24 hours before changing the medium to standard medium supplemented with 10 ng/mL TGF- β . Pellets were cultured for 14 days with medium changes twice a week.

2.2.4. Sheep bone marrow derived Mesenchymal Stromal Cells characterisation

2.2.4.1. Osteogenic differentiation

For osteogenic differentiation cells passage 5 were seeded at a density of 2.5×10^5 cells/well (n=18) in a 6-well tissue culture plate using ShMSCs standard medium. Cells were left to attach for 24 hours before changing the medium to osteogenic differentiation medium (Appendix 2.2.4.). Medium was changed twice a week for 21 days.

2.2.4.2. Adipogenic differentiation

For adipogenic differentiation cells passage 5 were seeded at a density of 5×10^4 cells/well (n=18) in a 12-well tissue culture plate using ShMSCs standard medium. Cells were left to attach for 24 hours before changing the medium to adipogenic differentiation medium (Appendix 2.2.5.). Medium was changed twice a week for 14 days.

2.2.4.3. Chondrogenic differentiation

For chondrogenic differentiation cells passage 5 were resuspended in ShMSCs standard medium to obtain 10×10^7 cells/ml, 50 μ L of cell suspension (n=24) were added to V-bottom 96-well non-treated tissue culture plate (Corning[®] Costar[®]). The plate was centrifuged at 500 x g for 5 minutes to pellet the cells. Pellets were incubated under normoxia conditions (37 °C, 5% CO₂) for 24 hours before changing the medium to chondrogenic medium (Appendix 2.2.6.). Medium was changed every two days for 21 days.

2.2.5. Histological staining

The ShCh cultured monolayers and pellets were washed three times with PBS and fixed with 7% paraformaldehyde (PFA) for 15 and 60 minutes respectively. Samples were washed three times again with PBS and then stained with alcian blue 8GX (Sigma-

Aldrich) at room temperature for 30 min. Then samples were washed three times with PBS and imaged using Nikon dissection microscope.

2.2.6. Viability studies

ShCh passage 0 day 7 and ShMSCs passage 5 were used for the viability studies. These studies were performed using LIVE/DEAD assay (Thermofisher). The LIVE/DEAD solution (Appendix 2.3.1) was added to the samples and samples were incubated for 45 minutes at room temperature. Images (n=9) were taken with fluorescence microscope in red and green channel. The numbers of live and dead cells were calculated respectively using the software ImageJ.

2.2.5.1. GelMA concentration effect on cells viability

Cells were resuspended in 10%, 20% and 30% GelMA solutions containing 0.05% photoinitiator Irgacure 2959 (Sigma-Aldrich). Cells concentration was 1×10^6 cells/ml. 100 μ l of the gel/cells suspension were placed at the bottom of the wells of a 48 well plate and incubated for 3 hours, then the wells were topped with 100 μ l of medium to dilute the GelMA and allow the cells to attach to the well plate for the assessment. Cells were cultured for 24 hours under normoxic conditions (37 °C, 5% CO₂) before the LIVE/DEAD assay.

2.2.5.2. Temperature effect on cells viability

Cells were resuspended in 10% w/v GelMA in ShCh standard medium at a concentration of 1×10^6 cells/ml. 4ml of cell solution was transferred to 10ml syringes to simulate the 3D printing cartridge. Three syringes were placed in the heating chamber (Regenhu) at 37°C, other three were left at room temperature (20°C) and the last three were placed in the cooling chamber (Regenhu) at 15°C. Samples of 500µl were taken out of the syringe at time 0, 15, 30, 60 and 120 minutes. Samples were transferred to 6-well tissue culture plates and 2ml of standard medium was added. Cells were left to attach for 4 hours before performing the LIVE/DEAD assay.

2.2.5.3. UV effect on cells viability

Cells were seeded at a concentration of 5×10^4 cells/well in 12-well tissue culture plate, standard culture medium was added and cells were left to attach for 24 hours. Cells were exposed to UV for 10, 20, 30, 40, 60, 120, 270, 360 and 720 seconds (n=3). Viability was assessed 1 hour after exposure.

2.2.5.4. Genotoxicity effect of UV on cells

Cells were seeded at a concentration of 5×10^4 cells/well in 12-well tissue culture plate, exposed and to UV light for 10, 60, 150 and 600 seconds with Omnicure s1000 lamp at 2% power, wavelength 365 nm. . After exposition cells were incubated for 24 hours at 37 °C 5% CO₂. Media was removed and cells were washed with PBS before fixing them with 1% PFA at 0 °C for 15 minutes. Following fixation cells were immersed in 70%

ethanol for 20 hours at -20 °C. Cells were washed twice in PBS and immersed in 0.2 % Triton-X-100/PBS 1% for 30 minutes. Then cells were incubated overnight in 1% BSA containing 5 µg/ml mouse anti-vertebrates phosphor-histone monoclonal antibody (Ser139; Millipore, UK) at 4 °C. This was followed by another wash with PBS and incubation with Alexa Fluor 488 goat anti-mouse IgG conjugated secondary antibody (1:200) (Abcam) for 30 minutes at room temperature. Finally, cells were co-stained with Hoechst 33258 1µ/ml (Sigma-Aldrich) for 15 minutes. Samples were imaged under the fluorescent microscope (Leica DM IRB).

2.2.5.6. Needle gauge effect on cells viability.

Cells were resuspended in 10% w/v gelMA (Sigma-Aldrich) in ShCh standard medium at a concentration of 1×10^6 cells/ml. 4 ml of cells suspension was transferred to the 10 ml 3D printing cartridge and placed in the 3D bioprinter (Regenhu). Samples (n=3) were dispensed for 5 seconds through two different needles: gauges G30 (internal diameter 150 µm) and G27 (internal diameter (210 µm). Needle length was 0.5 inch. The pressure used for dispensing was 2 bar. Samples were dispensed into a 12-well tissue culture plate. After dispensing, 1ml of medium was added into the wells and cells were incubated for 4 hours under normoxic conditions before viability assessment.

2.2.5.7. 3D Bioprinting process effect on cell viability

The samples were designed in a square shape 4 x 4 x 1 mm using the software BioCAD (Regenhu). Cells were resuspended in 10%, 20% and 30% GelMA solutions containing 0.05% photoinitiator. Cells concentration was 1×10^6 cells/ml. 4 ml of cells/GelMA

suspension were transferred into the 10 ml cartridge and placed into the cooling chamber in the 3D printer. Samples were printed using 2 bar pressure. Needle gauge was G27. After 3D printed the samples were incubated under normoxic conditions (37°C, 5% CO₂) with standard medium for 5 days. Viability was assessed on day 0, 1 and 5.

2.3. Results and discussion

2.3.1. Sheep chondrocytes isolation from different sources

Sheep primary chondrocytes and mesenchymal stromal cells were selected in this project due to availability. The effect of bioprinting process conditions on the viability of these two model cells were studied. Isolation of ShCh from the condyle, meniscus and ear was first investigated (Table 2.1). The isolation experiments were performed three times. In all the isolations it was observed that the cartilage from the condyle was digested after 4 hours in the collagenase medium, whereas the meniscus and the ear took 12 hours and still some pieces were not completely digested. Possibly because they were thicker. Secondly, we noticed that a pure population of rounded small cells (chondrocyte morphology) was obtained from the condyle whilst a mix of small rounded cells and spindle-like cells were found in samples from the meniscus and ear (Table 2.1).

It is hypothesised that the reason for obtaining a mixed population from the meniscus is because the middle part of the meniscus consists mainly of fibrochondrocytes whilst the outer one-third of the meniscus is populated mainly by fibroblast-like cells (Verdonk et al. 2005). Therefore, after the digestion a mixture of both cells was obtained. Conversely, the cartilage from the ear only consists of chondrocytes, but is surrounded by a thin layer of connective tissue called perichondrium that contains chondroblasts and fibroblasts (Togo et al. 2006). Even though, the perichondrium was removed before the collagenase digestion some fibroblasts still remained. This could be due to some remaining perichondrium given the difficulty to distinguish this thin layer and the cartilage. Another difficulty in isolating the cells from the ear was contamination. This

was due to the proximity of the cartilage tissue with the external environment and the difficulty of using a proper aseptic technique.

Table 2.1. Chondrocytes isolation from condyle, meniscus and ear.

Cell source	Attempt 1	Attempt 2	Attempt 3
condyle	Digestion in 4 h Pure population: chondrocytes	Digestion in 4 h Pure population: chondrocytes	Digestion in 4 h Pure population: chondrocytes
meniscus	Digestion 12 h Mixed population: Chondrocytes + fibroblast	Digestion 12 h Mixed population: Chondrocytes + fibroblast	Digestion 12 h Mixed population: Chondrocytes + fibroblast
ear	Digestion 12 h Contamination	Digestion 12 h Contamination	Digestion 12 h Mixed population: Chondrocytes + fibroblasts

After the digestion time, the cells were counted and the amount of cells per gram was calculated. The number of cells obtained from the condyle cartilage was 2.7 times higher than ear and meniscus (Table 2.2.). A possible explanation for this is that because the ear and meniscal cartilage needed longer time to digest, no all of the cells were recovered after 12 hours. The samples could be left for longer time in the digestion medium but that would not necessarily mean that more cells could be isolated because a longer digestion duration could affect the viability of the cells (Yonenaga et al. 2017).

Table 2.2 Cell counts from different cartilage sources

Cell source	number
condyle	4,940,000 cells per gram
meniscus	1,150,000 cells per gram
ear	1,800,000 cells per gram

It was decided to pursue the next experiments just with the cells obtained from the condyle for several reasons. Firstly, it was the only source where it was possible to obtain a pure chondrocytes population without the need of other purification steps to remove the fibroblasts. Secondly, the digestion time for condyle was shorter than the ear and meniscus. This is an important factor to consider because some studies have shown that the viability of the chondrocytes during the isolation process with collagenase can be affected depending on the concentration of the enzyme and the duration of the digestion. Cell viability was lower with higher concentration and longer duration(Yonenaga et al. 2010). Thirdly, a higher number of cells was isolated compared with the other two sources.

2.3.2. Sheep chondrocytes characterisation

2.3.2.1. Sheep chondrocytes expansion

To determine the maximum duration the cells can be expanded in monolayer without changing phenotype, the isolated cells were cultured in monolayer and the morphology changes were observed using a microscope. As shown in Figure 2.3A and B, it was noticed that the cells were still rounded and not fully attached by day 2. On day 3 (Figure 2.3C) the rounded phenotype was still observed and cells started to attach. After four days in culture (Figure 2.3D) the cells started to spread and some proliferation was also noticed. On day 7 (Figure 2.3E) the flask was fully confluent, and all cells showed a spindle-like shape. Mature chondrocytes of articular cartilage are post-mitotic ECM producers. They have the ability to produce high amounts of collagen types II, IX, XI and proteoglycans (Mendler et al. 1989). When chondrocytes are isolated from their ECM and cultured in monolayer they re-enter the cell cycle, proliferate, and with time change to a fibroblastic morphology, this process is called dedifferentiation (Schulze-Tanzil 2009). In addition to the morphological changes the chondrocytes also reduce their collagen II secretion (Schnabel et al. 2002), which affects the quality of the engineered cartilage .

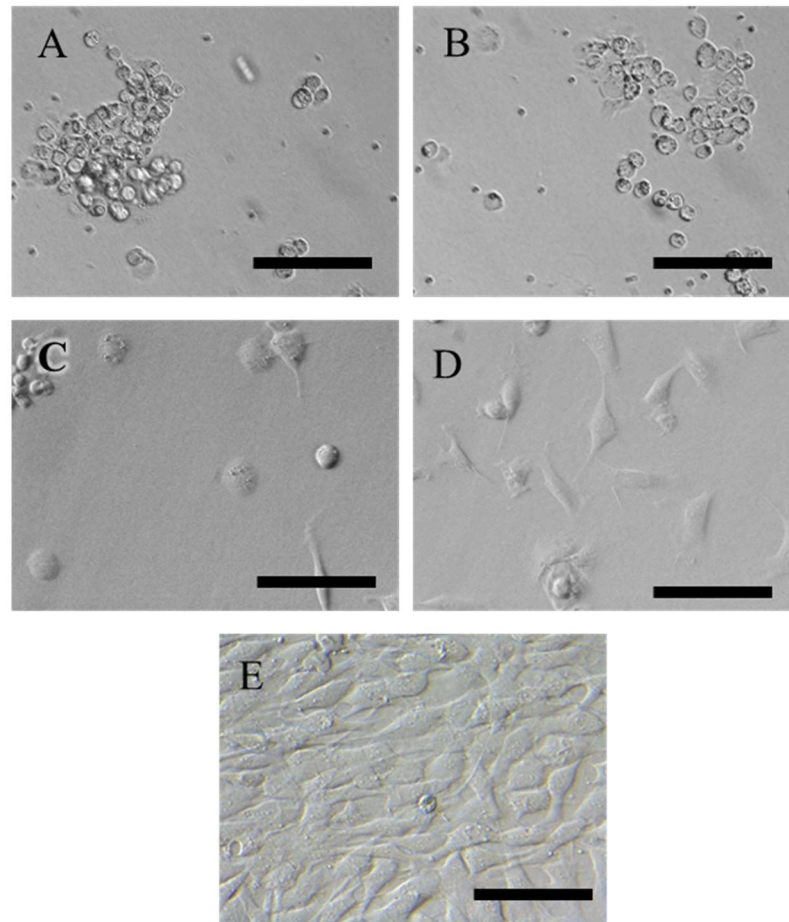


Figure 2.3 Representative images of Sheep Chondrocytes monolayer culture after isolation from the condyle. (A and B) Day 1 and 2 showing cells not fully attached and with rounded morphology, (C) On day 3 cells appear attached but still showing rounded morphology, (D) on day 4 the cells start to show a more spindle like morphology but no sign of proliferation (E) on day 7 the cells reach 100% confluency. Scale bars represent 50 μm .

Some studies have shown that the dedifferentiation process is reversible by culturing the chondrocytes with specific growth factors in 3D high density pellets or in hydrogels. This process is called redifferentiation (De Ceuninck et al. 2004)(Z. Zhang et al. 2004). Additionally, it has been shown that chondrocytes expanded in monolayer supplemented with TGF- β 1 and FGF-2 had more potential to redifferentiate when transferred to the 3D environment with the drawback that these growth factors slow the proliferation of

the cells (Jakob et al. 2001). We expanded the cells (passage one) in the presence of TGF- β -1 and FGF-2 for 7 days to study its effect on collagen II secretion. In Figure 2.4A ShCh day 1 are shown. Figure 2.4B and C corresponds to ShCh day 3 without and with TGF- β 1. The ShCh without TGF- β 1 had a more fibroblastic spindle-like morphology than those with TGF- β 1. By day 3 the cells were already confluent but the culture was continued for another 4 days in order to assess the secretion of collagen type II. On day 7 of culture (Figure 2.4D and E) cells were growing on top of each other but it was possible to see the difference in morphology of the cells on the top layer. ShCh cultured in supplemented medium showed a circular morphology (Figure 2.4E) while the non-supplemented (Figure 2.4D) ones demonstrated a spindle morphology.

Furthermore, the cells were stained with immunohistochemistry to evaluate the secretion of collagen type II. Previous studies have shown that dedifferentiated cells lose the ability to produce cartilage specific markers such as collagen II (G. Chen et al. 2003). Figure 2.4F and G shows collagen II deposition (green) in both of the conditions but is more obvious in the cells cultured with TGF- β 1 given that there are also less cells present (blue). In addition to this, the supplemented chondrocytes had a rounded morphology compared to the non-supplemented cells. These observations allowed us to confirm the importance of supplementing the cells with TGF- β 1 and FGF-2 during culture in order to maintain their phenotype (K. G. A. Yang et al. 2006).

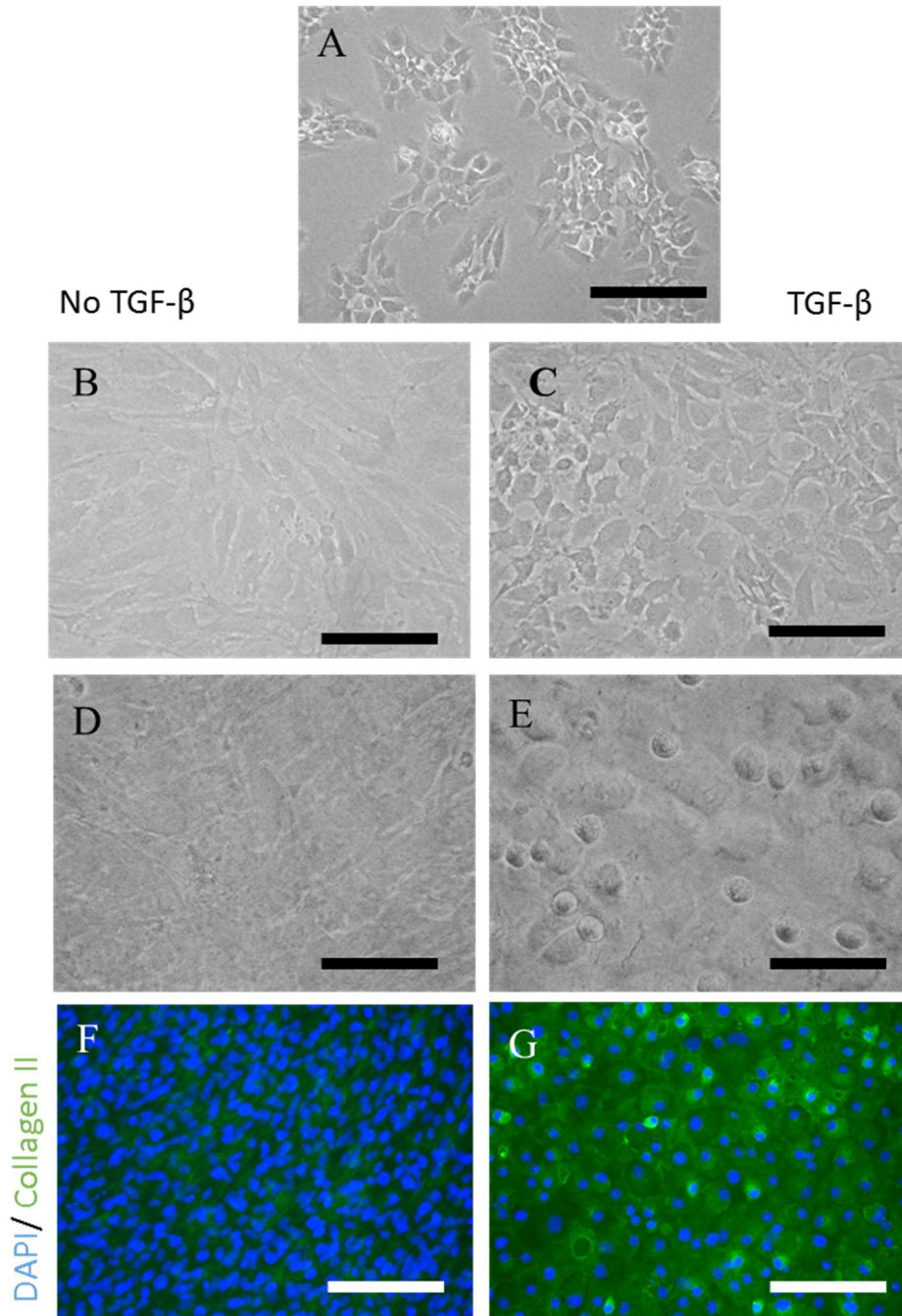


Figure 2.4 Representative images of monolayer cell culture of ShCh in standard medium and TGF- β supplemented medium. A) Day 1 of culture showing the cells with a spindle-like morphology after attached, B) and C) represent day 3 of culture without and with TGF- β 1 showing that the cells have a more spindle like morphology when cultured without it. D) and E) represent day 7 of culture and shows a rounded morphology of the cells cultured with TGF- β 1. F) and G) are representative images of ShCh day 14 immunostained for collagen type II (green) and DAPI (blue). The images show that the cells culture with TGF- β 1 expressed more collagen II than and proliferated slower than the ones cultured without. Scale bars represent 250 μ m.

As part of the characterisation process we expanded the ShCh for 3 passages to determine their expansion capacity. Population doublings and doubling time were quantified after passage 1, 2 and 3 (Table 2.3). Cells took 1.8 days to double during the first 7 days. Then after day 7 the cells started dividing much faster, and the population doubling time halved. Because previous work has reported that serial subculturing of cells from P0 to P4 resulted in the decrease of collagen type II secretion (Gosset et al. 2008) it was decided to expand the cells just for one passage.

Table 2.3 ShCh cultured in TGF- β supplemented medium population doublings and doubling time.

Passage #	days	PD	DT
1	0-7	3.7	1.8
2	7-9	1.9	1.03
3	9-12	3.2	0.91

2.3.2.2. Sheep chondrocytes differentiation

The final characterisation step was the evaluation of cartilage ECM secretion. Cells were cultured for 14 days in monolayer and in 3D pellets with TGF- β 1 supplemented medium. The cells were stained with Alcian blue to observe glycosaminoglycans (GAGs) secretion, which is one of the main markers for cartilage (Grogan et al. 2007). It can be observed that the cells cultured in monolayer secreted less GAGs than the pellets (Figure 2.5). Pellet culture is well known as a method to prevent the change of phenotype during chondrocyte expansion (Caron et al. 2012).

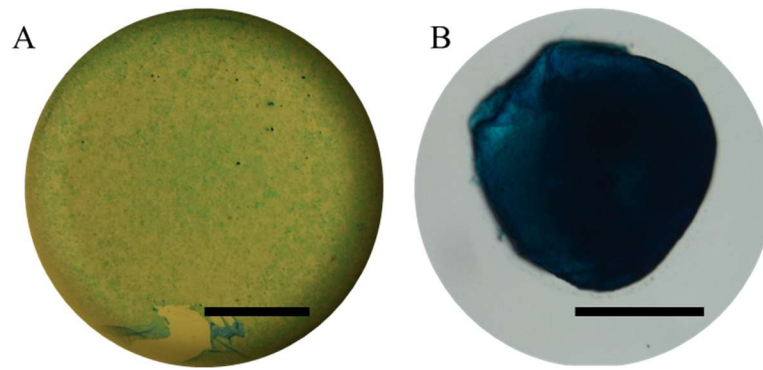


Figure 2.5 Alcian blue staining of ShCh cultured in monolayer and pellet for 14 days in and TGF- β supplemented medium.

2.3.3. Sheep bone marrow derived stromal cells isolation and characterisation

To characterise the ShMSCs we followed part of the criteria defined by the International Society for Cellular Therapy. These criteria define that mesenchymal stromal cells (MSC) must be plastic-adherent when maintained in standard culture conditions and must differentiate to osteoblast, adipocytes and chondroblast *in vitro*. After isolation of the primary cells just the adherent ones were used for expansion (Figure 2.6). The expanded cells were then cultured in chondrogenic, adipogenic and osteogenic medium for 14 days to differentiate them. The relevant histology staining showed successful trilineage differentiation with mineral deposition (Von Kossa staining) for the osteogenic differentiation (Figure 2.7A), lipid accumulation (Oil Red O staining) for the adipogenesis (Figure 2.7B) and glycosaminoglycan production (Alcian blue staining) for chondrogenesis (Figure 2.7C).

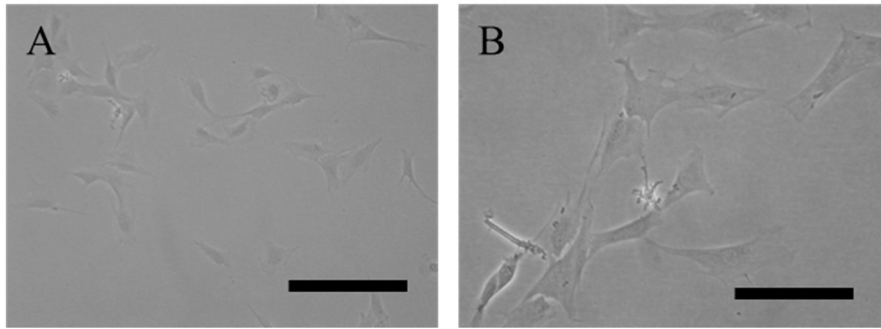


Figure 2.6. Sheep Bone Marrow derived Stem Cells monolayer culture. (A) Scale bar represents 250 μm and (B) Scale bar represents 50 μm .

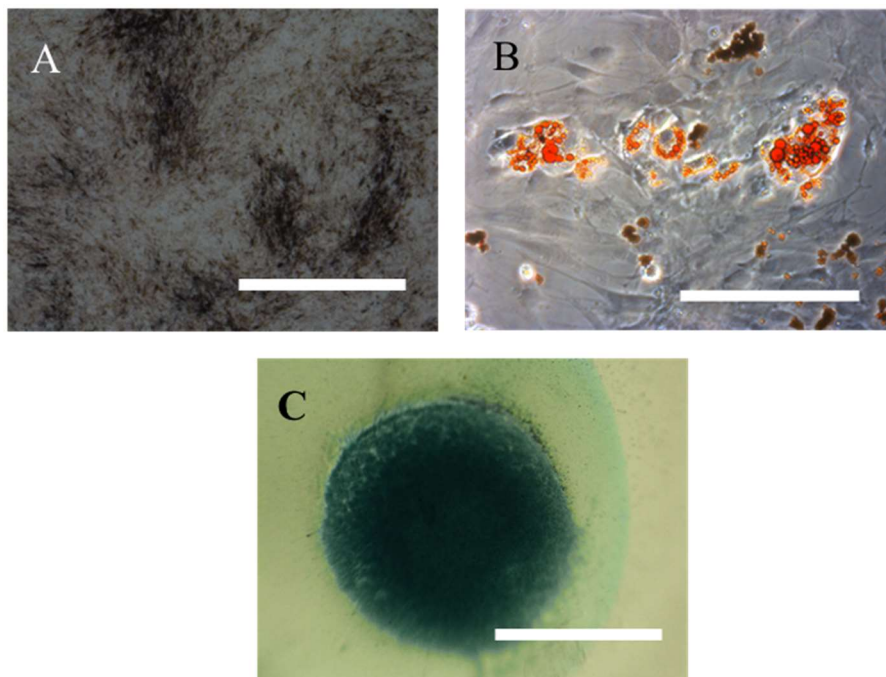


Figure 2.7. Trilineage differentiation of ShMSCs (A) Osteogenic differentiation. Von Kossa (black) staining showing the calcified nodules. Scale bar represents 250 μm . (B) Adipogenic differentiation. Oil Red O stained showing the adipocyte drops. Scale bar represents 100 μm . (C) Chondrogenic differentiation. Alcian blue staining showing the presence of glycosaminoglycans. Scale bar represents 1mm.

2.3.4. Viability studies of Sheep chondrocytes

Different processing conditions can affect cell viability during extrusion bioprinting processes. The ones that were considered were the concentration of GelMA, needle gauge, printing temperature, printing time and the UV exposure for crosslinking. All these parameters were studied individually in order to determine their effects on cell viability.

2.3.4.1. GelMA effect on sheep chondrocytes viability

During the printing process the cells have to remain encapsulated in non-crosslinked GelMA for a period of up to 3 hours. As part of the viability assessment the first step is to study if the non-crosslinked material has any cytotoxic effect on the cells. For this reason, the effect of different concentrations of GelMA (10%, 20%, 30%) on cell viability was assessed by encapsulating the cells within the material for 3 hours. Here, GelMA was not crosslinked because we are just evaluating the effect of the material. The results in Figure 2.8 demonstrated that there was no significant effect of the tested gel concentrations on cell viability with all showing 98% viable cells.

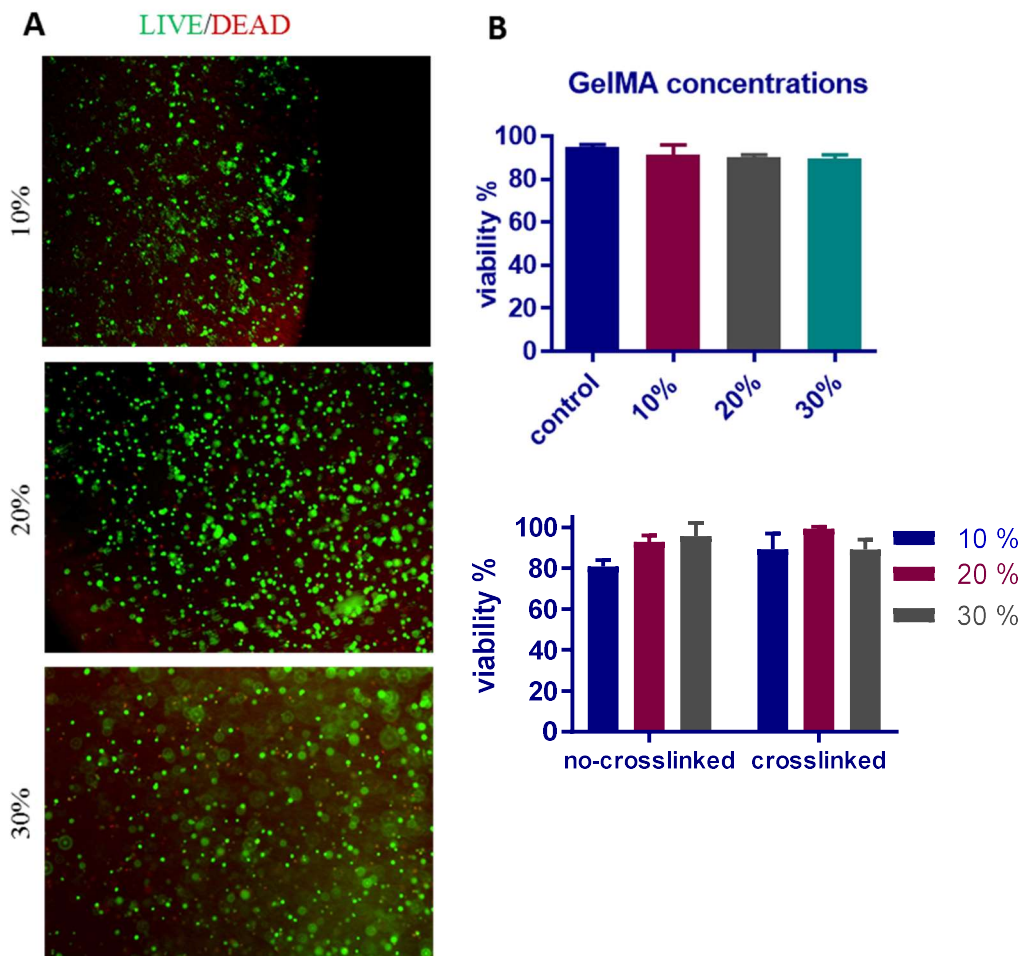


Figure 2.8. Viability of ShCh in different concentrations of GelMA after 3 hours incubation in just GelMA and 21 hours of diluted GelMA. (A) Representative images of ShCh cultured in 10%, 20% and 30% GelMA showing live cells (green) and dead cells (red). (B) Top: Control is monolayer of ShCh cultured at the bottom of the well in standard medium. No statistically significant difference was observed on the viability between the three different concentrations showing an average of 98% viable cells. Bottom: Control used to see if there was a difference in viability in between non-crosslinked and crosslinked GelMA. The crosslinked sample was exposed for 20 seconds to a dosage of 0.62 J/cm^2 .

2.3.4.2. Temperature effect on sheep chondrocytes viability

Other parameters that may influence cell viability include the printing temperature and time. Cells encapsulated in GelMA remained in a cooled syringe during printing. The printing time can vary from minutes to approximately 1 hour depending on the size of

the structure and the number of replicates. Three different temperatures 15°C, 20°C and 37°C were tested for their effect on cell viability with time frames from 15 minutes to 2 hours. Figure 2.9 shows that the three different temperatures did not have a significant effect on cells viability for the various printing time periods.

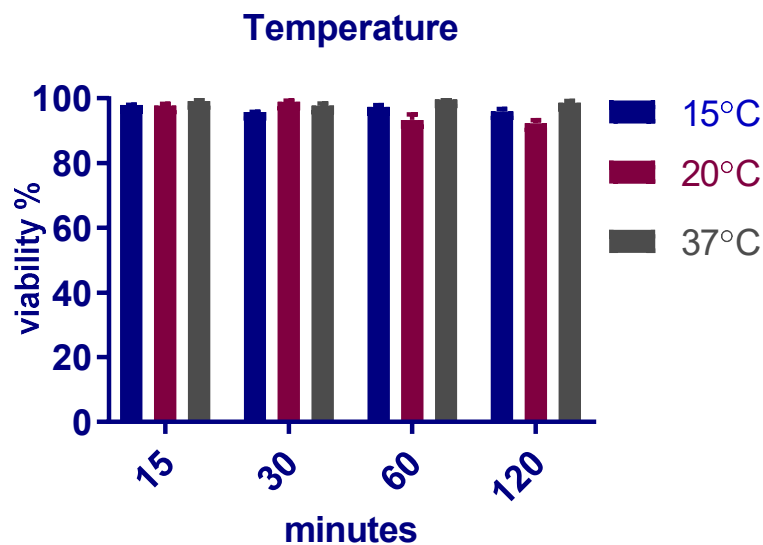


Figure 2.9. Viability of chondrocytes at different temperatures for different timing. There is no statistically significant difference in between all of the concentrations. The control is the cells kept at 37 °C.

2.3.4.3. UV exposure effect on sheep chondrocytes viability

As a UV-activatable photoinitiator (Irgacure 2959) was used for crosslinking GelMA, we investigated the effect of UV exposure on cell viability and genotoxicity. The UV cytotoxicity and genotoxicity can vary depending on the UV dosage which is determined by the UV intensity and the time during which the cells are exposed (UV dosage =

Intensity $\text{mW/cm}^2 \times \text{time (s)}$ (Z. Liu et al. 2012). From a preliminary test (section 4.3.1.3) it was determined that 20 seconds at an intensity of 31mW/cm^2 (UV dosage 0.62 J/cm^2) was the minimal dosage needed to crosslink GelMA. Chondrocytes were exposed to UV from 10 seconds to 12 minutes (dosages from 0.31 to 22 J/cm^2) because during the printing each layer will be cross-linked for 20 seconds being a total of 720 second (12 min) seconds for creating a 1 cm tall structure. Figure 2.10 shows that there is no significant effect on cell viability when UV exposure time varied from 10 seconds to 3 minutes, which agrees with previous work (Vermonden et al. 2008) (Coates, Riggan, and Fisher 2013)(Mironi-Harpaz et al. 2012). Only 80% of the cells remained viable after 6 minutes (UV dose 11.16 J/cm^2) and 60% after 12 minutes (UV dose 22.32 J/cm^2). UV light causes cell death by damaging the DNA which can affect transcription, replication or induce apoptosis (Dunkern, Fritz, and Kaina 2001).

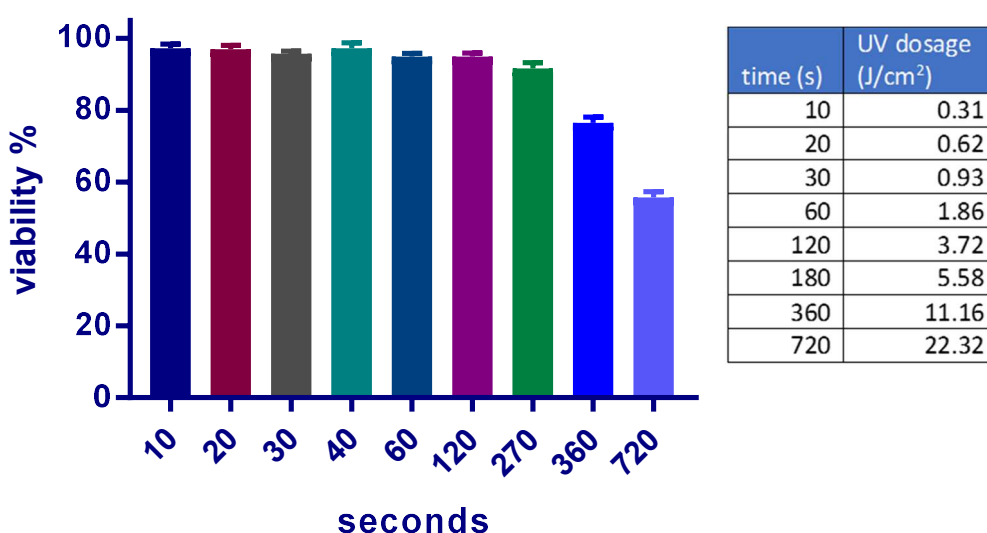


Figure 2.10 ShCh viability after UV exposure. Samples exposed from 10 to 270 seconds did not show any change in viability compared with the control sample. After 360 seconds viability got reduced to 80% and after 720 seconds to 60%.

2.3.4.4. Genotoxicity effect of UV exposure on sheep chondrocytes

Even that cells remained viable after UV exposure for up to 5.58 J/cm^2 , it is important to consider the genotoxicity that could induce further cell death or changes in genomic stability. This effect was assessed by measuring the expression of $\gamma\text{-H2}\alpha\text{X}$, an early detection marker of DNA damage (Kinner et al. 2008). Cells were exposed to UV from 10 seconds to 10 minutes (UV dosages in Figure 2.11B) and $\gamma\text{-H2}\alpha\text{X}$ expression was analysed 24 hours after the exposure. Quantification was performed by normalising the cells expressing $\gamma\text{-H2}\alpha\text{X}$ to the total cell number stained with DAPI in the fluorescence images (Figure 2.11A). Cells exposed to 10 seconds and 1 minute (UV dosage 0.31 and 1.86 J/cm^2) did not express DNA damage, while 50% of the cells exposed for 2.5 minutes (UV dosage 4.65 J/cm^2) were damaged. The damaged cell population increased to 90% after exposure for 10 minutes (UV dosage 18.6 J/cm^2) (Figure 2.11B).

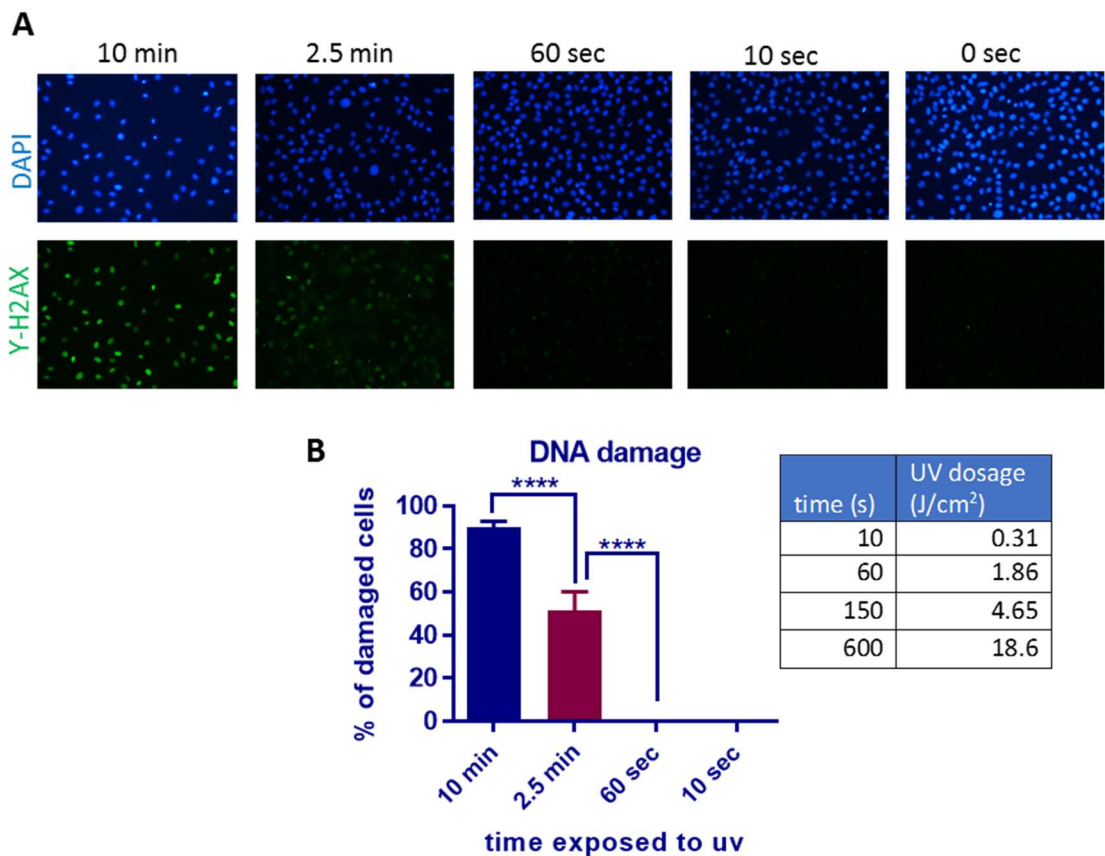


Figure 2.11 Genotoxicity assessment of ShCh after UV exposure for different timings. (A) Representative images of ShCh after UV exposure and Y-H2AX immunostaining (green). The nucleus of the cells was stained with DAPI (blue) to identify the total cell number present. (B) Quantification of the percentage of cells expressing Y-H2AX. Cells did not express Y-H2AX after 10 and 60 seconds of exposure. 50% of the cells express Y-H2AX after 2.5 minutes and 90% of the cells shown the expression after 10 minutes.

2.3.4.5. Effect of needle size on ShCh viability

Another parameter we assessed was the needle gauge. The shear stress that the cells experience during printing depends on the internal diameter of the needle and the dispensing pressure (Panwar and Tan 2016). Some studies have shown that high shear stress can cause cell death (Nair et al. 2009). Therefore, it is important to investigate the

viability of the primary chondrocytes after being dispensed through different nozzle sizes. For our studies, we used tapered shape needles with gauges 27 (ID=210 μm) and 30 (ID=150 μm) because high printing resolution (small strand diameter) was desirable. The dispensing pressure used was kept constant (2 bar). The viability was quantified on day 0 immediately after printing and on day 3. The viability of printed cells was 20% than no printed ones (Figure 2.8) showing that the shear stressed caused by printing definitely has an effect on the cells. An average of 80% viable cells was obtained with both needle gauges (Figure 2.12), which is comparable to results in previous publications (Billiet et al. 2014).

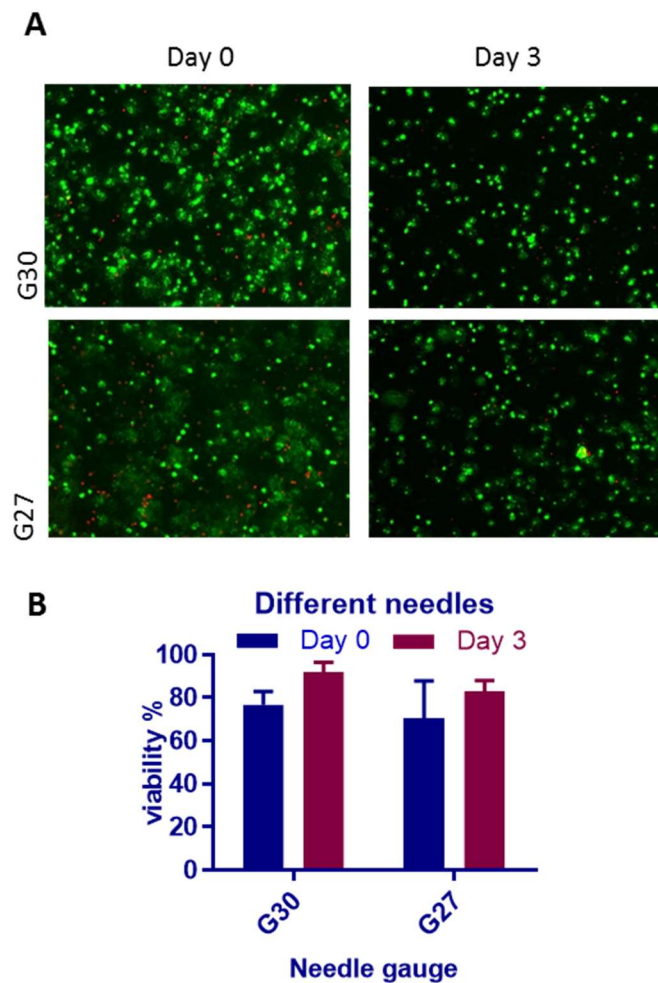


Figure 2.12. ShCh viability after been printed with different nozzle gauges. (A) Representative images of cells stained with LIVE/DEAD (green/red) after been printed with needle gauge G30 (180 μm) and G27 (203 μm). (B) Quantification of cells viability showing an average of 80% for all of them.

2.3.4.6. Effect of the complete 3D bioprinting process on ShCh viability

Following the assessment of the individual steps, sheep chondrocytes were exposed to the combined conditions of the 3D Bioprinting process. In Figure 2.13 the viability of the cells after 2 hours printing was shown to remain high at 80%. Similar high viability was observed after 1 and 5 days post printing. These results show how cells viability is within an acceptable range after printing.

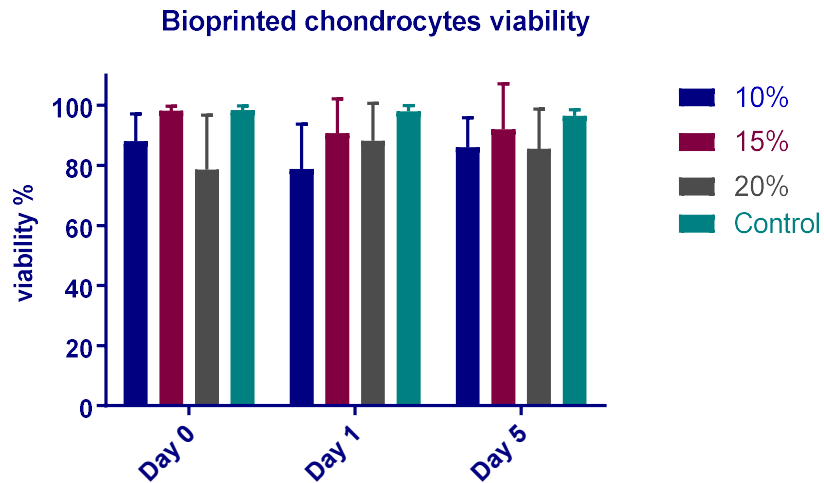


Figure 2.13 ShCh viability after being 3D Bioprinted in different GelMA concentrations. The viability of the cells exposed to the entire 3D Bioprinting process was an average of 80% compared with the control. The control is cells cultured in monolayer.

2.3.5. Viability studies of Sheep bone derived mesenchymal stromal cells

2.3.5.1. Effect of GelMA on the ShMSCs

A similar evaluation to the ShCh was performed on the ShMSCs to study the effect of the bioprinting process. ShMSCs were encapsulated in 10, 20 and 30% GelMA for 3 hours to assess the cytotoxicity. GelMA was not crosslinked because here just the material was evaluated. Figure 2.14 shows that there was no statistically significant difference among the different concentrations and cell viability was on average 80% after 24 hours in culture.

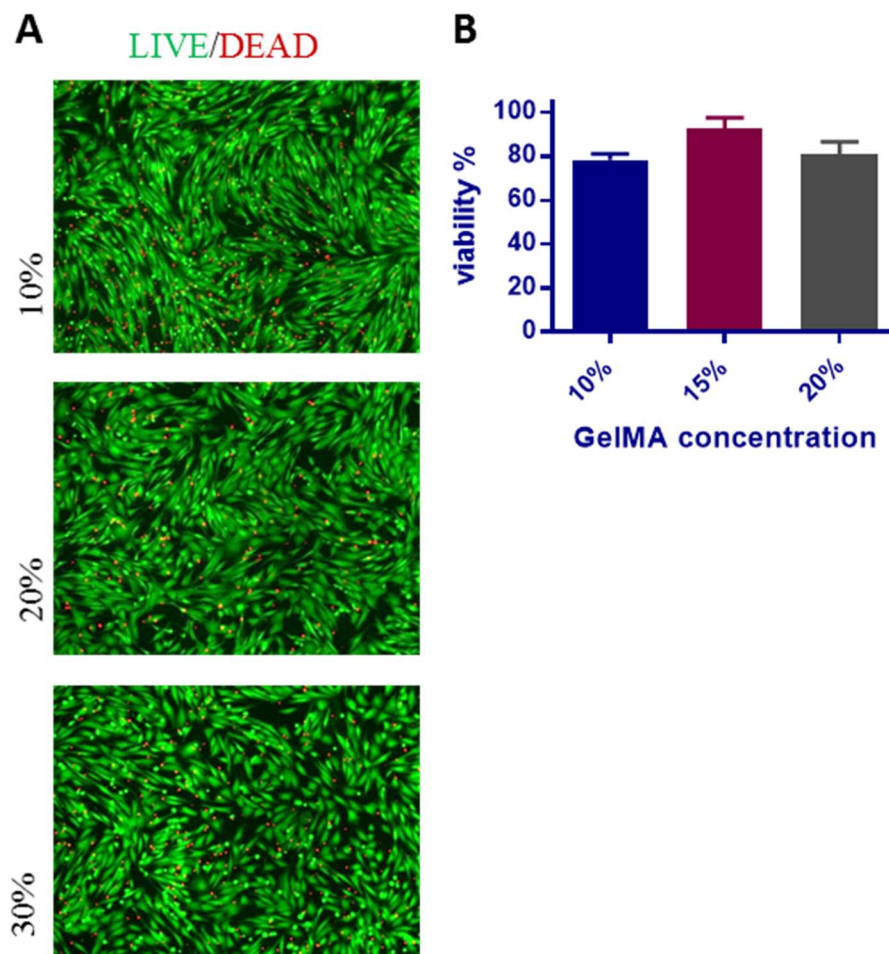


Figure 2.14 ShMSCs viability when cultured in different GelMA concentrations for 3 hours and in diluted GelMA for 21 hours. (A) Representative images showing the live cells (green) and dead cells (red). (B) 80% average viability of the cells within the three different concentrations with no statistically significant difference.

2.3.5.2. Effect of UV exposure on bone marrow derived mesenchymal stromal cells

ShMSCs were exposed to UV from 10 seconds to 12 minutes (dosages from 0.31 to 22 J/cm²) to evaluate its effect on the cells viability. Figure 2.15 shows that there is no significant effect on cells viability when UV exposure time varied from 10 seconds to 3 minutes. Moreover, only 20% of the cells remained viable after 6 minutes (UV dose

11.16 J/cm²) and 0% after 12 minutes (UV dose 22.32 J/cm²). These results were similar to those observed with the ShCh.

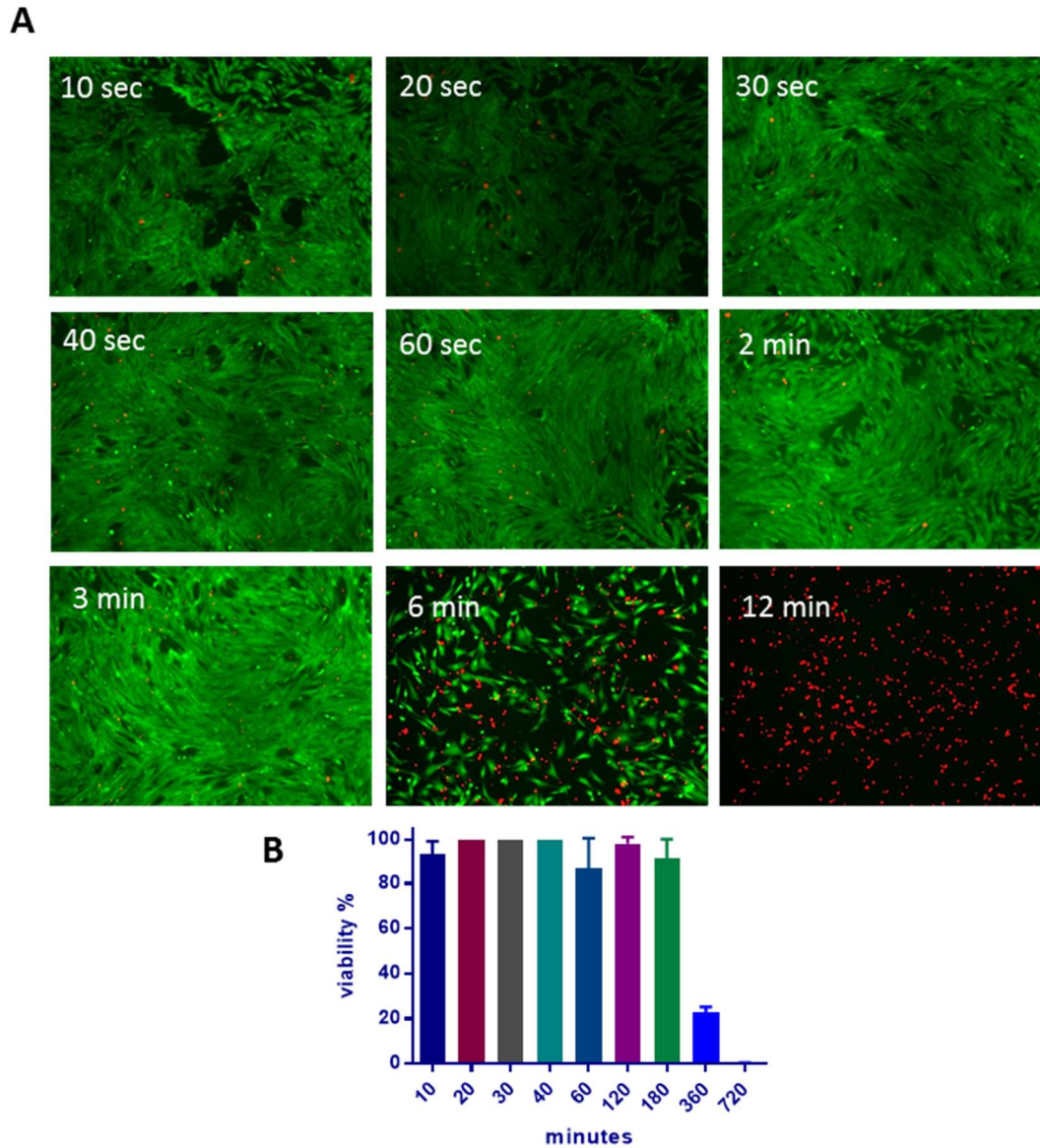


Figure 2.15. ShMSCs viability after UV exposure. (A) Representative images of ShMSCs exposed to UV from 10 seconds to 12 minutes and stained with LIVE/DEAD (green/red). Samples were in culture 24 hours before LIVE/DEAD stain. (B) Quantification of cells viability. No change in viability was observed for up to 180 seconds exposure compared with the control. After 360 seconds exposure viability got reduced to 20% and after 720 seconds to 0%

2.3.5.3. Effect of the complete Bioprinting process on bone marrow derived mesenchymal stromal cells

Following the assessment of cytotoxicity and UV exposure, sheep chondrocytes were exposed to the complete 3D Bioprinting process. The nozzle diameter used for bioprinting the ShMSCs was 210 μm . Figure 2.16 shows that viability of the ShMSCs after 24 hours of been printed was 90% in 10% GelMA, similar to the results of ShCh. However, the viability of the cells that were printed in 20% and 30% GelMA was 40% and 20% respectively. Previous studies have shown that parameter optimization based on a specific cell type might not be suitable for other types of cells, especially cells which are particularly sensitive to environment perturbations (Ouyang, Yao, et al. 2016), which is the case of mesenchymal stromal cells. The shear stress that the cells experience during printing is influenced by the dispensing pressure and the nozzle gauge (Nair et al. 2009). The higher the viscosity of the bioink the more pressure is needed for dispensing (Panwar and Tan 2016). As viscosity increases with hydrogel concentration, the higher the concentration of the hydrogel the more shear stress is experienced by the cells during printing. These explains why the cells viability reduced when the GelMA concentration increased. Given that the ShMSCs were more sensitive to the bioprinting process compared to the ShCh, it was decided that ShCh would be the cell type to use for the bioprinted cartilage constructs.

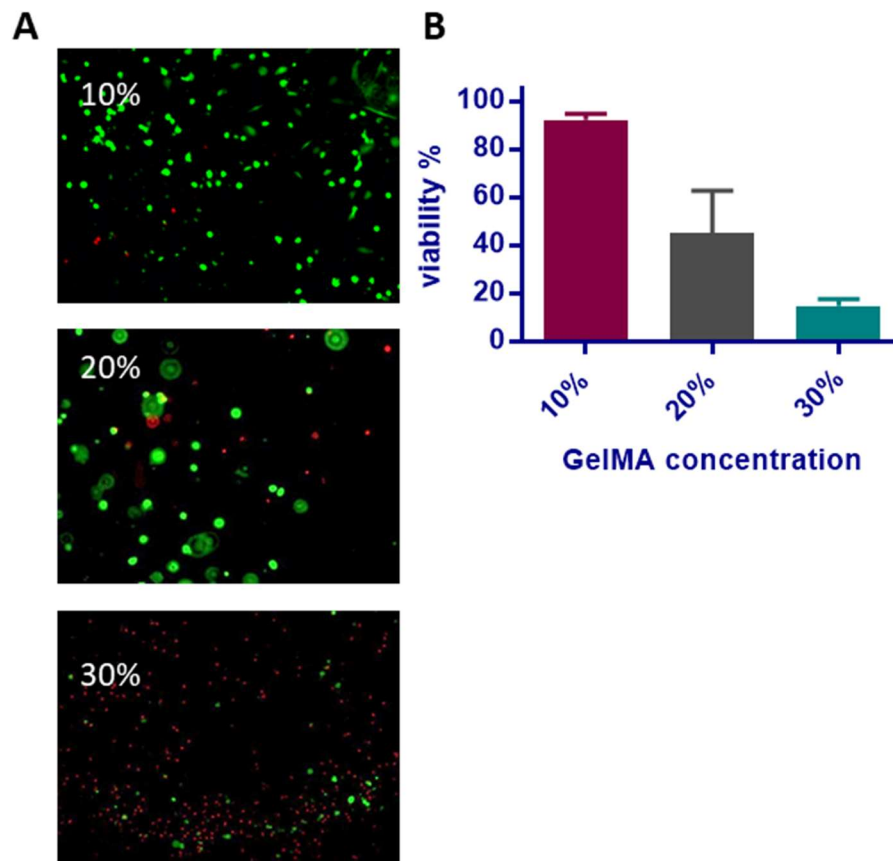


Figure 2.16 ShMSCs viability after being 3D bioprinted. (A) Representative images of cells viability after been exposed to the entire 3D printing process and stained with LIVE/DEAD (green/red). (B) Quantification of cells viability. Viability of the cells encapsulated and printed in 10%, 20% and 30% GelMA was 90%, 50% and 20%.

2.4. Conclusions

The work presented within this chapter described the *in vitro* characterisation of two possible cell sources to be used in 3D bioprinting of cartilage. Primary sheep articular chondrocytes (ShCh) and sheep bone marrow derived Mesenchymal Stromal Cells (ShMSCs) were isolated, expanded and differentiated. The effects of the 3D printing process parameters on cell viability and functionality were assessed. Chondrocytes were isolated from condyle, meniscus and ear cartilage. It was found that chondrocytes from condyle had the purest cell population and 50% shorter digestion time. We then compared them with primary sheep mesenchymal stromal cells. From these comparison, it was concluded that ShCh were a better source for 3D bioprinting given that they were easier to isolate due to less isolation steps needed and shorter characterisation process. From the viability studies it was identified that gelMA and the different printing temperatures did not have an effect on the cells. On the other hand, it was found that UV exposure times higher than 6 minutes were detrimental for the cells and that the shear stress caused by the nozzle killed 20% of the cells. Additionally, it was identified that ShCh were able to tolerate higher stress caused by the 3D printing process compared with ShMSCs. We obtained an 80% viable ShCh after the printing process while ShMSCs viability was between 50-20% for the cells encapsulated in 20% and 30% GelMA. Therefore, was decided that the cell type to be used for bioprinting cartilage constructs would be chondrocytes.

Chapter 3. Personalised 3D models design and development of techniques for 3D printing polycaprolactone and poly (lactic-co-glycolic acid)

3.1.Introduction

The use of additive manufacturing for medical applications and regenerative medicine has been growing rapidly in recent years (Banks 2013). The combination of this technology and advanced medical imaging enables the creation of patient- specific implants and the reproduction of the complex architecture of tissues (Parthasarathy 2014). A range of medical implants and tissue engineered constructs have been 3D printed using this technology combination for a range of applications including heart valves (Duan et al. 2013), ears (Reiffel et al. 2013), articular surface (C. H. Lee et al. 2010), meniscus (C. H. Lee et al. 2014), trachea splint (Morrison et al. 2015), bone (Bose, Vahabzadeh, and Bandyopadhyay 2013), cranium (Probst et al. 2010) and mandible (A. Cohen et al. 2009).

Advanced medical imaging includes the use of Computer Tomography (CT) or Magnetic Resonance Imaging in combination with post-processing tools and algorithms (Rengier et al. 2010). This post processing tools allows to convert the 2D images into three dimensional views of the anatomy (Wolf et al. 2005). After the imaging data is acquired, it is then saved in DICOM (Digital Imaging and Communications in Medicine) format. The DICOM files are then manipulated using 3D post processing tools which usually include thresholding, segmentation, sculpting,

trimming and smoothing tools. The contours of a segmented region of interest can be computationally transformed into a 3D triangle mesh. The mesh data then is further processed using (Computer-Aided Design) CAD software where additional smoothing and editing is performed to finally generate a 3D STL (stereolithography) file which is compatible with 3D printer software (Mitsouras et al. 2015).

Several 3D printing techniques have been used for medical and tissue engineering applications including hot melt extrusion 3D printing, stereolithography, inkjet printing, selective laser sintering and laser assisted bioprinting (Ventola 2014). Melt extrusion based additive manufacturing techniques that are mostly used are fused deposition modeling (FDM) and precision extrusion deposition (PED) (Mota et al. 2012). FDM involves the use of polymeric filaments that are provided to the extrusion nozzle by means of drive wheels, then melted in a liquefier head and finally deposited layer by layer on a construction platform (Mohamed, Masood, and Bhowmik 2015). PED is a technique based on a screw extruder, enabling the processing of polymer pellets for the controlled deposition of a melt filament (Shor et al. 2009). In both the techniques the material leaves the extruder in a liquid form and solidifies immediately. Advantages of this techniques are that it contains no toxic solvents, has minimum waste of material and is low cost (Masood 2007).

Various studies have been performed using these hot-melt techniques to prepare scaffolds for tissue regeneration. The first thermoplastic scaffolds fabricated using FDM studied their feasibility to be used for bone regeneration. These scaffolds were made

using polycaprolactone (PCL) (Dietmar W. Hutmacher et al. 2001). Among other materials that have been used are polypropylene mixed with ceramics (Kalita et al. 2003), PCL mixed calcium phosphate (Schantz et al. 2005), PCL mixed with hydroxyapatite (Chim et al. 2006) and PCL blended with poly (lactic acid) (PLA) (Patrício et al. 2013). All the previous scaffolds were used for hard tissue applications. These techniques have also been used to create support for scaffolds made with hydrogels or as a sacrificial material for complex shapes (Visser et al. 2013b). One of the examples include the work by Schuurman et al where PCL fibers were 3D printed with a wide range of hydrogels and cells (W Schuurman et al. 2011). A second example is the work by Shim et al where hybrid scaffolds formed by the thermoplastic polymers PCL, poly (lactic co glycolic acid) (PLGA) and the hydrogels hyaluronic acid, gelatin and collagen were co-printed in order to investigate hepatocytes viability and proliferation on these samples (J.-H. Shim et al. 2011).

Although various studies have been performed with hot-melt additive manufacturing techniques, the characteristics and properties of the thermoplastic 3D bioprinted scaffolds have not been fully investigated with all the materials. The properties of the scaffolds should be properly controlled because a change on them can affect the tissue engineered structures. Given the printing principles of these methods high forces and temperatures are continuously generated to dispense materials through the micro-nozzle (Domingos et al. 2009). These harsh conditions can affect the scaffold properties by thermal degradation, changing the molecular weight of the materials, thermal and mechanical properties. Hence, in this study we optimised the printing process of two different thermoplastic biocompatible polymers PCL and PLGA using PED printing

method. We investigated the influence of the printing process in terms of thermal degradation by measuring the properties of the materials before and after printing. Scaffolds were prepared, and their molecular weight (Mn), glass transition temperature (Tg), in vitro degradation, cytocompatibility and mechanical properties were assessed. Then, personalised 3D models were designed using the medical images from two patients, and scaffolds with the shapes of the models were 3D printed using PCL and PLGA with the optimised settings.

After studying the effects of the 3D printing process on the materials we characterised the pore size and porosity at the surface of the 3D printed scaffolds. A major disadvantage of FDM and PED is the pore occlusion at the surface of the models due to the build-up of the materials at the surface during the printing process (Leong, Cheah, and Chua 2003). Many studies have investigated the internal porosity and architecture of the printed structures (Moroni, de Wijn, and van Blitterswijk 2006) but very little attention has been paid to surface porosity. The pore size and porosity at the surface play an important role in cell ingrowth and vascularisation (C. M. Murphy, Haugh, and O'Brien 2010) (Wang et al. 2015). Additionally, the surface porosity may also affect surgical suturing through scaffolds. Implants are usually required to be secured in situ to prevent migration and extrusion.

For the reasons mentioned above, it is important to be able to control the surface porosity and pore size of 3D printed scaffolds. These surface properties depend greatly on the print head path in each layer during the printing process. Current commercial 3D printing software programmes that decide the print head path have not considered the

effect of the printing path on the surface architecture of scaffolds. Therefore, we used an in house developed software to control the printing path. The focus of this study was to investigate the surface geometry of 3D printed scaffolds. Scaffolds were 3D printed with varying surface porosities and pore sizes in order to understand the effect of the surface on cell infiltration and suturing.

3.2. Materials and methods

3.2.1. Design of 3D models, g-code generation and 3D printing

3.2.3.1. Design of the personalised nose models

The 3D nose model was designed using the medical images processing Mimics software (Materialise, Belgium). Anonymised CT scans were provided by the medical team. The DICOM file with the CT scan images from the patient was imported to the software (Figure 3.1). After importing the images they were filtered by gradient magnitude to detect the edges. A new mask was created by segmenting the images with the thresholding tool. The threshold was set between 43 and 331 (Figure 3.2 and Figure 3.3). The area of the nose was selected by cropping the mask till reaching the borders of the nose (Figure 3.4). The internal soft tissue from the nose was removed in the coronal view with the erasing tool (Figure 3.5). After finishing the editing a 3D model was created from the mask (Figure 3.6.) In order to get a uniform surface, the model was smoothed. After smoothing, the 3D model was exported to the processing software 3-Matic (Materialise, Belgium) for editing. The internal surface of the model was selected and expanded 1 mm. The model was subtracted from the expanded surface with the Boolean operations tool. The final 1mm thickness 3D model was exported from the software in a “.STL” format (Figure 3.7). Additional editing, smoothing, mirroring normal anatomy and device personalised design can be performed at this stage.

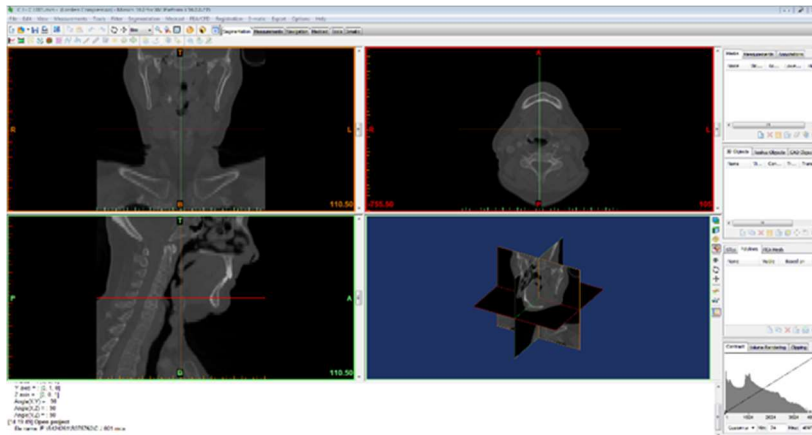


Figure 3.1 Import DICOM files

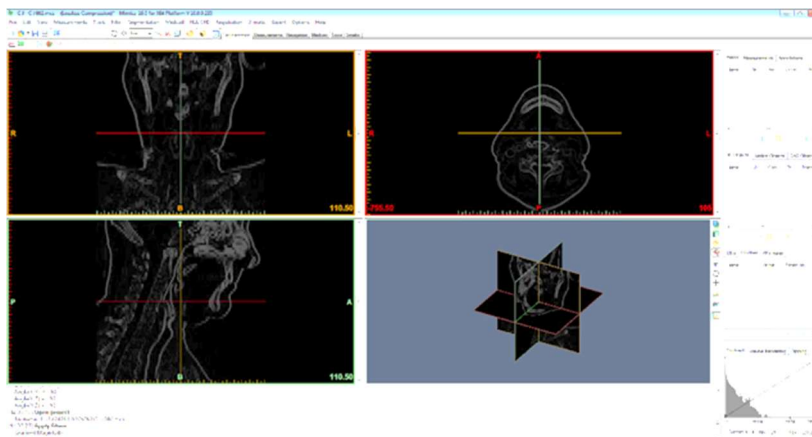


Figure 3.2 Thresholding. Threshold the images to obtain just the soft tissue

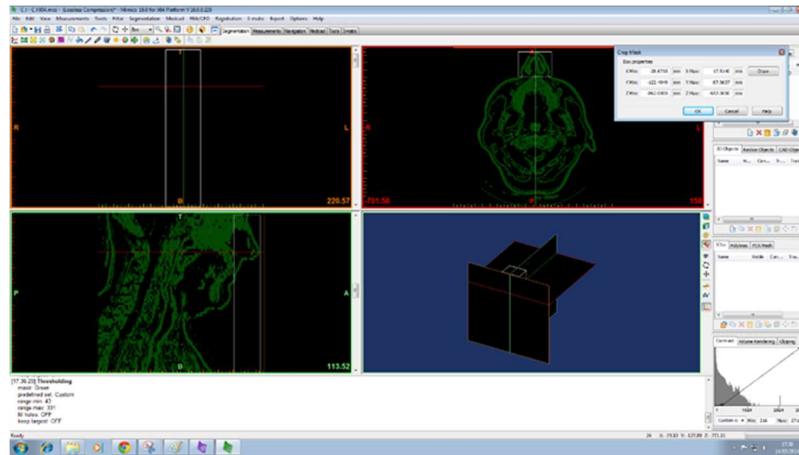


Figure 3.3. Segmentation. Create the mask based on the segmented area

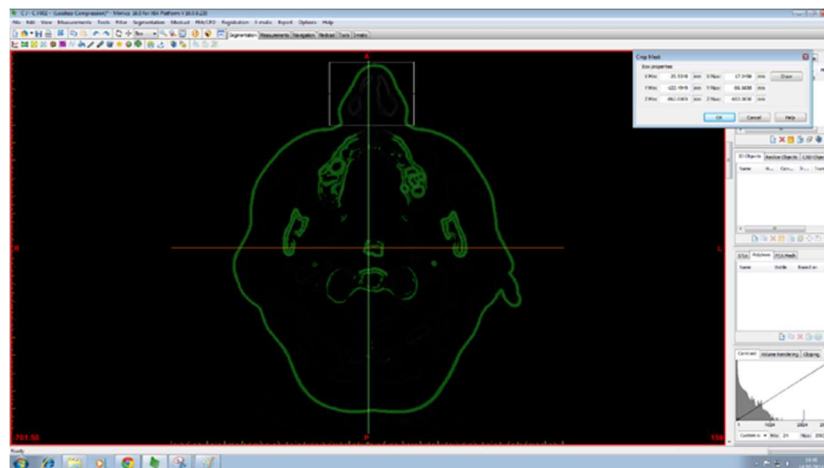


Figure 3.4. Cropping. Define the area of your model by cropping the mask eliminating the rest of the soft tissue that is not part of the nose.

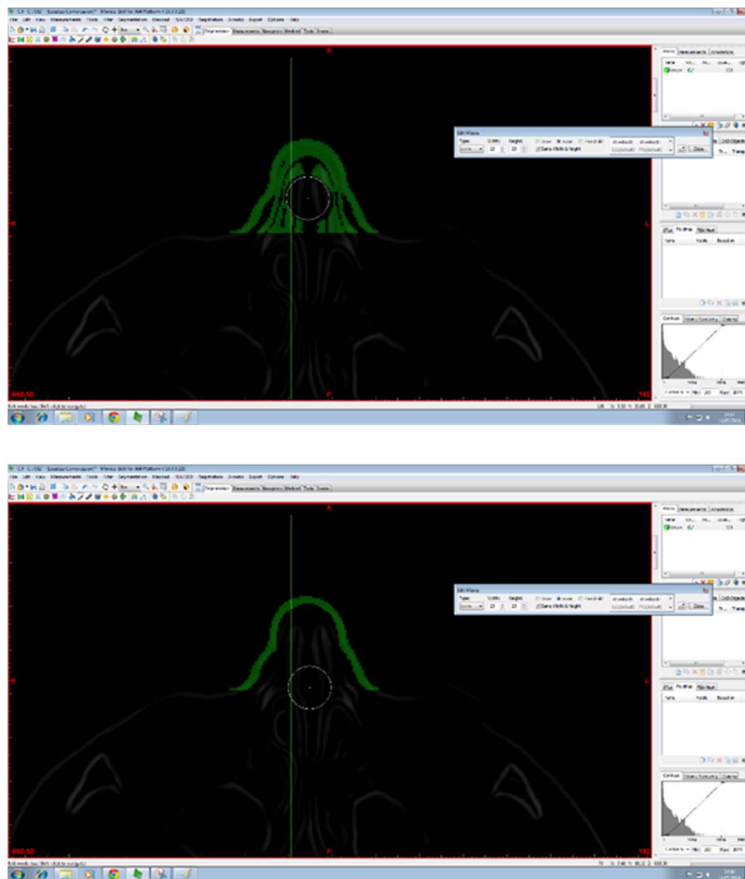


Figure 3.5. Cropping. Delete the internal tissue or parts in the model by editing the mask and erasing those parts.

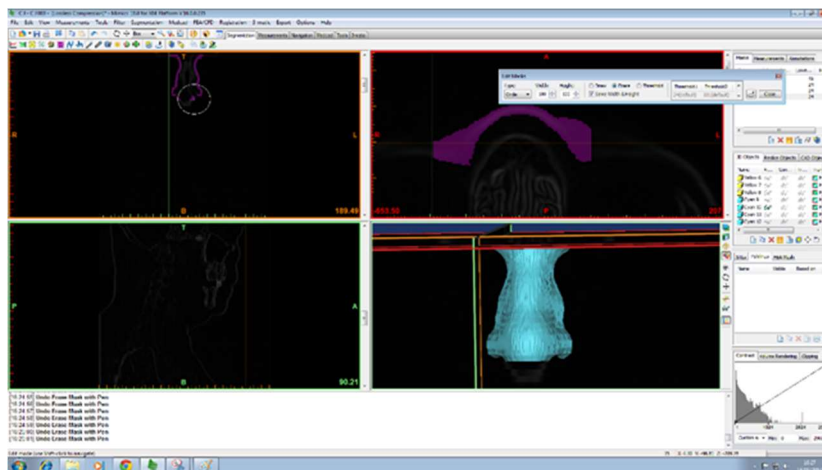


Figure 3.6. Create 3D model . Create a 3D triangle mesh based on the segmented region.

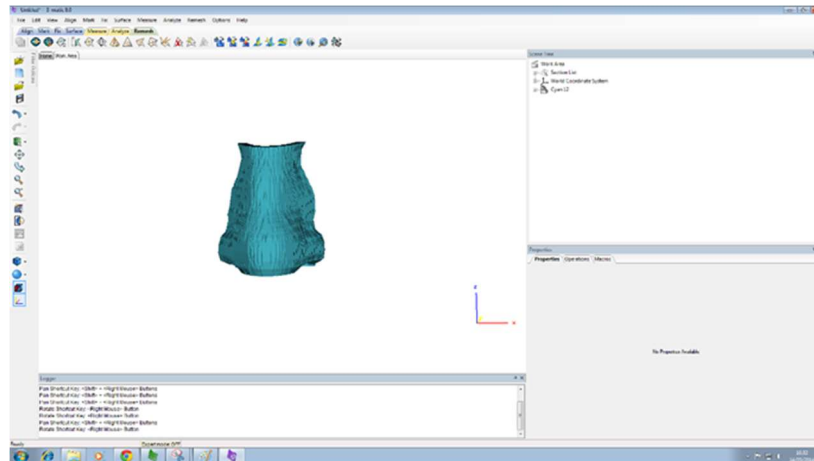


Figure 3.7 . Edition of 3D model and create STL file. The 3D object can be further edited by exporting it to the CAD software 3-MATICS or if not edition is needed the model can be exported as an SLT file.

3.2.3.2. 3D model CAD design and g-code generation using SLT converter

Two different 3D models were created to be used for the PCL 3D printing optimisation process. A dog bone shape and a rectangle shape model were designed using the open source software Sketchup. Samples size were 8 x 2 x 0.3 cm and 2.5 x 3.3 x 0.2 cm respectively. 3D models were exported in STL format. Then the models were imported to the STL converter software (Regenhu) to generate the g-codes. Here were selected different layer thicknesses, different space between strands ((ratio) distance between two lines based on a ratio of the strand diameter) and different building speed in order to find the best parameters. Once the parameters were selected the g-code was generated. For the 3D personalised PCL and PLGA nose models, the models were created as described in section 3.2.1. and then imported into the SLT converter. Layer thickness was set to 150 μm and distance between strands was 3 ratio.

3.2.3.3. Design of models with BioCAD

BioCAD software allows to design the shapes, select different parameters such as layer thickness and space between strands and generate the g-code with the printing pattern. Circular shape models 5mm diameter and 1 mm tick were designed using BioCAD (Regenhu) to be used for the PLGA 3D printing optimisation process. 3D models with different strand spaces were created and then the g-code was generated. Rectangular 3D models with space in between strand of 0.2, 0.6 and 1.2 mm were designed for the PCL tensile test and porosity measurements.

3.2.3.3. Design of the models with newly-developed software

Figure 3.8 shows 3D representations of the six scaffold structures utilised for studying the surface porosity. They were designed to give a range of surface porosities using newly-developed software integrated into an Excel spreadsheet. It generates machine-code that is imported into the 3D Discovery HMI software. The scaffolds were designed with overall dimensions 16.8 x 2.4 x 4.8 mm (length × width × height). The term surface porosity is used to refer to the porosity of the side-walls of the 3D printed scaffolds as highlighted by the dashed box in the figure. The figure shows how different surface porosities and pore sizes were achieved by controlling two design-aspects of the 3D printed scaffolds: the end angle and the number of repeated layers. The end angle refers to the angle at which the printhead moves from the end of one printed strand to the beginning of the next parallel strand. It was set to be either 45° or 90°. The number of repeated layers refers to the number of consecutive layers with the same printing path.

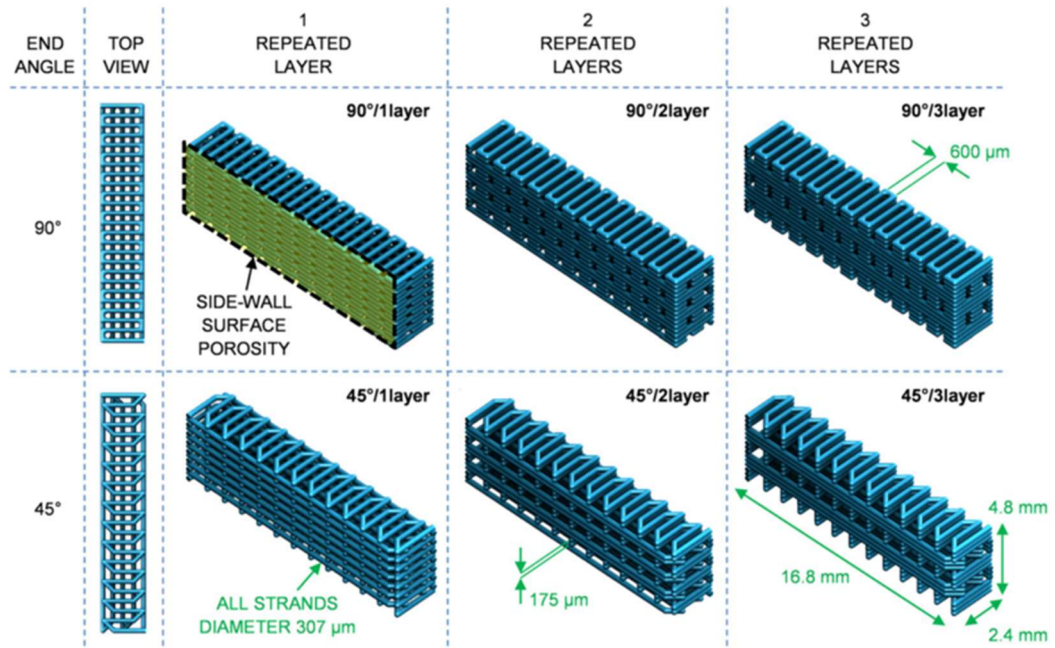


Figure 3.8 Schematic of the six scaffold types investigated in this study. The angle at which the printhead moves from the end of one strand to the beginning of a parallel strand (the end angle) is set to either 90° or 45° in order to control surface porosity. Also, identical layers are printed 1, 2 or 3 times before changing to a perpendicular orientation.

3.2.3.4. 3D printing thermoplastics

The 3D printing system that was used for extruding the thermoplastic polymers was precision extrusion deposition. The way the system works is as follows: the pellets of material get placed on the heating chamber, once the material is liquefied is pushed to the printing head by pressurised air. The printing head is formed by a single screw; the rotations of the screw determine the quantity of material that gets deposited through the nozzle. The g-codes were imported into the HMI software (Regenhu) and printing parameters were set. For printing thermoplastics the parameters that can be controlled in this software are temperature and feeding rate. Temperature of the chamber and printhead were set at 74°C for PCL and 160°C for PLGA. Different feeding rates and

building speeds were used to optimise the PCL 3D printing process. For the PCL and PLGA 3D nose models the feed rate was set to 20 rpm and building speed was 16 mm/s. Same settings were used to 3D print the PCL scaffolds designed to study the surface porosity. The environmental temperature was 37 °C for the 3D nose models and 27 °C for the scaffolds for surface porosity studies. This temperature was based on the results on section 3.3.3.3.

3.2.2. Material and 3D printed scaffolds characterisation

3.2.2.1. Rheological measurements

Thermoplastic poly(ϵ -caprolactone) pellet samples (Mn 14 000, 45 000 and 80 000) were subjected to rheological testing using a Physica MCR 302 rheometer (Anton Paar, Hertford, UK). The viscosity of PCL on relation to temperature changes was measured by increasing temperature from 60°C to 170°C. A 50 mm parallel plate was used with a measuring gap of 1 mm. Shear rate was kept constant at 100 1/s. To study the rheological properties under shear force, shear rate was increased from 0.001 to 100 1/s with a constant temperature of 170°C.

3.2.2.2. Differential Scanning calorimetry and gel permeation chromatography

The melting temperature (T_m) of PCL was determined by differential scanning calorimetry (DSC) (DSC TA Instruments Q2000) to investigate the thermal behaviour of the scaffolds before printing, after printing and after incubation at 37 °C in a humid environment for 14 days. Pellets and scaffolds were heated from 20 °C to 150 °C at a

rate of 10 °C/min. Three cycles were performed and all the measurements were n=3. The glass transition temperature (T_g) of PLGA was evaluated in exactly the same way but the temperature was set from 0 °C to 200 °C at a rate of 10 °C/min.

The polymer molecular weight distribution was determined by gel permeation chromatograph (GPC). The samples were dissolved in chloroform. Polystyrene standards were used to obtain the calibration curve.

3.2.2.3. MicroCT

Samples were analysed using Skyscan 1172 (Skyscan, Belgium) desktop x-ray CT scanner with a pixel resolution of 17.84 µm, x-ray source current 800 µA and voltage 50 kV. Samples were mounted vertically and rotated thorough 360°. Images were recorded every 0.400° of rotation. These images were reconstructed using using the NRecon software (Skyscan, Belgium). Porosity was quantified with 3D histomorphometric analysis using the CTAn software by thresholding the sample lower grey 27 upper grey 255. The 3D models were created using the same software with a pixel resolution of 17.2 µm.

For the surface characterisation studies, the surface of the 3D models was isolated using the netfabb Basic software (netfabb, Germany) to quantify porosity and pore size. Binary images of the surfaces were used for porosity characterisation using the ImageJ software. For the reconstruction of the cell-seeded samples, cells were stained with osmium tetroxide and the previous method was used to isolate the cells from the 3D pictures. The thresholds for the cells were lower grey 106 and upper grey 255.

3.2.2.4. Tensile and compression mechanical test

Mechanical testing was conducted on the samples with different internal porosity using TA.HD plus texture analyser (Stable micro systems). Each specimen was loaded until reach the maximum force of 5kg at a displacement rate of 1mm/min. All tests were performed in triplicates. Young's modulus (MPa) was calculated from the stress–strain curve as the slope of the initial linear portion of the curve (20%-70%), with any toe region due to the initial settling of the specimen neglected.

The compressive tests of the scaffolds designed to study the surface porosity were conducted using an Instron 5969 machine with a 5 kg load cell was used to compress unconstrained samples between two steel plates at a rate of 1mmmin^{-1} to 33%strain. Three samples were tested for each scaffold design. They were compressed parallel to the build direction (the direction in which layers were built-up during 3D printing process). The compressive moduli were calculated for all samples using a linear elastic compression phase as the applied force increased from 10 to 50 N.

3.2.2.5. Microscopy

Optical images of 3D printed scaffolds were taken using a Nikon stereo microscope.

3.2.3. Cell seeding in 3D printed scaffolds

3.2.3.1. Scaffolds treatment before seeding

PCL and PLGA 3D printed samples were disinfected with 70% industrial methylated spirit for 24 h, washed 5 times with phosphate buffer saline (PBS) and incubated overnight with FCS containing 2% antibiotic/ antimetabolic for protein adsorption. The samples were fully saturated with FCS before being transferred into the seeding vessels.

3.2.3.2. Static cell seeding

ShCh cells were cultured as mentioned in section 2.2.1.1. A suspension of 800 000 cells in 50 μ l was pipetted on the top of the scaffolds. Cells were left to attach for 2 h and subsequently samples were transferred to a new well containing 200 μ l of medium. Medium was changed every 3 d.

For seeding the scaffolds with different surface porosities the 3D printed scaffolds pre-saturated with FCS were placed into 96-well plates leaving one of the side-walls facing upwards. We followed a static seeding method used previously elsewhere (Buizer et al. 2013). A suspension of 800 000 cells in 50 μ l was pipetted on the top of one of the side-walls of the scaffolds. Cells were left to attach for 2 h and subsequently samples were transferred to a new well containing 200 μ l of medium. Medium was changed every 3 d. Four samples of each condition were seeded. Three were used for DNA quantification assay and one for osmium tetroxide staining.

3.2.3.3. Dynamic cell seeding

The 3D printed scaffolds™ were placed inside KIYATEC 3DKUBE (KIYATEC, USA) chambers with one of the side-walls facing the inlet of the chamber the other side-wall facing the outlet. A 3 ml cell suspension containing 800 000 cells was inoculated into the silicon tubing (Altec, UK) connected to the KIYATEC 3DKUBE. The cell suspension was perfused in a closed-loop for individual samples using a peristaltic pump (Watson Marlow 323, UK) at a flow rate of 0.5 ml min⁻¹ for 1 h. Perfusion was stopped and cells were left to attach to the scaffolds for 2 h. Four samples of each condition were seeded. Three were used for DNA quantification assay and one for osmium tetroxide staining.

3.2.3.4. Cell number quantification and proliferation

Cell number was evaluated by DNA quantification™ using Quant-iT PicoGreen® dsDNA Assay Kit (Life technologies, USA). Samples were freeze thawed three times for membrane disruption. Cells were lysed according to the manufacturer protocol. The fluorescence intensity was measured to quantify the amount of DNA using a TECAN plate reader (Tecan, Switzerland) at an excitation of 480nm and emission of 560 nm. The number of cells was correlated with the fluorescence intensity using a calibration curve. Cell proliferation was determined on days 1, 7 and 14 using a cell viability reagent PrestoBlue® (life technologies, USA). Samples were incubated for 1.5 h in the PrestoBlue® solution. Fluorescence intensity was measured at an excitation of 520nm and emission of 590 nm.

3.2.3.5. Osmium tetroxide and histological staining

Samples were fixed using 3% glutaraldehyde (Sigma- Aldrich, UK). Fixation was performed overnight at 4 °C. After fixation, samples were washed with PBS and stained with 1% osmium tetroxide for 2 h. Samples were then washed and left to dry in a fume hood for 4 d before microCT scanning. For the histological staining, the samples were fixed with 7% paraformaldehyde for 2 h at 4 °C. After fixing, samples were washed with PBS and stained using toluidine blue for 2 h followed by washing. Samples were then sectioned and imaged under a microscope.

3.3.Results and Discussion

3.3.1. Design of the models

The personalised 3D nose models were designed based on the CT images of two anonymous patients following the surgeon requirements. There are two main advantages of using 3D printing for nose reconstruction. The first one is the possibility of improving the aesthetic outcome by returning to the patient their own facial characteristics. The second advantage is the 3D printed implant will also act as a surgical guide, significantly shortening the surgical time. The structural support of the nose is the cartilage which also contributes greatly to the shape of the nose. Additional to the cartilage the soft tissues also contribute to the shape (section 1.1.1.). The 3D model was designed based on the entire shape of the nose not just the cartilage to be able to regenerate the shape and also provide full support to the skin flap that will cover the reconstructed tissue.

Figure 3.9 is an example of one of the designs created for the surgeon. In this case the surgical requirement was a full nose without the nasal septum. This design will be used just as a surgical guide and support for the cartilage grafts. For this reason, a channel in between of the nostrils was required to fix in place the cartilage grafts that will form the septum. The image at the bottom right of Figure 3.9 represents a half nose model. This model includes additional suturing holes for holding in place the cartilage grafts on the surface.

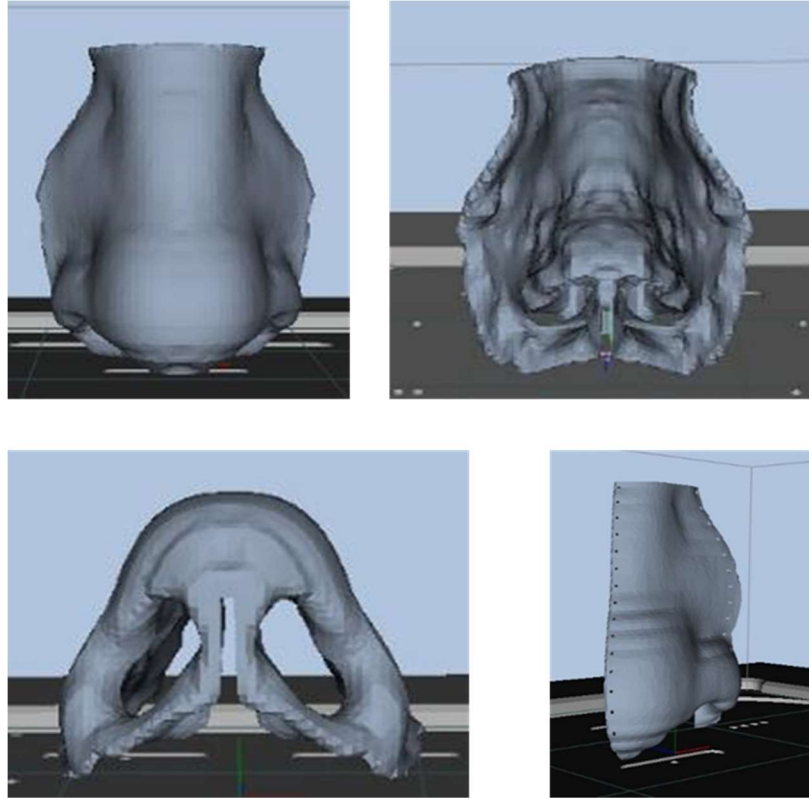


Figure 3.9 3D nose model created using the CT scan of the patient following surgeon requirements for an implant that will work as surgical guide and will degrade with time. The design at the bottom left includes a channel for inserting cartilage graft to create the nasal septum. The design at the bottom right is for a semi nasal defect and includes suturing holes.

3.3.2. Characterisation of 3D printing polycaprolactone

Polycaprolactone is a thermoplastic semi-crystalline polymer with a glass transition temperature of $-60\text{ }^{\circ}\text{C}$ and a melting point ranging between 59 and $64\text{ }^{\circ}\text{C}$ (Woodruff and Hutmacher 2010). In this section PCL is characterised by measuring its rheological and thermal properties pre-printing.

3.3.2.1. Rheological properties

Viscosity of the material is one of the most important parameters for 3D printing. The viscosity of PCL melts was measured by varying the temperature from 60 °C (melting point) to 160 °C. Molecular weight is the main parameter that influences polymer flow behaviour at temperatures above the glass transition temperature (for an amorphous material) or the melting point (for a semi-crystalline polymer) (Vinogradov and Malkin 1980); therefore different PCL MWs were investigated. A constant shear rate of 100 (1/s) was applied to Mn 14,000 (PCL 14) and 45,000 (PCL 45) whilst it was only possible to apply an average shear rate of 2.5 (1/s) to 80,000 (PCL 80) due to the high viscosity of the material and rheometer limitations. Figure 3.10 shows that viscosity of PCL is temperature and molecular weight dependent. Viscosity values for PCL 14 decreased from 15 to 5 Pa-s, from 80 to 18 Pa-s for PCL 45 and from 120 00 to 50 Pa-s for PCL 80.

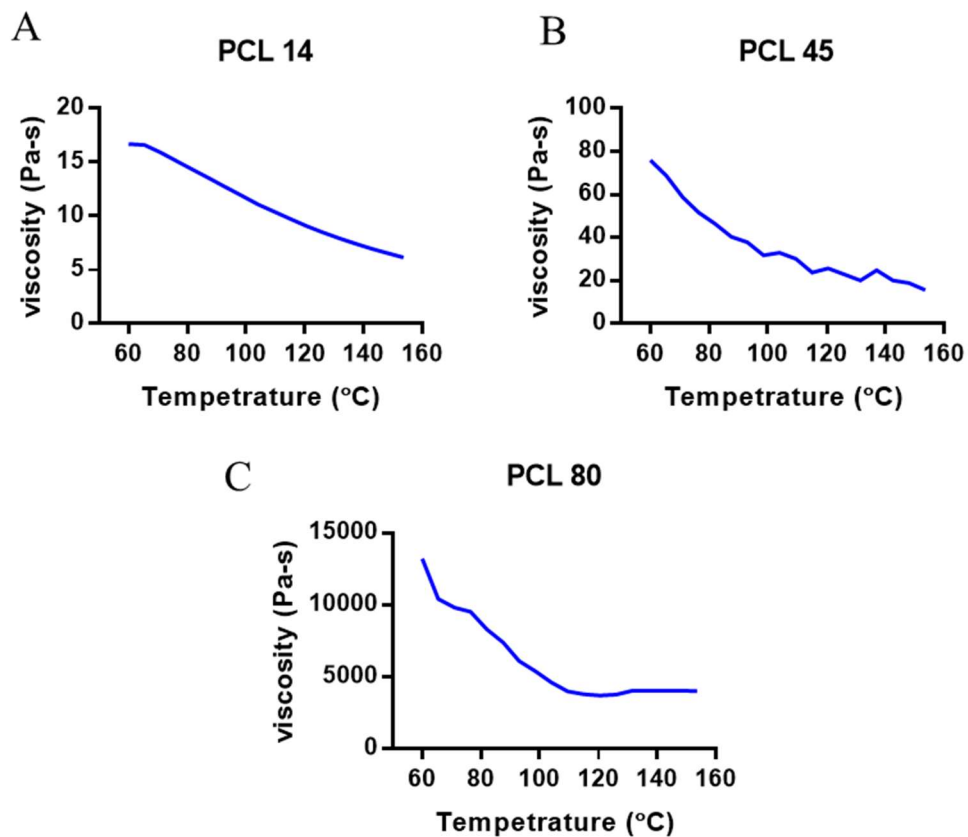


Figure 3.10 Viscosity of polycaprolactone against temperature from going from 60°C to 160 °C. (A) PCL 14 viscosity went from 15 Pa-s to 5 Pa-s. (B) PCL 45 viscosity went form 80 Pa-s to 20 Pa-s. (C) viscosity of PCL 80 went from 140000 Pa-s to 5000 Pa-s.

The viscosity of the PCL with different Mn was measured as function of increasing shear rate. A constant temperature was maintained for all of them at 160 °C. PCL 14 showed shear thinning behaviour at very low shear rate, but a shear rate of 0.01 (1/s) was reached a transition to a Newtonian behaviour was observed (Figure 3.11A). A similar performance was observed with PCL 45 (Figure 3.11B). Whereas with PCL 80 at low shear rates the viscosity was constant; after reaching a shear rate of 0.1 (1/s) the viscosity started to decrease (Figure 3.11C).

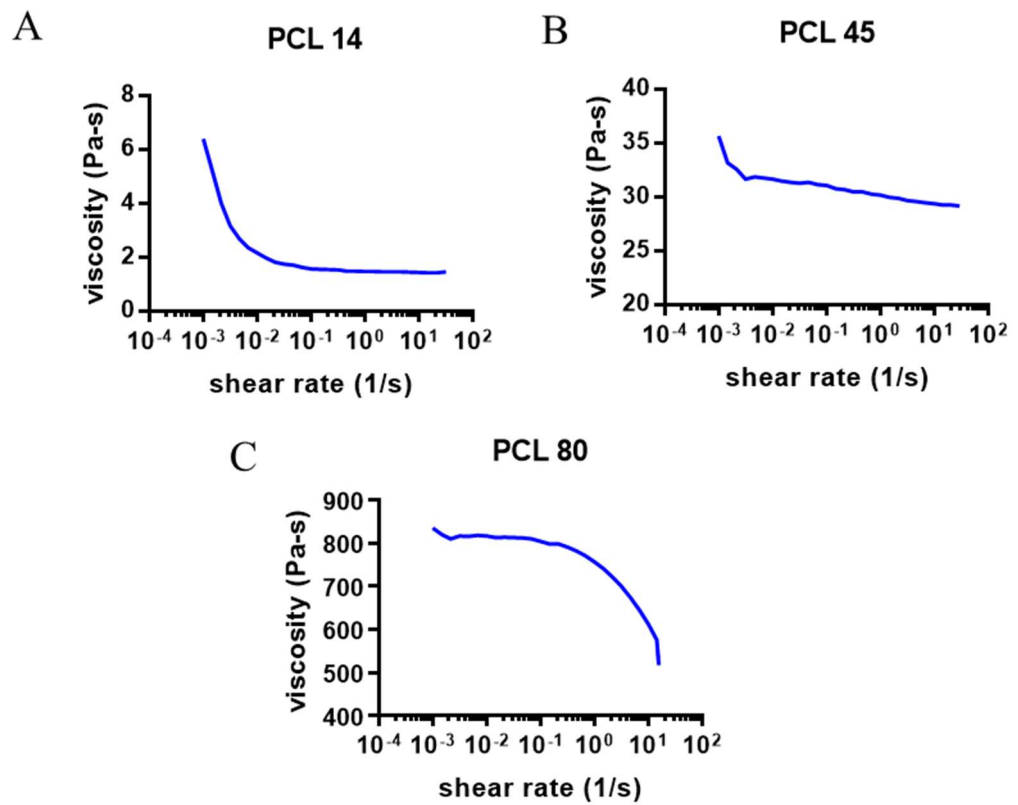


Figure 3.11 Viscosity of polycaprolactone with increasing shear rates going from 10^{-3} (1/s) to 10^2 (1/s).

It has been previously demonstrated that PCL 45 and PCL 80 are printable materials (Domingos et al. 2009, Hutmacher et al. 2001). From these two materials it was decided PCL 45 will be used given that the processing temperature is lower than PCL 80 and that will prevent thermal degradation happening.

3.3.2.2. Thermal analysis

The melting point of PCL 45 was assessed before processing it just to verify if there are any changes in the thermal properties of the material after been 3D printed. In Figure 3.12 is shown that the melting point of PCL was 58 °C before printing.

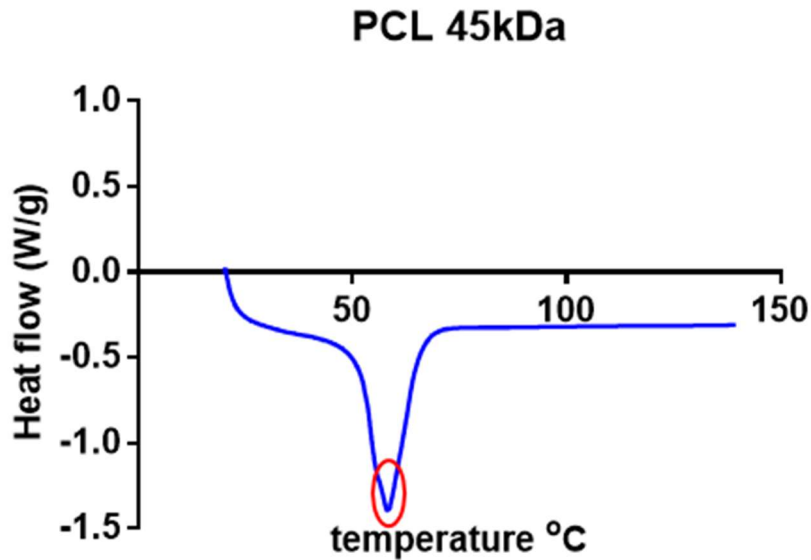


Figure 3.12 Polycaprolactone melting point measured with DSC was 58 °C

3.3.2.3. Characterisation of the 3D printing method for polycaprolactone

3.3.2.3.1. Feeding rate and building speed optimisation

The two main factors that are important for the formation and shape of strands are the feeding rate and building speed. The feeding rate is the rotations per minute (rpm) of the screw and the building speed is the speed that the printing head moves on x and y directions. Figure 3.13 shows the differences of the strand shape when the rpm is varied. 10 and 15 rpm did not allow enough material to be deposited, resulting in thinner and

weaker strands. 20 rpm was selected as the parameter to be used for extruding PCL. The building speed was also varied (Figure 3.14), with 16 mm/s being the speed that deposited the most uniform strands

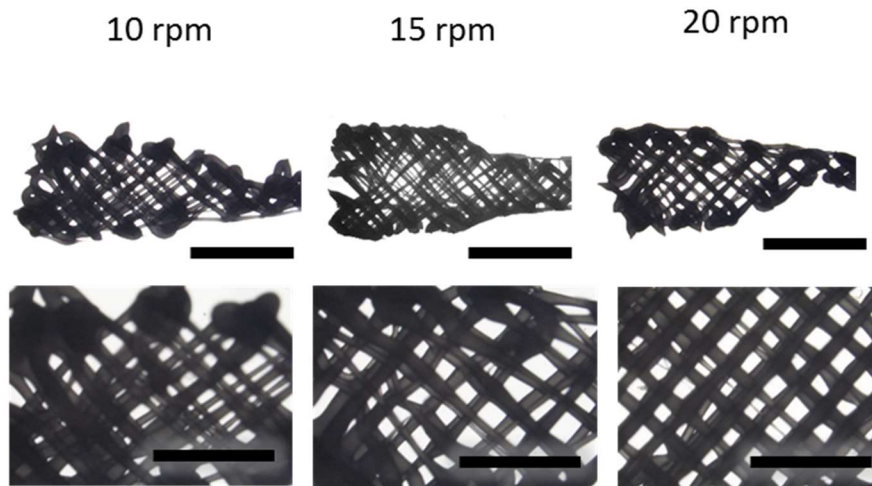


Figure 3.13. Images of samples 3D printed at feeding rates of 10, 15 and 20 rpm. Samples printed at feeding rates of 10 and 15 rpm show thinner and weaker strands compared with the samples printed at 20 rpm. Scale bar top row represents 5mm and bottom row 2mm.

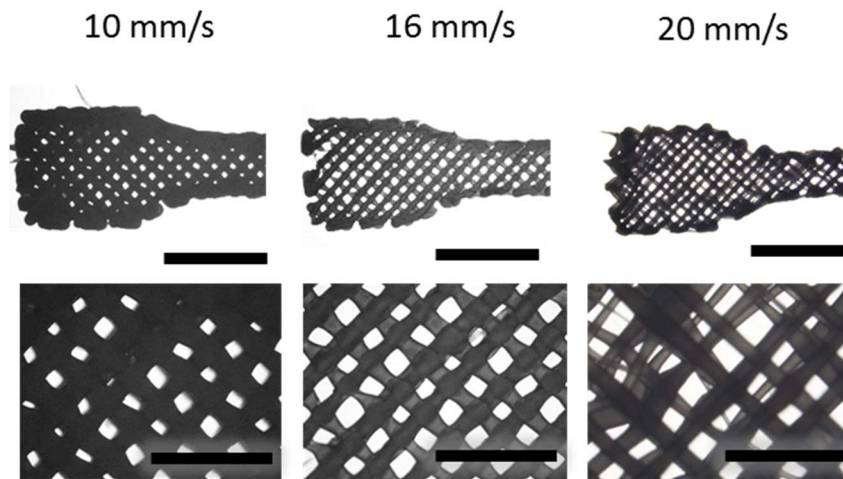


Figure 3.14. Samples 3D printed at building speeds of 10, 16 and 20 mm/s. The images of the samples printed at 20 mm/s show that the strands are thinner and more disorganised compared than 10 and 16 mm/s. Samples printed at 16mm/s show strands with uniform thickness. The samples printed at 10 mm/s had very thick strands and some pore closure was also observed. Scale bar top row represents 5mm and bottom row 2mm.

3.3.2.3.2. Optimisation of layer thickness and space between strands

The 3D printer (Regenhu) has two different software to create printing paths: BioCAD and SLT converter. BioCAD offers freedom in shape and printing path design but 3D models cannot be imported into it; the model has to be drawn manually. The STL converter allows the operator to import a 3D model designed using a different software, but it does not give the user much freedom on the printing path design compared to BioCAD. Because the personalised 3D nose models were generated using Mimics®, the printing process of PCL using the STL converter had to be optimised. The two parameters that needed to be optimised were layer thickness and space between strands (ratio between the diameter of the strands).

Figure 3.15 shows the layer thickness of 100 μm with ratios of 1,3 and 5. It was observed that when ratio 1 and 3 were used the scaffolds were completely solid (Figure 3.15 A and B). When ratio 5 was used the space between the strands was 287 μm (Figure 3.15C). Bigger strand space was observed when scaffolds were printed with layer thickness of 150 μm and ratio 3 and 5 (Figure 3.16B and C). The space were 380 μm and 587 μm respectively. Samples with ratio 1 were solid (Figure 3.16A).

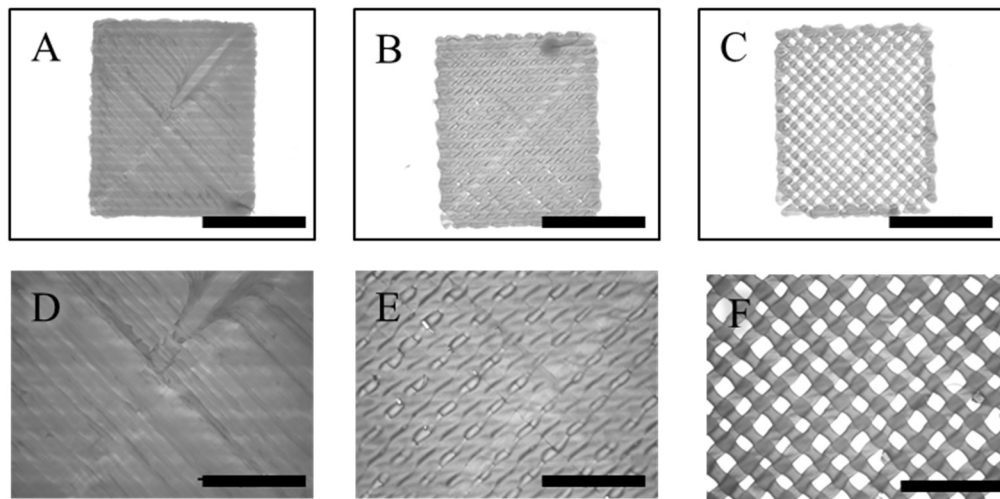


Figure 3.15 Scaffolds of layer thickness of 100 μm . Space ratio of space of 1 (A and D) and 3 (B and E) formed scaffolds without observable spaces between lines. A ratio of 5 result with line spaces between 286 μm (C and F). Scale bars representing 5 mm (A-C). Magnification pictures of A-C and scale bars representing 2 mm (D-F).

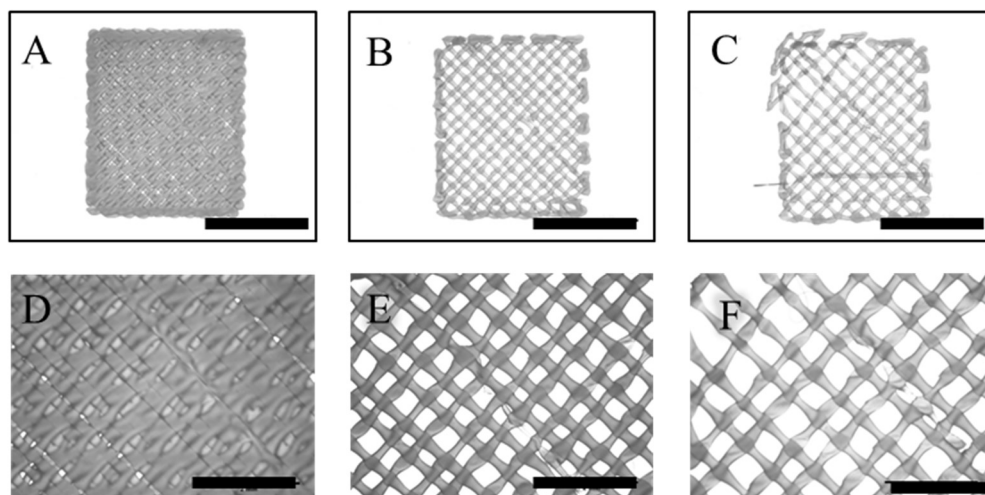


Figure 3.16 Scaffolds with layer thickness of $150\mu\text{m}$. A ratio of 1 between lines results in no uniform strands and non-observable spaces (A and D). A ratio of 3 between lines results in spaces of $380\mu\text{m}$ average (B and E) and ratio of 5 results in spaces of $587\mu\text{m}$ average. Scale bars representing 5 mm (A-C). Magnification pictures of A-C and scale bars representing 2 mm (D-F).

3.3.2.3.3. Control of the environmental temperature

Delamination of scaffolds was observed when printing was conducted at room temperature. The reason for this is that the previously printed layer, which is the substrate for the next layer, must be kept at a temperature just below the solidification point of the thermoplastic material to ensure good interlayer adhesion (Stansbury and Idacavage 2016). In order to achieve good bonding between layers, we designed a hood and adapted a fan connected to a water bath to control the temperature inside the hood (Figure 3.17). Then different temperatures and different printing times were tested in order to find the ideal temperature for small, medium and large structures (Figure 3.17). It was found that for samples that take between 1-5 min to be printed the ideal temperature was $23\text{-}25^{\circ}\text{C}$, for samples that take 5-30 minutes the ideal temperature was $24\text{-}27^{\circ}\text{C}$ and for samples that take 30-120 minutes the ideal temperature is $30\text{-}35^{\circ}\text{C}$. This was decided based on layer delamination (D), good interlayer adhesion (G) or

collapsing of the layers (M) because the PCL was still melted before the other layers got deposited on top.



		Printing time		
		1-5 min	5-30 min	30-120 min
Enclosure T (°C)	20	D	D	D
	23	G	D	D
	25	G	G	D
	27	M	G	D
	30	M	M	G
	35	M	M	G

Figure 3.17 Control of environmental printing temperature in order to improve interlayer adhesion. The top image shows the hood, fan and thermometer system constructed to control the temperature surrounding the 3D printer while the structures are printed. The table shows how the printing time and environmental temperature affect the final printed structure. D: delaminates G: good M: collapse of the structure due to melted strands.

3.3.2.4. Effect of porosity on mechanical properties

Porosity is an important factor to consider when designing scaffolds for tissue engineering (Nuernberger et al. 2011) but porosity can also affect the mechanical properties of the final structures. For this reason, understanding the effect that porosity has on the mechanical properties of the structures is essential. Rectangular structures were 3D printed with different porosities by varying the space between the strands. The porosity calculated with microCT for the samples with 1.2, 0.6 and 0.2 mm space between strands was 72, 52 and 24% respectively (Figure 3.18). Then, their mechanical properties were tested (Figure 3.19). As expected the samples with lower porosity (24%) (Figure 3.19A) had the highest Young's modulus of 100 MPa, followed by the sample with 57% (Figure 3.19B) porosity with a Young's modulus of 60 MPa and the 72% (Figure 3.19C) porosity with a modulus of 30 MPa.

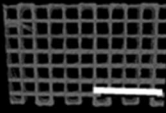
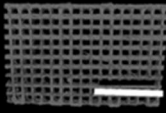
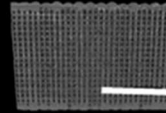
Space between strands	1.2 mm	0.6 mm	0.2 mm
microCT reconstruction			
porosity	72%	57%	24%

Figure 3.18 porosity of scaffolds related with spacing within the strands. Scaffolds with 1.2 mm, 0.6 mm and 0.2 mm had 72%, 57% and 24% porosity.

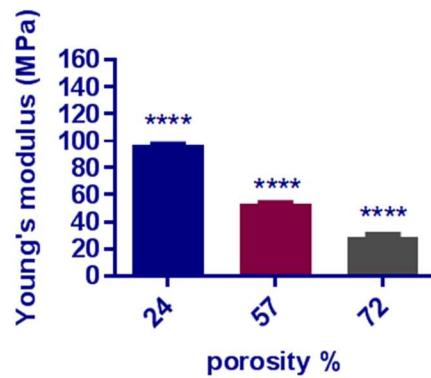
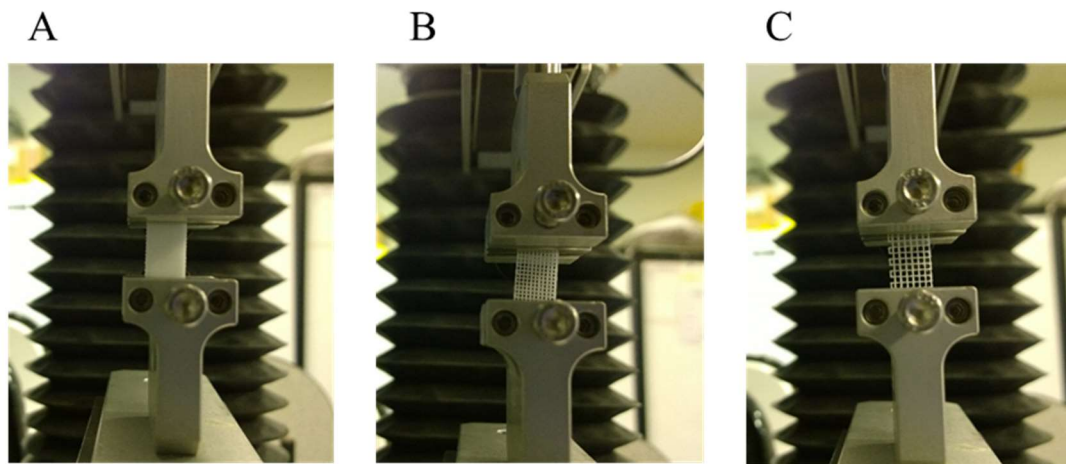


Figure 3.19 Mechanical properties of samples with (A) 24% porosity, (B) 57% porosity (C) and 72% porosity.

3.3.2.5. Effects of the heat on polycaprolactone during the 3d printing process

To investigate if the 3D printing process induces thermal degradation on PCL its molecular weight, thermal and mechanical properties before and after printing were assessed. Additionally, we also investigated the effect of the *in vitro* culture for 15 days. Figure 3.20A shows that the Mn of PCL does not change after printing and the material was stable during 14 days *in vitro* culture. From the thermal properties studies it was observed that the melting point of PCL reduced from 58 °C before printing to 55 °C

after printing (Figure 3.20B). No changes on melting point were observed during the *in vitro* culture. Figure 3.20C shows that there were no changes in the modulus of PCL scaffolds. Studies by Hutmacher et al (Dietmar W. Hutmacher et al. 2001) have shown that PCL 3D printed with FDM system does not affect the stability of the polymer. A possible explanation of the reduction in the melting point of PCL in our study but no change in Mn and mechanical properties is that the PCL could have got contaminated with other some leftover material in the printed head that could have acted as a plasticiser and reduced the melting point.

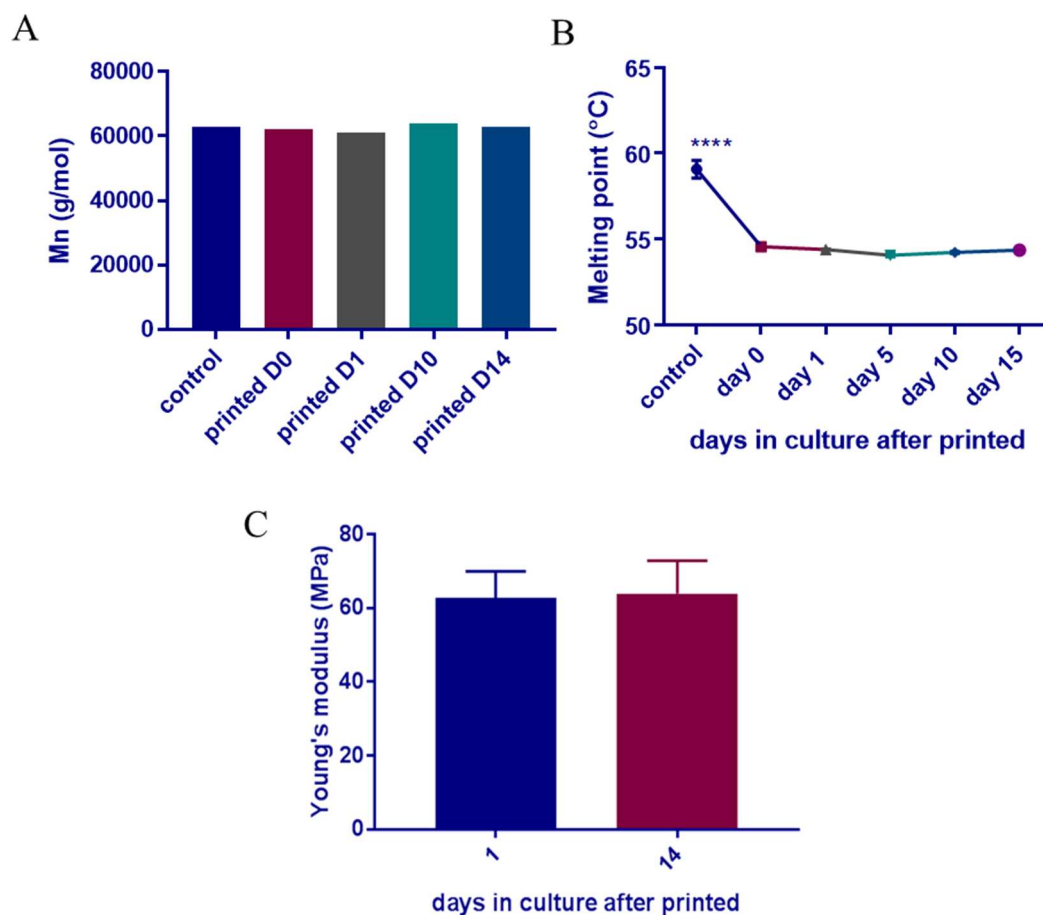


Figure 3.20 Effects of the heat during the 3D printing process on PCL stability. A) No changes were observed in the average molecular weight of PCL after printed and after 14 days of culture compared to the no printed samples. B) The melting point of PCL got reduced by 3 degrees after printed but no changes were observed during the 15 days culture period. C) No changes were observed in the mechanical properties of PCL scaffolds.

3.3.2.6. 3D printed PCL nose

Once the PCL 3D printing process was optimised we 3D printed personalised nose-shaped scaffolds. Two different designs were printed. One only included the shell of the nose (Figure 3.21A) and the second one included the base (nostrils) of the nose (Figure

3.21B). The printing parameters were exactly the same but the printing orientation was different. The first model was printed horizontally (Figure 3.21C) while the second one had to be printed vertically because the nostrils would not have any support if printed horizontally (Figure 3.21B). From these models it was observed that the porosity at the surface of the 3D models was different when printed horizontally (Figure 3.21E) than when printed vertically (Figure 3.21F). The explanation for this was the way in which the software generated the printing code. SLT converter allows the selection of the space between strands (ratio) but it creates the printing path in a random way and cannot be controlled by the user. Studies on how this problem was overcome can be found in section 3.3.4.

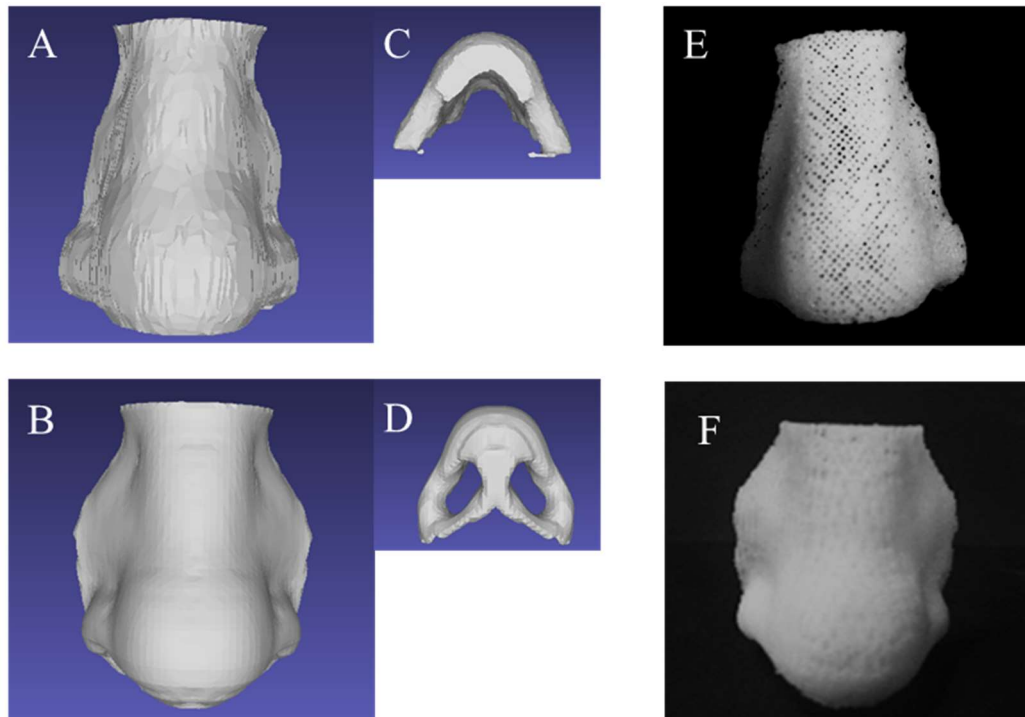


Figure 3.21 3D printed nose-shaped PCL scaffolds. (A) 3D nose model with no nostrils included on the design was printed (C) on horizontal direction. Resulting in a (E) porous surface. (B) 3D nose model including (D) nostrils on the design was 3D printed vertically as image on image B resulting in (F) solid surface.

3.3.2.7. Culture of chondrocytes on the 3d printed scaffolds PCL scaffolds

The seeded chondrocytes were cultured for 14 days in the simple rectangular (8 x 10 mm). PCL scaffolds. Afterwards the samples were stained with toluidine blue to visualize the cell distribution (Figure 3.22). We observed that the scaffolds were fully covered with cells (blue) after 14 days in culture. Additionally, it was noticed that the shape and size of the scaffolds was maintained the same after the 14 days of culture.

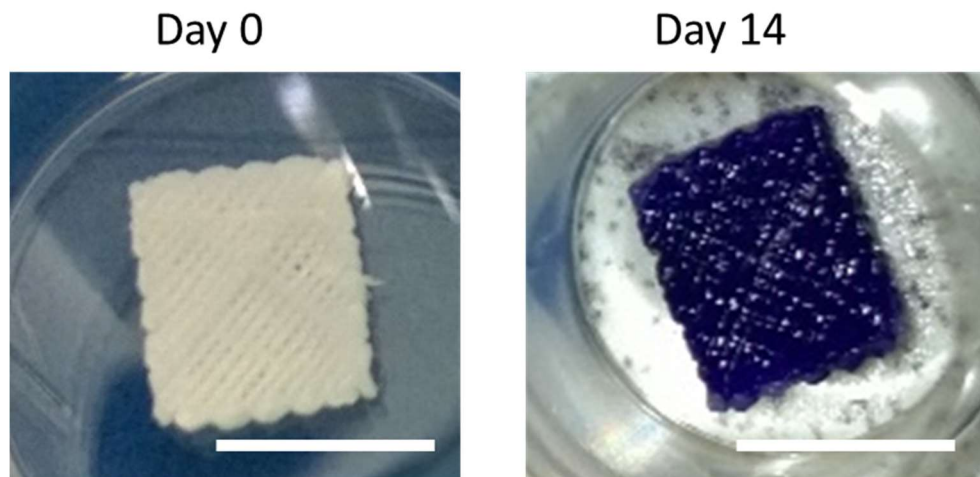


Figure 3.22 Chondrocytes seeded on PCL scaffolds after 14 days in culture. The scaffolds were stained with toluidine blue after 14 days in culture to show the distribution of the cells. Scale bar represents 8 mm.

3.3.3. Characterisation of 3D printing poly (lactic-co-glycolic acid)

Poly (lactic co glycolic acid) is a biodegradable co-polymer with a glass transition temperature between 45-60 °C. The melting point of PLGA can be very variable because depends on the isomeric form of the PLA and the ratio of LA and GA that form the polymer. A melting point will be present if the PLGA is formed by L-PLA but is not present if is formed by D,L-PLA (Steve, Makadia Hirenkumar and Siegel Steve, Drug, and Carrier 2012). PLGA was chosen because one of its main benefits of PLGA that the degradation time can be controlled by modifying the ratio of PLA and poly (glycolic acid) (PGA) (Gentile et al. 2014). Here, we characterised Poly (DL-Lactide-co-glycolide) 85:15 (PLGA) before and after printing by evaluating its rheological and thermal properties.

3.3.3.1. Rheological properties of PLGA

Similar to PCL, the viscosity of PLGA varies depending on the molecular weight. Two different PLGA molecular weight were evaluated 50,000 (PLGA 50) and 150,000 (PLGA 150) Mn. Viscosity of both polymers was evaluated against temperature (Figure 3.23). The viscosity of PLGA 150 was measured from 200 to 150 °C because at temperatures lower than 150°C the material was almost solid and the rheometer plate stopped rotating. Viscosity of PLGA 150 reduced from 259,000 Pa·s at 200 °C to 83,800 Pa·s at 150 °C. Even that the viscosity was reduced at higher temperature, the viscosity was still above the limit (10,000 Pa·s) at which the 3D printer can extrude. This molecular weight could possibly be printed using a different system such as FDM. Viscosity of PLGA 50 was lower than PLGA 150, being possible to measure it from 160 °C to its glass transition temperature of 50 °C. The viscosity of PLGA 50 increased linearly as the temperature increased from 29 Pa·s at 160 °C to 414,000 Pa·s at 50 °C. Based on the printing studies of PCL (section 3.3.2.) we choose 160 °C as the printing temperature for PLGA 50 because at this temperature it has the same viscosity as PCL at its printing temperature.

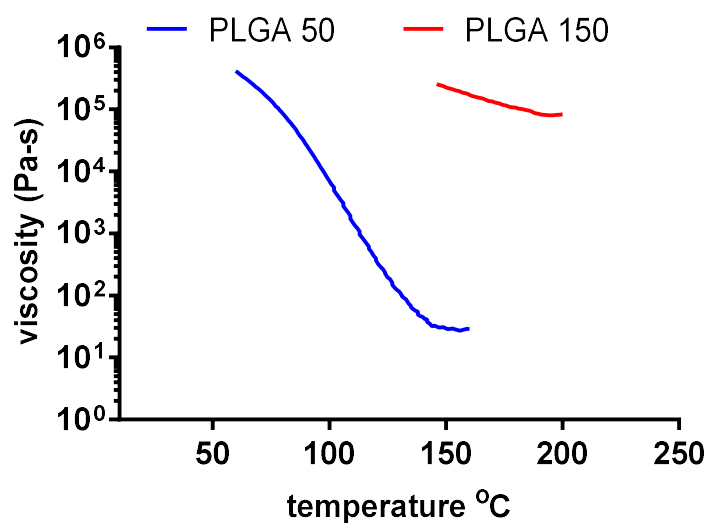


Figure 3.23 Viscosity of PLGA Mn 50,000 and 150,000. Viscosity of PLGA 150 reduced from 259,000 Pa·s at 200 °C to 83,800 Pa·s at 150 °C. The viscosity of PLGA 50 decreased linearly as the temperature decreased from 414,000 Pa·s at 50 °C to 29 Pa·s at 160 °C.

3.3.3.2. Thermal analysis of PLGA

On Figure 3.24 is shown that the glass transition temperature (T_g) of PLGA 50 is 42 °C and there is no melting point as expected given that poly (DL-Lactide-co-glycolide) is an amorphous polymer (Jain 2000).

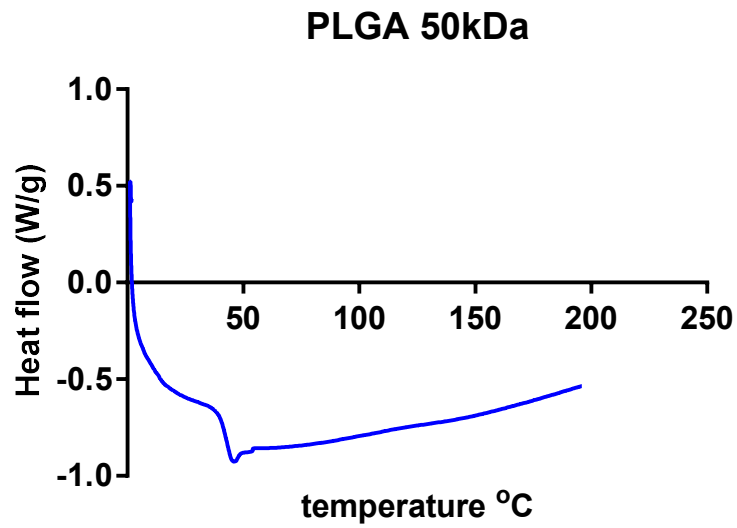


Figure 3.24 Glass transition temperature of PLGA is 42 °C according to DSC result.

3.3.3.3. Optimisation of the 3D printing method for PLGA

The optimisation experiments for 3D printing PLGA were based on the results obtained from the printing characterisation of PCL. Given that the printing temperature of PLGA was chosen to match the viscosity of PCL it was not needed to characterise the feeding rate and building speed. We used the same feeding rate and building speed that were found optimal for PCL (20rpm and 16 mm/s respectively). Optimal layer thickness (100 μm) was kept as well. Those parameters were used to 3D print PLGA scaffolds with different space between strands to obtain scaffolds with different porosities (Figure 3.25).

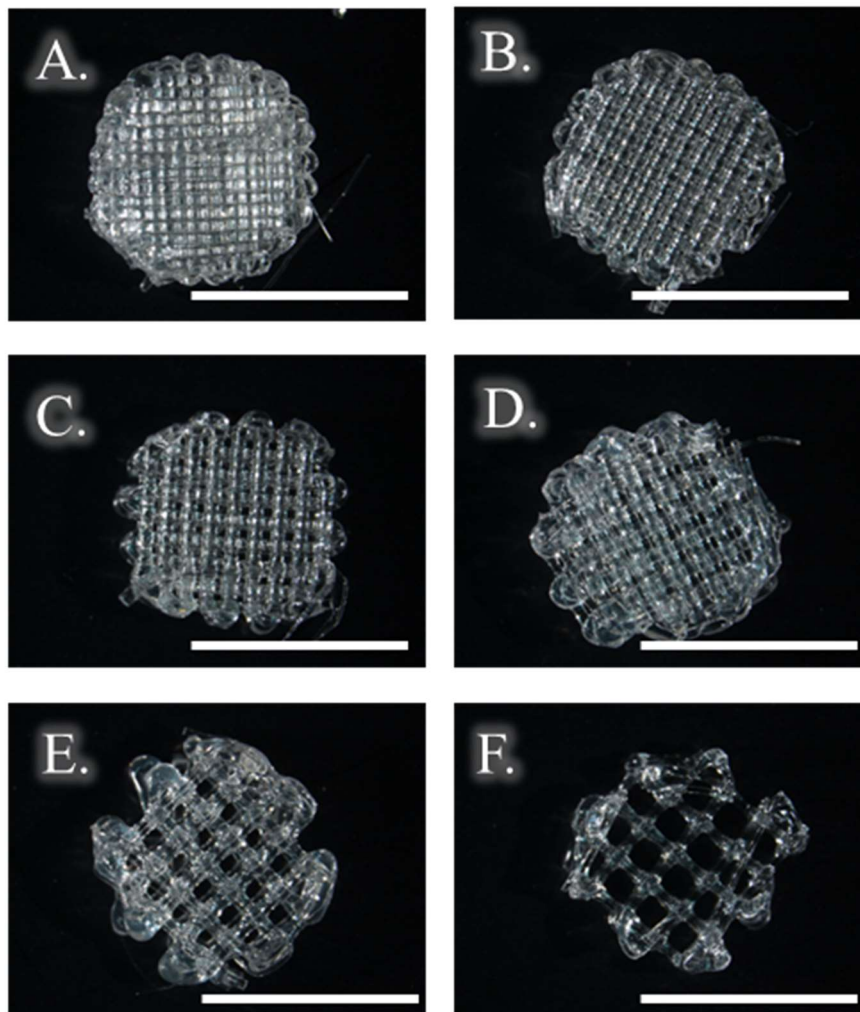


Figure 3.25 PLGA 3D printed scaffolds. Samples were 3D printed at room temperature. Samples were printed varying the space between the strands in order to obtain different porosities. Spacing: A) 100 μm , B) 200 μm , C) 400 μm , D) 600 μm , E) 800 μm , F) 1000 μm . Scale bars represent 5 mm.

The 3D printed scaffolds were incubated at 37 °C in PBS to simulate body conditions and observe if this conditions had any effect on them. After two hours of incubation it was noticed that the samples shrank (Figure 3.26). A possible explanation for the shrinkage is the residual stress (RS) in the polymer caused by rapid cooling (quenching) after the material is extruded (Siegman, Kening, and Buchman 1987). The temperature (37 °C) of incubation softened the polymer, which allowed the RS to deform the printed

structures (Q. Zhang et al. 2015). To solve this problem, the scaffolds were 3D printed at different environmental temperatures closer to The PLGA's Tg (42°C). The purpose of this is to allow the material to cool down slower and avoid the formation of residual stress (Figure 3.27). The temperature surrounding the samples was set at 40, 45 and 55 °C respectively. The samples were 3D printed and incubated for 24 hours, 6 days and 14 days to see if there was any change of shape. In Figure 3.27 it is shown that the scaffolds printed at 40 and 45 °C changed shape after 24 hours, while the ones printed at 55 °C retained its morphology even after 14 days of incubation. This suggests that in order to avoid residual stress the environmental temperature has to be slightly higher than the glass transition temperature of the material. A second observation from Figure 3.27 was that the scaffolds started changing in colour, going from transparent to white during the incubation period. This is due to the increase in crystallinity, which is induced by degradation because an amorphous site degrades at a faster rate than a crystalline site (Shibata, Yada, and Terakawa 2016).

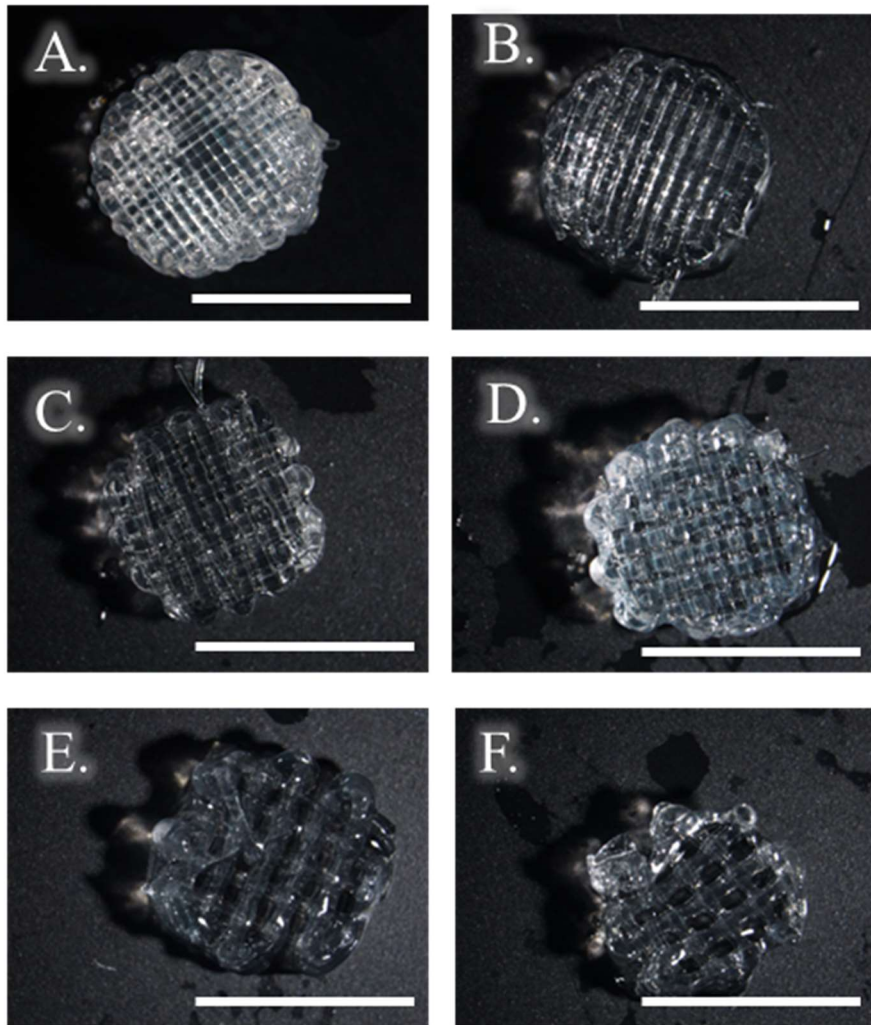


Figure 3.26 3D printed PLGA scaffolds. Samples after 2hr in PBS at 37 degrees. Spacing: A) 100 μm , B) 200 μm , C) 400 μm , D) 600 μm , E) 800 μm , F) 1000 μm . Scale bars represent 5 mm. Deformation and shrinking is observed in all of the samples.

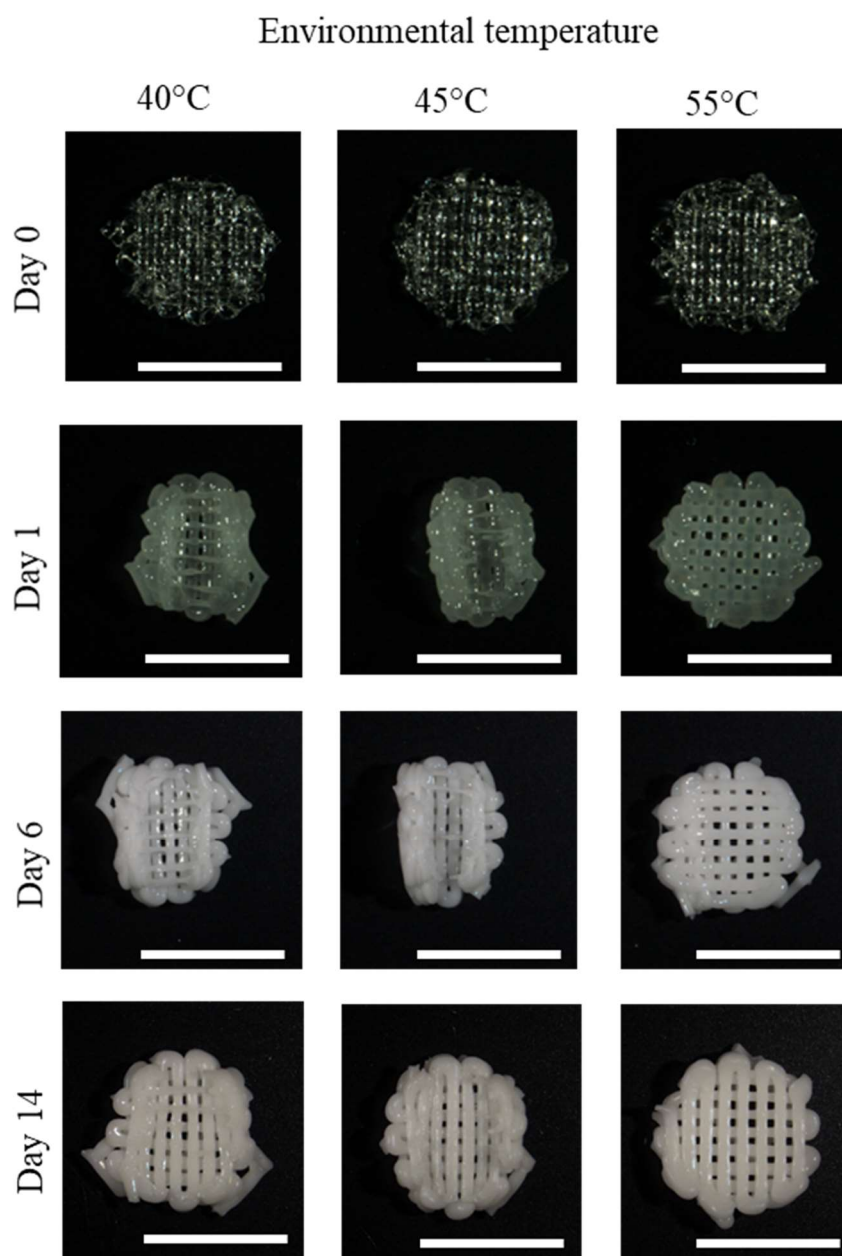


Figure 3.27 PLGA scaffolds printed at different environmental temperatures. Images show deformation of the scaffolds when printed at an environmental temperature of 40 °C and 45 °C. No deformation is observed on the samples printed at 55 °C. Scale bars represent 5 mm.

It was also noticed that deformation was not the same in scaffolds with different porosities. For this reason once the ideal environmental temperature was found,

scaffolds with different porosities were 3D printed (Figure 3.28) to confirm that shrinkage was eliminated for all of them.

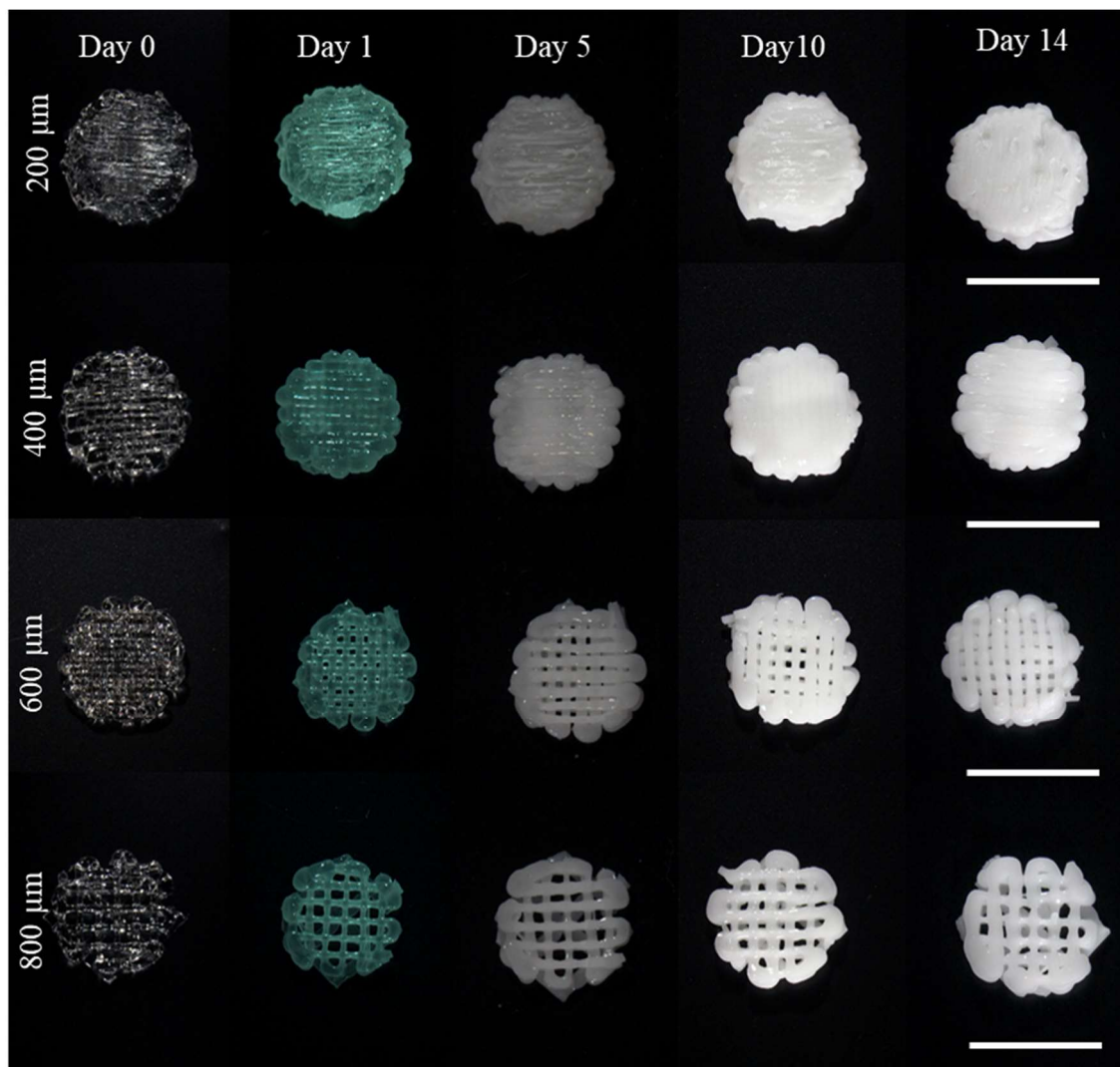


Figure 3.28 PLGA scaffolds after culture for 14 days in PBS at 37 °C. Gradual change in colour is observed in all of the samples.

3.3.3.4. Effects of the 3D printing process on poly (lactic-co-glycolic acid)

The effect of the 3D printing process on the material was investigated by measuring the Tg and molecular weight of the PLGA scaffolds before and after printing. Additionally, to confirm the degradation of the PLGA observed in the previous section we also measured the changes Mn and Tg during a 14-day incubation period at 37°C in PBS. Figure 3.29A shows that the molecular weight of PLGA halved after the 3D printing process and it continues decreasing during the incubation period. Meanwhile, the Tg decreased as well after printing and over the culture period (Figure 3.29B). The reduction of the Tg after printing explains the shrinkage of the samples when incubated at 37 °C which is very close to the Tg, hence allowing the material to release the residual stress and deform.

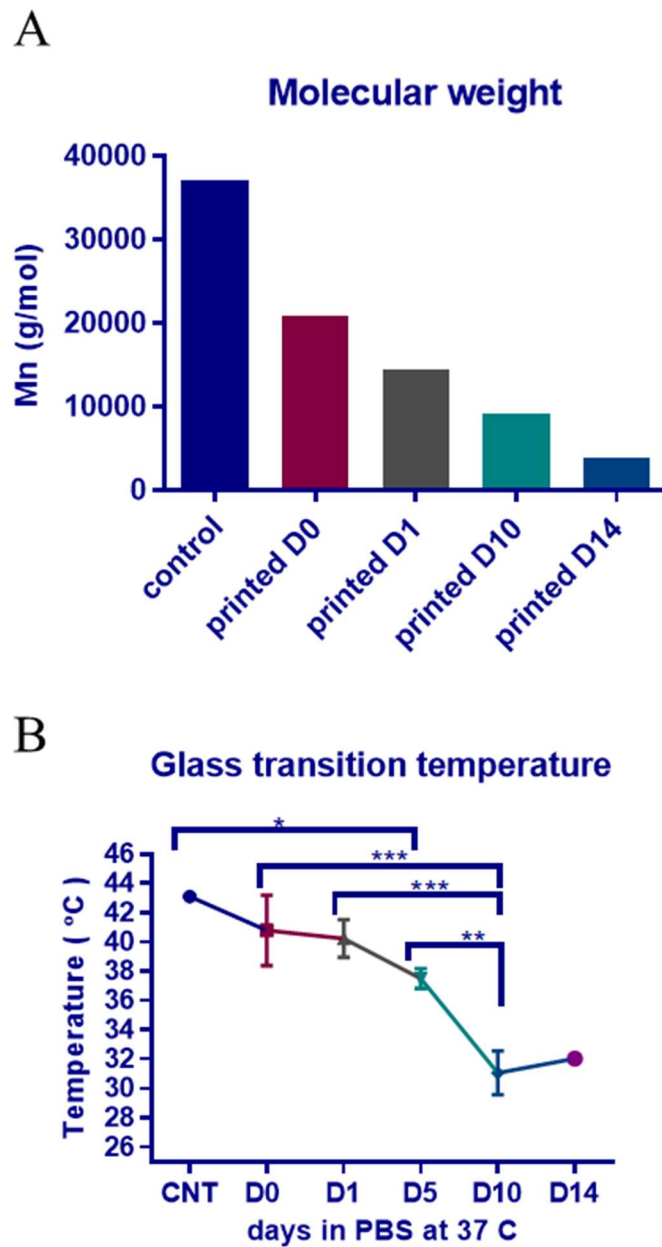


Figure 3.29 Effect of 3D printing on PLGA 50 material properties. (A) The Mn of PLGA got reduced by 50% during the printing process and then a linear reduction was observed during the culture period. (B) The glass transition temperature of PLGA got reduced from 43 °C to 40 °C during the printing process and it continue to decrease during the culture time having a final glass transition temperature of 31 °C by day 14.

3.3.3.5. Culture of cells on the PLGA 3D printed scaffolds

Primary chondrocytes were seeded on the scaffolds and cultured for 14 days to test the biocompatibility. It was noticed that scaffolds deformed when cultured with the cells (Figure 3.30A). Given that the scaffolds are in a soft state at 37°C there is a possibility that the cells and ECM forces deform the material (Engler et al. 2006) because this was not observed on the samples incubated without cells. These effect was also noticed in the PLGA 3D printed personalised nose (Figure 3.30B). The nose shape suffered a complete deformation after 1 day in culture. The shape of the nose was completely deformed by day 10 but it was observed that it was fully covered with cells and ECM showing that the material has good cell biocompatibility. The cells were able to attach and proliferate without the need of any surface modification on the scaffolds.

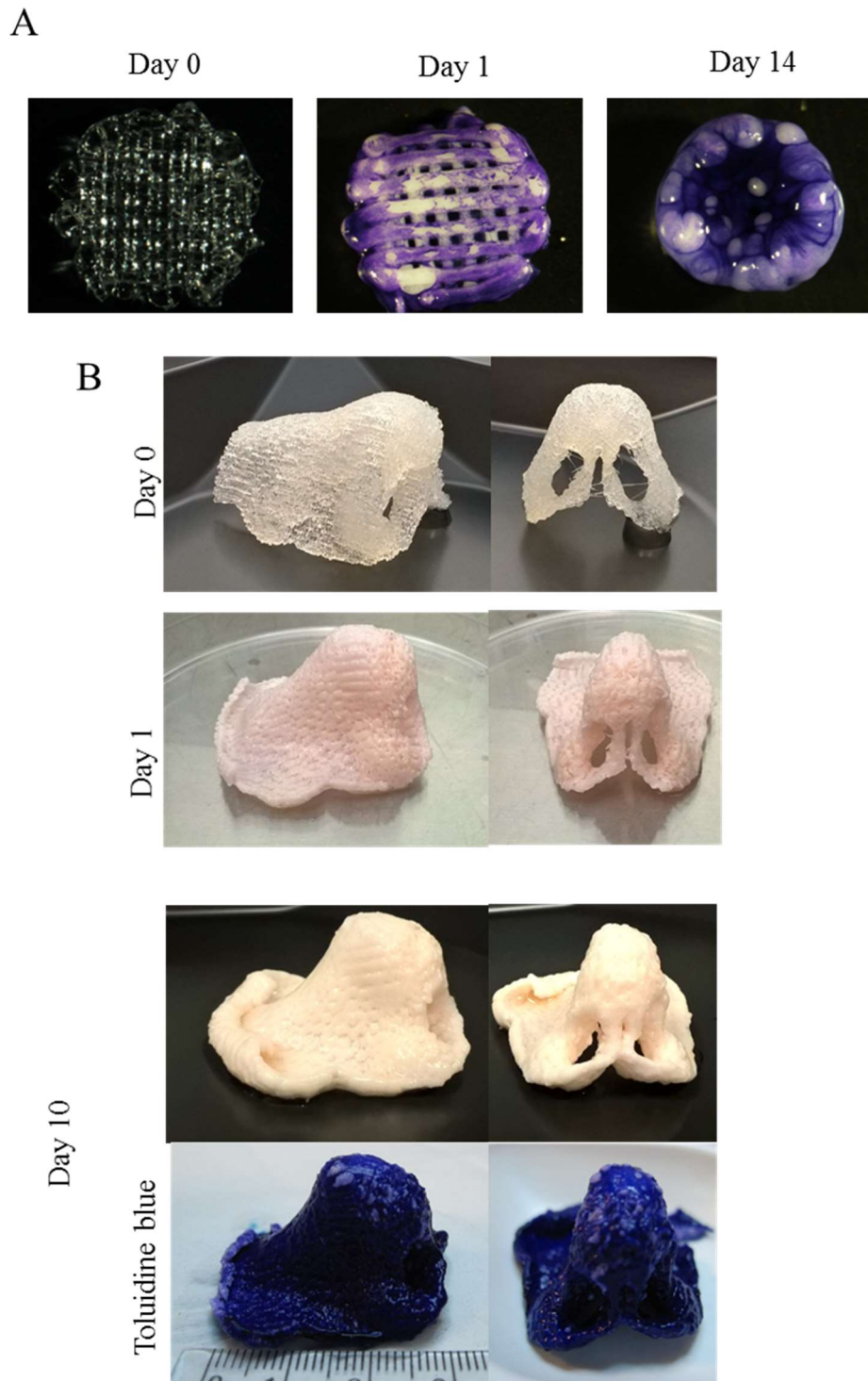


Figure 3.30 Chondrocytes seeded in PLGA scaffolds. (A) Representative images of PLGA scaffolds seeded with ShCh and cultured for 14 days. Samples were stained with toluidine blue to show cells distribution. Scaffold was completely deformed by day14 of culture (B) Images of PLGA scaffolds 3D printed in the nose shape and seeded with ShCh and cultured for 10 days.

3.3.4. Surgical test of the 3D printed nose scaffolds

The surgeon performed a mock nasal reconstruction surgery using the PCL 3D printed personalised nose models to test them (Figure 3.31). In this case he used the model as a surgical guide to suture the cartilage grafts on top of it. Suturing through scaffolds is an efficient way of securing the implant position in the host tissues. In addition to securing the implant, sutures can be used to secure free cartilaginous, osseous or vascularised osseous free flaps to the framework scaffold. This lamination of the framework scaffold with autologous grafts (free and vascularised) creates a composite graft/implant that can then be inserted into the recipient tissue bed. In these instances, the scaffold acts as a surgical guide, aiding the surgeon in reconstruction of highly complex 3D structures, such as in total nasal reconstruction. He decided that the models that have the nostrils were more suitable for this purpose because they will provide more support and a better aesthetic outcome could be achieved. On Figure 3.31A is shown the suturing of cartilage on top of the models. The feedback from the surgeon was that the pores on the model were not big enough for suturing. It required him too much force to be able to insert the needle. Also, he mentioned it was preferable to have the model divided in two parts so he could insert the nasal septum in the middle (Figure 3.31B) and then suture all together. Finally, he mentioned that the shape was right, the mechanical strength was sufficient and that the model is very useful as well for planning the forehead flap (Figure 3.31C).



Figure 3.31. Mock surgery using the PCL 3D printed nose model. A) Suturing of cartilage graft on top of the model. B) Insertion of the nasal septum in between the model. C) Suturing of forehead flap on top of the model.

3.3.5. Surface porosity characterisation

3.3.5.1. Surface porosity and pores size and mechanical properties

In order to increase the pores size and surface porosity of the scaffolds six structures with one, two or three repeated layers and end angles of 45° and 90° were designed and 3D printed according to section 3.2.3.3. and 3.2.3.4. Then, the surface porosity was analysed using microCT and optical microscopy. The end angle affects the print path near the surface of the scaffolds and the number of repeated layers affects the order in which printed strands are laid down on top of one another. Both parameters can be used to control the size and shape of pores. Figure 3.32 shows microscope and microCT images of the six different scaffolds. Figure 3.32A and B show top views of the 90° and 45° end angle scaffolds. It can be seen on this figures that there is a build-up of polymer at the side-wall of the scaffold when the printhead changes direction because there are only two to three pores in the top row of pores, adjacent to the side-wall, compared to five pores in the middle two rows. On Figure 3.32A and B can also be observed that the 45° end angle samples have wider pore because less polymer is 3D printed at or near the side- wall as highlighted by the triangular region. Figure 3.32C-H show the 3D printed side-walls where can also be seen that 45° end angle samples (Figure 3.32D, F and H) have wider pores compare with the 90° end angle Figure 3.32C,E and G). In addition, increasing the number of repeated layers increased the height of pores and therefore pore size, as can be seen in Figure 3.32C-H.

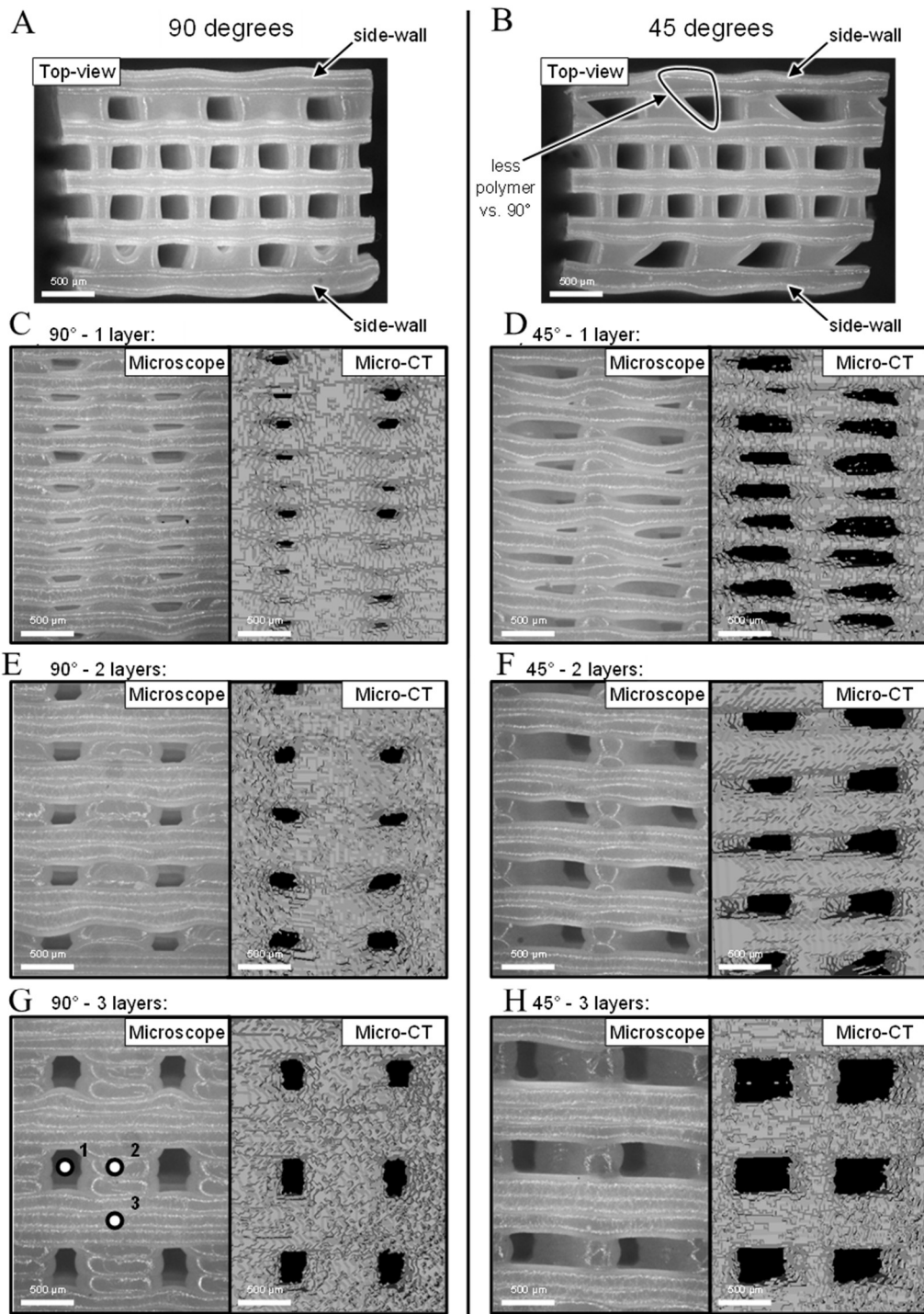


Figure 3.32 . Microscope and microCT images of the different scaffold designs. A) and B) are top view microscope images. (C), (E) and (G) are microscope and microCT images for the 90° end angle samples with 1, 2 and 3 repeated layers respectively. (D), (F) and (H) are images for the 45° end angle samples with 1, 2 and 3 repeated layers respectively.

Surface porosities for the side-wall of the six scaffold designs are plotted in Figure 3.33A. On average for all samples, the 45° end angle scaffolds demonstrated 348% greater surface porosity than the 90° end angle scaffolds with equivalent repeated layers. This is because the pores were wider. Figure 3.33B shows the pore sizes measured for the different scaffold designs. Commercial 3D printing software usually generates a printing pattern of 1 layer 90° end angle. The size of the pores with this pattern is 50 µm wide. Previous studies have reported the need of pores at least 100 µm in diameter for successful exchange of nutrients and oxygen for cell survival (Rouwkema et al. 2008). By modifying the printing pattern, we managed to generate larger pores. On average for all scaffolds, the 45° end angle samples had 361% larger pore sizes than 90° samples with equivalent repeated layers since the pores are wider, as discussed above. The 3 repeated layer samples had an average pore size 434% larger than the 1 repeated layer samples with equivalent end angles.

The bulk porosities of samples measured by microCT are shown in Figure 3.33C. There was a slight increase in porosity of the 45° end angle samples because the printhead travelled along a shorter printpath for each layer (due to cutting corners) and therefore deposited less polymer. However, on average for all scaffolds, the 45° end angle samples demonstrated just 12.7% increase in bulk porosity versus 90° samples with equivalent repeated layers. This is over an order of magnitude less than the effects of end angle on surface pore size and surface porosity. And increasing the number of repeated layers from one to two or three had less than 8.5% effect on bulk porosity. Therefore, the end angle and repeated layer design variables are able to control surface porosity and surface pore size with little impact on bulk porosity.

The compressive moduli measured for each scaffold design are presented in Figure 3.33D. The 45° end angle samples demonstrated an average reduction in compressive modulus of 21.3% versus the 90° samples. This reduction is likely due in part to the reduction of bulk porosity. Furthermore, Figure 3.32 shows that the 90° samples have almost solid sidewalls. Solid walls can considerably affect mechanical properties as demonstrated in a study previously (Eshraghi and Das 2010) where was found that scaffolds with solid walls to have a compressive modulus of 133.4 MPa versus 12.1 MPa for those without, whilst porosity only reduced from 61.9% to 44.8%. For larger scaffolds, the side-walls may have less of an effect on overall scaffold stiffness because the majority of the mechanical properties will be dictated by the large internal region of the scaffolds. However, the geometry of a scaffold may require a thin wall to suit a particular clinical application, such as a scaffold for nasal reconstruction, in which case the 3D printed side-wall is an important factor that must be considered with regards to stiffness. Other design factors including the strand width and spacing between strands have been shown to have a much larger effect on modulus (Ang et al. 2006). Therefore, the end-angle and number of repeated layers may be used to control the surface properties whilst alternative design aspects predominantly dictate mechanical properties, internal porosity and internal pore size. The samples in this study had relatively low bulk porosities (25%–36%). Consequently, their moduli were within the cancellous bone range and higher than those reported for cartilage. Human cartilage has been found to have a compressive modulus in the range of 0.44–20.4 MPa (Richmon et al. 2006) (Shepherd and Seedhom 1999). Increasing porosity has been shown to be able to decrease modulus. 3D printed PCL scaffolds showed compressive moduli ranging from 4 to 77 MPa with porosities between 48% and 77% (Zein et al. 2002).

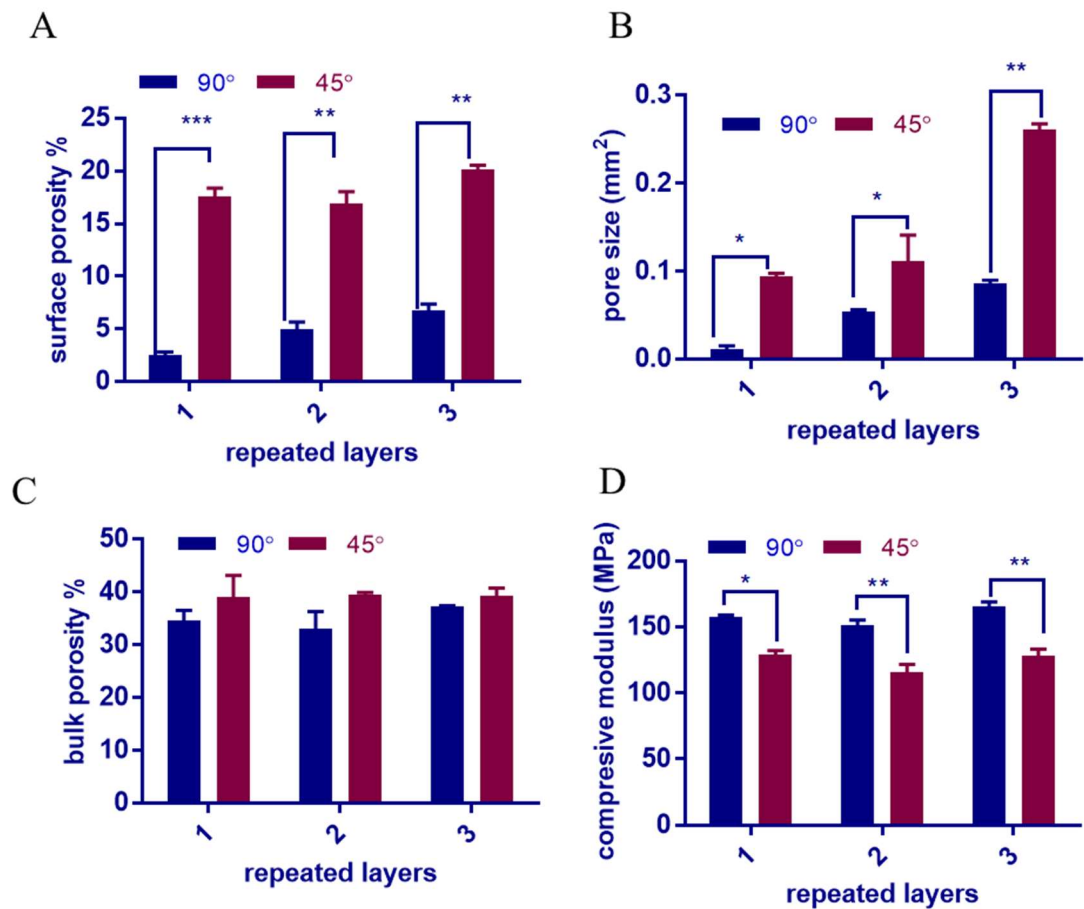


Figure 3.33. A) Surface porosity measured from microCT images, B) average pore size, and C) bulk porosity calculated for the different scaffold designs based on microCT images. D) Compressive modulus. * $p < 0.05$, ** $p < 0.009$.

3.3.5.2. Cells seeding with static and dynamic method

In order to investigate the effect of surface porosity and pore size on cell infiltration into the scaffolds, we seeded cells using a static method and a dynamic method. Chondrocytes were used as a model cell type. More cells were found in the scaffolds with the static method compared to the dynamic method, as shown in Figure 3.34A and D. As the same number of cells was used in both seeding methods, the difference in cell

number within the scaffolds was likely due to the loss of cells in the tubing in the dynamic method.

As shown in Figure 3.34A, for samples with 1 and 2 repeated layers seeded using the static method there is no significant difference in cell number between the different end angles. However, for samples with 3 repeated layers, a 90° end angle resulted in 70% more cells in the scaffold after static seeding compared to 45° end angle. This may be due to pores larger than 0.1 mm² in cross section having allowed the cell suspension to freely pass through the scaffold during seeding. In the static method the cell suspension enters the scaffold by gravity. Although all the suspension enters the scaffold, the amount that leaves the scaffold depends on the surface pore size and porosity; more liquid could pass through and leave the scaffold with high porosity and pore size. There is no correlation between cell number and porosity ($R^2 = 0.39$, Figure 3.34B) or pore size ($R^2 = 0.15$, Figure 3.34C).

With the dynamic method, the number of cells seeded was on average 1.4 times higher in 45° end angle samples compared to 90° end angle samples for all repeated layers (Figure 3.34D). There here is a weak correlation ($R^2 = 0.62$, Figure 3.34E) between porosity and cell number and there is no correlation between pores size and cell number ($R^2 = 0.076$, Figure 3.34F). Similar results were reported in a previous study that showed increased seeding efficacy with increased permeability of the scaffold when the cells were seeded using a perfusion system that is similar to the one we used in this study (Bartnikowski et al. 2014). The permeability of a scaffold depends on porosity,

pore size and pore orientation; when porosity and pore size are increased the permeability is increased as well (Al-Munajjed et al. 2008). If the permeability is low the liquid is more likely to travel around rather than through the scaffold and consequently fewer cells enter the scaffold.

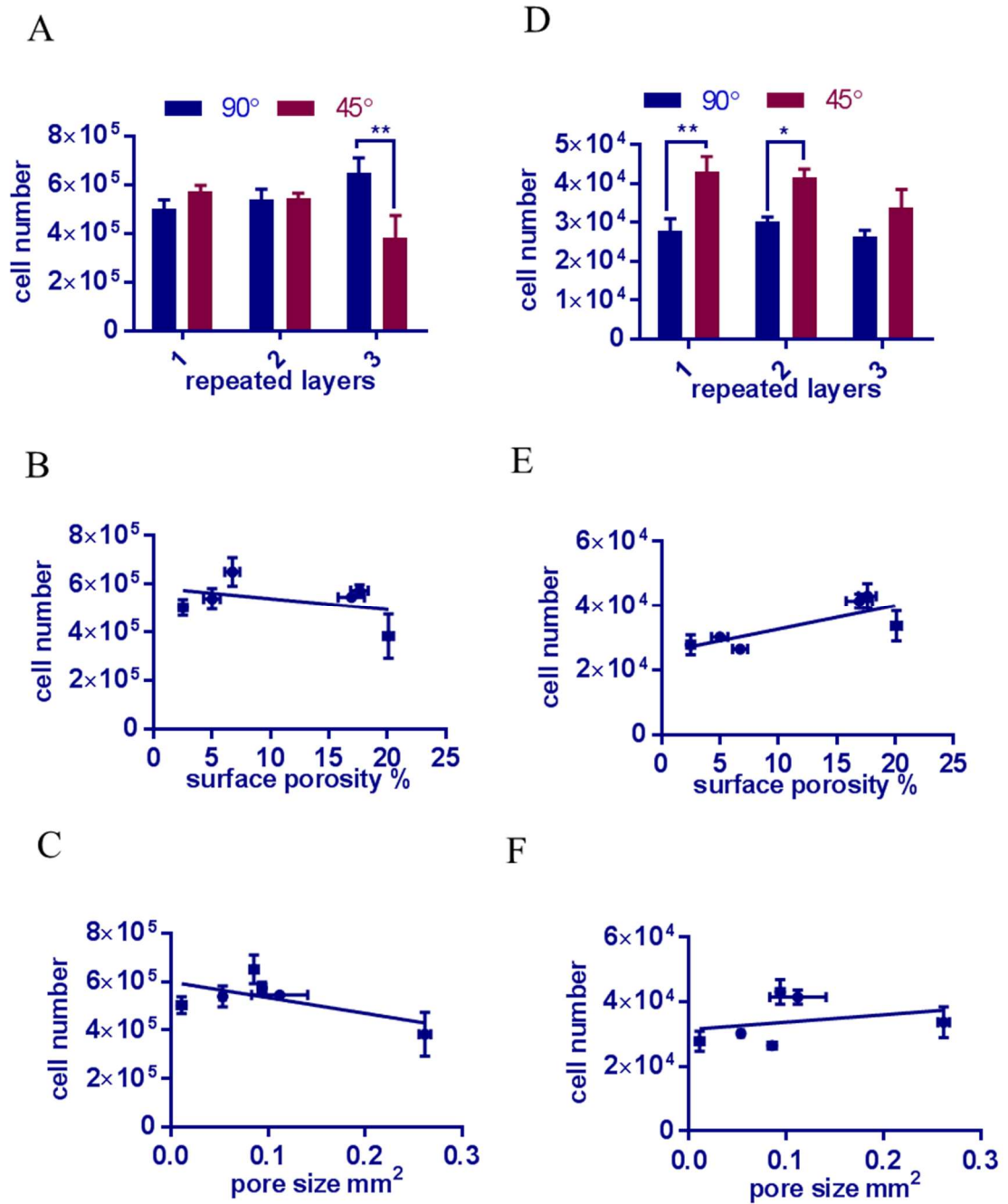
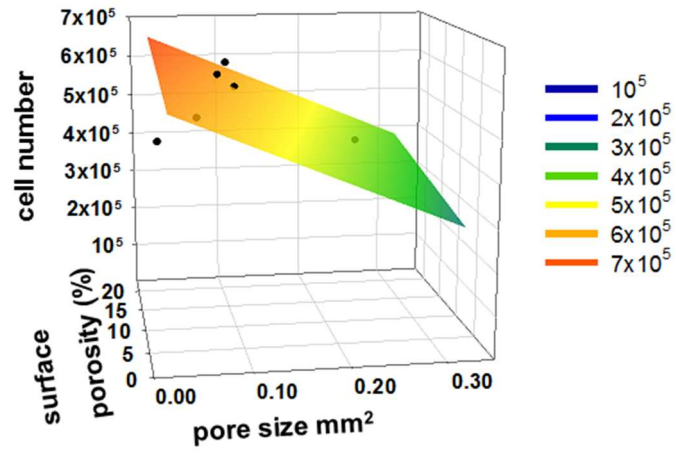


Figure 3.34. Cell infiltration into 3D printed scaffolds using both static and dynamic seeding methods. A) Cell number with static. B) and C) Individual relation between pore size, porosity and cell number with static seeding. D) Cell number with dynamic seeding. E and F Individual relation between pore size, porosity and cell number with dynamic seeding. * $p < 0.05$, ** $p < 0.009$.

To investigate the combined effect of porosity and pore size, we have plotted cell number versus these two parameters (Figure 3.35A and B). Multivariate regression analysis (colour planes) was performed for both seeding methods. Interestingly, a strong correlation ($R^2=0.97$) was identified for the dynamic method whereas the correlation for the static method is still weak ($R^2=0.42$). This finding suggests that cell infiltration is linearly dependent on both the pore size and porosity for dynamic seeding, whereas a simple relationship does not exist for static seeding.

A



B

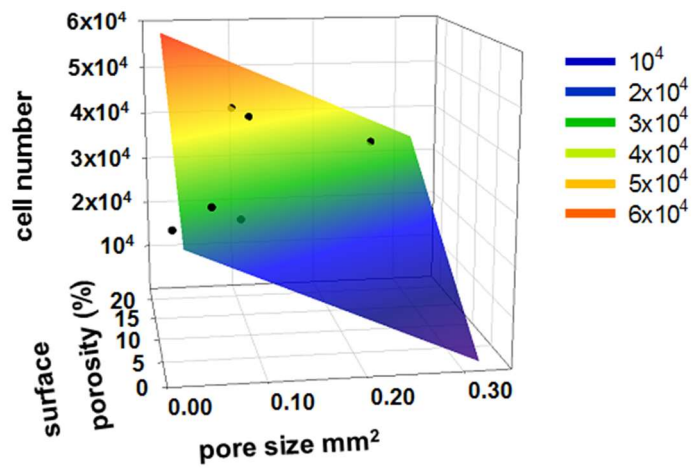


Figure 3.35. 3D plots representing the relation between pore size, porosity and cell number with static and dynamic seeding. Colour plane represents the multivariate (pore size and porosity) correlation based on the six measured data points.

3.3.5.3. Cells distribution and proliferation

We also investigated the distribution of seeded cells in the scaffolds. As shown in Figure 3.36 cells tended to form aggregates predominantly at the intersections of the strands. This pattern has been previously observed with osteoprogenitor cells growing on PCL scaffolds manufactured by fused deposition modelling (Dietmar W. Hutmacher et al. 2001). The cell aggregation at strand intersections could be due to the meniscus formation of cell suspension at these locations, which enhanced the retention of cells. To closely examine the cells within the structure we sectioned the samples and stained the cells with toluidine blue. Figure 3.37A shows blue-stained cell colonies growing at intersections.

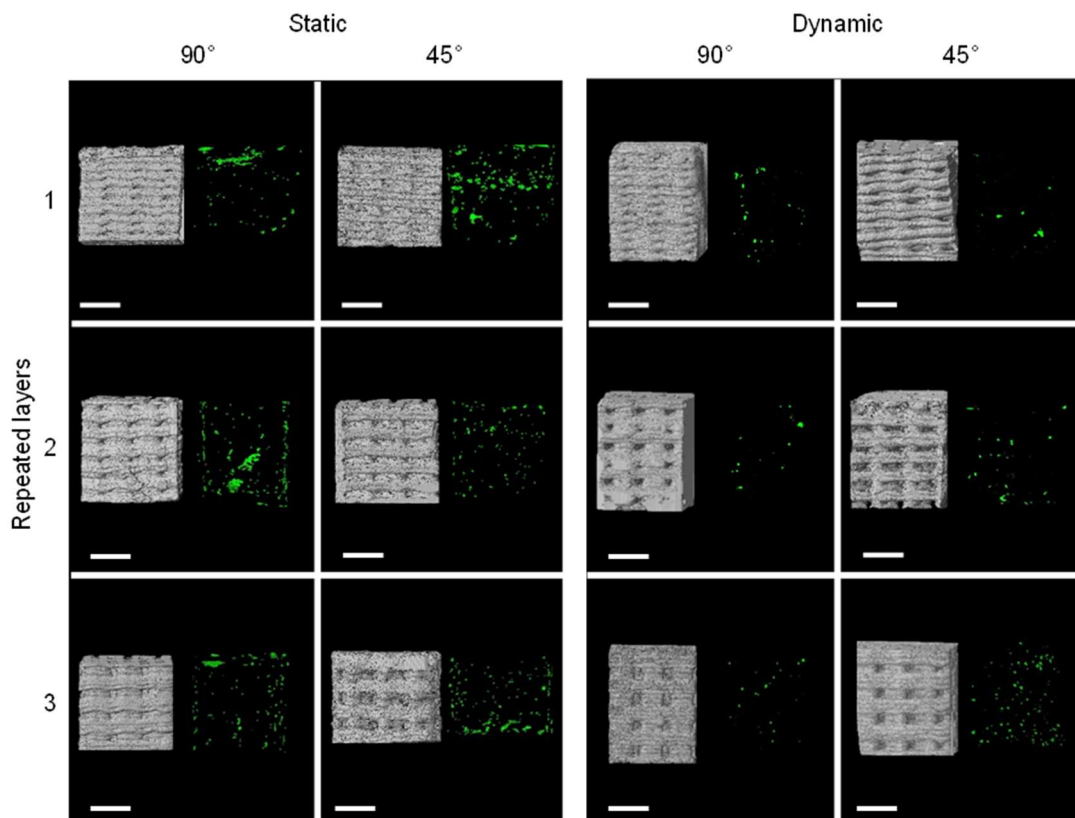


Figure 3.36. Cell distribution inside the scaffolds on day 1 for static and dynamic seeding. Both scaffolds and cells were imaged using microCT, the cells were false coloured. Scale bars represent 1 mm.

The surface porosity and pore size also have an effect on nutrients and waste exchange, which affects cells viability and proliferation (D W Hutmacher 2000). Therefore, we cultured the cell-seeded scaffolds to investigate how surface permeability affects the proliferation of the cells in static culture conditions. Samples with one repeated layer showed an increase in metabolic activity for both of the end angles but 45° had a statistically significant higher increase on day 7 and 14 (Figure 3.37B). The same trend was observed on the samples with two repeated layers (Figure 3.37C). For the three repeated layers samples there was no difference observed at day 7 but a statistically significant higher increase was noticed for 45° samples on day 14 (Figure 3.37D). The higher surface porosity and pore size associated with the three layers scaffolds might cause better mass exchange up to 7 days. The lower proliferation rate in scaffolds with 90° end angles could be due to the lower surface permeability and consequently lower exchange rate of nutrients and waste, which has been reported previously (Mitsak et al. 2011).

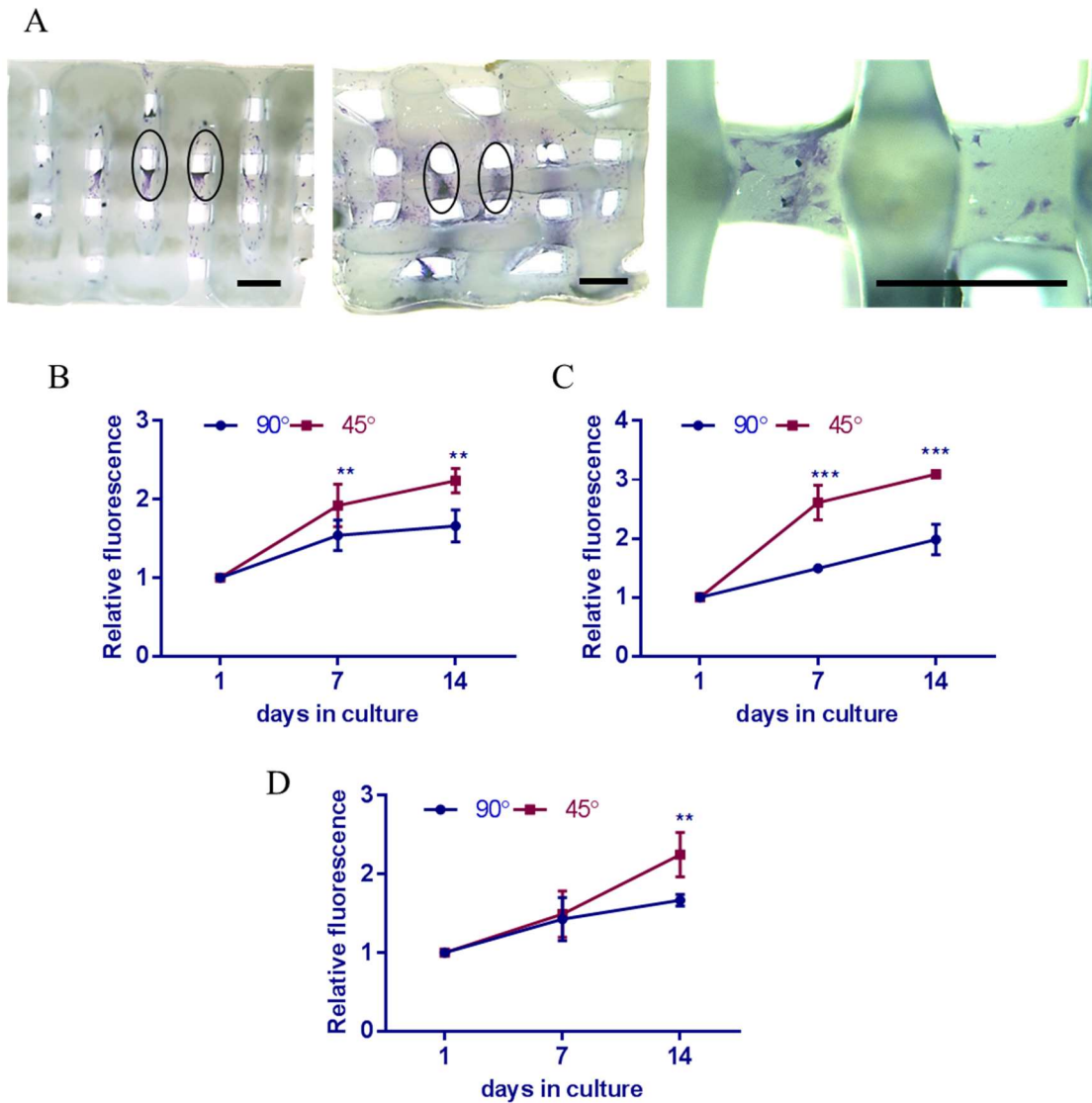


Figure 3.37. Cell proliferation on the different end angles and repeated layers. A) Representative images of chondrocytes stained with toluidine blue after 4 days in culture showing cell attachment and distribution. Chondrocytes distribution in 90 and 45 end angle. Closer view of cells attached to PCL strands. Scale bars represent 0.5 mm. A-C) Cell metabolic activity of static seeded samples after 7 and 14 days in culture. A) One repeated layer scaffolds, B) two repeated layer scaffolds, C) three repeated layer scaffolds. * $p < 0.05$, ** $p < 0.009$, *** $p < 0.0009$.

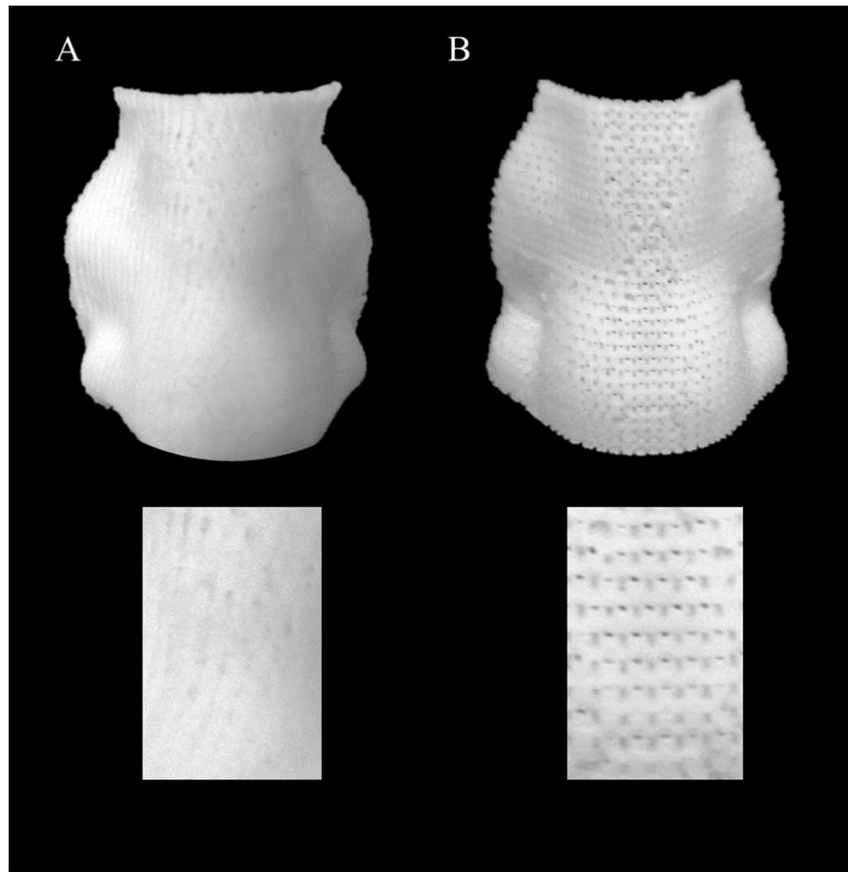


Figure 3.38 PCL nose 3D created with different software A) STL converter software and B) 90 end angle 3 repeated layers.

3.4. Conclusions

This chapter has focused on optimising the 3D printing methods of the thermoplastic polymers PCL and PLGA that we aimed to use as supporting materials for the implants. The optimal PCL printing temperature, feeding rate, building speed and layer thickness were 72 °C, 20 rpm, 16 mm/s and 100 µm respectively for. Additionally, it was found that the environmental temperature for PCL had to be in between 23 to 37 °C depending on the size of the structure in order to obtain good interlayer adhesion. Results showed that the 3D printing process and the culture conditions for 14 days did not have an effect on the stability of PCL. A personalised nose-shaped PCL scaffold was successfully 3D printed.

It was found that PLGA 50 was the only material that matches the printing viscosity of PCL when heated at 160 °C. The environmental temperature had to be controlled not only just to secure the interlayer adhesion but also to avoid the formation of residual stress within the material caused by rapid cooling. It was found that the optimal environmental temperature was 55 °C to avoid deformation of the scaffolds when incubated *in vitro* at 37 °C. PLGA degraded, causing a reduction of its molecular weight by almost a half. Consequently, the T_g also was lowered close to 37 °C. Because deformation of 3D printed scaffolds is not desirable, and PCL structures remained stable after printing and in culture whilst PLGA did not, it was concluded that PCL is the suitable material to be used in subsequent multimaterial printing processes.

A full characterisation of the surface porosity was performed in order to increase it to facilitate suturing. Because the porosity also affects cell infiltration into the scaffold, we quantified the effect of surface pores of 3D-printed scaffolds on mechanical properties, cell infiltration and proliferation. The control of end angle and the number of repeated layers during 3D printing path design and manufacturing enabled a range of surface porosities from 2.5% to 20.1% and surface pore sizes from 0.01 - 0.26 mm² to be made. The 3D printed scaffolds with different surface porosities was found to have compressive modulus differences up to 36%. In addition, increasing surface porosity enabled up to 55% more cells to be seeded within the scaffolds during dynamic seeding and up to 110% greater cell proliferation over 14 days. The results demonstrate that the external surface is an important factor for 3D printed scaffolds and that the presented method is able to control it.

Chapter 4. 3D bioprinting: characterisation of GelMA and 3D printing of multi-material cellular composites for cartilage regeneration

4.1. Introduction

3D bioprinting is an additive manufacturing technology used to precisely dispense cell-laden biomaterials layer by layer for the fabrication of complex 3D functional living tissues (S. V Murphy and Atala 2014). 3D bioprinting is based on three major 3D printing techniques: inkjet (T. Xu et al. 2013), laser-assisted (Kingsley et al. 2013) and extrusion (Kang et al. 2016). Each technique provides different advantages and disadvantages that will impact the final printed structure including cell viability, functionality post-printing, structure volume and scalability. Extrusion bioprinting technique comprises a dispensing head (pneumatic or mechanical) and an automated three-axis (x,y,z) robotic stage. This system allows the extrusion of a continuous filament of a viscous bio-ink rather than droplets. The biggest advantage of this technique is the ability to print with high viscous materials and high cell densities at a relatively high speed with acceptable cell viability (Duan et al. 2013). For these reasons, this technique is the most widely used for the fabrication of human-scale tissue constructs (Kang et al. 2016) (Visser et al. 2013b) (Kesti et al. 2015) and is the technique used in this research because the final aim is a 3D bioprinted full-size nose-shaped construct.

During the bioprinting process, biocompatible materials (bio-inks) are used to facilitate the printing and act as matrices for printed cells (Rutz et al. 2015). The bio-ink should

act as a cell carrier during the printing process and allow the cells to grow and secrete their own ECM post-printing. The bio-inks can be natural, synthetic materials or combinations of both. Polymeric hydrogels, highly hydrated three-dimensional polymeric networks, are one of the most viable classes of bio-inks because of their structural similarities to natural tissue and can offer a synthetic surrogate of ECM. (Kirchmayer, Gorkin III, and in het Panhuis 2015). Hydrogels can facilitate matrix remodelling, cell migration and cell-cell interactions necessary for normal development of functional tissue (Drury and Mooney 2003). The bio-ink properties that need to be considered for deciding if it is suitable for printing include viscosity, shear-thinning, viscoelasticity, cytocompatibility, gelation kinetics and biodegradation. These properties will determine the fidelity, stability and functionality of the final cell-laden construct (Chimene et al. 2016).

Another important factor to consider is the material compatibility with the type of tissue aimed to engineer. In the case of cartilage tissue engineering, hydrogels are materials that have been widely used for this application (Chung et al. 2008)(Kim, Mauck, and Burdick 2011)(Park et al. 2013) (Jianqi Wang et al. 2017) (S. Chen et al. 2016). In this study the hydrogel gelatin methacrylate (GelMA) is used as the bio-ink. Gelatin is a proteinaceous material obtained by hydrolytic degradation of collagen (von Hippel 1965). Gelatin is soluble in water at 37°C and forms thermoreversible hydrogels upon cooling (Djabourov, Leblond, and Papon 1988). Some of the advantages of gelatin as a biomaterial are: low antigenicity (Wormall 1944), biodegradability in vivo and tuneable physicochemical properties (Elzoghby 2013). Additionally, it contains the bioactive sequences arginine- glycine-aspartic acid (RGD) which support cell attachment

(Davidenko et al. 2016). Gelatin can be crosslinked either without prior modification or after functionalization of its side groups. Unmodified gelatin can be crosslinked in various ways to form a covalent network, such as by chemical or enzymatic crosslinking (Sung et al. 1999). The addition of functional groups to the gelatin backbone is a crosslinking strategy with a high degree of control over hydrogel design and properties, compared. Reaction of methacrylic anhydride with amine groups on gelatin gives rise to GelMA macromers. GelMA can be covalently crosslinked by undergoing photoinitiated radical polymerization (Van Den Bulcke et al. 2000).

Recently, a great number of GelMA based bio-inks have been developed for 3D bioprinting (Yue et al. 2015). Most of the studies have focused on optimising the printability of GelMA by modifying its viscosity either by combining it with other materials or by controlling its printing temperature (Klotz et al. 2016). Schuurman et al demonstrated that GelMA 20% was not viscous enough to form strands when extruded at room temperature, but by combining it with hyaluronic acid 2.4 % the viscosity increased and strands were properly extruded. The study showed the potential of GelMA to be used as a bio-ink for bioprinting chondrocytes (Wouter Schuurman et al. 2013). Billiet et al reported that GelMA 20% can be successfully 3D printed by decreasing the temperature and controlling the gelation of the material. Additionally the bioprinting of hepatocytes-laden GelMA was demonstrated (Billiet et al. 2014). Kolesky et al also demonstrated that GelMA can be printed by reducing the environment temperature. They bioprinted constructs with vascular-like channels using GelMA as a cell carrier and Pluronic F127 as a sacrificial material (Kolesky et al. 2014). Mouser et al investigated the bioprinting of chondrocyte-laden GelMA/gellan gum by varying both

GelMA concentration and printing temperature. A range of different concentrations of GelMA (3%-20%) with different concentration of gellan gum (0%-1.5%) were extruded at temperatures ranging from 15 °C to 37 °C. They found that thirteen of these combinations were within the printability window but not all of them led to good cartilage formation, with relatively high gellan gum concentrations compromising cartilage matrix production (Mouser et al. 2016b).

To fabricate patient-specific nose/ear constructs suitable for implantation, 3D bioprinting is emerging as an alternative approach (J.-S. Lee et al. 2014). Compared to conventional scaffolding and post-fabrication cell seeding based approaches, 3D bioprinting can fabricate patient-specific scaffolds/constructs with controlled architectures without moulding. In addition, cells can be printed within the scaffolds/constructs with greater precision. Nose-shaped hydrogel constructs have been made using bioprinting of chondrocyte-laden alginate/gellan. Shape fidelity of the bioprinted constructs was high, and secretion of cartilage-related matrices was identified during *in vitro* cultivation. The cells within the central region of constructs showed reduced viability due to insufficient nutrient and oxygen transport. The mechanical properties of the hydrogel were low compared with native cartilage (Kesti et al. 2015). To facilitate sufficient mechanical stability and transport of oxygen and nutrients, multi-material bioprinting has been developed in which materials that promote cartilage regeneration and offer mechanical support, respectively, are combined to form 3D composite structures. In this multi-material bioprinting approach, a cell-laden blend hydrogel containing gelatin, fibrinogen, hyaluronic acid and glycerol and PCL have been co-printed into ear-shaped constructs. Micro channels were incorporated within

the structures in order to enhance nutrients and oxygen transport (Kang et al. 2016). The promising multi-material bioprinting approach (J. Shim, Lee, and Kim, n.d.) (Pati et al. 2014) has encouraged the fabrication of nose-shaped cartilage constructs using this method. The previous chapter demonstrated the ability to create personalised 3D nose-shaped constructs with controlled surface porosity using PCL only (Ruiz-Cantu et al. 2016). The focus of this chapter is to investigate the feasibility of multi-material 3D bioprinting of porous constructs using PCL and chondrocyte-laden GelMA for cartilage tissue engineering. First, the printing conditions for different GelMA concentrations were optimised by controlling the printing temperature, needle diameter and pressure. Then primary sheep articular chondrocytes were encapsulated in GelMA 15% and 20% and bioprinted for the evaluation of cells proliferation, cartilage-specific matrix secretion and mechanical properties after a 50 day culture period. From the evaluation of the results, a suitable GelMA concentration was selected for the multi-material printing. Cells were encapsulated in the selected GelMA concentration and co-printed with PCL to create porous multi-material cellular structures and assess cells proliferation and ECM secretion in culture for 21 days.

4.2. Materials and methods

4.2.1. Gelatin methacrylation

GelMA was prepared by reaction of skin porcine gelatin type A (Sigma-Aldrich) with methacrylic anhydride (Sigma-Aldrich), as previously described (Nichol et al. 2010). Briefly, a 10% gelatin solution was prepared at 50°C, after an hour 8 ml of methacrylic anhydride (Sigma-Aldrich) was added dropwise at a speed of 0.5ml/min to the gelatin solution and allowed to react for 3 hrs. To stop the reaction, the solution was diluted 5X with warm PBS. The mixture was dialysed against distilled water using 80kD dialysis membranes for 1 week. The final solution was freeze-dried for 7 days and stored at -80°C.

The degree of methacrylation (DM) was defined as the percentage of 3-amino groups of gelatin (lysine, hydroxylysine) that are modified in GelMA. For the quantification of the DM by ¹H NMR the spectra were normalized to the phenylalanine signal (6.9–7.5 ppm), which represents the concentration of gelatin. Subsequently, the lysine methylene signals (2.8–2.95 ppm) of gelatin spectra and GelMA spectra were integrated to obtain the areas [A (lysine methylene of unmodified gelatin)] and [A (lysine methylene of GelMA)] (Figure 4.1). The DMs of the different GelMA batches were calculated as (Hoch et al. 2013)

$$DM[\%] = \left(1 - \frac{A(\text{lysine methylene of gelMA})}{A(\text{Lysine methylene of unmodified gelatin})}\right) \times 100$$

Figure 4.1. Formula to calculate GelMA degree of methacrylation

4.2.2. GelMA hydrogels preparation

Different concentrations of GelMA hydrogels (10, 15 and 20% w/v) were prepared by dissolving the material in α -MEM medium overnight at 37 °C at constant rotation. The pH was neutralised with sodium hydroxide. Separately, a 100% w/v concentration of the photoinitiator Irgacure 2959 was prepared in DMSO. Then the photoinitiator was added to the different GelMA solutions at a concentration of 0.05% v/v.

4.2.3. Rheological testing

Rheological evaluation was performed on a MRC rheometer (Anton-Paar). To evaluate the viscosity of different concentrations of GelMA a 25 mm diameter parallel plate was used with a 0.5 mm gap. Viscosity in relation with shear rate measured by increasing shear rate from 0.1 to 500 (1/s) at room temperature. To study the effect of temperature on the viscosity of GelMA the different concentrations were subjected to a temperature decrease ramp in the range of 37-10 °C with a decrease rate of 5 °C min at a constant shear rate of 100 (1/s).

To evaluate the effect that the UV lamp power and time of exposure has on the crosslinking of the samples; 200 μ l of GelMA was added on the rheometer and crosslinked with different power from 1-3 and for a range of time from 10-30 seconds

using the UV lamp Omnicure Series 1000 (Lumen Dynamics). After UV crosslinking the complex modulus of the samples was measured using an 8 mm diameter plate at a frequency of 1 Hz.

To measure the complex modulus of cross linked gels the samples were prepared using an 8 mm diameter parallel plate 0.5 mm deep silicone moulds. 200 μ l of GelMA was added to each of the moulds and crosslinked for 20 seconds at an intensity of 31 mW/cm² using the UV lamp Omnicure Series 1000 (Lumen Dynamics). Complex modulus was measured using 8 mm diameter plate with a frequency range of 1-100Hz. All measurements were conducted in triplicates.

4.2.4. 3D printing of GelMA hydrogels

Small square models were designed using bioCAD software for the GelMA printing optimisation experiments. Sample dimensions were 10 mm X 10 mm X 0.2 mm. The space between strands from centre to centre was set to 1 mm and the layer increments on z direction were 200 μ m. The samples were 3D printed using the 3D discovery bioprinter (Regenhu). The different GelMA concentrations were warmed up to 37 °C and loaded into the 10 cc cartridges while they were in the liquid state. Cartridges were placed into the printhead adapted with a cooling chamber. Cooling chamber temperature for 20%, 15% and 10% GelMA was set at 22 °C, 18 °C and 15 °C respectively. Cartridges were left for 15 minutes in the printhead before starting to print to bring the GelMA to the required printing temperature. Samples were 3D printed with two different needle gauges 27 (210 μ m) and 30 (150 μ m) at different pressures (2-4 bar).

4.2.5. 3D bioprinting and cell culture of GelMA/chondrocytes constructs

GelMA 10%, 15% and 20% hydrogels were prepared as in section 4.2.4. The GelMA solutions were then warmed up to 37 °C, vortexed and sterile filtered before use. GelMA was stored at 37 °C while preparing the cells. Passage 1 ShCh were detached using trypsin EDTA, centrifuged at 700 x g for 5 min and resuspended in GelMA at a concentration of 5 X 10⁶ cells/ml. The solution was transferred to the printing cartridge and to stabilise the temperature at the respective printing temperatures (15°C, 18°C, and 21°C for 10%, 15% and 20% GelMA) in the cooling chamber for 15 minutes.

Circular scaffolds were designed using BioCAD software with overall dimensions of 5 mm diameter and 2 mm height. Layer height was set at 300 µm, space between strands from centre to centre was 200 µm and deposition speed was 10 mm/s. Twelve samples were bioprinted in a continuous way. The crosslinking process was also incorporated into the design; the UV light head was set to go over each sample for 20 seconds every layer. Before printing the pressure was set at 2 bar. GelMA/chondrocytes were 3D bioprinted using the 3D Discovery Bioprinter (Regenhu) and a conical 27G needle gauge. Samples were transferred into a 12 well plate containing standard ShCh medium (Appendix 2.2.1.). Samples were cultured for 50 days on an orbital shaker with media changes three times per week.

Square scaffolds were bioprinted in the same way as previously described the only difference being the geometry design. They were designed using bioCAD software with

overall dimensions of 5 mm X 5 mm X 2 mm height. Layer height was set at 300 μm , space between strands from centre to centre was 1 mm and deposition speed was 10 mm/s. Twelve samples were bioprinted in a continuous way.

4.2.6. Microscopy

Samples were imaged under a dissecting microscope (LEICA MZ10F). For overall visualisation and colour change they were imaged in bright field mode. For visualising the cells distribution, the samples were stained with LIVE/DEAD solution as mentioned in section 2.3.4 and imaged using the green fluorescent channel.

The stained histological sections were examined using a light microscope (Leica DM IRB).

4.2.7. Turbidity assay

Three replicates of samples collected on day 0, 5, 14, 21 and 50 were transferred to a 96 well plate and the absorbance of the samples was read using the plate reader (Tecan M200).

4.2.8. Biochemical assays

Three replicates of each sample were collected on day 0, 14, 21 and 50. They were washed with PBS and frozen until day 50 when all the samples were analysed together. Once the 50 days culture finished and all time points were collected samples were

thawed, transferred to 1 ml eppendorf tubes and digested overnight in 1 ml papain solution (Appendix 2.2.8.) (L-cysteine 0.042 mg/ml, PBS, papain 25 µg/ml, EDTA 0.005 M) at 60 °C (Sigma-Aldrich).

4.2.7.1. DMMB assay

The DMMB solution and Chondroitin sulphate stock solution were prepared according to appendix 2.3.3 and 2.3.4, then the chondroitin stock solution was diluted 1:10 in papain blank solution to obtain a final concentration of 125 µg/ml. Standard curve was prepared as shown in Table 4.1. Then, 50 µl of each standard, blank and sample were transferred in triplicates into a 96 well plate. Each well was topped with 200 µl of the DMMB solution. Total GAG content was determined by photospectrometry at 520 nm after reaction with dimethylmethylene blue using a microplate reader (Tecan M200). The GAG content was quantified using the chondroitin sulphate (Sigma-Aldrich) standard.

Table 4.1 chondroitin sulphate standards

chondroitin (µl)	papain (µl)	final concentration (µg/ml)
0	50	0
2.5	47.5	1.25
5	45	2.5
10	40	5
15	35	7.5
20	30	10

4.2.7.2. DNA content assay

Total DNA was quantified using a Quant-iT™ PicoGreen™ dsDNA Assay Kit (Invitrogen). Buffer, Quant-iT™ PicoGreen® reagent and standards were prepared according to the manufacturer's instructions. Then, 100 µl of each standard and samples were transferred in triplicates into 96 well plates. Wells were topped with 100 µl of the Quant-iT™ PicoGreen® reagent and then the plate was incubated at 37 °C for 5 minutes. Fluorescence was read at an excitation of 480nm and emission of 520nm.

4.2.9. Histological analysis

4.2.10. Cryo sectioning

Samples were washed three times with PBS, fixed in PFA for 2 hours and washed again three times with PBS. Then, they were immersed in 15% sucrose for 24 hours and in 30% sucrose for 12 hours. Samples were transferred into 10 mm foil moulds, embedded in OCT and frozen using liquid nitrogen. Samples were sectioned into 10 µm slides using a cryostat (Leica CM11000).

4.2.11. Histological staining

Weigert's Iron Hematoxylin, fast green, acetic acid and safranin O working solutions were prepared according to appendix 2.2.10. Then, glass slides were hydrated and then immersed in Weigert's Iron Hematoxylin for 10 minutes. Slides were washed with tap

water for 10 minutes and then immersed in fast green solution for 5 minutes. They were rinsed with 1 % acetic acid for 15 seconds and then stained in 0.1% safranin O (Sigma-Aldrich) solution. Samples were rinsed in tap water and imaged immediately.

4.2.12. Immunohistochemistry

Samples were stained by immunohistochemistry for detection of collagen II. All the solutions were prepared according to appendix 2.5. Samples were permeabilised with 0.1 % Triton X in PBS and blocked in 3% donkey serum albumin. Next, sections were incubated with the primary antibodies for collagen type II (ab34712 rabbit anti-collagen type II antibody, ab34712, Abcam) at 4 °C overnight. Subsequently, sections were incubated with the secondary antibody Alexa Fluor 488 (ab150073 Donkey anti-rabbit IgG, Abcam) at room temperature for two hours. Finally, cells were co-stained with Hoechst 33258 1 μ /ml (Sigma-Aldrich) for 15 minutes. Samples were imaged under the fluorescent microscope (Leica DM IRB).

4.2.13. Mechanical testing

Compression testing was conducted on the samples using texture analyser (TA. HD plus Stable micro systems). Each specimen was loaded until it reached the maximum force of 5 N at a displacement rate of 1 mm/min. All tests were performed in triplicates. Young's modulus (MPa) was calculated from the stress–strain curve as the slope of the initial linear portion of the curve (5%-10%), with any toe region due to the initial settling of the specimen neglected.

4.2.14. 3D multi-material bioprinting

GelMA 20%/chondrocytes solution was prepared the same way as mentioned in section 4.2.5. Structures were designed using newly-developed software integrated into an Excel spreadsheet ('Scaffold Designer') (Ruiz-Cantu et al. 2016). Scaffolds were designed with the overall dimensions 2cm X 2cm X 2mm. PCL pellets (Sigma-Aldrich, UK) were extruded at a temperature of 74 °C at a rate of 16 mm/s and the pressure in the PCL chamber was 2 bar. PCL strands were printed 2 mm apart and GelMA was printed in the central part in between the two PCL strands. One layer of GelMA was printed every two repeated layers of PCL. The number of repeated layers refers to the number of consecutive layers with the same printing path (Figure 4.2). A total of 8 layers of PCL and 4 layers of GelMA were printed. GelMA was cross linked for 20 sec.

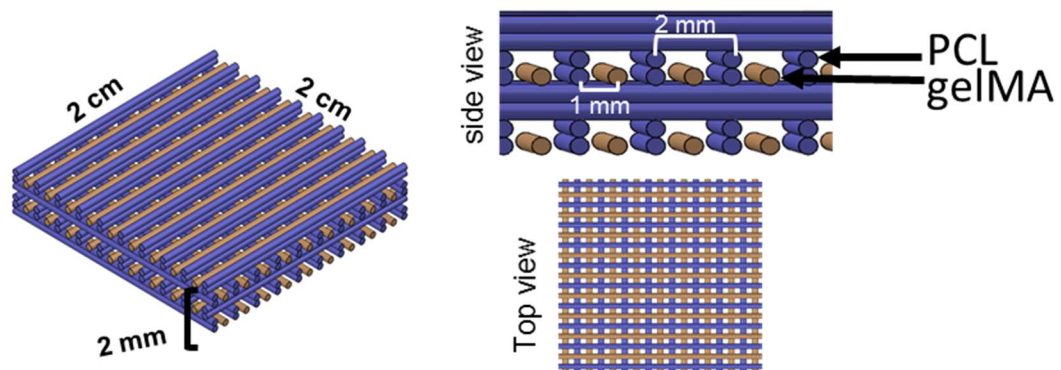


Figure 4.2. Model for the multi-material bioprinting of PCL and GelMA/chondrocytes. Scaffold dimensions are 2 cm X 2 cm X 2 mm. The space in between PCL and PCL strands centre to centre is 2 mm and the space in between PCL and GelMA strands centre to centre is 1 mm. One layer of GelMA was printed every two repeated layers of PCL.

4.3. Results and Discussion

4.3.1. GelMA characterisation

4.3.1.1. GelMA degree of methacrylation

The DM was measured as stated in section 4.2.1. The ^1H NMR spectra can be observed in Figure 4.3; the phenylalanine signal has been highlighted in red, the methacrylic groups signal in green and the lysine methylene signal in blue. Three different batches of GelMA were compared with gelatin. The phenylalanine signal was used for normalisation. Compared to unmodified gelatin new signals could be observed in the spectra of GelMA at 5.3-5.7 ppm representing the new methacrylate groups and also the decreasing of the lysine methylene signal at 2.9 ppm. The data suggest that the gelatin was successfully modified on the molecular level by the conversion of the amino groups. From the quantitative analysis of the NMR spectra it was calculated that the DM for GelMA 1, 2 and 3 was 99%, 66 % and 87% respectively. The variation on the DM of the different samples could have been caused by user variability when adding the methacrylic anhydride dropwise. Nichol et al. 2010 demonstrated that the DM affects the mechanical properties of the final GelMA structures showing that high DM (81%) performed best for micropatterning applications and the low degree (20%) formed very weak gels. They also showed that the compressive modulus of high DM was 2-fold higher than medium and 6.6 fold higher than low. Given that the DM has a big effect on the final structures it is very important to be able to control it and consequently have less batch-to-batch variation. It was decided not to use the batch 2 because the DM was very low compared to 1 and 3. These differences in DM could have been caused by user errors because the protocol for synthesis of the three batches was the same.

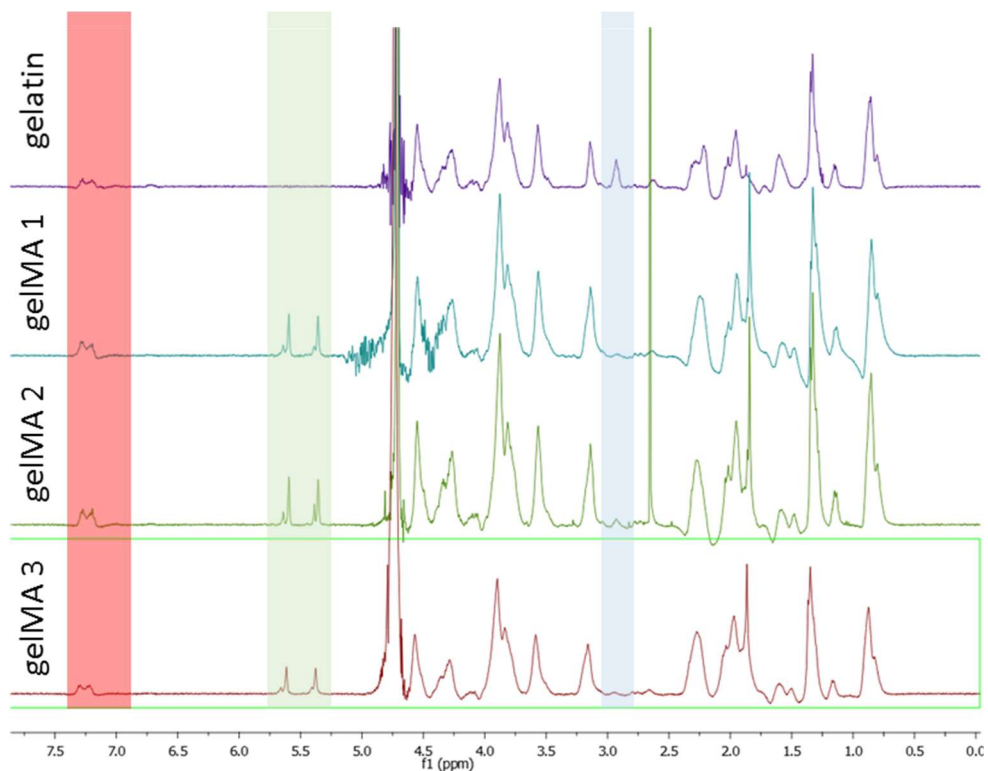


Figure 4.3 ^1H NMR spectra of gelatin and GelMA samples. The phenylalanine signal (highlighted in red) is used for normalisation, the methacrylic groups signal (highlighted in green) represents the addition of the new methacrylate groups and the lysine methylene signal (highlighted in blue) decreases in the modified GelMA.

4.3.1.2. GelMA rheological properties

During printing a low viscosity is generally desirable to avoid excessive shear stress and needle clogging. Upon deposition, a high viscosity or solidification rate is needed so that the filament retains its shape in order to maintain high fidelity of the printed structures (Ouyang, Highley, et al. 2016). Previously, a viscosity range for extrusion 3D printing from 0.03 to 60000 Pa·s (Arslan-yildiz et al. n.d.) (Malda et al. 2013) (Murphy & Atala 2014) have been reported. Factors such as needle gauge, pressure and fidelity

also need to be considered when establishing a suitable viscosity because some materials cannot be extruded with small needle gauges or low pressure but they could be extruded with bigger needle gauges and higher pressure (He et al. 2016). To find a suitable concentration of GelMA a rheological study was performed by measuring viscosity against shear rate and temperature. Viscosity of 10%, 15% and 20% GelMA was measured first as a function of shear rate. All concentrations showed shear thinning behaviour (Figure 4.4 A, B and C) as previously demonstrated by Liu et al. 2017. Shear thinning is a desirable feature for bio-inks. When bio-inks are exposed to high shear rates inside a nozzle during bioprinting, a decreased viscosity or shear stress will be present, which favours the survival of encapsulated cells. Meanwhile, a sudden decrease of shear rates upon deposition causes a sharp increase in viscosity, resulting in a high printing fidelity (You, Eames, and Chen 2017). It was also observed that the viscosity of GelMA is temperature and concentration dependant as shown in Figure 4.4D. The viscosity range of hydrogels that have been successfully 3D bioprinted using extrusion deposition varies from 1 to 10 Pa·s at a shear rate of 100 s⁻¹ (Malda et al. 2013). Using this data, a range from 1 to 10 Pa·s of GelMA viscosities for 3D printing was established from the results gathered in Figure 1. As temperatures lower than 15°C could be detrimental for cell viability (Juan Wang et al. 2017) a printability window was set from 15 to 37 °C. From the three different concentrations only 15% and 20% GelMA fit into this printability window (Figure 4.4D).

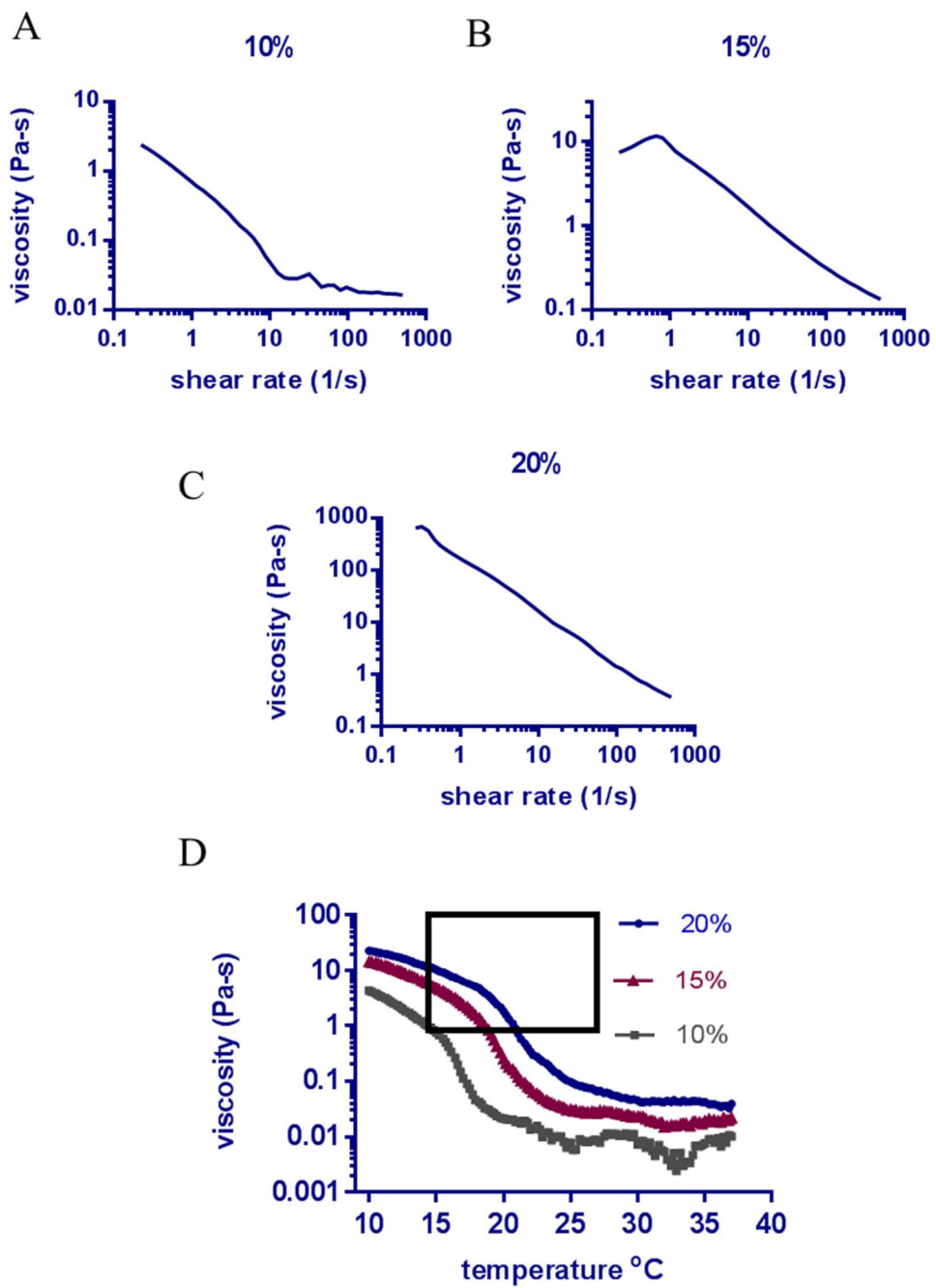


Figure 4.4. Rheological properties of GelMA. Viscosity of GelMA (A) 10 %, (B) 15% and (C) 20% as function of increasing shear rate. D) GelMA viscosity as function of temperature increasing temperature. Shear rate was constants at 100 1/s. The viscosity printability window is the area inside the square.

4.3.1.3. Effect of UV crosslinking time on GelMA complex modulus

Printability for a bioink can be determined by the ease with which it could be printed with good resolution and maintenance of its structure after printing (Panwar and Tan 2016). In the previous section it was shown how the viscosity of GelMA can be controlled with temperature fitting it within the printability window. Once the strand is deposited it can be immediately UV crosslinked, allowing the strand to preserve its structure and support itself without the need of temperature control. The minimal UV dosage necessary to crosslink GelMA and increase its complex modulus was investigated in this section. Different concentrations of GelMA were exposed to UV for 10, 20 and 30 seconds and the complex modulus was measured. In Figure 4.5. is shown the increase in the complex modulus with the increase of UV exposure. After 10 seconds of exposure a 100-fold increase was observed in all of the concentrations. A 1.5, 3.4 and 4.1-fold increase was observed after 20 seconds and a 2.5, 1.4 and 1.5-fold increase after 30 seconds for 10%, 15% and 20% GelMA respectively. 20 seconds was chosen as the crosslinking time because the modulus was higher than 100 Pa which will give the strand enough strength to support itself but lower than 1000 Pa. A recent study shown that shown that low hydrogel modulus (1000 Pa) are preferable for chondrocytes differentiation and collagen type II secretion than high hydrogel modulus (4500 Pa) (X. Li et al. 2016)

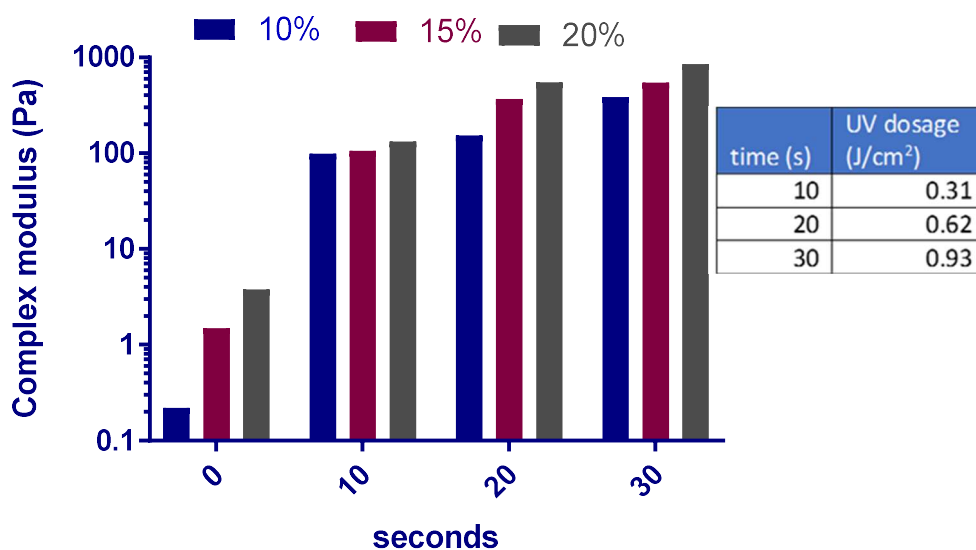


Figure 4.5. Complex modulus of 10%, 15% and 20% GelMA after UV exposure for 10, 20 and 30 seconds.

4.3.2. Optimisation of GelMA printing process

Despite that just GelMA 15% and 20% fitted within the printability window based on the rheology data; it was decided to evaluate all of the concentrations for their ability to form a filament when printed with different needles and pressures. Two layers of material were printed in order to observe the interaction between them. Figure 4.6A shows that the filaments of 10% GelMA tend to spread and merge together when deposited. The filaments merged completely when printed using 3 and 4 bar pressure. Some pores could be observed when 2 bar was used, but spreading was still noticed even with the smallest needle diameter (150 μm). GelMA 15% (Figure 4.6B) had a similar behaviour to 10%, filament spreading and merging was observed. Given that GelMA 20% is more viscous than the other two concentrations, consistent strands (not spreading) were formed when printed with needle diameters 150 and 210 μm and 2 bar

pressure (Figure 4.6C). Viscosity of all the concentrations was supposed to be the same during extrusion because the temperature was varied according to the rheological results to keep the viscosities the same. A possible explanation of why 10% and 15% filaments spread more than 20% is that once the material is deposited and touches the substrate its viscosity immediately reduces as the environment is at room temperature. Some studies have shown that is possible to 3D print lower concentrations of GelMA and obtain consistent structures without deformation by reducing its temperature to 4 °C (W. Liu et al. 2017) but this strategy can affect the viability of the cells. A different strategy to print GelMA 10% was used by Bertassoni et al. 2014, in which the GelMA was dispensed into a glass capillary, UV crosslinked and then deposited onto the platform in a cylinder shape.

For experiments presented in this thesis 15% and 20% GelMA were the most appropriate concentrations to use without the need for adding any thickeners, modification of the 3D printer or using non-cell friendly temperatures.

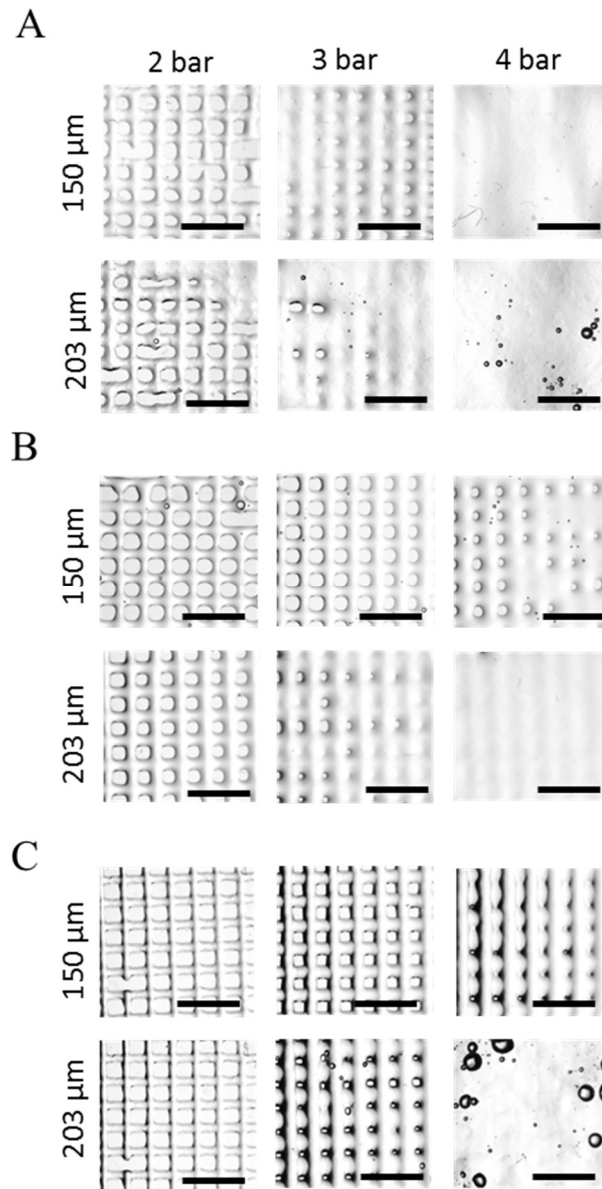


Figure 4.6. Images of GelMA printing optimisation using needle diameters 150 μm (G30) and 203 μm (G27); and different pressures (2, 3 and 4 bar). A) 10 % GelMA, B) 15% GelMA and C) 20% GelMA. Scale bars represent 2.5 mm. Feeding rate was kept constant at 10 mm/s

4.3.3. Bioprinting of cells encapsulated in GelMA and characterisation of the tissue engineered cartilage-like structures

4.3.3.1. Non-porous GelMA/chondrocytes constructs.

From the printability studies, it was observed that just 15% and 20% GelMA were printable. For this reason chondrocyte proliferation and secretion of cartilage ECM following 3D bioprinting were examined in GelMA with two concentrations (15% and 20%) for up to 50 days. Solid constructs formed by six layers of printed GelMA were used for this study. Figure 4.7A shows that all samples changed from transparent on day 0 to a white opaque colour on day 46. The change in optical density was quantified with a turbidity assay (Figure 4.7B). No statistically significant difference was observed between the concentrations at the same time points, except day 46. For each concentration, the opacities at different time points were statistically significantly different. This change in colour suggested cell proliferation and ECM production, which was confirmed by the proliferation and GAGs assay results (Figure 4.8).

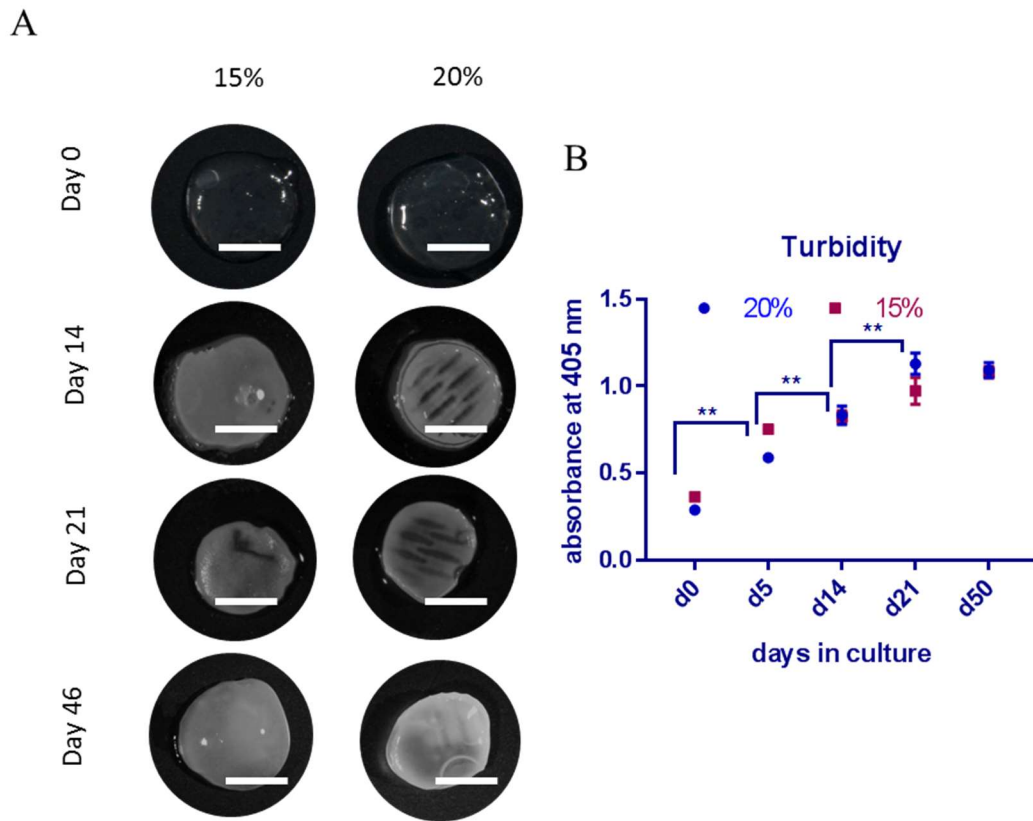


Figure 4.7. Overall change in appearance of the 3D bioprinted GelMA/chondrocytes constructs from day 0 to 46. A) Brighfield images of the structures showing a change in colour in the constructs after 14 days of culture. Scale bar represents 2.5 mm. B) Quantification of the optical density measured at an absorbance of 405 nm.

Proliferation of the ShCh was quantified from day 0 to 50 based on the DNA content of the samples. Figure 4.8A shows that cells proliferated in both of the concentrations from day 0 to 21. After day 21 just the cells encapsulated in 20% GelMA exhibited an increment in cell number while the 15% did not. Then, the amount of ECM secreted by the chondrocytes was assessed by quantifying the amount of GAGs present in the samples. Increase in GAGs was noticed after day 21 for both of the concentrations (Figure 4.8B). From day 21 to 50 the cells embedded in 20% GelMA had a 2-fold increase in GAGs; the cells embedded in 15% GelMA remained the same. Even though the cells in 15% stopped secreting GAGs earlier, at day 45 of the cultured period no

statistically significant difference between the concentrations was observed. Figure 4.8. Cells proliferation and GAGs secretion during 50 days in culture. is shown how the cells are growing mostly at the periphery of the scaffolds. This behaviour has been previously observed when cells are culture in 3D do not get enough nutrients at the centre and is known as necrotic core (Sant and Johnston 2017). For this reason is important to integrate pores in the printed structures.

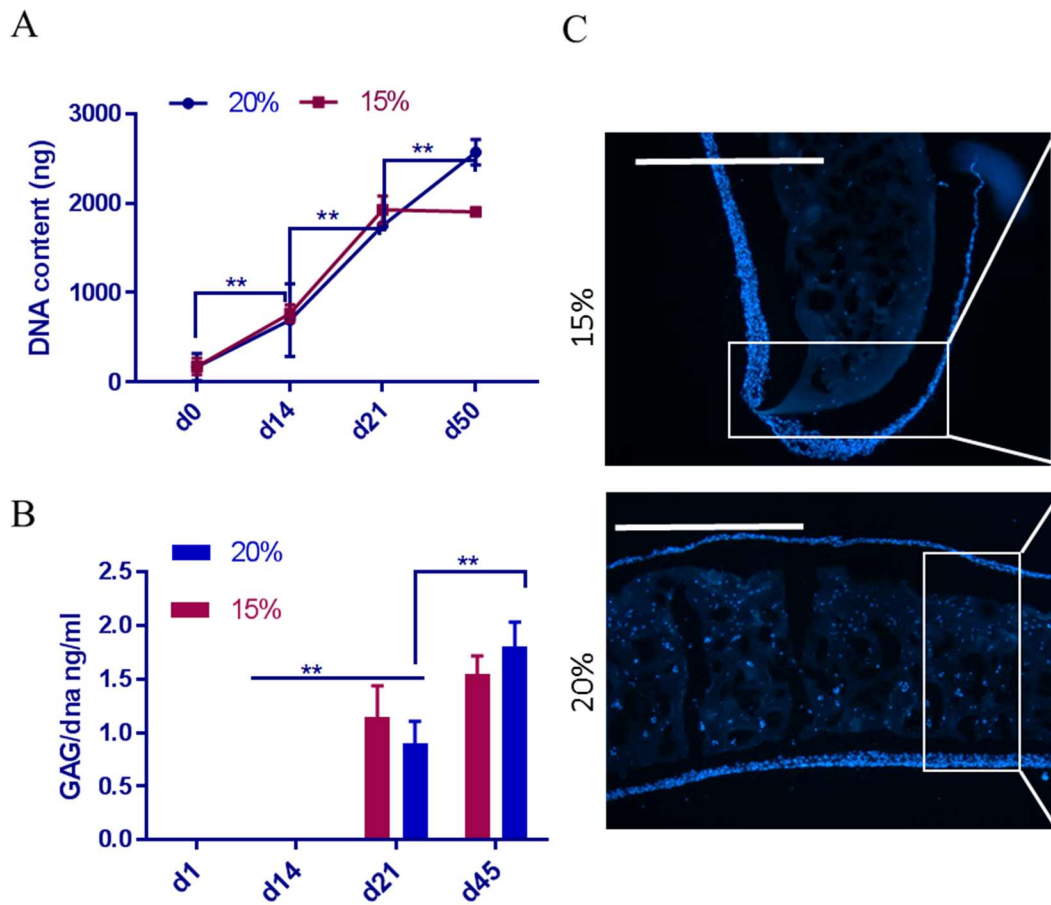


Figure 4.8. Cells proliferation and GAGs secretion during 50 days in culture. A) Cell proliferation based on DNA number. Cells encapsulated in 20% GelMA showed a linear increase from day 0 to day 50. Cells encapsulated in 15% GelMA also showed a linear increase but just from day 0 to 21, afterwards cells number did not increase. B) Quantification of chondrocytes GAGs secretion from day 0 to day 45. Secretion was observed after 21 days in culture. C) Cross sections of the samples at day 45 showing the cells (blue) distribution.

4.3.3.2. Porous GelMA/chondrocytes constructs

GelMA/chondrocytes porous constructs were 3D bioprinted for the second study using GelMA 15% and 20%. Samples were formed by 6 layers of printed GelMA. During cultivation, cell proliferation and mechanical properties of the cell-laden constructs were

quantified at day 0, 14, 21 and 50. Gross morphology of the samples, cell distribution, GAG and collagen II secretion were assessed at the end of the culture period.

Firstly, it was observed that samples printed in 20% GelMA had more uniform strands and pores compared to 15% GelMA due to higher viscosity (Figure 4.9 day 0). Secondly, the 3D bioprinted GelMA/chondrocytes samples were porous and translucent on day 0, and became solid and opaque by day 50 (Figure 4.9). This change in gross morphology of the structures was due to the cell expansion into the pores and the secretion of ECM. In order to observe cell distribution within the entire sample, cells were stained with calcein AM (green) (Figure 4.10A). The pores at day 50 were occupied by cells stained in green (Figure 4.10B).

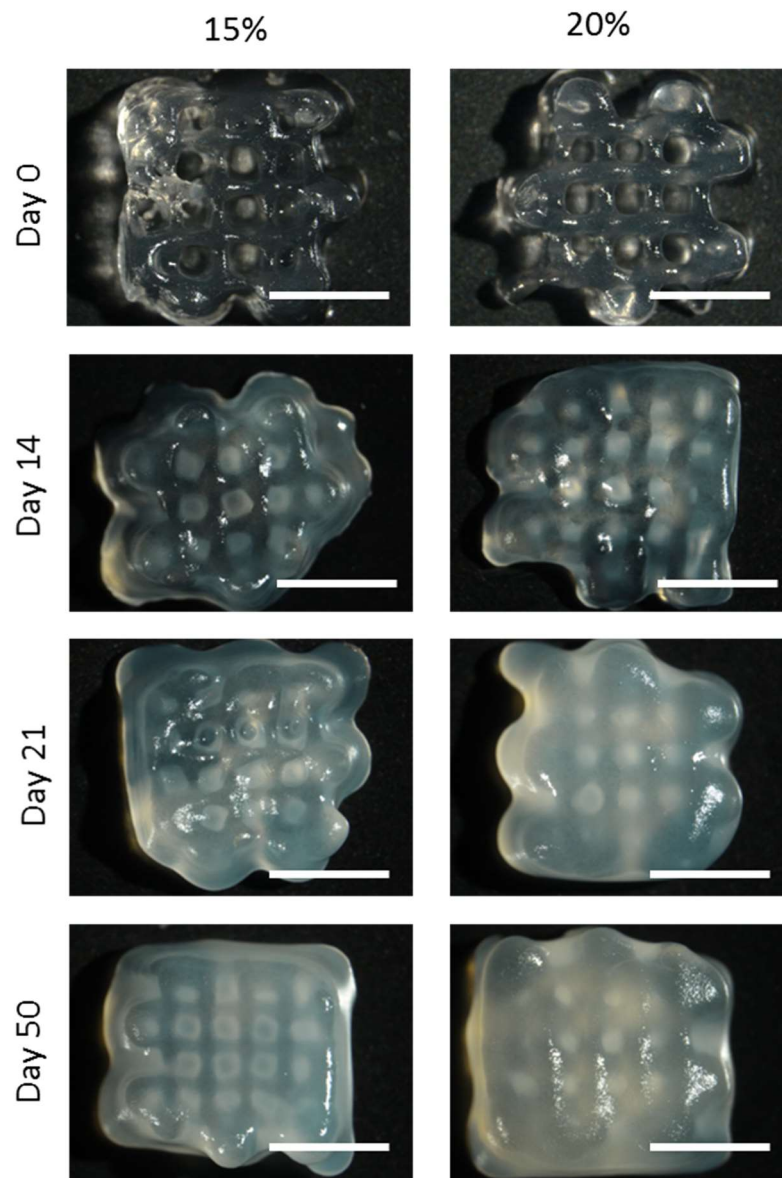


Figure 4.9. Images of the gross morphology of 3D bioprinted porous GelMA cell laden constructs from day 0 to 50 in culture. Pores can be observed in both samples at day 0. Pores were fully filled day 14 and change in the colour of the constructs was also observed been more noticeable by day 21. Scale bars represent 2.5 mm.

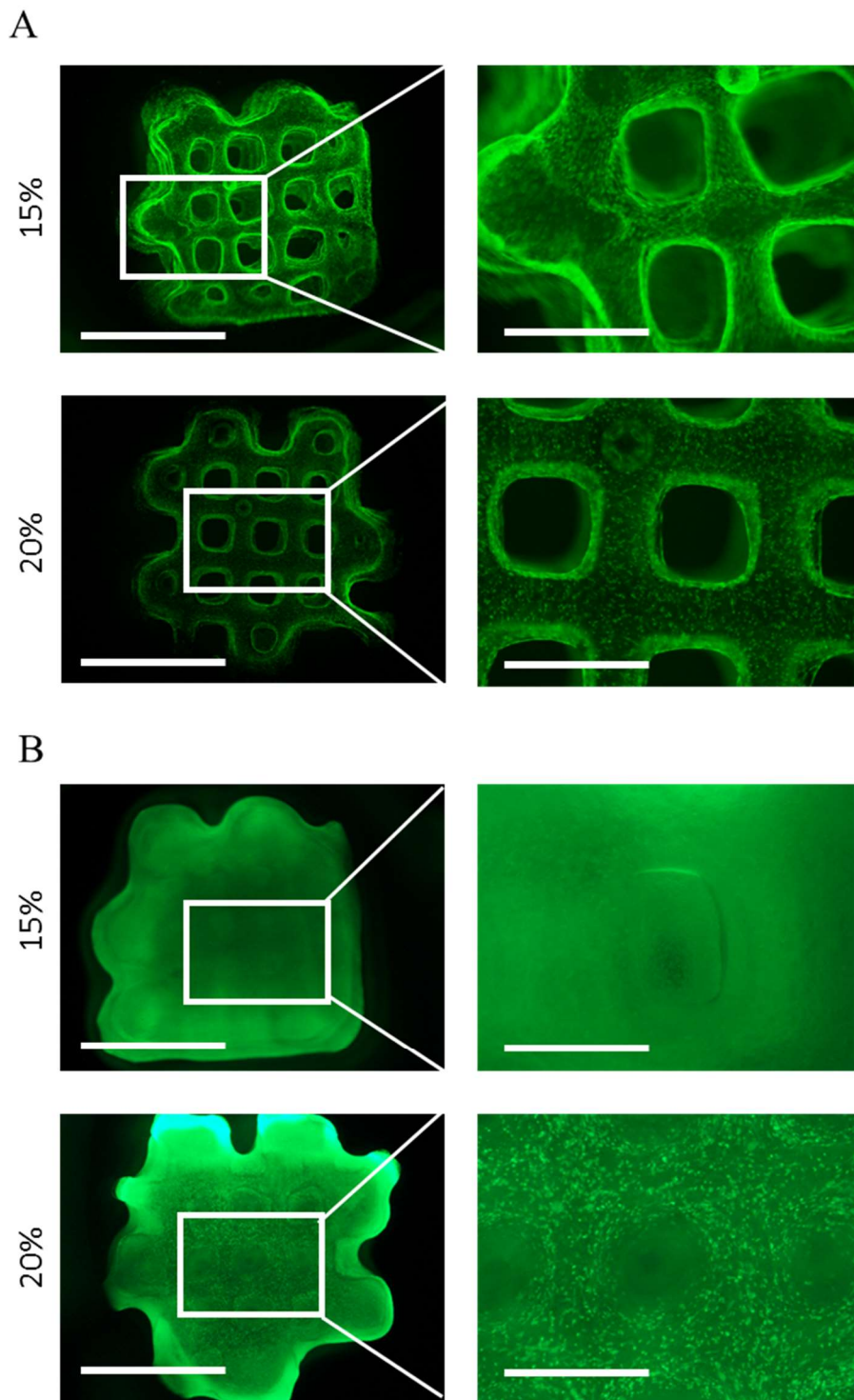


Figure 4.10. Chondrocytes stained with calcein AM (green) to study cell distribution. (A) Day 0. The cells (green) are spread uniformly within the strands and pores all fully open (B) Day 50. Cells migration can be observed within the pores filling the spaces completely. Scale bar in the left column represents 2.5 mm and in the right column 1mm.

To study the exact position of the cells, samples cultured for 50 days were cryo-sectioned and the nuclei were stained with DAPI. Due to the auto fluorescence of GelMA (in red), it was possible to observe the distribution of GelMA. It was observed that the cells mostly located at the periphery of the samples and inside the pores (Figure 4.11 left and middle column). Less cells were within the GelMA strands (Figure 4.11 middle and right column). This effect could be due to the lower transport of nutrients and oxygen within the strands once the pores were filled with ECM. These results suggested that the porosity had a positive effect by allowing the cells to proliferate and migrate into the pores while non-porous structures usually show cell death at the centre of the scaffolds due to the lack of mass transportation.

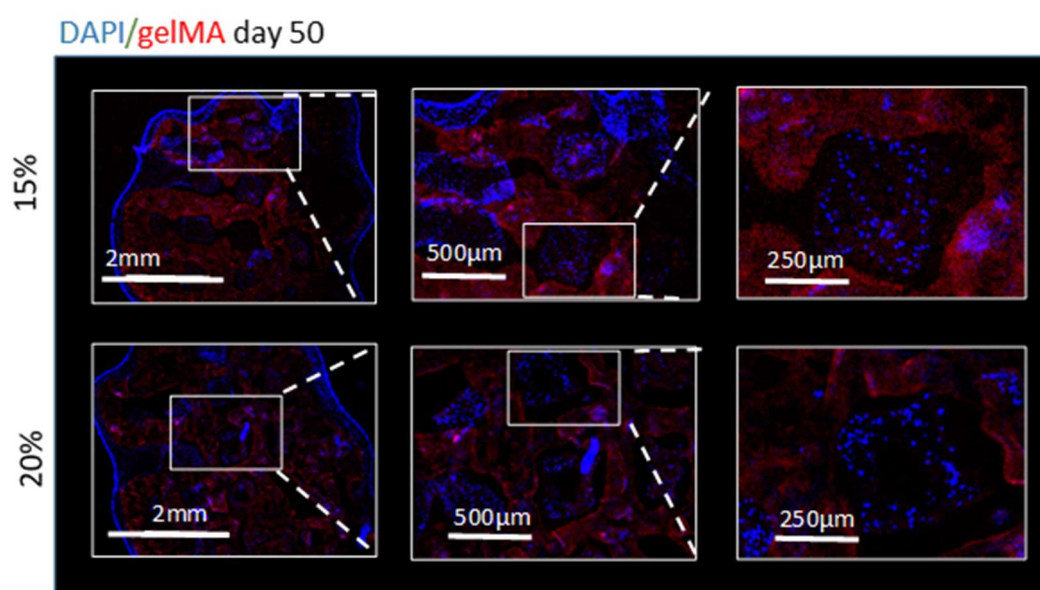


Figure 4.11. Cryo sections of day 50 GelMA/chondrocytes constructs stained with DAPI (blue) representing cells distribution. GelMA distribution is represented in red. Images region increased magnification from left to right. It can be observed that cells (blue) are mostly concentrated in the periphery of the construct and within the pores.

Proliferation of the cells was quantified at different time points of the culture period based on DNA content. A 2.5 fold increase in cell number was observed from day 0 to 14 in both of the concentrations (Figure 4.12A) and after day 14 no proliferation was observed in either. This was expected because primary chondrocytes tend to stop proliferating and senesce after several weeks of *in vitro* culture (Ashraf et al. 2016).

Evaluation of the ECM synthesised by the chondrocytes was done by quantifying the amount of GAGs, histological staining of GAGs and immunohistochemistry staining of collagen type II. The amount of GAGs in the samples increased 2.6 times over the period of 50 days (Figure 4.12B). There was no statistically significant difference in the secreted amount between the two different concentrations. Histological observations of samples stained with Safranin O matched the quantitative results (Figure 4.12C top row). Immunohistochemistry results confirmed the presence of collagen II in both GelMA concentrations (Figure 4.12C bottom row). These results show that the chondrocytes preserve their ability to secrete cartilage ECM after 3D printing.

The mechanical properties of the engineered tissue are an important factor to consider because the tissue has to possess the necessary strength and elasticity to withstand surgical manipulation as well as mechanical stresses *in situ* after implantation to avoid collapse of the reconstructed nose (Caffrey et al. 2013). The young's moduli of the samples were measured on four different time points of the culture period by compression testing. The Young's modulus of 20% GelMA was approximately twice the value of the 15% GelMA at day 0. The moduli of both cell-laden gels increased from

day 0 to day 21 and the ratio of modulus between the 20% and the 10% gel decreased slightly. At day 50 the Young's modulus of 20% and 15% were 4 and 6 times higher, respectively, compared to day 0 (Figure 4.12D). The modulus of 20% cell-laden gels at day 50 (0.8 MPa) was similar to that of lateral nasal cartilage (0.98 MPa) but lower than septal cartilage (2.72 MPa) (Griffin et al. 2016). Due to the limitation in mechanical properties of the cell-laden gels, it is important to add a reinforcement material within the 3D printed structures to increase overall structural mechanical properties. To overcome this issue, previous studies have developed hybrid (multi-material) cartilage bioprinting by alternating printing of bio-inks and thermoplastic polymer fibres (Kundu et al. 2015) (Kang et al. 2016) (Pati et al. 2014) (Wouter Schuurman et al. 2013).

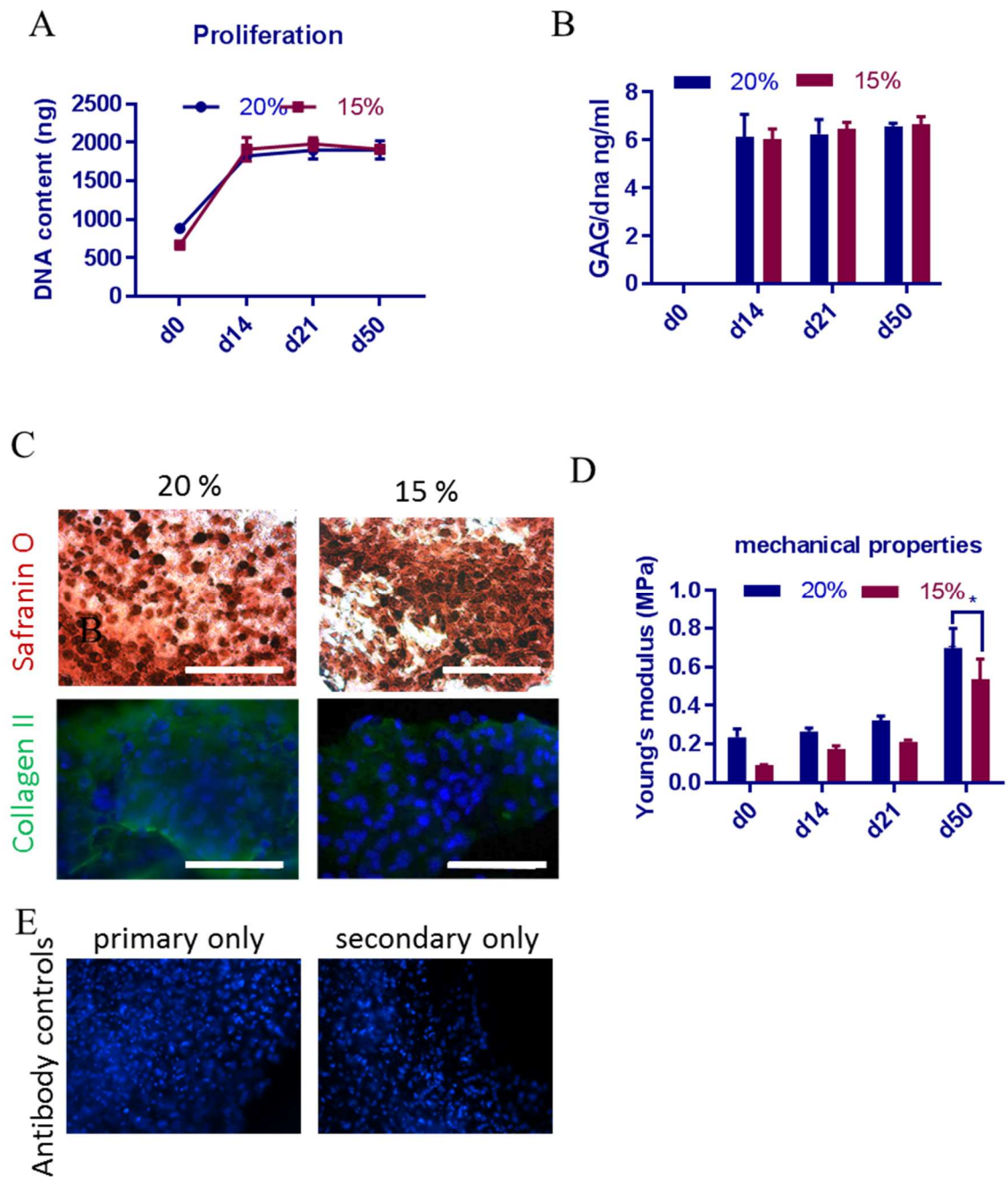


Figure 4.12. Proliferation, GAGs secretion and mechanical properties of 3D bioprinted GelMA/chondrocytes constructs during culture. (A) Proliferation of chondrocytes based in DNA content quantification on day 0, 14, 21 and 50 of culture. (B) GAGs quantification on day 0, 14, 21 and 50 of culture. (C) Histological stain on day 50. Top row shows representative images of samples stained for GAGs using Safranin O. GAGs appear orange-red and the nucleus of the cells appears on a darker black/red. Bottom row shows representative images stained for collagen II in green and DAPI in blue. Scale bars represent 100 μ m. (D) Mechanical properties of samples at different time

points. (E) Primary and secondary antibody negative controls.**Co-printing thermoplastics and GelMA**

Chondrocyte-laden GelMA and polycaprolactone were combined to create a hybrid construct that could potentially be used in nose reconstruction. PCL was used as a reinforcement material to create 3D constructs with mechanical stability. 20% GelMA was used as a cell carrier rather than 15% because of better printability and no difference on the effect that the concentration has on the cells as shown in section 4.3.3. Chondrocytes were encapsulated in GelMA and 3D bioprinted between the PCL strands (Figure 4.13A). In Figure 4.13 it is possible to observe the pores that were designed to allow nutrient diffusion and cell migration. The pores were approximately 650 μm wide. The importance of pores in bioprinted constructs has been demonstrated previously (Kang et al. 2016) and in the work presented on this thesis was also observed that cells tended to migrate and proliferate within the pores of the GelMA bioprinted. Additionally, figure 4.13C shows the homogenous distribution of the GelMA strands containing the cells compared to figure 4.14 where the pores get blocked if the PCL scaffolds are just immersed in GelMA solution rather than co-printed.

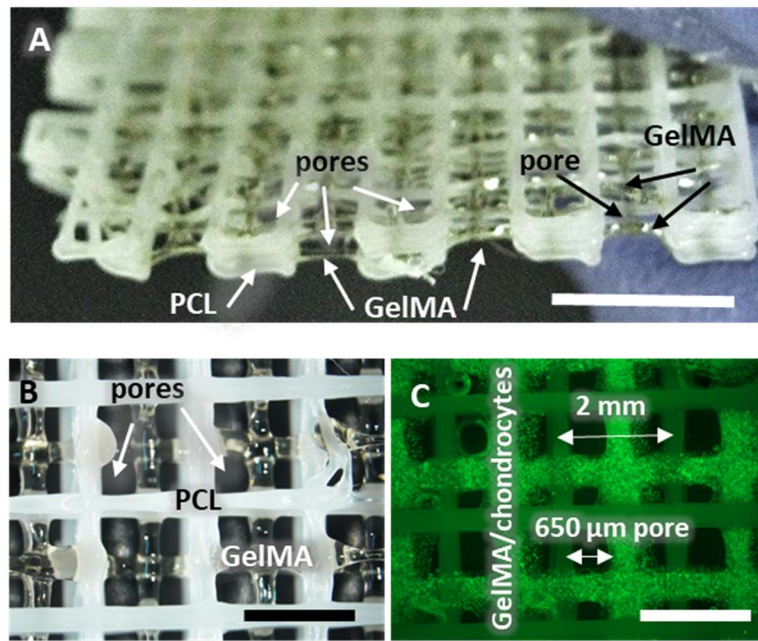


Figure 4.13. Multi-material constructs An image of a co-printed porous construct formed by 8 layers of PCL and 4 layers of GelMA on the z direction. Sample dimensions are 20 mm x 20 mm x 2 mm. Scale bar represents 5 mm. Arrows indicate PCL strands, GelMA/chondrocytes strands and pores.

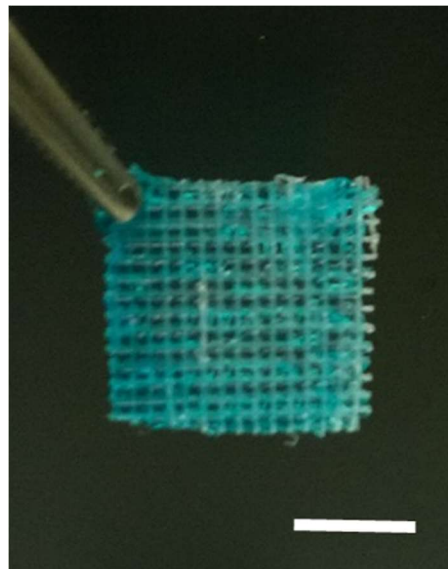


Figure 4.14. Control showing the PCL scaffold submerged in GelMA and crosslinked. It can be observed that GelMA is covering the entire structure and there is no open pores left. Scale bar represents 1 cm.

To study the regeneration of neocartilage tissue *in vitro*, the samples were cultured for a period of 21 days and analysed at different time points. Changes in gross morphology were observed by microscopy. A change in GelMA colour was noticeable, changing from transparent to a white/opaque colour. In addition, the strands gradually became thicker increasing from $\approx 300 \mu\text{m}$ to $\approx 900 \mu\text{m}$ after 21 days of culture (Figure 4.15) which could suggest cell proliferation and ECM secretion. Swelling could be another explanation for strands thickness increase but previous studies have shown that GelMA 20% has a swelling percentage of 10% (Hu et al. 2009) which in our case the GelMA strands would be of $330 \mu\text{m}$ not $900 \mu\text{m}$. The fluorescence images (Figure 4.16A) also show that cell-laden GelMA strands filled some of the pores by day 21. Expansion of the cells was confirmed by the proliferation results (DNA content) (Figure 4.16B) which showed a gradual increase in cell number. These observations demonstrate the importance of designing the size of the pores during scaffold design to allow enough space for cell expansion. Secretion of cartilage related matrix was confirmed by the quantified amount of GAGs, showing a rapid increase from day 0 to day 7 followed by a more gradual increase till day 21 (Figure 4.16C). Collagen II and GAGs were also detected after immuno and histological staining of the strands (Figure 4.16D).

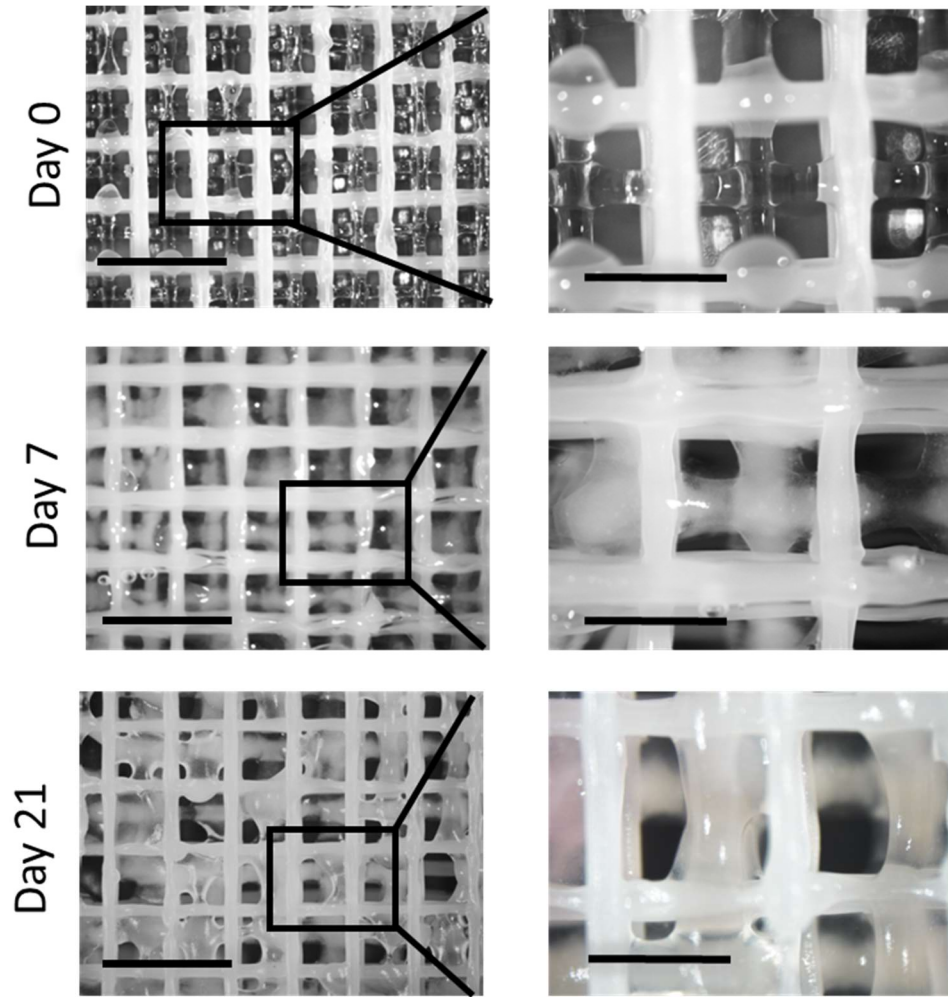


Figure 4.15. Bright field images of gross change in colour and shape of the co-printed PCL/GelMA/chondrocytes constructs in culture for 21 days. Scale bars represent 1mm.

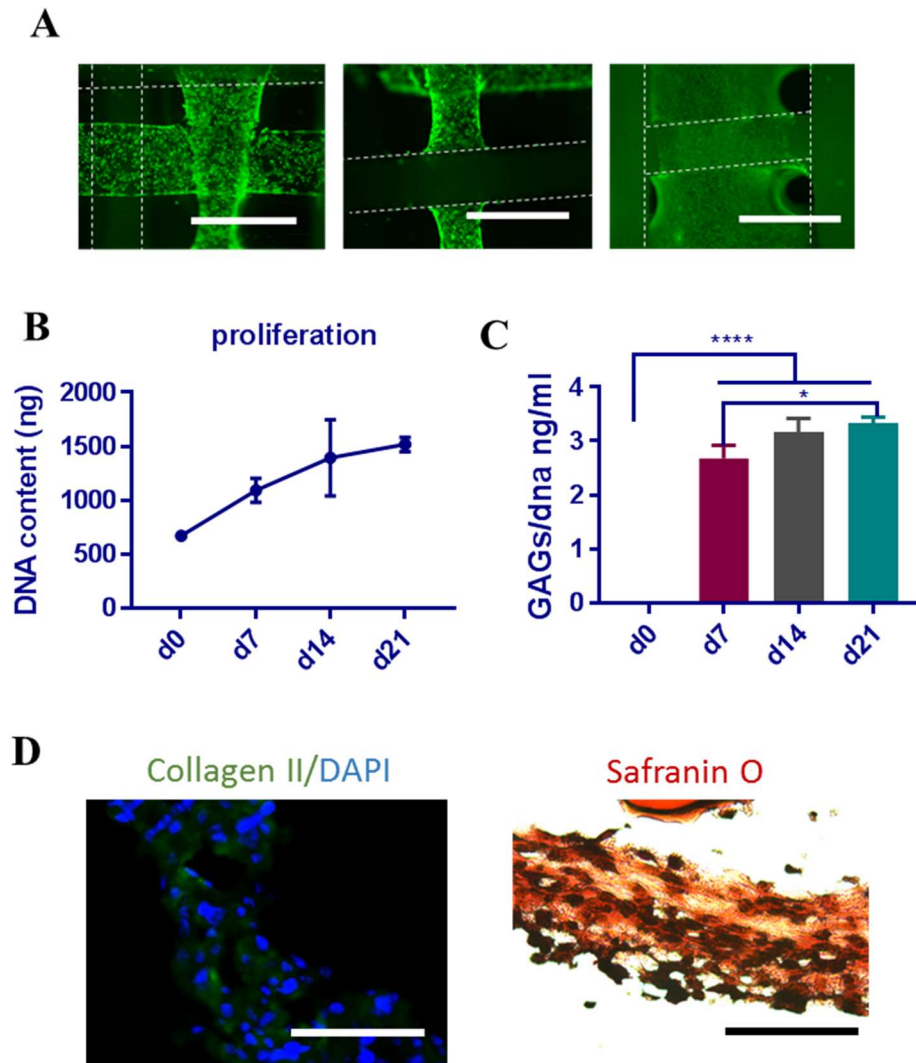


Figure 4.16. Co-printed GelMA/PCL samples in culture. (A) representative fluorescence images of chondrocytes (green) distribution. PCL is highlighted within the dashed lines. Scale bars represent 1mm. B) Chondrocytes proliferation measured by DNA quantification during 21 days. C) Chondrocytes GAGs quantification during 21 days in culture. D) Histological sections of samples on day 21. Left: Immunostaining for collagen II in green and cell nuclei in blue. Right: Safranin O staining of GAGs. Scale bars represent 200 μ m.

4.4. Conclusions

This chapter investigated the feasibility of using multi-material 3D bioprinting to create constructs that could be used for major nasal reconstruction. From the assessment of GelMA's rheological properties it was found that all GelMA concentrations could be printed by controlling the printing temperature. However, 10% GelMA needed temperatures lower than 15°C to be viscous enough to be printed. Then different needles and pressures were tested to print the two materials. It was found that low pressure and small needle size produced better printing fidelity. From the 50-day culture study of the bioprinted chondrocytes in 15% and 20% GelMA, it was found that 20% was the better concentration to be used in terms of printability and cell functionality. Finally, the co-printed cell-laden GelMA and PCL structures showed that this combination of materials allowed the chondrocytes to secrete cartilage specific matrix. These findings have demonstrated the feasibility of making personalised nose-shaped structures using 3D multimaterial bioprinting.

Chapter 5. Summary and future directions

3D printing (additive manufacturing) refers to a group of techniques which apply the additive shaping principle and thereby build physical 3D geometries by successive addition of material (ISO/TEC 261 2015). It has been suggested that one of the greatest advantages that 3D printing provides in medical applications is the freedom to produce custom-made medical products (Parthasarathy 2014). Utilising 3D printing to create custom-made implants, fixtures, and surgical tools can have a positive impact in terms of the time required for surgery, patient recovery time, and the success of the surgery or implant (Morrison et al. 2015) (N. Xu et al. 2016)(M. Yang et al. 2015).

3D bioprinting is a specialised branch of 3D printing that involves the use of biomaterials and living cells incorporated into the printing process (S. V Murphy and Atala 2014). Both plastic and reconstructive surgeries are potential beneficiaries of this technology as it simplifies the fabrication of patient-specific tissue replacements and allows for traits of the original tissue to be more easily incorporated. These could include mechanistic functions such as cellular release of growth factors, or recapitulation of mechanical properties (Chae et al. 2015).

Of these restorative surgeries, one pertinent example is nasal reconstruction. The nose is at the centre of the face and is a critical component associated with the identity of a person. Deformities caused by trauma, cancer surgery and malformations can have both physical and psychological effects on the patients (Amodeo 2007). Reconstructing the

3-dimensional structure of the nose requires the maintenance of its aesthetic form and function. Restoration of the correct dimension, projection, skin quality, symmetrical contour, and function remains problematic (Winslow et al. 2003). Primarily these challenges are associated with tissue sourcing and surgical complexity.

The current state of the art for nasal reconstruction is a three-stage surgery that requires the restoration of the internal nasal lining (mucosa), the reconstruction of the nasal framework (cartilage and bone) and a forehead flap covering (skin) (Cannady et al. 2009). Among the drawbacks of this surgical strategy is the need to harvest cartilage grafts from the ribs which can cause donor site morbidity such as post-operative pain. Additionally, this surgery is very time consuming and requires a highly skilled surgeon to perform it. These drawbacks have encouraged the surgeons to find a better alternative that could remove the cartilage grafting step and simplify the surgical procedure, and improve the aesthetic outcome.

The combination of cartilage tissue engineering and 3D bioprinting could tackle the challenges associated with nasal reconstruction. The primary aim of the work presented in this thesis was to investigate the feasibility of using 3D bioprinting as proof of concept to fabricate personalised cartilage constructs that can potentially be used for nasal reconstruction. This aim was divided in two main objectives, the first one was to create a personalised biodegradable 3D framework that would be used as a surgical guide for suturing cartilage grafts on top of it and reduce the operating time in the surgical theatre. The second objective was to 3D bioprint a multi-material implant containing cells that

would regenerate the cartilage and reduce the amount of cartilage needed to harvest from the patient. Several work packages were conducted, and relevant results were presented in the chapters. Chapter 2 was focused on investigating two potential cell types for bioprinting cartilage and the effect of 3D bioprinting on the cells viability. Chapter 3 was dedicated to create the personalised 3D nose models and characterise the printing process of the materials that would be used for the surgical guides and provide the structural support to the multi material nose implants. Finally, chapter 4 aimed to optimise the printing process of the cell carrier (GelMA), to 3D bioprint and culture *in vitro* the chondrocytes encapsulated in GelMA and to construct the multi-material implants.

The first step in in chapter 2 was to find the cells to 3D bioprint. Sheep primary chondrocytes (ShCh) and sheep bone marrow derived mesenchymal stromal cells (ShMSCs) were studied in this project, primarily due to their reliable availability and their relevance to the final clinical application in which human chondrocytes or MSCs can potentially be used. The effect of the 3D bioprinting process was studied for both ShCh and ShMSCs. Carrier material (GelMA), temperature, UV exposure and needle internal diameter are all factors that could affect cell viability during the bioprinting process. Thus, all of these factors were assessed individually. The materials used as a cell carrier (GelMA 10%, 20% and 30%) were not found to have an effect on the viability of the ShCh and ShMSC. Similarly, the printing temperature (15°C-37°C) did not appear to affect the viability of the ShCh. The assessment of exposure to UV from 10 seconds to 12 minutes showed that viability of the ShCh and ShMSC remained high up to 3 minutes, but longer exposure began to reduce viability. When the effect UV

exposure on the cell DNA was assessed, it was observed that after 2.5 minutes of exposure 50% of ShCh cells had damaged DNA. These results indicate that even though the cells remained viable after 3 minutes, their DNA was damaged which could lead to cellular mutation. However, due to the obvious negative effects UV can have on cells, it was established not to expose the cells to UV for longer time than 1 minute. Each printed layer had to be crosslinked for 20 seconds therefor in order to print structures with more than three layers the layers below have to be protected from the UV. Future work has to involve the investigation of a method to protect the cells in the first printed layers from more UV exposure. One of the possibilities could be the construction of a water bath that contains ZnO nanoparticles which have shown the ability to absorb UV (Adamcakova-Dodd et al. 2014).

It has been previously shown that the shear stress during the bioprinting processes can cause cell death (Billiet et al. 2014). Wall shear stress is due to the walls of the nozzle (needle) and depends upon dispensing pressure and nozzle diameter (Panwar and Tan 2016), the nozzle diameter parameter was investigated during the viability studies. From that study it was observed that after the ShCh were printed through the needles G27 and G30 (203 and 180 μm diameter respectively) the viability was reduced to 80%, suggesting that the shear stress experienced in the needle affected the cells. To improve the viability, larger needle gauges could be used but that would also increase the thickness of the strands which can affect nutrient diffusion and create a necrotic core. G27 because has a bigger diameter than G30 and therefore should cause less stress. Once all the parameters were assessed individually the cells were exposed to the entire bioprinting process resulting in ShCh 80% viability with all of the concentrations whilst

just 50% and 20% of the ShMSCs remained viable using 20% and 30% GelMA. This result suggested that ShCh are able to tolerate the printing process better than MSCs. Therefore, ShCh cells were chosen as the cell model for 3D bioprinting the cartilage constructs. After finding the right cell model, the next step was to design the personalised 3D models and optimise the 3D printing process with the different materials.

The design of personalised 3D models based on medical imaging data (CT scan) and the optimisation of the 3D printing processes for PCL and PLGA were studied in chapter 3. PCL and PLGA were chosen as candidates to be used for printing the surgical guide and serve as structural support of the multi-material constructs because they are biodegradable thermoplastic polymers and they have been previously used in cartilage tissue engineering applications (Mats Brittberg and Lindahl 2008). From the optimisation process was found that the right parameters to 3D print PCL were 72 °C chamber melting temperature, 20 rpm feeding rate, 16 mm/s building speed and 100 µm layer thickness. Same parameters were used for printing PLGA except for the chamber melting temperature which was 160 °C. It was also found that controlling the environmental temperature was essential in order to get good interlayer adhesion and no deformation after cooling. The environmental temperature for printing PCL was 25 °C and for PLGA 55 °C.

In addition to finding the right printing parameters, in chapter 3 it was also studied the effect that the precision extrusion deposition process has on the materials. This

evaluation was performed because some previous studies have shown that the high temperature that the material is exposed to during the printing process can cause degradation of the polymer and changes in the Tg and mechanical properties (J.-H. Shim et al. 2010) . PCL and PLGA were characterised by measuring their melting point, Tg, molecular weight and mechanical properties before and after printing. The printing process did not have an effect on any of these material properties for PCL. On the other hand, the molecular weight of PLGA was reduced by 50% after printing and its Tg decreased from 43°C to 38°C. This reduction in Tg led to deformation of the printed scaffolds at body temperature (37 °C), which is not ideal. Therefore, PCL was chosen as the material to print the surgical guides and as supportive material of the final constructs.

Personalised 3D nose models were designed based on the CT scan of a patient. Afterwards these 3D models were 3D printed using PCL and tested by the surgeon to evaluate their suitability for nose reconstruction. One of the feedbacks was the lack of pores for suturing through the scaffolds. In order to improve the surface porosity of the 3D scaffolds a newly developed software was used to design the printing pattern of the 3D models. Six different structures were designed by varying the number of repeated layers printed in the same direction and the end angles (90° and 45°). By increasing the number of repeated layers the height of the pores increased from 100 µm to 250 µm. By changing the end angle from 90° to 45° the width of the pores increased from 250 µm to 500 µm. This increment in size of the pores not only improved the surface for suturing but also enabled up to 55% more cells to be seeded within the scaffolds during dynamic seeding and up to 110% greater cell proliferation over 14 days. The results demonstrated

that the external surface is an important factor for 3D printed scaffolds. A method that is able to control the surface porosity of 3D printed scaffolds was developed. This method was chosen to be used as the fabrication method for multi-material PCL/gelMA/chondrocytes constructs in chapter 4.

Chapter 4 describes the optimisation and characterisation process of 3D printing GelMA, 3D bioprinting and culture of ShCh/GelMA constructs and the multi-material approach of 3D bioprinting of PCL/GelMA/ShCh constructs. Firstly, GelMA was synthesized with a degree of methacrylation of 87%. Then in order to find at which temperature GelMA has the right viscosity for printing its rheological properties were measured at different temperatures. It was found that the right printing temperature for 10%, 15% and 20% GelMA was 12 °C, 18 °C and 22 °C. Using the right printing temperatures, the printability of different concentrations was evaluated by varying the pressures (2-4 bar) and needle gauges (G27 and G30). It was found that 20% GelMA preserved the structural shape of the strands after deposition on the platform more accurately compared with 10% and 15% GelMA. GelMA 10% was not chosen for the next steps because it needs a temperature lower than 15 °C in order to be printed with accuracy, and this can be detrimental for the cells. GelMA 15% and 20% were chosen as candidates to be used as cell carrier.

ShCh were encapsulated and bioprinted in GelMA 15% and 20%. On the first bioprinting studies the design did not have any pores integrated and after in vitro culture and cryosection it was found that the cells at the core died. For that reason, new samples

were bioprinted with pores integrated in the design. Then the 3D bioprinted constructs were cultured *in vitro* for 50 days. The ability of the chondrocytes to proliferate and secrete cartilaginous ECM was studied. The results demonstrated that chondrocytes proliferated for 14 days and the secretion of GAGs and collagen type II after 50 days of culture. There was no statistically significant difference between 15% and 20% GelMA on cell proliferation and the secretion of GAGs. Hence, 20% GelMA was chosen to 3D bioprint the multi-material constructs because it has better printing fidelity than 15%.

Finally, porous multi-material constructs were 3D bioprinted using PCL as a structural support and 20% GelMA as the cell carrier. The samples were designed to contain pores in order to improve nutrients and waste diffusion. In order to get pores also in the z direction one layer of GelMA was printed every two repeated layers of PCL as described in chapter 3. The multi-material printed samples were cultured for 21 days *in vitro* in order to assess cell proliferation and cartilage ECM secretion. Cells proliferated for 14 days and secreted GAGs and collagen type II by day 21. There was a 1.5 fold difference in the GAGs secretion if the co-printed samples compared to the just GelMA samples and this could be due to some of the cells attaching to the PCL and secreting less GAGs than when attached to GelMA. Longer term studies have to be done to fully show the effect of PCL on the cells but these findings are the first step to demonstrate the feasibility for 3D printing of the personalised full nose shape structures using this combination of materials. In order to print the multi-material nose implant further work has to be done in developing a software that can import SLT files and create a multi material printing path.

The work presented in this thesis has demonstrated the feasibility for 3D bioprinting personalised nose-shaped cartilage implants with multiple materials. *In vivo* evaluation of the 3D bioprinted structures would be the next logical step towards clinical translation. Additionally, improvement on the software for the design of multi-material printing pattern of complex 3D shapes would be of significant benefit in the translational process.

The model cell type (ShCh) was selected primarily due to the availability of sheep articular tissues at UoN and to mimic human primary chondrocytes which are a potential cell type for bioprinted nose-shaped constructs. Additionally, these cells demonstrated acceptable viability during the printing process. ShMSCs's viability reduced to 50% after the bioprinting process when printed in 20% and 30% GelMA with exception of 10% GelMA. Bioprinting of MSCs in 10% GelMA with addition of thickeners could be investigated to ameliorate this problem. Different cell types such as adipose derived stromal cells, chondroprogenitors and induced pluripotent stromal cells could also be examined.

Different thermoplastic polymers that possess a shorter degradation time than PCL could be investigated as the structural support. PCL degradation time is of 2 years, but according to literature a period of 1 year would be enough for the tissue to regenerate. In the work presented on this thesis PLGA showed excessive thermal degradation during

the printing process, but future work could investigate the addition of plasticisers to the materials to reduce its melting point and possibly reduce the thermal degradation.

The printing time for large structures such as the nose takes a minimum of two hours. During this time the deposited hydrogel can dry, affecting the viability of the cells. The use of a water bath that contains medium at 37 °C and progressively fills as the 3D printing process continues could be investigated. This water bath can also contain something that blocks the UV for the layers under the liquid.

References

- Adamcakova-Dodd, Andrea, Larissa V Stebounova, Jong Sung Kim, Sabine U Vorrink, Andrew P Ault, Patrick T O'Shaughnessy, Vicki H Grassian, and Peter S Thorne. 2014. "Toxicity Assessment of Zinc Oxide Nanoparticles Using Sub-Acute and Sub-Chronic Murine Inhalation Models." *Particle and Fibre Toxicology* 11 (1). Particle and Fibre Toxicology: 15. doi:10.1186/1743-8977-11-15.
- Al-Munajjed, Amir a., Matthias Hien, Richard Kujat, John P. Gleeson, and Joachim Hammer. 2008. "Influence of Pore Size on Tensile Strength, Permeability and Porosity of Hyaluronan-Collagen Scaffolds." *Journal of Materials Science: Materials in Medicine* 19 (8): 2859–64. doi:10.1007/s10856-008-3422-5.
- Albrecht, Christian, Carla-Antonia Reuter, David Stelzener, Lukas Zak, Brigitte Tichy, Sylvia N?rnberger, Sandra Boesmueller, et al. 2017. "Matrix Production Affects MRI Outcomes After Matrix-Associated Autologous Chondrocyte Transplantation in the Knee." *The American Journal of Sports Medicine*, 36354651770749. doi:10.1177/0363546517707499.
- Albritton, Jacob L., and Jordan S. Miller. 2017. "3D Bioprinting: Improving *in Vitro* Models of Metastasis with Heterogeneous Tumor Microenvironments." *Disease Models & Mechanisms* 10 (1): 3–14. doi:10.1242/dmm.025049.
- Amodeo, Chiara Andretto. 2007. "The Central Role of the Nose in the Face and the Psyche: Review of the Nose and the Psyche." *Aesthetic Plastic Surgery* 31 (4): 406–10. doi:10.1007/s00266-006-0241-2.
- Ang, Ker Chin, Kah Fai Leong, Chee Kai Chua, and Margam Chandrasekaran. 2006. "Investigation of the Mechanical Properties and Porosity Relationships in Fused Deposition Modelling-Fabricated Porous Structures." *Rapid Prototyping Journal* 12: 100–105. doi:10.1108/13552540610652447.
- Ashraf, S., B. H. Cha, J. S. Kim, J. Ahn, I. Han, H. Park, and S. H. Lee. 2016. "Regulation of Senescence Associated Signaling Mechanisms in Chondrocytes for Cartilage Tissue Regeneration." *Osteoarthritis and Cartilage* 24 (2). Elsevier Ltd: 196–205. doi:10.1016/j.joca.2015.07.008.
- Aulin, Cecilia, Kristoffer Bergman, Marianne Jensen-Waern, Patricia Hedenqvist, Jöns Hilborn, and Thomas Engstrand. 2011. "In Situ Cross-Linkable Hyaluronan Hydrogel Enhances Chondrogenesis." *Journal of Tissue Engineering and Regenerative Medicine* 5 (8). John Wiley & Sons, Ltd.: e188–96. doi:10.1002/term.415.
- Baker, Shan R. 2011. *Principles of Nasal Reconstruction*. 2nded. New York: Springer-Verlag. doi:10.1007/978-0-387-89028-9.
- Banks, Jim. 2013. "Adding Value in Additive Manufacturing: Researchers in the United Kingdom and Europe Look to 3D Printing for Customization." *IEEE Pulse* 4 (6): 22–26. doi:10.1109/MPUL.2013.2279617.

- Barry, F, R E Boynton, B Liu, and J M Murphy. 2001. "Chondrogenic Differentiation of Mesenchymal Stem Cells from Bone Marrow: Differentiation-Dependent Gene Expression of Matrix Components." *Experimental Cell Research* 268 (2). United States: 189–200. doi:10.1006/excr.2001.5278.
- Bartnikowski, Michal, Travis J. Klein, Ferry P W Melchels, and Maria a. Woodruff. 2014. "Effects of Scaffold Architecture on Mechanical Characteristics and Osteoblast Response to Static and Perfusion Bioreactor Cultures." *Biotechnology and Bioengineering* 111 (7): 1440–51. doi:10.1002/bit.25200.
- Behrens, Peter, Thomas Bitter, Bodo Kurz, and Martin Russlies. 2006. "Matrix-Associated Autologous Chondrocyte Transplantation/implantation (MACT/MACI)-5-Year Follow-Up." *Knee* 13 (3): 194–202. doi:10.1016/j.knee.2006.02.012.
- Bentley, G, L C Biant, S Vijayan, S Macmull, J A Skinner, and R W J Carrington. 2012. "Minimum Ten-Year Results of a Prospective Randomised Study of Autologous Chondrocyte Implantation versus Mosaicplasty for Symptomatic Articular Cartilage Lesions of the Knee." *Journal of Bone & Joint Surgery, British Volume* 94–B (4): 504 LP-509. <http://www.bjj.boneandjoint.org.uk/content/94-B/4/504.abstract>.
- Bertassoni, Luiz E, Juliana C Cardoso, Vijayan Manoharan, Ana L Cristino, Nupura S Bhise, Wesleyan a Araujo, Pinar Zorlutuna, et al. 2014. "Direct-Write Bioprinting of Cell-Laden Methacrylated Gelatin Hydrogels." *Biofabrication* 6 (2): 24105. doi:10.1088/1758-5082/6/2/024105.
- Bhardwaj, Nandana, Dipali Devi, and Biman B. Mandal. 2015. "Tissue-Engineered Cartilage: The Crossroads of Biomaterials, Cells and Stimulating Factors." *Macromolecular Bioscience* 15 (2): 153–82. doi:10.1002/mabi.201400335.
- Bianco, Paolo, Xu Cao, Paul S Frenette, Jeremy J Mao, Pamela G Robey, Paul J Simmons, and Cun-Yu Wang. 2013. "The Meaning, the Sense and the Significance: Translating the Science of Mesenchymal Stem Cells into Medicine." *Nature Medicine* 19 (1). Nature Publishing Group: 35–42. doi:10.1038/nm.3028.
- Billiet, Thomas, Elien Gevaert, Thomas De Schryver, Maria Cornelissen, and Peter Dubrueel. 2014. "The 3D Printing of Gelatin Methacrylamide Cell-Laden Tissue-Engineered Constructs with High Cell Viability." *Biomaterials* 35 (1). Elsevier Ltd: 49–62. doi:10.1016/j.biomaterials.2013.09.078.
- Bleys, Ronald L a W, Mariola Popko, Jan-Willem De Groot, and Egbert H Huizing. 2007. "Histological Structure of the Nasal Cartilages and Their Perichondrial Envelope. II. The Perichondrial Envelope of the Septal and Lobular Cartilage." *Rhinology* 45 (2): 153–57. <http://www.ncbi.nlm.nih.gov/pubmed/17708464>.
- Bose, Susmita, Sahar Vahabzadeh, and Amit Bandyopadhyay. 2013. "Bone Tissue Engineering Using 3D Printing." *Materials Today* 16 (12): 496–504. doi:10.1016/j.mattod.2013.11.017.
- Bouapao, Leevameng, Hideto Tsuji, Kohji Tashiro, Jianming Zhang, and Makoto Hanesaka. 2009. "Crystallization, Spherulite Growth, and Structure of Blends of

- Crystalline and Amorphous Poly(lactide)s.” *Polymer* 50 (16): 4007–17. doi:http://dx.doi.org/10.1016/j.polymer.2009.06.040.
- Brittberg, M, A Lindahl, A Nilsson, C Ohlsson, O Isaksson, and L Peterson. 1994. “Treatment of Deep Cartilage Defects in the Knee with Autologous Chondrocyte Transplantation.” *The New England Journal of Medicine* 331 (14). United States: 889–95. doi:10.1056/NEJM199410063311401.
- Brittberg, Mats. 2014. “Knee Cartilage Repair with Hyalograft® (Hyaff-11 Scaffold with Seeded Autologous Chondrocytes).” In *Techniques in Cartilage Repair Surgery*, edited by A Ananthram Shetty, Seok-Jung Kim, Norimasa Nakamura, and Mats Brittberg, 227–35. Berlin, Heidelberg: Springer Berlin Heidelberg. doi:10.1007/978-3-642-41921-8_19.
- Brittberg, Mats, and Anders Lindahl. 2008. “Tissue Engineering of Cartilage.” *Tissue Engineering* 60 (2): 533–57. doi:10.1016/B978-0-12-370869-4.00018-5.
- Bryant, Stephanie J., and Kristi S. Anseth. 2002. “Hydrogel Properties Influence ECM Production by Chondrocytes Photoencapsulated in Poly(ethylene Glycol) Hydrogels.” *Journal of Biomedical Materials Research* 59 (1): 63–72. doi:10.1002/jbm.1217.
- Buizer, Arina T, Albert G Veldhuizen, Sjoerd K Bulstra, and Roel Kuijer. 2013. “Static versus Vacuum Cell Seeding on High and Low Porosity Ceramic Scaffolds.” *Journal of Biomaterials Applications* 29 (1): 3–13. doi:10.1177/0885328213512171.
- Burget, Gary C, and Robert L Walton. 2007. “Optimal Use of Microvascular Free Flaps, Cartilage Grafts, and a Paramedian Forehead Flap for Aesthetic Reconstruction of the Nose and Adjacent Facial Units.” *Plastic and Reconstructive Surgery* 120 (5): 1171-207-16. doi:10.1097/01.prs.0000254362.53706.91.
- Caffrey, Jason P., M , Anton M. Kushnaryov, Van , Marsha S. Reuther, Robert L. Sah W. Wong, Kristen K. Briggs,, Koichi Masuda, and and Deborah Watson. 2013. “Flexural Properties of Native and Tissue Engineered Human Septal Cartilage.” *Otolaryngol Head Neck Surg* 4 (164): 576–81. doi:10.1126/scisignal.2001449.Engineering.
- Cannady, Steven B, Ted a Cook, and Mark K Wax. 2009. “The Total Nasal Defect and Reconstruction.” *Facial Plastic Surgery Clinics of North America* 17 (2). Elsevier Ltd: 189–201. doi:10.1016/j.fsc.2009.01.002.
- Cannady, Steven B, Ted A Cook, Mark K Wax, and C Frcs. 2009. “The Total Nasal Defect and Reconstruction.” *Facial Plastic Surgery Clinics of NA* 17 (2). Elsevier Ltd: 189–201. doi:10.1016/j.fsc.2009.01.002.
- Caron, M. M J, P. J. Emans, M. M E Coolsen, L. Voss, D. A M Surtel, A. Cremers, L. W. van Rhijn, and T. J M Welting. 2012. “Redifferentiation of Dedifferentiated Human Articular Chondrocytes: Comparison of 2D and 3D Cultures.” *Osteoarthritis and Cartilage* 20 (10). Elsevier Ltd: 1170–78. doi:10.1016/j.joca.2012.06.016.
- Chae, Michael P., Warren M. Rozen, Paul G. McMenamain, Michael W. Findlay, Robert

- T. Spychal, and David J. Hunter-Smith. 2015. "Emerging Applications of Bedside 3D Printing in Plastic Surgery." *Frontiers in Surgery* 2 (June): 1–14. doi:10.3389/fsurg.2015.00025.
- Chang, Carlos C, Eugene D Boland, Stuart K Williams, and James B Hoying. 2011. "Direct-Write Bioprinting Three-Dimensional Biohybrid Systems for Future Regenerative Therapies." *Journal of Biomedical Materials Research. Part B, Applied Biomaterials* 98 (1): 160–70. doi:10.1002/jbm.b.31831.
- Chang, Robert, Jae Nam, and Wei Sun. 2008. "Direct Cell Writing of 3D Microorgan for *In Vitro* Pharmacokinetic Model." *Tissue Engineering Part C: Methods* 14 (2): 157–66. doi:10.1089/ten.tec.2007.0392.
- Chen, Guoping, Takashi Sato, Takashi Ushida, Rei Hirochika, and Tetsuya Tateishi. 2003. "Redifferentiation of Dedifferentiated Bovine Chondrocytes When Cultured in Vitro in a PLGA-Collagen Hybrid Mesh." *FEBS Letters* 542 (1–3). England: 95–99.
- Chen, Shangwu, Qin Zhang, Tomoko Nakamoto, Naoki Kawazoe, and Guoping Chen. 2016. "Gelatin Scaffolds with Controlled Pore Structure and Mechanical Property for Cartilage Tissue Engineering." *Tissue Engineering Part C: Methods* 22 (3): 189–98. doi:10.1089/ten.tec.2015.0281.
- Chim, H, D W Hutmacher, A M Chou, A L Oliveira, R L Reis, T C Lim, and J.-T. Schantz. 2006. "A Comparative Analysis of Scaffold Material Modifications for Load-Bearing Applications in Bone Tissue Engineering." *International Journal of Oral and Maxillofacial Surgery* 35 (10): 928–34. doi:http://dx.doi.org/10.1016/j.ijom.2006.03.024.
- Chung, Cindy, and Jason A Burdick. 2008. "Engineering Cartilage Tissue." *Advanced Drug Delivery Reviews* 60 (2): 243–62. doi:https://doi.org/10.1016/j.addr.2007.08.027.
- Chung, Cindy, Isaac E Erickson, Robert L Mauck, and Jason a Burdick. 2008. "Differential Behavior of Auricular and Articular Chondrocytes in Hyaluronic Acid Hydrogels." *Tissue Engineering. Part A* 14 (7): 1121–31. doi:10.1089/ten.tea.2007.0291.
- Coates, Emily E, Corinne N Riggan, and John P Fisher. 2013. "Photocrosslinked Alginate with Hyaluronic Acid Hydrogels as Vehicles for Mesenchymal Stem Cell Encapsulation and Chondrogenesis." *Journal of Biomedical Materials Research. Part A* 101 (7): 1962–70. doi:10.1002/jbm.a.34499.
- Cohen, Adir, Amir Laviv, Phillip Berman, Rizan Nashef, and Jawad Abu-Tair. 2009. "Mandibular Reconstruction Using Stereolithographic 3-Dimensional Printing Modeling Technology." *Oral Surgery, Oral Medicine, Oral Pathology, Oral Radiology and Endodontology* 108 (5). Elsevier Inc.: 661–66. doi:10.1016/j.tripleo.2009.05.023.
- Cohen, Daniel L., Evan Malone, Hod Lipson, and Lawrence J. Bonassar. 2006. "Direct Freeform Fabrication of Seeded Hydrogels in Arbitrary Geometries." *Tissue Engineering* 12 (5): 1325–35. doi:10.1089/ten.2006.12.1325.

- Comb, James W., William R. Priedeman, and Patrick W. Turley. 1994. "FDM Technology Process Improvements." *Solid Freeform Fabrication Proceedings*, 42–49. <http://www.dtic.mil/cgi-bin/GetTRDoc?AD=ADA290949#page=49>.
- Cui, Xiaofeng, and Thomas Boland. 2009. "Human Microvasculature Fabrication Using Thermal Inkjet Printing Technology." *Biomaterials* 30 (31): 6221–27. doi:10.1016/j.biomaterials.2009.07.056.
- Dahlin, Rebecca L, Lucas A Kinard, Johnny Lam, Clark J Needham, Steven Lu, F Kurtis Kasper, and Antonios G Mikos. 2014. "Articular Chondrocytes and Mesenchymal Stem Cells Seeded on Biodegradable Scaffolds for the Repair of Cartilage in a Rat Osteochondral Defect Model." *Biomaterials* 35 (26): 7460–69. doi:<http://doi.org/10.1016/j.biomaterials.2014.05.055>.
- Davidenko, Natalia, Carlos F. Schuster, Daniel V. Bax, Richard W. Farndale, Samir Hamaia, Serena M. Best, and Ruth E. Cameron. 2016. "Evaluation of Cell Binding to Collagen and Gelatin: A Study of the Effect of 2D and 3D Architecture and Surface Chemistry." *Journal of Materials Science: Materials in Medicine* 27 (10). Springer US. doi:10.1007/s10856-016-5763-9.
- De Ceuninck, Frédéric, Christophe Lesur, Philippe Pastoureau, Audrey Caliez, and Massimo Sabatini. 2004. "Culture of Chondrocytes in Alginate Beads." *Methods in Molecular Medicine* 100 (January): 15–22. doi:10.1385/1-59259-810-2:015.
- Derby, Brian. 2008a. "Bioprinting : Inkjet Printing Proteins and Hybrid Cell-Containing Materials and Structures," 5717–21. doi:10.1039/b807560c.
- . 2008b. "Bioprinting: Inkjet Printing Proteins and Hybrid Cell-Containing Materials and Structures." *Journal of Materials Chemistry* 18 (47): 5717. doi:10.1039/b807560c.
- . 2010. "Inkjet Printing of Functional and Structural Materials: Fluid Property Requirements, Feature Stability, and Resolution." *Annual Review of Materials Research* 40 (1): 395–414. doi:10.1146/annurev-matsci-070909-104502.
- Djabourov, Madeleine, Jacques Leblond, and Pierre Papon. 1988. "Gelation of Aqueous Gelatin Solutions. I. Structural Investigation." *Journal de Physique* 49: 319–32. doi:10.1051/jphys:01988004902031900.
- Domingos, Marco, Dinuccio Dinucci, Stefania Cometa, Michele Alderighi, Paulo Jorge Bártolo, and Federica Chiellini. 2009. "Polycaprolactone Scaffolds Fabricated via Bioextrusion for Tissue Engineering Applications." *International Journal of Biomaterials* 2009 (January): 239643. doi:10.1155/2009/239643.
- Dominici, M, K Le Blanc, I Mueller, I Slaper-Cortenbach, Fc Marini, Ds Krause, Rj Deans, a Keating, Dj Prockop, and Em Horwitz. 2006. "Minimal Criteria for Defining Multipotent Mesenchymal Stromal Cells. The International Society for Cellular Therapy Position Statement." *Cytotherapy* 8 (4): 315–17. doi:10.1080/14653240600855905.
- Dong, Yuqing, Guorui Jin, Changchun Ji, Rongyan He, Min Lin, Xin Zhao, Ang Li, Tian Jian Lu, and Feng Xu. 2017. "Non-Invasive Tracking of Hydrogel Degradation Using Upconversion Nanoparticles." *Acta Biomaterialia* 55. Acta

- Materialia Inc.: 410–19. doi:10.1016/j.actbio.2017.04.016.
- Driscoll, B P, S R Baker, and B P Drisco. 2001. “Reconstruction of Nasal Alar Defects.” *Archives of Facial Plastic Surgery* 3 (2): 91–99. <http://www.ncbi.nlm.nih.gov/pubmed/24918707>.
- Drummer, Dietmar, Sandra Cifuentes-Cuéllar, and Dominik Rietzel. 2012. “Suitability of PLA/TCP for Fused Deposition Modeling.” *Rapid Prototyping Journal* 18 (6): 500–507. doi:10.1108/13552541211272045.
- Drury, Jeanie L., and David J. Mooney. 2003. “Hydrogels for Tissue Engineering: Scaffold Design Variables and Applications.” *Biomaterials* 24 (24): 4337–51. doi:10.1016/S0142-9612(03)00340-5.
- Duan, Bin, Laura a Hockaday, Kevin H Kang, and Jonathan T Butcher. 2013. “3D Bioprinting of Heterogeneous Aortic Valve Conduits with Alginate/gelatin Hydrogels.” *Journal of Biomedical Materials Research. Part A* 101 (5): 1255–64. doi:10.1002/jbm.a.34420.
- Dulguerov, P, Abdelkarim S Allal, Willy Lehmann, and Thomas Calcaterra. 2001. “Nasal and Paranasal Sinus Carcinoma- Are We Making Progress” 92 (12): 3012–29. doi:10.1002/cncr.10131.
- Dunkern, Torsten R, Gerhard Fritz, and Bernd Kaina. 2001. “Ultraviolet Light-Induced DNA Damage Triggers Apoptosis in Nucleotide Excision Repair-deficient Cells via Bcl-2 Decline and Caspase-3 / -8 Activation,” 6026–38.
- Elzoghby, Ahmed O. 2013. “Gelatin-Based Nanoparticles as Drug and Gene Delivery Systems: Reviewing Three Decades of Research.” *Journal of Controlled Release* 172 (3): 1075–91. doi:<http://dx.doi.org/10.1016/j.jconrel.2013.09.019>.
- Emadedin, M, N Aghdami, L Taghiyar, R Fazeli, R Moghadasali, S Jahangir, R Farjad, and M B Eslaminejad. 2012. “Intra-Articular Injection of Autologous Mesenchymal Stem Cells in Six Patients with Knee Osteoarthritis.” *Archives of Iranian Medicine* 15 (7): 422–28. doi:012157/AIM.0010.
- Engler, Adam J, Shamik Sen, H Lee Sweeney, and Dennis E Discher. 2006. “Matrix Elasticity Directs Stem Cell Lineage Specification.” *Cell* 126 (4): 677–89. doi:<http://dx.doi.org/10.1016/j.cell.2006.06.044>.
- Eshraghi, Shaun, and Suman Das. 2010. “Mechanical and Microstructural Properties of Polycaprolactone Scaffolds with One-Dimensional, Two-Dimensional, and Three-Dimensional Orthogonally Oriented Porous Architectures Produced by Selective Laser Sintering.” *Acta Biomaterialia* 6 (7). Acta Materialia Inc.: 2467–76. doi:10.1016/j.actbio.2010.02.002.
- Fedorovich, Natalja E, Jacqueline Alblas, Joost R de Wijn, Wim E Hennink, Ab J Verbout, and Wouter J a Dhert. 2007. “Hydrogels as Extracellular Matrices for Skeletal Tissue Engineering: State-of-the-Art and Novel Application in Organ Printing.” *Tissue Engineering* 13 (8): 1905–25. doi:10.1089/ten.2006.0175.
- Fussenegger, Martin, Johann Meinhart, Walter Höbling, Werner Kullich, Siegfried Funk, and Günther Bernatzky. 2003. “Stabilized Autologous Fibrin-Chondrocyte

- Constructs for Cartilage Repair in Vivo.” *Annals of Plastic Surgery* 51 (5): 493–98. doi:10.1097/01.sap.0000067726.32731.E1.
- Garcia-Giralt, N, R Izquierdo, X Nogués, M Perez-Olmedilla, P Benito, J L Gómez-Ribelles, M a Checa, J Suay, E Cáceres, and J C Monllau. 2008. “A Porous PCL Scaffold Promotes the Human Chondrocytes Redifferentiation and Hyaline-Specific Extracellular Matrix Protein Synthesis.” *Journal of Biomedical Materials Research. Part A* 85 (4): 1082–89. doi:10.1002/jbm.a.31670.
- Gentile, Piergiorgio, Valeria Chiono, Irene Carmagnola, and Paul V Hatton. 2014. “An Overview of Poly(lactic-Co-Glycolic) Acid (PLGA)-Based Biomaterials for Bone Tissue Engineering.” *International Journal of Molecular Sciences* 15 (3): 3640–59. doi:10.3390/ijms15033640.
- Gibbons, D F. 1992. “Tissue Response to Resorbable Synthetic Polymers BT - Degradation Phenomena on Polymeric Biomaterials.” In , edited by Heinrich Planck, Martin Dauner, and Monika Renardy, 97–105. Berlin, Heidelberg: Springer Berlin Heidelberg. doi:10.1007/978-3-642-77563-5_8.
- Gosset, Marjolaine, Francis Berenbaum, Sylvie Thirion, and Claire Jacques. 2008. “Primary Culture and Phenotyping of Murine Chondrocytes.” *Nature Protocols* 3 (8): 1253–60. doi:10.1038/nprot.2008.95.
- Griffin, M. F., Y. Premakumar, A. M. Seifalian, M. Szarko, and P. E M Butler. 2016. “Biomechanical Characterisation of the Human Nasal Cartilages; Implications for Tissue Engineering.” *Journal of Materials Science: Materials in Medicine* 27 (1). Springer US: 1–6. doi:10.1007/s10856-015-5619-8.
- Grimaud, Eva, Dominique Heymann, and Françoise Rédini. 2002. “Recent Advances in TGF-Beta Effects on Chondrocyte Metabolism. Potential Therapeutic Roles of TGF-Beta in Cartilage Disorders.” *Cytokine & Growth Factor Reviews* 13 (3): 241–57. doi:10.1016/s1359-6101(02)00004-7.
- Grogan, Shawn Patrick, Andrea Barbero, Jose Diaz-Romero, Anne-Marie Cleton-Jansen, Stephan Soeder, Robert Whiteside, Pancras C W Hogendoorn, et al. 2007. “Identification of Markers to Characterize and Sort Human Articular Chondrocytes with Enhanced in Vitro Chondrogenic Capacity.” *Arthritis and Rheumatism* 56 (2): 586–95. doi:10.1002/art.22408.
- Guillemot, Fabien, Agnès Souquet, Sylvain Catros, and Bertrand Guillotin. 2010. “Laser-Assisted Cell Printing: Principle, Physical Parameters versus Cell Fate and Perspectives in Tissue Engineering.” *Nanomedicine (London, England)* 5 (3): 507–15. doi:10.2217/nnm.10.14.
- He, Yong, FeiFei Yang, HaiMing Zhao, Qing Gao, Bing Xia, and JianZhong Fu. 2016. “Research on the Printability of Hydrogels in 3D Bioprinting.” *Scientific Reports* 6 (1). Nature Publishing Group: 29977. doi:10.1038/srep29977.
- Hoch, Eva, Thomas Hirth, Günter E. M. Tovar, and Kirsten Borchers. 2013. “Chemical Tailoring of Gelatin to Adjust Its Chemical and Physical Properties for Functional Bioprinting.” *Journal of Materials Chemistry B* 1 (41): 5675. doi:10.1039/c3tb20745e.

- Hoffman, Allan S. 2012. "Hydrogels for Biomedical Applications." *Advanced Drug Delivery Reviews* 64 (SUPPL.). Elsevier B.V.: 18–23. doi:10.1016/j.addr.2012.09.010.
- Holden, Paul K, Li-Huei Liaw, and Brian J-F Wong. 2008. "Human Nasal Cartilage Ultrastructure: Characteristics and Comparison Using Scanning Electron Microscopy." *The Laryngoscope* 118 (7): 1153–56. doi:10.1097/MLG.0b013e31816ed5ad.
- Hölzl, Katja, Shengmao Lin, Liesbeth Tytgat, Sandra Van Vlierberghe, Linxia Gu, and Aleksandr Ovsianikov. 2016. "Bioink Properties Before, during and after 3D Bioprinting." *Biofabrication* 8 (3). IOP Publishing: 32002. doi:10.1088/1758-5090/8/3/032002.
- Homicz, Mark R, Stanley H Chia, Barbara L Schumacher, Koichi Masuda, Eugene J Thonar, Robert L Sah, and Deborah Watson. 2003. "Human Septal Chondrocyte Redifferentiation in Alginate, Polyglycolic Acid Scaffold, and Monolayer Culture." *The Laryngoscope* 113 (1): 25–32. doi:10.1097/00005537-200301000-00005.
- Hong, Hyun Jun, Jae Won Chang, Ju Kyeong Park, Jae Won Choi, Yoo Suk Kim, Yoo Seob Shin, Chul Ho Kim, and Eun Chang Choi. 2014. "Tracheal Reconstruction Using Chondrocytes Seeded on a poly(L-Lactic-Co-Glycolic Acid)-Fibrin/hyaluronan." *Journal of Biomedical Materials Research - Part A* 102 (11): 4142–50. doi:10.1002/jbm.a.35091.
- Howlander, N., AM Noone, M Krapcho, D Miller, K Bishop, CL Kosary, M Yu, et al. 2017. "SEER Cancer Statistics Review, 1975-2014."
- Hu, Xiaohong, Lie Ma, Chengchao Wang, and Changyou Gao. 2009. "Gelatin Hydrogel Prepared by Photo-Initiated Polymerization and Loaded with TGF- β 1 for Cartilage Tissue Engineering." *Macromolecular Bioscience* 9 (12): 1194–1201. doi:10.1002/mabi.200900275.
- Huizing, E.H. Egbert H. E.H., and J.M. John A. M. J.M. Groot. 2003. "Functional Reconstructive Nasal Surgery." *Thieme*, 386 p. doi:10.1016/j.jcms.2004.04.003.
- Hull, C W. 1986. "Apparatus for Production of Three-Dimensional Objects by Stereolithography." Google Patents. <http://www.google.co.uk/patents/US4575330>.
- Hutmacher, D W. 2000. "Scaffolds in Tissue Engineering Bone and Cartilage." *Biomaterials* 21 (24): 2529–43. doi:10.1016/S0142-9612(00)00121-6.
- Hutmacher, Dietmar W., Thorsten Schantz, Iwan Zein, Kee Woei Ng, Swee Hin Teoh, and Kim Cheng Tan. 2001. "Mechanical Properties and Cell Cultural Response of Polycaprolactone Scaffolds Designed and Fabricated via Fused Deposition Modeling." *Journal of Biomedical Materials Research* 55 (4): 203–16. doi:10.1002/1097-4636(200105)55:2<203::AID-JBM1007>3.0.CO;2-7.
- Hwang, Nathaniel S, Myoung Sook Kim, Somponnat Sampattavanich, Jin Hyen Baek, Zijun Zhang, and Jennifer Elisseff. 2006. "Effects of Three-Dimensional Culture and Growth Factors on the Chondrogenic Differentiation of Murine Embryonic

- Stem Cells.” *Stem Cells (Dayton, Ohio)* 24 (2). United States: 284–91. doi:10.1634/stemcells.2005-0024.
- Ingber, Donald E., Van C. Mow, David Butler, Laura Niklason, Johnny Huard, Jeremy Mao, Ioannis Yannas, David Kaplan, and Gordana Vunjak-Novakovic. 2006. “Tissue Engineering and Developmental Biology: Going Biomimetic.” *Tissue Engineering* 12 (12): 3265–83. doi:10.1089/ten.2006.12.3265.
- ISO/TEC 261. 2015. “ISO/ASTM 52900:2015 (ASTM F2792) Preview Additive Manufacturing -- General Principles -- Terminology.” *International Organization for Standardization*, 19.
- Jain, Rajeev A. 2000. “The Manufacturing Techniques of Various Drug Loaded Biodegradable Poly(lactide-Co-Glycolide) (PLGA) Devices.” *Biomaterials* 21 (23): 2475–90. doi:http://dx.doi.org/10.1016/S0142-9612(00)00115-0.
- Jakab, Karoly, Cyrille Norotte, Brook Damon, Francoise Marga, Adrian Neagu, Cynthia L Besch-Williford, Anatoly Kachurin, et al. 2008. “Tissue Engineering by Self-Assembly of Cells Printed into Topologically Defined Structures.” *Tissue Engineering. Part A* 14 (3). United States: 413–21. doi:10.1089/tea.2007.0173.
- Jakob, M, O Démarteau, D Schäfer, B Hintermann, W Dick, M Heberer, and I Martin. 2001. “Specific Growth Factors during the Expansion and Redifferentiation of Adult Human Articular Chondrocytes Enhance Chondrogenesis and Cartilaginous Tissue Formation in Vitro.” *Journal of Cellular Biochemistry* 81 (2). John Wiley & Sons, Inc.: 368–77. doi:10.1002/1097-4644(20010501)81:2<368::AID-JCB1051>3.0.CO;2-J.
- Jeong, Claire G., Huina Zhang, and Scott J. Hollister. 2012. “Three-Dimensional Polycaprolactone Scaffold-Conjugated Bone Morphogenetic Protein-2 Promotes Cartilage Regeneration from Primary Chondrocytes in Vitro and in Vivo without Accelerated Endochondral Ossification.” *Journal of Biomedical Materials Research - Part A* 100 A (8): 2088–96. doi:10.1002/jbm.a.33249.
- Jones, N. 2001. “The Nose and Paranasal Sinuses Physiology and Anatomy.” *Advanced Drug Delivery Reviews* 51 (1–3): 5–19. http://www.ncbi.nlm.nih.gov/pubmed/11516776.
- Kalita, Samar Jyoti, Susmita Bose, Howard L Hosick, and Amit Bandyopadhyay. 2003. “Development of Controlled Porosity Polymer-Ceramic Composite Scaffolds via Fused Deposition Modeling.” *Materials Science and Engineering: C* 23 (5): 611–20. doi:http://dx.doi.org/10.1016/S0928-4931(03)00052-3.
- Kang, Hyun-Wook, Sang Jin Lee, In Kap Ko, Carlos Kengla, James J Yoo, and Anthony Atala. 2016. “A 3D Bioprinting System to Produce Human-Scale Tissue Constructs with Structural Integrity.” *Nature Biotechnology* 34 (3). Nature Publishing Group: 312–19. doi:10.1038/nbt.3413.
- Kesti, Matti, Christian Eberhardt, Guglielmo Pagliccia, David Kenkel, Daniel Grande, Andreas Boss, and Marcy Zenobi-Wong. 2015. “Bioprinting Complex Cartilaginous Structures with Clinically Compliant Biomaterials.” *Advanced Functional Materials*, 7406–17. doi:10.1002/adfm.201503423.

- Kim, Iris L, Robert L Mauck, and Jason A Burdick. 2011. "Hydrogel Design for Cartilage Tissue Engineering: A Case Study with Hyaluronic Acid." *Biomaterials* 32 (34): 8771–82. doi:http://dx.doi.org/10.1016/j.biomaterials.2011.08.073.
- Kingsley, DM, AD Dias, DB Chrisey, and DT Corr. 2013. "Single-Step Laser-Based Fabrication and Patterning of Cellencapsulated Alginate Microbeads." *Biofabrication* 5: 211–20. doi:10.1007/s11103-011-9767-z.Plastid.
- Kinner, a., W. Wu, C. Staudt, and G. Iliakis. 2008. "-H2AX in Recognition and Signaling of DNA Double-Strand Breaks in the Context of Chromatin." *Nucleic Acids Research* 36 (17): 5678–94. doi:10.1093/nar/gkn550.
- Kirchmajer, D. M., R. Gorkin III, and M. in het Panhuis. 2015. "An Overview of the Suitability of Hydrogel-Forming Polymers for Extrusion-Based 3D-Printing." *J. Mater. Chem. B* 3 (20): 4105–17. doi:10.1039/C5TB00393H.
- Klotz, Barbara J., Debby Gawlitta, Antoine J W P Rosenberg, Jos Malda, and Ferry P W Melchels. 2016. "Gelatin-Methacryloyl Hydrogels: Towards Biofabrication-Based Tissue Repair." *Trends in Biotechnology* 34 (5). Elsevier Ltd: 394–407. doi:10.1016/j.tibtech.2016.01.002.
- Kolesky, David B., Ryan L. Truby, A. Sydney Gladman, Travis A. Busbee, Kimberly A. Homan, and Jennifer A. Lewis. 2014. "3D Bioprinting of Vascularized, Heterogeneous Cell-Laden Tissue Constructs." *Advanced Materials* 26 (19): 3124–30. doi:10.1002/adma.201305506.
- Kruth, J P, X Wang, T Laoui, and L Froyen. 2003. "Lasers and Materials in Selective Laser Sintering." *Assembly Automation* 23 (4). Emerald: 357–71. doi:10.1108/01445150310698652.
- Kundu, Joydip, Jin-Hyung Shim, Jinah Jang, Sung-Won Kim, and Dong-Woo Cho. 2015. "An Additive Manufacturing-Based PCL-Alginate-Chondrocyte Bioprinted Scaffold for Cartilage Tissue Engineering." *Journal of Tissue Engineering and Regenerative Medicine* 9 (11). England: 1286–97. doi:10.1002/term.1682.
- Lee, Chang H, James L Cook, Avital Mendelson, Eduardo K Moioli, Hai Yao, and Jeremy J Mao. 2010. "Regeneration of the Articular Surface of the Rabbit Synovial Joint by Cell Homing: A Proof of Concept Study." *Lancet (London, England)* 376 (9739). England: 440–48. doi:10.1016/S0140-6736(10)60668-X.
- Lee, Chang H, Scott A Rodeo, Lisa Ann Fortier, Chuanyong Lu, Cevat Eriskan, and Jeremy J Mao. 2014. "Protein-Releasing Polymeric Scaffolds Induce Fibrochondrocytic Differentiation of Endogenous Cells for Knee Meniscus Regeneration in Sheep." *Sci Ence Translational Medicine*. 6 (266). doi:10.1126/scitranslmed.3009696.Protein-releasing.
- Lee, David A, Tom Reisler, and Dan L Bader. 2003. "Expansion of Chondrocytes for Tissue Engineering in Alginate Beads Enhances Chondrocytic Phenotype Compared to Conventional Monolayer Techniques." *Acta Orthopaedica Scandinavica* 74 (1). England: 6–15. doi:10.1080/00016470310013581.
- Lee, Jung-Seob, Jung Min Hong, Jin Woo Jung, Jin-Hyung Shim, Jeong-Hoon Oh, and Dong-Woo Cho. 2014. "3D Printing of Composite Tissue with Complex Shape

- Applied to Ear Regeneration.” *Biofabrication* 6: 24103. doi:10.1088/1758-5082/6/2/024103.
- Lee, Kuen Yong, and David J. Mooney. 2001. “Hydrogels for Tissue Engineering.” *Chemical Reviews* 101 (7): 1869–79. doi:10.1021/cr000108x.
- Leong, K. F., C. M. Cheah, and C. K. Chua. 2003. “Solid Freeform Fabrication of Three-Dimensional Scaffolds for Engineering Replacement Tissues and Organs.” *Biomaterials* 24 (13): 2363–78. doi:10.1016/S0142-9612(03)00030-9.
- Li, Ke, Chunqiu Zhang, Lulu Qiu, Lilan Gao, and Xizheng Zhang. 2017. “Advances in Application of Mechanical Stimuli in Bioreactors for Cartilage Tissue Engineering.” *Tissue Engineering Part B: Reviews* 0 (0): ten.TEB.2016.0427. doi:10.1089/ten.TEB.2016.0427.
- Li, Xiaomeng, Shangwu Chen, Jingchao Li, Xinlong Wang, Jing Zhang, Naoki Kawazoe, and Guoping Chen. 2016. “3D Culture of Chondrocytes in Gelatin Hydrogels with Different Stiffness.” *Polymers* . doi:10.3390/polym8080269.
- Lin, Yu-Ju, Chi-Nan Yen, Yu-Chen Hu, Yung-Chih Wu, Chun-Jen Liao, and I-Ming Chu. 2009. “Chondrocytes Culture in Three-Dimensional Porous Alginate Scaffolds Enhanced Cell Proliferation, Matrix Synthesis and Gene Expression.” *Journal of Biomedical Materials Research. Part A* 88 (1): 23–33. doi:10.1002/jbm.a.31841.
- Liu, Wanjun, Marcel A. Heinrich, Yixiao Zhou, Ali Akpek, Ning Hu, Xiao Liu, Xiaofei Guan, et al. 2017. “Extrusion Bioprinting of Shear-Thinning Gelatin Methacryloyl Bioinks.” *Advanced Healthcare Materials* 6 (12): 1–11. doi:10.1002/adhm.201601451.
- Liu, Zhongrong, Hulin Chen, Huilan Yang, Jie Liang, and Xuemei Li. 2012. “Low-Dose UVA Radiation-Induced Adaptive Response in Cultured Human Dermal Fibroblasts.” *International Journal of Photoenergy* 2012. doi:10.1155/2012/167425.
- MacNeil, Sheila. 2007. “Progress and Opportunities for Tissue-Engineered Skin.” *Nature* 445 (7130): 874–80. doi:10.1038/nature05664.
- Maher, P.S., R.P. Keatch, K. Donnelly, R.E. Mackay, and J.Z. Paxton. 2009. “Construction of 3D Biological Matrices Using Rapid Prototyping Technology.” *Rapid Prototyping Journal* 15 (3): 204–10. doi:10.1108/13552540910960307.
- Makris, Eleftherios A, Andreas H Gomoll, Konstantinos N Malizos, Jerry C Hu, and Kyriacos A Athanasiou. 2015. “Repair and Tissue Engineering Techniques for Articular Cartilage.” *Nature Reviews. Rheumatology* 11 (1). Nature Publishing Group: 21–34. doi:10.1038/nrrheum.2014.157.
- Malda, Jos, Jetze Visser, Ferry P Melchels, Tomasz Jüngst, Wim E Hennink, Wouter J a Dhert, Jürgen Groll, and Dietmar W Huttmacher. 2013. “25th Anniversary Article: Engineering Hydrogels for Biofabrication.” *Advanced Materials (Deerfield Beach, Fla.)* 25 (36): 5011–28. doi:10.1002/adma.201302042.
- Mandrycky, Christian, Zongjie Wang, Keekyoung Kim, and Deok Ho Kim. 2016. “3D

- Bioprinting for Engineering Complex Tissues.” *Biotechnology Advances* 34 (4). Elsevier B.V.: 422–34. doi:10.1016/j.biotechadv.2015.12.011.
- Masood, S.H. 2007. “Application of Fused Deposition Modelling in Controlled Drug Delivery Devices.” *Assembly Automation* 27 (3): 215–21. doi:10.1108/01445150710763231.
- Melchels, Ferry P. W., Wouter J. A. Dhert, Dietmar W. Huttmacher, and Jos Malda. 2014. “Development and Characterisation of a New Bioink for Additive Tissue Manufacturing.” *Journal of Materials Chemistry B* 2 (16): 2282. doi:10.1039/c3tb21280g.
- Melchels, Ferry P.W., Marco a.N. Domingos, Travis J. Klein, Jos Malda, Paulo J. Bartolo, and Dietmar W. Huttmacher. 2012. “Additive Manufacturing of Tissues and Organs.” *Progress in Polymer Science* 37 (8). Elsevier Ltd: 1079–1104. doi:10.1016/j.progpolymsci.2011.11.007.
- Mendler, M., S. G. Eich-Bender, L. Vaughan, K. H. Winterhalter, and P. Bruckner. 1989. “Cartilage Contains Mixed Fibrils of Collagen Types II, IX, and XI.” *Journal of Cell Biology* 108 (1): 191–97. doi:10.1083/jcb.108.1.191.
- Menick, Frederick J. 2009. “Nasal Reconstruction with a Forehead Flap.” *Clinics in Plastic Surgery* 36 (3). Elsevier Ltd: 443–59. doi:10.1016/j.cps.2009.02.015.
- Michelotti, B, and D Mackay. 2012. “Nasal Reconstruction.” *Clinical Anatomy (New York, N.Y.)* 25 (1): 86–98. doi:10.1002/ca.21295.
- Mironi-Harpaz, Iris, Dennis Yingquan Wang, Subbu Venkatraman, and Dror Seliktar. 2012. “Photopolymerization of Cell-Encapsulating Hydrogels: Crosslinking Efficiency versus Cytotoxicity.” *Acta Biomaterialia* 8 (5). Acta Materialia Inc.: 1838–48. doi:10.1016/j.actbio.2011.12.034.
- Mitsak, Anna G, Jessica M Kemppainen, Matthew T Harris, and Scott J Hollister. 2011. “Effect of Polycaprolactone Scaffold Permeability on Bone Regeneration in Vivo.” *Tissue Engineering. Part A* 17 (13–14): 1831–39. doi:10.1089/ten.TEA.2010.0560.
- Mitsouras, Dimitris, Peter Liacouras, Amir Imanzadeh, Andreas A Giannopoulos, Tianrun Cai, Kanako K Kumamaru, Elizabeth George, et al. 2015. “Medical 3D Printing for the Radiologist.” *RadioGraphics* 35 (7). Radiological Society of North America: 1965–88. doi:10.1148/rg.2015140320.
- Mohamed, Omar A., Syed H. Masood, and Jahar L. Bhowmik. 2015. “Optimization of Fused Deposition Modeling Process Parameters: A Review of Current Research and Future Prospects.” *Advances in Manufacturing* 3 (1): 42–53. doi:10.1007/s40436-014-0097-7.
- Moroni, L, J R de Wijn, and C A van Blitterswijk. 2006. “3D Fiber-Deposited Scaffolds for Tissue Engineering: Influence of Pores Geometry and Architecture on Dynamic Mechanical Properties.” *Biomaterials* 27 (7): 974–85. doi:10.1016/j.biomaterials.2005.07.023.
- Morrison, R. J., S. J. Hollister, M. F. Niedner, M. G. Mahani, A. H. Park, D. K. Mehta,

- R. G. Ohye, and G. E. Green. 2015. "Mitigation of Tracheobronchomalacia with 3D-Printed Personalized Medical Devices in Pediatric Patients." *Science Translational Medicine* 7 (285): 285ra64-285ra64. doi:10.1126/scitranslmed.3010825.
- Mota, Carlos, Dario Puppi, Federica Chiellini, and Emo Chiellini. 2012. "Additive Manufacturing Techniques for the Production of Tissue Engineering Constructs." *Journal of Tissue Engineering and Regenerative Medicine* 4 (7): 524–31. doi:10.1002/term.
- . 2015. "Additive Manufacturing Techniques for the Production of Tissue Engineering Constructs," no. November 2012: 174–90. doi:10.1002/term.
- Mouser, Vivian H M, Ferry P W Melchels, Jetze Visser, Wouter J A Dhert, Debby Gawlitta, and Jos Malda. 2016a. "Yield Stress Determines Bioprintability of Hydrogels Based on Gelatin-Methacryloyl and Gellan Gum for Cartilage Bioprinting." *Biofabrication* 8 (3). IOP Publishing: 35003. doi:10.1088/1758-5090/8/3/035003.
- . 2016b. "Yield Stress Determines Bioprintability of Hydrogels Based on Gelatin-Methacryloyl and Gellan Gum for Cartilage Bioprinting." *Biofabrication* 8 (3). IOP Publishing: 35003. doi:10.1088/1758-5090/8/3/035003.
- Murphy, Ciara M, Matthew G Haugh, and Fergal J O'Brien. 2010. "The Effect of Mean Pore Size on Cell Attachment, Proliferation and Migration in Collagen-Glycosaminoglycan Scaffolds for Bone Tissue Engineering." *Biomaterials* 31 (3): 461–66. doi:10.1016/j.biomaterials.2009.09.063.
- Murphy, Sean V, and Anthony Atala. 2014. "3D Bioprinting of Tissues and Organs." *Nature Biotechnology* 32 (8). Nature Publishing Group: 773–85. doi:10.1038/nbt.2958.
- Murr, Lawrence E, Sara M Gaytan, Diana A Ramirez, Edwin Martinez, Jennifer Hernandez, Krista N Amato, Patrick W Shindo, Francisco R Medina, and Ryan B Wicker. 2012. "Metal Fabrication by Additive Manufacturing Using Laser and Electron Beam Melting Technologies." *Journal of Materials Science & Technology* 28 (1): 1–14. doi:http://dx.doi.org/10.1016/S1005-0302(12)60016-4.
- Naderi-Meshkin, Hojjat, Kristin Andreas, Maryam M. Matin, Michael Sittinger, Hamid Reza Bidkhorji, Naghmeh Ahmadiankia, Ahmad Reza Bahrami, and Jochen Ringe. 2014. "Chitosan-Based Injectable Hydrogel as a Promising in Situ Forming Scaffold for Cartilage Tissue Engineering." *Cell Biology International* 38 (1): 72–84. doi:10.1002/cbin.10181.
- Nair, Kalyani, Milind Gandhi, Saif Khalil, Karen Chang Yan, Michele Marcolongo, Kenneth Barbee, and Wei Sun. 2009. "Characterization of Cell Viability during Bioprinting Processes." *Biotechnology Journal* 4 (8): 1168–77. doi:10.1002/biot.200900004.
- Natvig, P, L a Sether, R P Gingrass, and W D Gardner. 1971. "Anatomical Details of the Osseous-Cartilaginous Framework of the Nose." *Plastic and Reconstructive Surgery*. http://www.ncbi.nlm.nih.gov/pubmed/5141270.

- Neves, Sara C, Liliana S Moreira Teixeira, Lorenzo Moroni, Rui L Reis, Clemens a Van Blitterswijk, Natália M Alves, Marcel Karperien, and João F Mano. 2011. "Chitosan/poly(epsilon-Caprolactone) Blend Scaffolds for Cartilage Repair." *Biomaterials* 32 (4). Elsevier Ltd: 1068–79. doi:10.1016/j.biomaterials.2010.09.073.
- Nguyen, Quynhhoa T, Yongsung Hwang, Albert C Chen, Shyni Varghese, and Robert L Sah. 2012. "Cartilage-like Mechanical Properties of Poly (Ethylene Glycol)-Diacrylate Hydrogels." *Biomaterials* 33 (28). Elsevier Ltd: 6682–90. doi:10.1016/j.biomaterials.2012.06.005.
- Nichol, Jason W, Sandeep T Koshy, Hojae Bae, Chang M Hwang, Seda Yamanlar, and Ali Khademhosseini. 2010. "Cell-Laden Microengineered Gelatin Methacrylate Hydrogels." *Biomaterials* 31 (21). Elsevier Ltd: 5536–44. doi:10.1016/j.biomaterials.2010.03.064.
- Nuernberger, Sylvia, Norbert Cyran, Christian Albrecht, Heinz Redl, Vilmos Vécsei, and Stefan Marlovits. 2011. "The Influence of Scaffold Architecture on Chondrocyte Distribution and Behavior in Matrix-Associated Chondrocyte Transplantation Grafts." *Biomaterials* 32 (4). Elsevier Ltd: 1032–40. doi:10.1016/j.biomaterials.2010.08.100.
- Oneal, Robert M, and Richard J Beil. 2010. "Surgical Anatomy of the Nose." *Clinics in Plastic Surgery* 37 (2): 191–211. doi:http://dx.doi.org/10.1016/j.cps.2009.12.011.
- Ouyang, Liliang, Christopher B. Highley, Christopher B. Rodell, Wei Sun, and Jason A. Burdick. 2016. "3D Printing of Shear-Thinning Hyaluronic Acid Hydrogels with Secondary Cross-Linking." *ACS Biomaterials Science and Engineering* 2 (10): 1743–51. doi:10.1021/acsbomaterials.6b00158.
- Ouyang, Liliang, Rui Yao, Yu Zhao, and Wei Sun. 2016. "Effect of Bioink Properties on Printability and Cell Viability for 3D Bioplotting of Embryonic Stem Cells." *Biofabrication* 8 (3). IOP Publishing: 35020. doi:10.1088/1758-5090/8/3/035020.
- Pabla, Ravinder, Michael Gilhooly, and Bhavin Visavadia. 2013. "Total Nasal Reconstruction Using Composite Radial Forearm Free Flap and Forehead Flap as a One-Stage Procedure with Minor Revision." *The British Journal of Oral & Maxillofacial Surgery* 51 (7). British Association of Oral and Maxillofacial Surgeons: 662–64. doi:10.1016/j.bjoms.2013.05.005.
- Panwar, Amit, and Lay Poh Tan. 2016. "Current Status of Bioinks for Micro-Extrusion-Based 3D Bioprinting." *Molecules* 21 (6). doi:10.3390/molecules21060685.
- Park, Hyejin, Bogyu Choi, Junli Hu, and Min Lee. 2013. "Injectable Chitosan Hyaluronic Acid Hydrogels for Cartilage Tissue Engineering." *Acta Biomaterialia* 9 (1). Acta Materialia Inc.: 4779–86. doi:10.1016/j.actbio.2012.08.033.
- Parthasarathy, Jayanthi. 2014. "3D Modeling, Custom Implants and Its Future Perspectives in Craniofacial Surgery." *Annals of Maxillofacial Surgery* 4 (1). India: Medknow Publications & Media Pvt Ltd: 9–18. doi:10.4103/2231-0746.133065.
- Pati, Falguni, Jinah Jang, Dong-Heon Ha, Sung Won Kim, Jong-Won Rhie, Jin-Hyung Shim, Deok-Ho Kim, and Dong-Woo Cho. 2014. "Printing Three-Dimensional

- Tissue Analogues with Decellularized Extracellular Matrix Bioink.” *Nature Communications* 5 (January). Nature Publishing Group: 3935. doi:10.1038/ncomms4935.
- Patrício, T., M. Domingos, A. Gloria, and P. Bártolo. 2013. “Characterisation of PCL and PCL/PLA Scaffolds for Tissue Engineering.” *Procedia CIRP* 5 (January): 110–14. doi:10.1016/j.procir.2013.01.022.
- Peretti, Giuseppe M, Jian-Wei Xu, Lawrence J Bonassar, Carl Hendrick Kirchhoff, Michael J Yaremchuk, and Mark A Randolph. 2006. “Review of Injectable Cartilage Engineering Using Fibrin Gel in Mice and Swine Models.” *Tissue Engineering* 12 (5). United States: 1151–68. doi:10.1089/ten.2006.12.1151.
- Pescosolido, Laura, Wouter Schuurman, Jos Malda, Pietro Matricardi, Franco Alhaique, Tommasina Coviello, P. René Van Weeren, Wouter J.A. Dhert, Wim E. Hennink, and Tina Vermonden. 2011. “Hyaluronic Acid and Dextran-Based Semi-IPN Hydrogels as Biomaterials for Bioprinting.” *Biomacromolecules* 12 (5): 1831–38. doi:10.1021/bm200178w.
- Pittenger, M F, a M Mackay, S C Beck, R K Jaiswal, R Douglas, J D Mosca, M a Moorman, D W Simonetti, S Craig, and D R Marshak. 1999. “Multilineage Potential of Adult Human Mesenchymal Stem Cells.” *Science (New York, N.Y.)* 284 (5411): 143–47. <http://www.ncbi.nlm.nih.gov/pubmed/10102814>.
- Probst, F A, D W Hutmacher, D F Müller, H.-G. Machens, and J.-T. Schantz. 2010. “Rekonstruktion der Kalvaria durch ein präfabriziertes bioaktives Implantat TT - Calvarial Reconstruction by Customized Bioactive Implant.” *Handchir Mikrochir plast Chir* 42 (6): 369–73. doi:10.1055/s-0030-1248310.
- Reiffel, Alyssa J., Concepcion Kafka, Karina A. Hernandez, Samantha Popa, Justin L. Perez, Sherry Zhou, Satadru Pramanik, et al. 2013. “High-Fidelity Tissue Engineering of Patient-Specific Auricles for Reconstruction of Pediatric Microtia and Other Auricular Deformities.” *PLoS ONE* 8 (2). doi:10.1371/journal.pone.0056506.
- Rengier, F, a Mehndiratta, H von Tengg-Kobligk, C M Zechmann, R Unterhinninghofen, H-U Kauczor, and F L Giesel. 2010. “3D Printing Based on Imaging Data: Review of Medical Applications.” *International Journal of Computer Assisted Radiology and Surgery* 5 (4): 335–41. doi:10.1007/s11548-010-0476-x.
- Richmon, Jeremy D., August Sage, Van W. Wong, Albert C. Chen, Robert L. Sah, and Deborah Watson. 2006. “Compressive Biomechanical Properties of Human Nasal Septal Cartilage.” *American Journal of Rhinology* 20 (5): 496–501. doi:10.2500/ajr.2006.20.2932.
- Richter, Dustin L., Robert C. Schenck, Daniel C. Wascher, and Gehron Treme. 2016. “Knee Articular Cartilage Repair and Restoration Techniques.” *Sports Health: A Multidisciplinary Approach* 8 (2): 153–60. doi:10.1177/1941738115611350.
- Ringeisen, Bradley R., Heungsoo Kim, Jason A. Barron, David B. Krizman, Douglas B. Chrisey, Shawna Jackman, R.Y.C. Auyeung, and Barry J. Spargo. 2004. “Laser

- Printing of Pluripotent Embryonal Carcinoma Cells." *Tissue Engineering* 10 (3–4): 483–91. doi:10.1089/107632704323061843.
- Rodriguez-Prieto, Manuel Angel, Teresa Alonso-Alonso, and Pedro Sánchez-Sambucety. 2009. "Nasal Reconstruction with Titanium Mesh." *Dermatologic Surgery : Official Publication for American Society for Dermatologic Surgery [et Al.]* 35 (2): 282–86. doi:10.1111/j.1524-4725.2008.34425.x.
- Rogers, Catherine M., Terry S. Woolley, Simon C. Cruwys, Lee D K Buttery, Felicity R A J Rose, and Kevin M. Shakesheff. 2012. "Engineering an in-Vitro Model of Rodent Cartilage." *Journal of Pharmacy and Pharmacology* 64 (6): 821–31. doi:10.1111/j.2042-7158.2012.01491.x.
- Rose, James B., Settimio Pacelli, Alicia J. El Haj, Harminder S. Dua, Andrew Hopkinson, Lisa J. White, and Felicity R a J Rose. 2014. "Gelatin-Based Materials in Ocular Tissue Engineering." *Materials* 7 (4): 3106–35. doi:10.3390/ma7043106.
- Ruiz-Cantu, Laura, Andrew Gleadall, Callum Faris, Joel Segal, Kevin Shakesheff, and Jing Yang. 2016. "Characterisation of the Surface Structure of 3D Printed Scaffolds for Cell Infiltration and Surgical Suturing." *Biofabrication* 8 (1). IOP Publishing: 15016. doi:10.1088/1758-5090/8/1/015016.
- Rutz, Alexandra L., Kelly E. Hyland, Adam E. Jakus, Wesley R. Burghardt, and Ramille N. Shah. 2015. "A Multimaterial Bioink Method for 3D Printing Tunable, Cell-Compatible Hydrogels." *Advanced Materials* 27 (9): 1607–14. doi:10.1002/adma.201405076.
- Sajjadian, Ali, Roe Rubinstein, and Nima Naghshineh. 2010. "Current Status of Grafts and Implants in Rhinoplasty: Part I. Autologous Grafts." *Plastic and Reconstructive Surgery* 125 (2): 40e–49e. doi:10.1097/PRS.0b013e3181c82f12.
- Sant, Shilpa, and Paul A. Johnston. 2017. "The Production of 3D Tumor Spheroids for Cancer Drug Discovery." *Drug Discovery Today: Technologies* 23. Elsevier Ltd: 27–36. doi:10.1016/j.ddtec.2017.03.002.
- Savioli Lopes, M., A. L. Jardini, and R. Maciel Filho. 2012. "Poly (Lactic Acid) Production for Tissue Engineering Applications." *Procedia Engineering* 42 (August): 1402–13. doi:10.1016/j.proeng.2012.07.534.
- Schantz, Jan-Thorsten, Arthur Brandwood, Dietmar Werner Hutmacher, Hwei Ling Khor, and Katharina Bittner. 2005. "Osteogenic Differentiation of Mesenchymal Progenitor Cells in Computer Designed Fibrin-Polymer-Ceramic Scaffolds Manufactured by Fused Deposition Modeling." *Journal of Materials Science: Materials in Medicine* 16 (9): 807–19. doi:10.1007/s10856-005-3584-3.
- Schnabel, M, S Marlovits, G Eckhoff, I Fichtel, L Gotzen, V Vécsei, and J Schlegel. 2002. "Dedifferentiation-Associated Changes in Morphology and Gene Expression in Primary Human Articular Chondrocytes in Cell Culture." *Osteoarthritis and Cartilage* 10 (1): 62–70. doi:http://dx.doi.org/10.1053/joca.2001.0482.
- Schulze-Tanzil, Gundula. 2009. "Activation and Dedifferentiation of Chondrocytes: Implications in Cartilage Injury and Repair." *Annals of Anatomy - Anatomischer Anzeiger* 191 (4): 325–38. doi:http://dx.doi.org/10.1016/j.aanat.2009.05.003.

- Schuurman, W, V Khristov, M W Pot, P R van Weeren, W J A Dhert, and J Malda. 2011. "Bioprinting of Hybrid Tissue Constructs with Tailorable Mechanical Properties." *Biofabrication* 3 (2): 21001. doi:10.1088/1758-5082/3/2/021001.
- Schuurman, Wouter, Peter a Levett, Michiel W Pot, Paul René van Weeren, Wouter J a Dhert, Dietmar W Hutmacher, Ferry P W Melchels, Travis J Klein, and Jos Malda. 2013. "Gelatin-Methacrylamide Hydrogels as Potential Biomaterials for Fabrication of Tissue-Engineered Cartilage Constructs." *Macromolecular Bioscience* 13 (5): 551–61. doi:10.1002/mabi.201200471.
- Seol, Young-Joon, Hyun-Wook Kang, Sang Jin Lee, Anthony Atala, and James J Yoo. 2014. "Bioprinting Technology and Its Applications." *European Journal of Cardio-Thoracic Surgery: Official Journal of the European Association for Cardio-Thoracic Surgery* 46 (July): 342–48. doi:10.1093/ejcts/ezu148.
- Serra, Tiziano, Monica Ortiz-Hernandez, Elisabeth Engel, Josep A Planell, and Melba Navarro. 2014. "Relevance of PEG in PLA-Based Blends for Tissue Engineering 3D-Printed Scaffolds." *Materials Science & Engineering. C, Materials for Biological Applications* 38 (May): 55–62. doi:10.1016/j.msec.2014.01.003.
- Seth, Rahul, Peter C Revenaugh, Joseph Scharpf, Taha Z Shipchandler, and Michael a Fritz. 2013. "Free Anterolateral Thigh Fascia Lata Flap for Complex Nasal Lining Defects." *JAMA Facial Plastic Surgery* 15 (1): 21–28. doi:10.1001/2013.jamafacial.5.
- Shepherd, D E, and B B Seedhom. 1999. "The 'Instantaneous' Compressive Modulus of Human Articular Cartilage in Joints of the Lower Limb." *Rheumatology (Oxford, England)* 38 (2). England: 124–32.
- Shibata, Akimichi, Shuhei Yada, and Mitsuhiro Terakawa. 2016. "Biodegradability of Poly(lactic-Co-Glycolic Acid) after Femtosecond Laser Irradiation." *Scientific Reports* 6 (May). Nature Publishing Group: 27884. doi:10.1038/srep27884.
- Shim, Jin-Hyung, Jong Young Kim, Jung Kyu Park, Sei Kwang Hahn, Jong-Won Rhie, Sun-Woong Kang, Soo-Hong Lee, and Dong-Woo Cho. 2010. "Effect of Thermal Degradation of SFF-Based PLGA Scaffolds Fabricated Using a Multi-Head Deposition System Followed by Change of Cell Growth Rate." *Journal of Biomaterials Science, Polymer Edition* 21 (8–9): 1069–80. doi:10.1163/092050609X12457428919034.
- Shim, Jin-Hyung, Jong Young Kim, Min Park, Jaesung Park, and Dong-Woo Cho. 2011. "Development of a Hybrid Scaffold with Synthetic Biomaterials and Hydrogel Using Solid Freeform Fabrication Technology." *Biofabrication* 3 (3): 34102. doi:10.1088/1758-5082/3/3/034102.
- Shim, Jin-hyung, Jung-seob Lee, and Jong Young Kim. n.d. "Bioprinting of a Mechanically Enhanced Three-Dimensional Dual Cell-Laden Construct for Osteochondral Tissue Engineering Using a Multi-Head Tissue / Organ Building System" 85014. doi:10.1088/0960-1317/22/8/085014.
- Shim, Jin-Hyung, Jung-Seob Lee, Jong Young Kim, and Dong-Woo Cho. 2012. "Bioprinting of a Mechanically Enhanced Three-Dimensional Dual Cell-Laden

- Construct for Osteochondral Tissue Engineering Using a Multi-Head Tissue/organ Building System.” *Journal of Micromechanics and Microengineering* 22 (8): 85014. doi:10.1088/0960-1317/22/8/085014.
- Shor, Lauren, Selçuk Güçeri, Robert Chang, Jennifer Gordon, Qian Kang, Langdon Hartsock, Yuehuei An, and Wei Sun. 2009. “Precision Extruding Deposition (PED) Fabrication of Polycaprolactone (PCL) Scaffolds for Bone Tissue Engineering.” *Biofabrication* 1 (1): 15003. doi:10.1088/1758-5082/1/1/015003.
- Shu, Alan Faulkner-Jones and Catherine Fyfe and Dirk-Jan Cornelissen and John Gardner and Jason King and Aidan Courtney and Wenmiao. 2015. “Bioprinting of Human Pluripotent Stem Cells and Their Directed Differentiation into Hepatocyte-like Cells for the Generation of Mini-Livers in 3D.” *Biofabrication* 7 (4): 44102. <http://stacks.iop.org/1758-5090/7/i=4/a=044102>.
- Siegman, A., S. Kening, and A. Buchman. 1987. “Residual Stresses in Injection-Moulded Amorphous Polymers.” *Polymer Engineering and Science* 27: 1069–78.
- Signori, Francesca, Maria Beatrice Coltelli, and Simona Bronco. 2009. “Thermal Degradation of Poly(lactic Acid) (PLA) and Poly(butylene Adipate-Co-Terephthalate) (PBAT) and Their Blends upon Melt Processing.” *Polymer Degradation and Stability* 94 (1). Elsevier Ltd: 74–82. doi:10.1016/j.polymdegradstab.2008.10.004.
- Skardal, Aleksander, Jianxing Zhang, and Glenn D. Prestwich. 2010. “Bioprinting Vessel-like Constructs Using Hyaluronan Hydrogels Crosslinked with Tetrahedral Polyethylene Glycol Tetracrylates.” *Biomaterials* 31 (24). Elsevier Ltd: 6173–81. doi:10.1016/j.biomaterials.2010.04.045.
- Smith, Cynthia M., Alice L. Stone, Robert L. Parkhill, Robert L. Stewart, Mark W. Simpkins, Anatoly M. Kachurin, William L. Warren, and Stuart K. Williams. 2004. “Three-Dimensional BioAssembly Tool for Generating Viable Tissue-Engineered Constructs.” *Tissue Engineering* 10 (9): 1566–76. doi:10.1089/1076327042500274.
- Snyder, J E, Q Hamid, C Wang, R Chang, K Emami, H Wu, and W Sun. 2011. “Bioprinting Cell-Laden Matrigel for Radioprotection Study of Liver by pro-Drug Conversion in a Dual-Tissue Microfluidic Chip.” *Biofabrication* 3 (3): 34112. doi:10.1088/1758-5082/3/3/034112.
- Solorio, Loran D, Andrew S Fu, Roberto Hernández-Irizarry, and Eben Alsberg. 2010. “Chondrogenic Differentiation of Human Mesenchymal Stem Cell Aggregates via Controlled Release of TGF-beta1 from Incorporated Polymer Microspheres.” *Journal of Biomedical Materials Research. Part A* 92 (3): 1139–44. doi:10.1002/jbm.a.32440.
- Song, Seung Joon, Jaesoon Choi, Yong Doo Park, Jung Joo Lee, So Young Hong, and Kyung Sun. 2010. “A Three-Dimensional Bioprinting System for Use with a Hydrogel-Based Biomaterial and Printing Parameter Characterization.” *Artificial Organs* 34 (11): 1044–48. doi:10.1111/j.1525-1594.2010.01143.x.
- Sridhar, Balaji V., John L. Brock, Jason S. Silver, Jennifer L. Leight, Mark A. Randolph,

- and Kristi S. Anseth. 2015. "Development of a Cellularly Degradable PEG Hydrogel to Promote Articular Cartilage Extracellular Matrix Deposition." *Advanced Healthcare Materials* 4 (5): 702–13. doi:10.1002/adhm.201400695.
- Stansbury, Jeffrey W, and Mike J Idacavage. 2016. "3D Printing with Polymers: Challenges among Expanding Options and Opportunities." *Dental Materials* 32 (1): 54–64. doi:http://dx.doi.org/10.1016/j.dental.2015.09.018.
- Steve, Makadia Hirenkumar and Siegel Steve, Poly, Controlled Drug, and Delivery Carrier. 2012. "Poly Lactic-Co-Glycolic Acid (PLGA) as Biodegradable Controlled Drug Delivery Carrier." *Polymers* 3 (3): 1–19. doi:10.3390/polym3031377.Poly.
- Sung, Hsing Wen, Don Mou Huang, Wen Hsiang Chang, Rong Nan Huang, and Jer Chen Hsu. 1999. "Evaluation of Gelatin Hydrogel Crosslinked with Various Crosslinking Agents as Bioadhesives: In Vitro Study." *Journal of Biomedical Materials Research* 46 (4): 520–30. doi:10.1002/(SICI)1097-4636(19990915)46:4<520::AID-JBM10>3.0.CO;2-9.
- Tasoglu, Savas, and Utkan Demirci. 2013. "Bioprinting for Stem Cell Research." *Trends in Biotechnology* 31 (1): 10–19. doi:http://dx.doi.org/10.1016/j.tibtech.2012.10.005.
- Taylor, M S, A U Daniels, K P Andriano, and J Heller. 1994. "Six Bioabsorbable Polymers: In Vitro Acute Toxicity of Accumulated Degradation Products." *Journal of Applied Biomaterials: An Official Journal of the Society for Biomaterials* 5 (2). United States: 151–57. doi:10.1002/jab.770050208.
- Thornton, Mona Anne, and Martyn Mendelsohn. 2006. "Total Skeletal Reconstruction of the Nasal Dorsum." *Archives of Otolaryngology--Head & Neck Surgery* 132 (11): 1183–88. doi:10.1001/archotol.132.11.1183.
- Togo, Takeshi, Atsushi Utani, Motoko Naitoh, Masayoshi Ohta, Yasumi Tsuji, Noriyuki Morikawa, Motonobu Nakamura, and Shigehiko Suzuki. 2006. "Identification of Cartilage Progenitor Cells in the Adult Ear Perichondrium: Utilization for Cartilage Reconstruction." *Laboratory Investigation; a Journal of Technical Methods and Pathology* 86 (5): 445–57. doi:10.1038/labinvest.3700409.
- Urgery, S, I Ncorporated, and Hydrogel-expanded Chondrocytes. 2014. "Improved Chondrogenic Capacity of Collagen," 1109–17.
- Valkenaers, H, F Vogeler, Eleonora Ferraris, a Voet, and J.-P. Kruth. 2013. "A Novel Approach to Additive Manufacturing: Screw Extrusion 3D-Printing." *4M Conference*, no. c: 235–38. doi:10.3850/978-981-07-7247-5-359.
- Van Den Bulcke, An I, Bogdan Bogdanov, Nadine De Rooze, Etienne H Schacht, Maria Cornelissen, and Hugo Berghmans. 2000. "Structural and Rheological Properties of Methacrylamide Modified Gelatin Hydrogels." *Biomacromolecules* 1 (1): 31–38. doi:10.1021/bm990017d.
- Van den Steen, Philippe E, Bénédicte Dubois, Inge Nelissen, Pauline M Rudd, Raymond a Dwek, and Ghislain Opdenakker. 2013. "Biochemistry and Molecular Biology of Gelatinase B or Matrix Metalloproteinase-9 (MMP-9)." *Crit. Rev. Biochem.*

Mol. Biol. 37 (6): 375–536. doi:10.1080/10409230290771546.

- Ventola, C Lee. 2014. “Medical Applications for 3D Printing: Current and Projected Uses.” *P & T: A Peer-Reviewed Journal for Formulary Management* 39 (10): 704–11. doi:10.1016/j.infsof.2008.09.005.
- Verdonk, P C M, R G Forsyth, J Wang, K F Almqvist, R Verdonk, E M Veys, and G Verbruggen. 2005. “Characterisation of Human Knee Meniscus Cell Phenotype.” *Osteoarthritis and Cartilage* 13 (7): 548–60. doi:http://dx.doi.org/10.1016/j.joca.2005.01.010.
- Vermonden, Tina, Natalja E. Fedorovich, Daphne van Geemen, Jacqueline Alblas, Cornelus F. van Nostrum, W. J A Dhert, and Wim E. Hennink. 2008. “Photopolymerized Thermosensitive Hydrogels: Synthesis, Degradation, and Cytocompatibility.” *Biomacromolecules* 9 (3): 919–26. doi:10.1021/bm7013075.
- Vinatier, Claire, Dominique Mrugala, Christian Jorgensen, Jérôme Guicheux, and Danièle Noël. 2009. “Cartilage Engineering: A Crucial Combination of Cells, Biomaterials and Biofactors.” *Trends in Biotechnology* 27 (5): 307–14. doi:10.1016/j.tibtech.2009.02.005.
- Vinogradov, G.V., and A.Y. Malkin. 1980. *Rheology of Polymers*. Berlin: Springer-Verlag Berlin Heidelberg.
- Visser, Jetze, Ferry P W Melchels, June E Jeon, Erik M Van Bussel, Laura S Kimpton, Helen M Byrne, Wouter J A Dhert, Paul D Dalton, Dietmar W Huttmacher, and Jos Malda. 2015. “Reinforcement of Hydrogels Using Three-Dimensionally Printed Microfibre.” *Nature Communications*. Nature Publishing Group, 1–10. doi:10.1038/ncomms7933.
- Visser, Jetze, Benjamin Peters, Thijs J Burger, Jelle Boomstra, Wouter J a Dhert, Ferry P W Melchels, and Jos Malda. 2013a. “Biofabrication of Multi-Material Anatomically Shaped Tissue Constructs.” *Biofabrication* 5: 35007. doi:10.1088/1758-5082/5/3/035007.
- Visser, Jetze, Benjamin Peters, Thijs J Burger, Jelle Boomstra, Wouter J A Dhert, Ferry P W Melchels, and Jos Malda. 2013b. “Biofabrication of Multi-Material Anatomically Shaped Tissue Constructs.” *Biofabrication* 5 (3): 35007. doi:10.1088/1758-5082/5/3/035007.
- von Hippel, Peter H. 1965. “The Macromolecular Chemistry of Gelatin.” *Journal of the American Chemical Society* 87 (8). American Chemical Society: 1824. doi:10.1021/ja01086a059.
- Wakitani, S, T Mitsuoka, N Nakamura, Y Toritsuka, Y Nakamura, and S Horibe. 2004. “Autologous Bone Marrow Stromal Cell Transplantation for Repair of Full-Thickness Articular Cartilage Defects in Human Patellae: Two Case Reports.” *Cell Transplant* 13 (5): 595–600. doi:10.3727/000000004783983747.
- Walton, Robert L., Gary C. Burget, and Elisabeth K. Beahm. 2005. “Microsurgical Reconstruction of the Nasal Lining.” *Plastic and Reconstructive Surgery* 115 (7): 1813–29. doi:10.1097/01.PRS.0000164683.34767.2F.

- Wan, Leo Q, D Ph, Jie Jiang, Diana E Miller, X Edward Guo, Van C Mow, and Helen H Lu. 2011. "Matrix Deposition Modulates the Viscoelastic Shear Properties of Hydrogel-Based Cartilage Grafts" 17. doi:10.1089/ten.tea.2010.0379.
- Wang, Chen-Chie, Kai-Chiang Yang, Keng-Hui Lin, Yen-Liang Liu, Hwa-Chang Liu, and Feng-Huei Lin. 2012. "Cartilage Regeneration in SCID Mice Using a Highly Organized Three-Dimensional Alginate Scaffold." *Biomaterials* 33 (1). Elsevier Ltd: 120–27. doi:10.1016/j.biomaterials.2011.09.042.
- Wang, Jianqi, Fengjie Zhang, Wing Pui Tsang, Chao Wan, and Chi Wu. 2017. "Fabrication of Injectable High Strength Hydrogel Based on 4-Arm Star PEG for Cartilage Tissue Engineering." *Biomaterials* 120: 11–21. doi:http://dx.doi.org/10.1016/j.biomaterials.2016.12.015.
- Wang, Juan, Yun Wei, Shasha Zhao, Ying Zhou, Wei He, Yang Zhang, and Wensheng Deng. 2017. "The Analysis of Viability for Mammalian Cells Treated at Different Temperatures and Its Application in Cell Shipment," 1–16.
- Wang, Mingjie, Zhiguo Yuan, Ning Ma, Chunxiang Hao, Weimin Guo, Gengyi Zou, Yu Zhang, et al. 2017. "Advances and Prospects in Stem Cells for Cartilage Regeneration." *Stem Cells International* 2017. doi:10.1155/2017/4130607.
- Wang, Shuai, Jia Min Lee, and Wai Yee Yeong. 2015. "Smart Hydrogels for 3D Bioprinting." *International Journal of Bioprinting*. doi:10.18063/IJB.2015.01.005.
- Watelet, J B, and P Van Cauwenberge. 1999. "Applied Anatomy and Physiology of the Nose and Paranasal Sinuses." *Allergy* 54 Suppl 5 (1): 14–25. http://www.ncbi.nlm.nih.gov/pubmed/10565476.
- Wilson, W. Cris, and Thomas Boland. 2003. "Cell and Organ Printing 1: Protein and Cell Printers." *The Anatomical Record* 272A (2): 491–96. doi:10.1002/ar.a.10057.
- Winslow, Catherine P, Ted A Cook, Alan Burke, and Mark K Wax. 2003. "Total Nasal Reconstruction" 5: 159–63.
- Wolf, Ivo, Marcus Vetter, Ingmar Wegner, Thomas Böttger, Marco Nolden, Max Schöbinger, Mark Hastenteufel, Tobias Kunert, and Hans-Peter Meinzer. 2005. "The Medical Imaging Interaction Toolkit." *Medical Image Analysis* 9 (6): 594–604. doi:http://dx.doi.org/10.1016/j.media.2005.04.005.
- Wong, Joyce Y, Jennie B Leach, and Xin Q Brown. 2004. "Balance of Chemistry, Topography, and Mechanics at the Cell–biomaterial Interface: Issues and Challenges for Assessing the Role of Substrate Mechanics on Cell Response." *Surface Science* 570 (1): 119–33. doi:http://dx.doi.org/10.1016/j.susc.2004.06.186.
- Woodruff, Maria Ann, and Dietmar Werner Hutmacher. 2010. "The Return of a Forgotten polymer—Polycaprolactone in the 21st Century." *Progress in Polymer Science* 35 (10): 1217–56. doi:10.1016/j.progpolymsci.2010.04.002.
- Wormall, A. 1944. "Non-Antigenicity of Gelatin." *Nature*, no. 154: 332.
- Xu, Mingen, Xiaohong Wang, Yongnian Yan, Ri Yao, and Yakun Ge. 2010. "An Cell-Assembly Derived Physiological 3D Model of the Metabolic Syndrome, Based on

- Adipose-Derived Stromal Cells and a Gelatin/alginate/fibrinogen Matrix.” *Biomaterials* 31 (14). Elsevier Ltd: 3868–77. doi:10.1016/j.biomaterials.2010.01.111.
- Xu, Nanfang, Feng Wei, Xiaoguang Liu, Liang Jiang, Hong Cai, Zihe Li, Miao Yu, Fengliang Wu, and Zhongjun Liu. 2016. “Reconstruction of the Upper Cervical Spine Using a Personalized 3D-Printed Vertebral Body in an Adolescent With Ewing Sarcoma.” *Spine* 41 (1). http://journals.lww.com/spinejournal/Fulltext/2016/01000/Reconstruction_of_the_Upper_Cervical_Spine_Using_a.21.aspx.
- Xu, Tao, Joyce Jin, Cassie Gregory, James Hickman, and Thomas Boland. 2005. “Inkjet Printing of Viable Mammalian Cells.” *Biomaterials* 26 (1): 93. <http://dx.doi.org/10.1016/j.biomaterials.2004.04.011>.
- Xu, Tao, Weixin Zhao, Jian Ming Zhu, Mohammad Z. Albanna, James J. Yoo, and Anthony Atala. 2013. “Complex Heterogeneous Tissue Constructs Containing Multiple Cell Types Prepared by Inkjet Printing Technology.” *Biomaterials* 34 (1). Elsevier Ltd: 130–39. doi:10.1016/j.biomaterials.2012.09.035.
- Yan, Jingyuan, Yong Huang, and Douglas B Chrisey. 2012. “Laser-Assisted Printing of Alginate Long Tubes and Annular Constructs.” *Biofabrication* 5 (1): 15002. doi:10.1088/1758-5082/5/1/015002.
- Yang, K G Auw, D B F Saris, R E Geuze, Y J M Van Der Helm, M H P Van Rijen, a J Verbout, W J a Dhert, and L B Creemers. 2006. “Impact of Expansion and Redifferentiation Conditions on Chondrogenic Capacity of Cultured Chondrocytes.” *Tissue Engineering* 12 (9): 2435–47. doi:10.1089/ten.2006.12.ft-210.
- Yang, Mingyuan, Chao Li, Yanming Li, Yingchuan Zhao, Xianzhao Wei, Guoyou Zhang, Jianping Fan, et al. 2015. “Application of 3D Rapid Prototyping Technology in Posterior Corrective Surgery for Lenke 1 Adolescent Idiopathic Scoliosis Patients.” *Medicine* 94 (8): e582. doi:10.1097/MD.0000000000000582.
- Yonenaga, Kazumichi, Satoru Nishizawa, Takumi Nakagawa, Yuko Fujihara, Yukiyo Asawa, Atsuhiko Hikita, Tsuyoshi Takato, and Kazuto Hoshi. 2017. “Optimal Conditions of Collagenase Treatment for Isolation of Articular Chondrocytes from Aged Human Tissues.” *Regenerative Therapy* 6 (June): 9–14. doi:<https://doi.org/10.1016/j.reth.2016.08.001>.
- You, Fu, B. Frank Eames, and Xiongbiao Chen. 2017. “Application of Extrusion-Based Hydrogel Bioprinting for Cartilage Tissue Engineering.” *International Journal of Molecular Sciences* 18 (7): 8–14. doi:10.3390/ijms18071597.
- You, Fu, Xia Wu, Ning Zhu, Ming Lei, B. Frank Eames, and Xiongbiao Chen. 2016. “3D Printing of Porous Cell-Laden Hydrogel Constructs for Potential Applications in Cartilage Tissue Engineering.” *ACS Biomaterials Science and Engineering* 2 (7): 1200–1210. doi:10.1021/acsbiomaterials.6b00258.
- Young, Charlotte, John Cherrie, Martie Van Tongeren, Lea Fortunato, Sally Hutchings, and Lesley Rushton. 2010. “The Burden of Occupational Cancer in Great Britain.”

Institute of Occupational Medicine.

- Yue, Kan, Grissel Trujillo-de Santiago, Mario Moisés Alvarez, Ali Tamayol, Nasim Annabi, and Ali Khademhosseini. 2015. "Synthesis, Properties, and Biomedical Applications of Gelatin Methacryloyl (GelMA) Hydrogels." *Biomaterials* 73. Elsevier Ltd: 254–71. doi:10.1016/j.biomaterials.2015.08.045.
- Zeifang, Felix, Doris Oberle, Corinna Nierhoff, Wiltrud Richter, Babak Moradi, and Holger Schmitt. 2010. "Autologous Chondrocyte Implantation Using the Original Periosteum-Cover Technique versus Matrix-Associated Autologous Chondrocyte Implantation." *The American Journal of Sports Medicine* 38 (5): 924–33. doi:10.1177/0363546509351499.
- Zein, Iwan, Dietmar W. Hutmacher, Kim Cheng Tan, and Swee Hin Teoh. 2002. "Fused Deposition Modeling of Novel Scaffold Architectures for Tissue Engineering Applications." *Biomaterials* 23 (4): 1169–85. doi:10.1016/S0142-9612(01)00232-0.
- Zhang, Liangming, Peiqiang Su, Caixia Xu, Junlin Yang, Weihua Yu, and Dongsheng Huang. 2010. "Chondrogenic Differentiation of Human Mesenchymal Stem Cells: A Comparison between Micromass and Pellet Culture Systems." *Biotechnology Letters* 32 (9): 1339–46. doi:10.1007/s10529-010-0293-x.
- Zhang, Quan, Dong Yan, Kai Zhang, and Gengkai Hu. 2015. "Pattern Transformation of Heat-Shrinkable Polymer by Three-Dimensional (3D) Printing Technique." *Scientific Reports* 5: 8936. doi:10.1038/srep08936.
- Zhang, Yingying, Fei Yang, Kai Liu, Hong Shen, Yueqian Zhu, Wenjie Zhang, Wei Liu, Shenguo Wang, Yilin Cao, and Guangdong Zhou. 2012. "The Impact of PLGA Scaffold Orientation on in Vitro Cartilage Regeneration." *Biomaterials* 33 (10): 2926–35. doi:http://dx.doi.org/10.1016/j.biomaterials.2012.01.006.
- Zhang, Zijun, J Michael McCaffery, Richard G S Spencer, and Clair a Francomano. 2004. "Hyaline Cartilage Engineered by Chondrocytes in Pellet Culture: Histological, Immunohistochemical and Ultrastructural Analysis in Comparison with Cartilage Explants." *Journal of Anatomy* 205 (3): 229–37. doi:10.1111/j.0021-8782.2004.00327.x.
- Zhao, Xing, David A Bichara, Libin Zhou, Katherine M Kulig, Alan Tseng, Christopher M Bowley, Joseph P Vacanti, Irina Pomerantseva, Cathryn A Sundback, and Mark A Randolph. 2015. "Conditions for Seeding and Promoting Neo-Auricular Cartilage Formation in a Fibrous Collagen Scaffold." *Journal of Cranio-Maxillo-Facial Surgery: Official Publication of the European Association for Cranio-Maxillo-Facial Surgery* 43 (3): 382–89. doi:10.1016/j.jcms.2014.12.007.
- Zopf, David A, Colleen L Flanagan, Matthew Wheeler, J Scott, and Glenn E Green. 2014. "Treatment of Severe Porcine Tracheomalacia with a 3-Dimensionally Printed, Bioresorbable, External Airway Splint." *JAMA Otolaryngology–Head & Neck Surgery* 140 (61): 66–71. doi:10.1001/jamaoto.2013.5644.Treatment.

Appendices

Appendix 1: videos

Appendices presented here must be viewed as a media file using the provided link. These demonstrate acquired video files so supplement the observations contained within this thesis.

Appendix 1.1. PCL 3D printed nose

<https://www.dropbox.com/s/z50l0obz173xdh3/3d%20printing%20PCL%20nose.wmv?dl=0>

Appendix 1.2. PCL-GelMA co-printing

<https://www.dropbox.com/s/5lvfx25lmlgl3a9/gelma.mp4?dl=0>

Appendix 2: solutions

2.1. Isolation of cells

2.1.1. PBS solution

PBS	1 tablet
dH ₂ O	100 ml

PBS tablets were dissolved in dH₂O and autoclaved at 120 °C. PBS was stored until required.

2.1.2. PBS A/A

PBS solution 90 ml

Antibiotic antimicotic solution 10 ml

PBS A/A was stored at 4°C until required.

2.1.3. Collagenase digestion medium (0.2%)

α -MEM 50 ml

Gentamicin 10mg/ml 500 μ l

Collagenase from *Clostridium histolyticum* 100mg

2.1.4. Heparinised medium

Heparin sodium 1 ml

α -MEM 500 ml

2.2. Cell culture

2.2.1. Standard ShCh culture medium

FCS 25 ml

NEAA 5 ml

L-glutamine 5 ml

Antibiotic antimycotic solution	5 ml
Ascorbic acid-2-phosphate	0.025g
L-proline	0.023 g
α -MEM	500 ml

All supplements were passed through a 0.2 μ M filter into the α -MEM. Medium was stored at 4 °C.

2.2.2. ShMSCs culture medium

FCS	100 ml
NEAA	5 ml
L-glutamine	5 ml
Antibiotic antimycotic solution	5 ml
Ascorbic acid-2-phosphate	0.025g
DMEM	400 ml

All supplements were passed through a 0.2 μ M filter into the α -MEM. Medium was stored at 4 °C.

2.2.3. Cryopreservation medium

DMSO 5 ml

FCS 45 ml

Cryopreservation medium was passed through a 0.2 μ M filter and stored at -20 °C

2.2.4. Osteogenic medium

ShMSCs culture medium 200 ml

Dexamethasone 1.1 μ M

Beta glycerol phosphate 8 Mm

NEAA 2 ml

All supplements were passed through a 0.2 μ M filter into the ShMSCs culture medium.

Medium was stored at 4 °C.

2.2.5. Adipogenic medium

ShMSCs culture medium 200 ml

Dexamethasone 1.1 μ M

IBMX 10 μ g/ml

All supplements were passed through a 0.2 μ M filter into the ShMSCs culture medium.

Medium was stored at 4 °C.

2.2.6. Chondrogenic differentiation medium

NEAA	5 ml
L-glutamine	5 ml
Antibiotic antimycotic solution	5 ml
Ascorbic acid-2-phosphate	0.025g
TFG- β	10 ng/ml
ITS	1% (v/v)
DMEM	400 ml

All supplements were passed through a 0.2 μ M filter into the ShMSCs culture medium.

Medium was stored at 4 °C.

2.3. Biochemical analysis

2.3.1. LIVE/DEAD solution

PBS	10 ml
Calcein AM	2 μ M
EthD-1	4 μ M

2.3.2. Papain solution

2.3.2.1. Papain buffer

Dibasic sodium phosphate	1.4 g (0.1 M)
Cysteine hydrochloride	0.079 g (0.005 M)
EDTA	0.186 g (0.005 M)
dH ₂ O	100 ml

Papain buffer can be prepared up to 3 months in advance and stored 4°C.

2.3.2.2. Papain solution

Papain buffer	25 ml
Papain	0.0241g

Papain solution was prepared 2 hours before use.

2.3.3. DMMB solution

Sodium formate	2 g (0.03 M)
DMMB	0.016 g (0.046 mM)
Ethanol	5 ml
Formic acid	2 ml
dH ₂ O	990 ml

DMMB was stored at room temperature in a foil-wrapped bottle for up to 3 months.

2.3.4. Chondroitin sulphate stock solution

Chondroitin-4-sulphate 0.01g

dH₂O 10 ml

2.4. Histological analysis

2.4.1. Histology working solutions

2.4.1.1. Safranin O

Safranin O 0.1g

dH₂O 100 ml

2.4.1.2. Fast green solution

Fast green 0.02g

dH₂O 100 ml

2.5. Immunohistochemistry analysis

2.5.1. Triton X-100 in PBS

Triton X-100 100 µl

PBS 100 ml

2.5.2. Blocking solution

Donkey serum 4 ml

PBS 100 ml

2.5.3. BSA (1 % w/v) in PBS

BSA 0.1 g

PBS 10 ml

